Plate Tectonic Constraints on Flat Subduction
and
Paleomagnetic Constraints on Rifting

Thesis by

Steven Michael Skinner

In Partial Fulfillment of the Requirements for the degree
of
Doctor of Philosophy

CALIFORNIA INSTITUTE OF TECHNOLOGY
Pasadena, California
2013
(Defended May 27, 2013)

AMS

"[...] the method of choice for fabric studies in tuffs"
— *Ellwood, B., MacDonald, J., & Wolff, W. (1991)*

"[...] also has its drawbacks"
— *Seaman, S., & Williams, M. (1992)*

Acknowledgements

Seven years of study at Caltech creates a long list of people that need to be thanked and I am sure that someone will be left off this list. I have to thank Clarence Hall for setting me on the path I have taken. I am incredibly grateful to my two advisors Rob Clayton and Joann Stock. They have let me pursue all of my diverse interests, without too much scowling. Joann was always understanding when Rob would send me to lead an instrument installation team in Peru for the summer, and Rob was always understanding when Joann would send me out to the Salton Sea to read tile drain maps or load explosives. They were both very understanding when I decided to go on a wild ride with the Argentine in Antarctica.

I would like to thank Joe Kirschvink for giving me the opportunity to go on an unforgettable Antarctic adventure. In addition, Joe has very generously given me free range of his lab and has taught me a great deal about paleomagnetics. The 136 series, championed by Joe, has given me the chance to visit many geologically interesting locations in the Southwest, and then revisit some of those place and share my knowledge with others. Jason Saleeby has provided countless stimulating experiences in the field; from around LA, to the southern Sierra, and in Hawaii. After several of his firehose lectures I feel like I have come away with a much better understanding of the evolution of California. Jean-Philippe Avouac has been a wonderful academic advisor, always trying to keep me on course.

Thanks to all of the paleomagnetists, that have filtered through the lab while I have been here, for stimulating discussion: Tim Raub, Plinio Jaqueto, Jeroen Hansma, Angel Olguin-Villa, and Florencia Milanese. A large portion of my rockmagnetic work was carried out at the Institute for Rock Magnetism. I am indebted to Dario Bilardello, Peat Solheid, and most of all Michael Jackson, for allowing me to repeatedly break their machines and all of their help collecting and interpreting data.

All my fellow students in GPS have made my time here more than enjoyable. Andrew Matzen and Willy Amidon always provided excitement in the field. Caitlin Murphy was always ready for a churro and Dole whip, or breakfast before any restaurants were open. I have to thank my pit-mates for their continued friendship and support even past our time in the basement. Steve Chemtob, Anne Dekas, Celia Schiffman, Maia Schweizer, Nithya Thiagarajan, and Wang Yu. All of the occupants of 310 NM past and present: Charlie Verdel, Ryan Petterson, Aaron Meltzner, Alan Chapman, Kristel Chanard, Jeff Thompson, Marion Thomas, Erika Swanson, Jen Hamon, and Jason Price.

I have to thank the field team in Peru for making high altitude digging so much fun: Victor Aguilar, Kristen Phillips, Alan Husker, Erin Burkett, Igor Stubailo, Jenifer Sery, Emily Foote, and Richard Guy. The field crew in the Salton Sea for some great offroad adventures in Vinagre Wash: Frank Sousa, Kathy Davenport, Liz Rose, and Panda. Ricardo Arce always got us to and from IAG safely. Arturo Martin-Barajas is invaluable for his support in the field and for all of his help with the logistics of working in Mexico in addition to scientific discussions. My field assistants on IAG, Sarah Slotznick and Rene Fernandez, for making hauling seawater uphill every day an enjoyable task. Alison Piasecki, as my field assistant on the peninsula, saved me from walking into a hive of bees and was always mindful of conserving drinking water.

I have to thank the GPS division, John Eiler, and Paul Asimow for two enriching trips to the Alps and Japan. The behind-the-scenes staff of GPS has made getting my job done so much easier. Donna Mireles and Rosemary Miller always made sure my reimbursements went through as quickly as possible. Dian Buchness and Marsha Hudson for M&M breaks, plus all the actual work they have helped me with. Tony Diaz and the late Jim O'Donnell helped me gain access to any resource I needed. Mark Garcia was always ready with a new saw blade and he muscle needed to change it. Terry Gennaro for still handing over the keys after I had covered the new truck in mud and thrown a rod on the old one. Mark Turner was always receptive to my new ideas for GPlates. Lisa Christiansen was always available with a suggestion whenever Arc would not do what I wanted it to. I have to thank Heather for making every day at work just like another day in paradise.

Most of all I have to thank my friends and family (157th , eastbay, and windeck-stein) for their unending support and putting up with me and my increasingly large rock collection.

Abstract

Plate tectonics shapes our dynamic planet through the creation and destruction of lithosphere. This work focuses on increasing our understanding of the processes at convergent and divergent boundaries through geologic and geophysical observations at modern plate boundaries. Recent work had shown that the subducting slab in central Mexico is most likely the flattest on Earth, yet there was no consensus about what caused it to originate. The first chapter of this thesis sets out to systematically test all previously proposed mechanisms for slab flattening on the Mexican case. What we have discovered is that there is only one model for which we can find no contradictory evidence. The lack of applicability of the standard mechanisms used to explain flat subduction in the Mexican example led us to question their applications globally. The second chapter expands the search for a cause of flat subduction, in both space and time. We focus on the historical record of flat slabs in South America and look for a correlation between the shallowing and steepening of slab segments with relation to the inferred thickness of the subducting oceanic crust. Using plate reconstructions and the assumption that a crustal anomaly formed on a spreading ridge will produce two conjugate features, we recreate the history of subduction along the South American margin and find that there is no correlation between the subduction of a bathymetric highs and shallow subduction. These studies have proven that a subducting crustal anomaly is neither a sufficient or necessary condition of flat slab subduction. The final chapter in this thesis looks at the divergent plate boundary in the Gulf of California. Through geologic reconnaissance mapping and an intensive paleomagnetic sampling campaign, we try to constrain the location and orientation of a widespread volcanic marker unit, the Tuff of San Felipe. Although

the resolution of the applied magnetic susceptibility technique proved inadequate to contain the direction of the pyroclastic flow with high precision, we have been able to detect the tectonic rotation of coherent blocks as well as rotation within blocks.

Contents

List of Figures

Appendix II

List of Tables

Introduction

Plate boundaries create dramatic physiography and are the location of the driving forces of plate tectonics. This thesis uses geologic and geophysical data to shed light on the processes at two types of plate boundaries. Part I of this thesis looks at causes of change in subduction zone geometry. Part II of this thesis is a detailed paleomagnetic and rock magnetic study of an important volcanic unit used to constrain rifting in the Gulf of California.

Part I of this thesis consists of two chapters that explore the causes for shallow and flat subduction. Shallow subduction occurs at 10% of global subduction zones. Many hypotheses have been proposed to try and explain the changes that we observe in the geometry of the subducting slabs at subduction zones. The age of the subducting plate, mantle wind, mantle wedge suction, and overthrusting of the upper plate have all been put forth as causes for shallow subduction. The most common explanation for shallow subduction is the buoyant impactor hypothesis. This hypothesis draws a correlation between the subduction of a bathymetric anomaly or zone of thickened oceanic crust and zones of shallow subduction. Chapter 1 focused on the flat slab in central Mexico, which cannot be explained by the buoyant impactor hypothesis. We systematically investigate all previously proposed causes for flat subduction in Mexico. Of all the proposed mechanisms for flat slabs in Mexico, the only one that we cannot falsify is the hydration hypothesis. We believe that hydration of the mantle wedge has lowered its viscosity and can explain the geometry of the subducting slab and the decoupling of the two plates along the horizontal interface. Chapter 2 takes a more global look at the buoyant impactor hypothesis of shallow subduction. We find that this hypothesis is not universally applicable. There are subduction zones where bathymetric anomalies subduct without changing the geometry of the down-going plate and there are locations where there is a flat or shallow slab that does not have an associated subducting bathymetric anomaly. We have determined that there is no spatial correlation between bathymetric anomalies and flat slabs. We have extended our investigation of the bathymetric anomaly hypothesis back in time by using plate reconstructions to track conjugate bathymetric features is both space and time relative to the historic flat slabs of South America. We again find that there is no direct correlation between the subduction of a bathymetric anomaly and zones of flat subduction. Our reconstruction of conjugate features in the Pacific basin also reveals that the conjugate to the Marquesas plateau was previously mislocated. The Peruvian flat slab extends well beyond the width of the subducting Nazca ridge, which is proposed as its cause. The conjugate to the Marquesas was proposed as a cause of increased buoyancy that could support the northern extent of the Peruvian flat slab. Our reconstructions are robust and are able to predict the location of observable bathymetric features and show that the conjugate to the Marquesas is not located near the Peruvian flat slab.

Part II of this thesis tests a new approach for locating piercing points to aid in the identification and measurement of fault offset in the Gulf of California extensional province. Half of the displacement expected from the rifting of Baja California from mainland Mexico has yet to be identified in the field. The magnitude and timing of displacement within the Gulf of California itself has been well documented; however, the paleogeographic location of Isla Angel de la Guarda is not well constrained. We have intensively sampled a regionally extensive volcanic deposit, the Tuff of San Felipe, for paleomagnetic analysis. Anisotropy of magnetic susceptibility (AMS) measurements were made on all samples collected, in order to define the flow direction of the pyroclastic density current and identify regions of coherent flow that could then be used to constrain the offset of the unit. Our sampling on the island was spatially and stratigraphically extensive in order to capture the full three-dimensional nature of the flow. Our results show that AMS is not an appropriate tool for recognizing small-scale coherent flow. The AMS fabric is highly sensitive to the local conditions at the point of deposition and does not aid in the recognition of coherent flow patterns. Extensive rock magnetic experiments constrain the magnetic mineralogy and grain size and indicate that there is no significant variation that can explain the deviations we observe in the AMS fabric. Our paleomagnetic measurements reveal a rotation within the tuff, and several hypotheses are put forth toward explaining it.

Part I

Plate Tectonic Constraints on Flat Subduction

Chapter 1

An Evaluation of proposed mechanisms of slab flattening in central Mexico

Originally published in:

Skinner, S. M., & Clayton, R. W. (2010). An Evaluation of Proposed Mechanisms of Slab Flattening in Central Mexico. Pure and Applied Geophysics, 168(8-9), 1461-1474. doi: 10.1007/s00024-010-0200-3

Abstract

Central Mexico is the site of an enigmatic zone of flat subduction. The general geometry of the subducting slab has been known for some time and is characterized by a horizontal zone bounded on either side by two moderately dipping sections. We systematically evaluate proposed hypotheses for shallow subduction in Mexico based on the spatial and temporal evidence, and we find no simple or obvious explanation for the shallow subduction in Mexico. We are unable to locate an oceanic lithosphere impactor, or the conjugate of an impactor, that is most often called upon to explain shallow subduction zones as in South America, Japan, and Laramide deformation in the US. The only bathymetric feature that is of the right age and in the correct position on the conjugate plate is a set of unnamed seamounts that are too small to have a significant effect on the buoyancy of the slab. The only candidate that we cannot dismiss is a change in the dynamics of subduction through a change in wedge viscosity, possibly caused by water brought in by the slab. The incoming plate adjacent to the flat subduction is anomalously rough, providing a possible source for water to enter the slab.

Introduction

The major driving force of plate motion is slab buoyancy and the pull of subducting slabs descending into the mantle (Billen and Hirth, 2007; Chapple and Tullis, 1977; Forsyth and Uyeda, 1975). However, the current understanding of the initiation of subduction zones and the balance of forces controlling the 3D geometry and evolution of a subducting slab is not well understood (Billen, 2008). The angle of subduction influences the overall state of stress in the overriding slab, the resulting mode of deformation, and the location and type of arc volcanism.

Shallow or flat subduction occurs in 10% of the subduction zones present today (van Hunen et al., 2002). The global variation of slab dips is shown in Figure 1. Present day zones of shallow subduction include the Nankai trough of Japan, northern and southern Peru, Central Chile, East Aleutians in Alaska, and Mexico. A number of these are coincident with oceanic impactors, anomalously thick crust in the form of an aseismic ridge or plateau, that are presumed to be the cause of the shallow geometry. The Chilean flat slab coincides with the subduction of the Juan-Fernandez ridge (Anderson et al., 2007; Kay and Abbruzzi, 1996; Pilger, 1981). The Peruvian flat slab is a combination of two adjacent flat segments resulting from subduction of the Nazca ridge and the Inca plateau (Gutscher et al., 1999b). There is a possible flat slab segment in Ecuador that correlates with the subduction of the Carnegie Ridge (Gutscher et al., 1999a). Oceanic lithosphere of the Caribbean oceanic plateau might be causing a flat slab in northwestern Columbia (Gutscher et al., 2000a). Subduction of the Cocos ridge has led to a flat slab in Costa Rica (Protti et al., 1995; Sak et al., 2009), and the Yakutat terrane is subducting in the zone of the East Aleutian flat slab (Brocher et al., 1994; Fuis et al., 2008). The flat slab of southwestern Japan has been linked to subduction of the Izu Bonin arc and the Palau-Kyushu ridge (Gutscher et al., 2000b), and western New Guinea has a flat segment linked to subduction of the Euripik ridge (Gutscher et al., 2000b). In northern Chile, the current dip of the slab is not flat but is actively flattening due to the subduction of the Iquique Ridge (Espurt et al., 2008).

However, in two cases there is no obvious impactor associated with the flat subduction. In the Cascadia subduction zone, for example, there is no evidence for thickened crust subducting along the shallow dipping Washington segment (Gutscher et al., 2000c). The flat slab in

Mexico has been attributed to the Tehuantepec ridge (Gutscher et al., 2000c), however the Tehuantepec ridge is being subducted at a point where the slab is dipping at 30 degrees and appears to have little effect on the angle. In locations where an impactor has been identified, the spatial correlation between the impactor and zone of shallow subduction does not hold up when looked at in detail. In the Nankai trough for example, the Palau-Kyushu ridge is entering the trench at the southern limit of the shallow zone. Figure 2 shows the anticorrelation between the shallow zone and where ridges are subducting. The fact that the impactor and zone of shallow subduction do not align suggest that it is not the buoyancy of the ridge itself that is holding up the slab but a dynamic process that continues to operate in the wake trailing the impacting ridge.

As shown in Figure 3, there are also cases where apparent buoyant impactors have little to no effect on the geometry of the subducting slab. The Emperor seamounts are subducting at the Kurile trench, the Ogasawara plateau, Magellan seamounts, and Caroline ridge are all subducting at the Mariana trench, the Ozbourn-Louisville seamounts are subducting at the Kermadec trench, and the Chile rise is subducting at the Peru-Chile trench. These are just a sample of the largest thickness anomalies that are subducting without shallowing the dip of the downgoing slab.

Current state of subduction in central Mexico

The central Mexico subduction zone is of particular interest because it does not have an impacting ridge yet is one of the shallowest slabs that has been measured. Understanding the flat slab in Mexico is key to reevaluating the proposed mechanisms for shallow slabs around the globe. Along the western Mexico margin, the Cocos plate is subducting under the North America plate at a rate varying between 4.7 and 6.8 cm/yr (Demets et al., 1994). As shown in Figure 4, the subducted slab is shown by receiver function analysis to transition from a normal dip at the trench to sub-horizontal at 80 km from the trench (Kim et al., 2010; Pardo and Suárez, 1995; Pérez-Campos et al., 2008; Suárez et al., 1999). The horizontal slab persists to 250 km from the trench where it descends into the mantle with a 75° dip and is recognizable in tomographic images to a depth of 500 km (Husker and Davis, 2009; Kim et al., 2010; Pérez-Campos et al., 2008). An ultra low velocity layer, approximately 3 km thick is imaged on top of the slab from the trench through the horizontal section. The overriding plate appears to be in an overall state of extension rather than compression (Singh and Pardo, 1993) which is counterintuitive when considering the compressive forces associated with the subduction collision and the traction of an underplated slab (De Franco et al., 2007; Keppie, 2009; Moran-Zenteno et al., 2007; Nieto-Samaniego et al., 2006).

The Trans Mexican Volcanic Belt (TMVB) has embayments along the landward projection of the Rivera, Orozoco, and Clipperton fracture zones suggesting that the Cocos plate is being further divided into smaller plates by tearing of the slab (Blatter et al., 2007; Menard, 1978). The breakup of the Cocos plate allows the smaller fragments to rollback faster and results in the along trench dip variation (Billen, 2008).

History of subduction in Mexico

The western Mexican margin has been a subduction margin for the past 160 Myr (Keppie, 2004; Solari et al., 2007). The Sierra Madre Occidental, the subduction-related arc of western Mexico, initiated in the Jurassic and contains a continuous record of subduction related magmatism from the Cretaceous and throughout the Cenozoic. The area has undergone moderate compressional deformation that correlates in time with Laramide deformation further north. Extension began in the early Eocene and continued through the Oligocene. Associated with the extension is an ignimbrite flareup that signals slab rollback or detachment of the slab (Ferrari et al., 2007). All of this early extension occurred while the margin was still under the compressive forces of subduction.

The details of the assembly of southwestern Mexico are complicated, but there are some aspects that can constrain the evolution of the slab geometry. The extent and migration of Cenozoic volcanism is related to the location of the subducted slab. Age data from the North American Volcanic Database (Navdat) and Moran-Zenteno et al. (2007) are plotted in Figure 5 against distance from the paleotrench to show the space and time evolution of subduction related magmatic activity. At 20 Ma the locus of subduction magmatism jumps 200 km inland from the trench. At 10 Ma a rollback phase starts as the volcanism migrates toward the trench.

The migration of the arc needs to be viewed in relation to the reorganization of the oceanic plates offshore, namely the ridge jumps at 25, 12.5-11, and 6.5-3.5 Ma (Klitgord and Mammerickx, 1982; Mammerickx and Klitgord, 1982; Moran-Zenteno et al., 2007). The southern Mexican margin has undergone a major reshaping in Tertiary time (Moran-Zenteno et al., 1996). The truncation of structural trends in addition to the juxtaposition of the modern trench and the Paleogene batholith suggests subsequent forearc removal (Karig, 1978; Moran-Zenteno et al., 2007; MoranZenteno et al., 1996; Schaaf et al., 1995). The Chortis block is often assumed to be the missing forearc, though this correlation is just as often called into question (Keppie and Moran-Zenteno, 2005; Moran-Zenteno et al., 2009; Ortega-Gutierrez et al., 2007; Ortega-Obregon et al., 2008). Recent studies evaluating the multiple reconstructions proposed for the Chortis block do not find much evidence to support the hypothesis that it represents the missing forearc and prefer a model of wholesale subduction erosion (Keppie, 2009).

Proposed causes of zones of shallow subduction

There are several factors that affect the geometry of subduction zones. A rapid convergence rate, trench-ward absolute motion of the upper plate, subduction of thickened oceanic crust, and young oceanic lithosphere are four factors that lead to shallowing of subducting plates (Cross and Pilger, 1982) . These factors are discussed specifically for Mexico.

Tehuantepec Ridge

The southern Mexico subduction zone near the Isthmus of Tehuantepec, exhibits all of the four factors that would lead to a shallow slab geometry as described by Cross and Pilger (1982): the convergence rate of the Cocos and North American plates is rapid (approximately 6 cm/yr); the North American plate is overriding the Cocos plate in an absolute motion reference frame; the Tehuantepec ridge is currently being subducted; and the subducting lithosphere has been younger than 10Ma for the past 40Ma (Cross and Pilger, 1982; Müller et al., 2008). These factors predict that the subducted Cocos plate in this region should have a very shallow dip, but it actually has a moderate dip of 30 degrees.

One of the most obvious positive seafloor anomalies on the Cocos plate is the Tehuantepec Ridge. The ridge is a compression structure that stretches for more than 200 kilometers along the Clipperton fracture zone. The ridge marks the boundary of oceanic lithosphere that is on average 7 million years younger and 800 meters shallower to the north (Manea et al., 2005). The ridge itself has a maximum relief of roughly 1 kilometer relative to the seafloor to the north and is on average 10 km wide. Assuming the Tehuantepec Ridge is simply a kilometer increase in oceanic crust; the resultant buoyancy increase is only 0.12% (see Figure 6). The Tehuantepec Ridge is thought to have formed as a transform fault on the Guadalupe plate at 15-20 Ma, in addition it is currently encountering the trench at the transition zone of shallow to steep subduction and has no historic or kinematic link to the current zone of flat subduction (Manea et al., 2005). The Tehuantepec ridge has a trend perpendicular to the trench which reduces the effect of any positive buoyancy (Martinod et al., 2005). The Tehuantepec ridge impacts in the wrong place (500km to the southeast of the zone of flat subduction) and has no history of lateral movement along the trench (Manea et al., 2005).

Seamounts

There is a seamount chain on the Pacific plate (Moonless Mountains) between the Murray and Clarion fracture zones that may have had a correlative chain, the Chumbia seamount ridge, on the now subducted Farallon plate (Keppie and Moran-Zenteno, 2005). The seamounts in this chain do not have flexural or gravity moats around them, indicating that they were formed on or very near the spreading ridge (Watts and Ribe, 1984). The lithosphere that surrounds the Moonless Mountains is roughly 40 million years old (Müller et al., 2008). When the Cocos plate started to shallow 30 million years ago, as evidenced by migration of volcanism, the lithosphere at the trench was 10 million years old (Müller et al., 2008) and would be neutrally buoyant. If a corollary to the Moonless Mountains did exist on the Cocos plate, it is of the right age to contribute to the flattening of the slab, however, reconstructions based on the rotation poles and error analysis of Doubrovine and Tarduno (2008) (see Figure 7) show that the Moonless mountains mirror image would intersect the Mexican margin further to the north than the extent of the zone of shallow subduction, and hence is not likely the cause of it.

By using the stage rotations of Doubrovine and Tarduno (2008), a conjugate to the current Mexican margin can be rotated to indicate the area of the Pacific plate that corresponds to the area on the Farallon plate that subducted at 30Ma when the slab shallowed. As shown in Figure 8, this rotation reveals a set of small unnamed seamounts that would have intersected the margin around the latitude of Acapulco and can be correlated in space and time to the flat segment of the slab. The buoyancy of these seamounts alone is insufficient to cause a flat slab (Cloos, 1993). We can use a simplified geometry to estimate the volumetric differences and resulting changes in buoyancy due to various forms of thickened oceanic lithosphere. From global bathymetry data we extract a representative width and height of the given bathymetric anomaly then calculate the volume assuming a conical shape for a seamount or a triangular prism for an aseismic ridge. The estimated increase in crustal volume is then normalized by the aerial extent of the feature in order to compare thickening per unit area. Using this method the unnamed mountains are approximately 10% of the crustal volume increase associated with the Nazca or Juan Fernandez ridge.

Age of the subducting plate

One of the predictions of plate tectonics is that the angle of subduction is a function of the age of the subducting plate, because as a plate ages it cools and increases in density (Billen and Hirth, 2007; Parsons and Sclater, 1977) . The relationship between age and density is clearly seen in the half space cooling models of Figure 6. However, when the angle of subduction and the age of actual subduction zones are analyzed, the correlation is quite weak (Cruciani et al., 2005; Jarrard, 1986). This is evident in the case of central Mexico, where the Cocos plate exhibits steep subduction in the north where the subducting oceanic lithosphere is younger than the lithosphere of the flat segment to the south (Müller et al., 2008; Pardo and Suárez, 1993; Pardo and Suárez, 1995) (see Figure 4).

It is possible for an ephemeral spreading center to have existed between the Farallon and an unknown microplate. If this failed ridge was near the trench it could produce very young and buoyant lithosphere that would decrease the angle of subduction. This hypothetical ridge would be entirely contained within subducted Farallon plate, and the evidence for it completely subducted. Although the tectonic plates in the area underwent frequent reorganization around the time of the slab shallowing there is no evidence for such a spreading ridge in the geologic or geochemical record of the upper plate.

Hydrothermal alteration

Age alone may not be the sole cause for the angle of the Cocos slab, but could be a major component. The seafloor on both sides of the spreading ridge in the zone of flat subduction is extremely rough. The area is the site of numerous fracture zones and failed rifting events. One of the mapped failed rifts on the Pacific plate was dredged as part of the Ocean Drilling Project and the recovered sample contained serpentinite (Lonsdale, 2005). The alteration or serpentinization of the oceanic lithosphere causes a decrease in the average density of the lithosphere and could increase the buoyancy of the slab, causing it to go flat. Hydrothermal alteration will likely increase with increased fracturing, although we have no way of knowing the fracture density of the plate that subducted at 20Ma given the fact that fracture causing events such as ridge jumps and forearc bulges are not necessarily recorded symmetrically about the new spreading center. The bending of the Cocos plate preferentially induces the reactivation of faults and fractures, creating a horst and graben structure (Aubouin et al., 1982; Grevemeyer et al., 2005; Ruff, 1989). The faulting of the lithosphere allows water to penetrate into the young warm slab and alter the density. This is a process that occurs at all subduction zones, however, due to the consistently young lithosphere subducting in this area the higher temperature of the slab will increase hydrothermal alteration independent of the degree of fracturing. Altering the top 5 km of the mantle lithosphere by 15% serpentinization doubles the length of time for which a slab is neutrally buoyant (see Figure 6). Recent geophysical studies in Mexico have determined that there is a hydrous layer at the plate interface (Kim et al., 2010). Remobilization of fluids entrained with the downgoing slab by serpentinization may be the source of these hydrous phases.

Slab detachment and flexure

Tomographic images reveal the foundering segments of the Farallon slab beneath North America. The tomographic model of Gorbatov and Fukao (2005) reveals a southward propagating tear in the slab at 600 km depth that is a result of the differential motion between the Cocos and subducted Farallon plates. They speculate that the tear and differential rotation buckles the Cocos plate and caused uplift of the slab in the region of the TMVB, producing the flat slab geometry. There are also large discrepancies between tomographic models of the region. The more detailed tomographic model of Husker and Davis (2009) places the truncated edge of the slab roughly 500 km to the south of where Gorbatov and Fukao locate it, which makes the uplift mechanism less likely . Other tomographic models locate a shallower gap in the slab under northern Central America (Rogers et al., 2002) , and it is not clear how truncation of the slab at a depth of 300 km beneath Guatemala, Honduras, and Nicaragua would relate to the model of Gorbatov and Fukao.

Chortis Block

The origin and location of the Chortis block (present day Nicaragua) through time is highly debated. One reconstruction places the Chortis block along the Acapulco trench at 50 Ma (Pindell et al., 1988; Ross and Scotese, 1988). The block then migrates to the east with the Farallon-North America-Caribbean triple junction which changes the margin from a North American-Caribbean to North American-Farallon plate boundary (MoranZenteno et al., 1996). The change in the plate pair exposes the southern Mexican margin to the faster Farallon-North America convergence rate, which may lead to the flattening of the slab, though it is unclear why the margin to the north with the same convergence rate would not also be flat. Other studies (Keppie, 2009; Keppie and Moran-Zenteno, 2005) propose models for the evolution of the Chortis block that make it unrelated to the flat slab in central Mexico. It is unlikely that the Chortis block is the cause of the flat slab, yet the knowledge of its location through time is needed for a complete model of the area.

Continental root

Slab suction is an important force influencing the geometry at subduction zones. Viscously driven flow of the asthenosphere by the downgoing slab creates a zone of negative pressure in the mantle wedge (Tovish et al., 1978). The suction force alone may not provide enough lift to drive slabs flat but may prove more effective when combined with excessively buoyant lithosphere in the form of an oceanic plateau (van Hunen et al., 2004). The suction force in the mantle wedge can be greatly increased by a continental root that penetrates the asthenosphere (O'Driscoll et al., 2009). The crustal root blocks flow perpendicular to the trench resulting in a higher negative pressure in the space between the trench and the root that can assist in pulling up the slab. This mechanism is proposed as a contributing factor for the Laramide, and has been suggested for central Mexico because the elevated TMVB may indicate the presence of the a crustal root (Urrutia-Fucugauchi and Flores-Ruiz, 1996) . However, as shown in Pérez-Campos et al. (2008), the crust under the TMVB is only 45 km thick and hence there is no deep crustal root.

Hydration of the mantle wedge

The viscosity of the mantle wedge can be decreased by the addition of fluids released from the slab, this low viscosity wedge or channel can change the dip of the downgoing slab and has been modeled to create flat lying slabs as observed in Mexico (Manea and Gurnis, 2007). There is some evidence in the attenuation study of Chen and Clayton (2009) that zones of low Q in the mantle wedge may be due to fluids from the slab. Geochemical studies of the TMVB show that the sub-arc mantle is highly heterogeneous and have found locations with a magmatic water content in excess of 8 wt% (Blatter and Carmichael, 1998; Johnson et al., 2009). We know that excess hydration can cause a slab to flatten, however, the cause of excess water in the Mexican subduction zone has yet to be explained. Tectonic erosion is one way to subduct large amounts of water laden sediments (Dominguez et al., 2000). In Mexico there is evidence for extreme tectonic erosion, namely, the entire Oligocene forearc is missing and the associated batholith is sitting adjacent to the modern trench (Keppie et al., 2009a; Keppie et al., 2009b; Moran-Zenteno et al., 2007). The juxtaposition of the Oligocene arc with the modern trench and the truncation of other structural features reveals how much of the Mexican margin has been lost to tectonic erosion.

Seamounts may not have enough positive buoyancy to flatten the slab, but they do create a long lived period of subducting extreme relief that could lead to a prolonged period of subduction erosion (von Huene and Scholl, 1991). The subduction on individual seamounts has been shown through analog models to cause erosion of the overriding plate (Dominguez et al., 1998; Dominguez et al., 2000). The unnamed mountains range in age from roughly 35 to 25 Ma and stretch across 500 kilometers (see Figure 8). The convergence rate along the Middle America Trench varies widely though averaging in space and time the margin would be continually impacted for a span of 6 Ma assuming a perfect mirroring of the unnamed mountains (Doubrovine and Tarduno, 2008; Müller et al., 2008). The erosion of the margin corresponds with a 29 to 19 Ma gap in arc magmatism (Keppie et al., 2009b). Recent numerical modeling has shown the rapid removal of large blocks of continental forearc as one possible mode of subduction erosion that shaped the Mexican margin (Keppie et al., 2009a). The eroded forearc would be highly fractured in this catastrophic event leading to an increase in pore space for fluids to be entrained with the downgoing plate. Modeling indicates that the eroded material could be underplated or transported deep into the mantle (Keppie et al., 2009a). The low viscosity channel that forms from the subducted material and fluid would also decouple the upper and lower plates and cause the lack of compression that we see in

Mexico.

Discussion

Looking for a single cause of flat slab subduction, reveals the complexity and multifaceted nature of subduction zone dynamics. Single trench correlations quickly break down when extended to the global scale. The often called upon correlation between the location of flat slabs and the presence of a subducting aseismic ridge or plateau is quite strong, however this does not imply direct causation. Most flat slabs have an associated subducting ridge, but not all subducting ridges produce flat slabs. The fact that the correlation between ridges and shallow zones is not one to one means that it is not likely the sole cause of flat subduction. We have shown, adding a second variable, in this case age, we are able to explain some of the zones where a ridge is subducting yet fails to produce a shallow slab segment (see Figure 9). This is just one example of the need for a comprehensive evaluation of the parameters that influence the dip of subducting plates. One proposed cause of the Laramide flat slab is the subduction of a conjugate oceanic plateau to the Shatsky Rise, though as we have shown, subduction of thickened oceanic lithosphere is neither a sufficient or necessary condition for shallow subduction. We find hydration of the mantle wedge to be the only mechanism that there is no evidence against causing the flat slab in Mexico. Further study of the fluid budget of the downgoing slab and the change in mantle viscosity with the addition of fluids is needed to evaluate hydration as the cause of the Mexican flat slab and possibly the key mechanism for shallow slabs worldwide.

Conclusions

Subducting buoyant ridges, seamounts, and plateaus do not directly cause flat slabs but are rather a catalyst of other dynamic mantle processes. Determining the combination of forces that lead to flat slabs in important not only for our understanding of the current zones of flat subduction but also the geologic history of western North America and inferred periods of flat subduction in the past. The geometry that we see in the present day Mexican flat slab appears to be the result of the dynamic response of subduction to hydration of the mantle wedge that occurred thirty million years ago. The direct evidence for the flattening mechanism has long been destroyed, and the is no suitable impactor on the conjugate plate. Hydration of the mantle wedge is the only feasible mechanism to change the slab geometry in Mexico, although the process is not completely understood. The cause of the intense subduction erosion that leads to the hydration has yet to be identified, yet appears to be the only viable explanation to explain the geometry of both the slab and the margin.

Acknowledgements

This study was supported by the Gordon and Betty Moore Foundation through the Tectonics Observatory at Caltech. This is contribution number 136 from the Caltech Tectonics Observatory.

References

Anderson, M., Alvarado, P., Zandt, G. and Beck, S. (2007), Geometry and Brittle Deformation of the Subducting Nazca Plate, Central Chile and Argentina, Geophysical Journal International 171, 419-434.

Aubouin, J., Stephan, J.F., Roump, J. and Renard, V. (1982), The Middle America Trench as an Example of a Subduction Zone, Tectonophysics 86, 113-132.

Billen, M.I. (2008), Modeling the Dynamics of Subducting Slabs, Annual Review of Earth and Planetary Sciences 36, 325-356.

Billen, M.I. and Hirth, G. (2007), Rheologic Controls on Slab Dynamics, Geochemistry Geophysics Geosystems 8, Q08012, doi:10.1029/2007gc001597.

Bird, P. (2003), An Updated Digital Model of Plate Boundaries, Geochemistry Geophysics Geosystems 4, 1027, doi:10.1029/2001gc000252.

Blatter, D.L. and Carmichael, I.S.E. (1998), Hornblende Peridotite Xenoliths from Central Mexico Reveal the Highly Oxidized Nature of Subarc Upper Mantle, Geology 26, 1035-1038.

Blatter, D.L., Farmer, G.L. and Carmichael, I.S.E. (2007), A North-South Transect across the Central Mexican Volcanic Belt at Similar to 100 Degrees W: Spatial Distribution, Petrological, Geochemical, and Isotopic Characteristics of Quaternary Volcanism, Journal of Petrology 48, 901-950.

Brocher, T.M., Fuis, G.S., Fisher, M.A., Plafker, G., Moses, M.J., Taber, J.J. and Christensen, N.I. (1994), Mapping the Megathrust beneath the Northern Gulf of Alaska Using Wide-Angle Seismic Data, Journal of geophysical research 99, 11663-11685.

Chapple, W.M. and Tullis, T.E. (1977), Evaluation of Forces That Drive Plates, Journal of geophysical research 82, 1967-1984.

Chen, T. and Clayton, R.W. (2009), Seismic Attenuation Structure in Central Mexico: Image of a Focused High-Attenuation Zone in the Mantle Wedge, Journal of geophysical research 114, B07304, doi:10.1029/2008jb005964.

Cloos, M. (1993), Lithospheric Buoyancy and Collisional Orogenesis; Subduction of Oceanic Plateaus, Continental Margins, Island Arcs, Spreading Ridges, and Seamounts, Geological Society of America Bulletin 105, 715-737.

Cross, T.A. and Pilger, R.H. (1982), Controls of Subduction Geometry, Location of Magmatic Arcs, and Tectonics of Arc and Back-Arc Regions, Geological Society of America Bulletin 93, 545-562.

Cruciani, C., Carminati, E. and Doglioni, C. (2005), Slab Dip Vs. Lithosphere Age: No Direct Function, Earth and Planetary Science Letters 238, 298-310.

De Franco, R., Govers, R. and Wortel, R. (2007), Numerical Comparison of Different Convergent Plate Contacts: Subduction Channel and Subduction Fault, Geophysical Journal International 171, 435-450.

Demets, C., Gordon, R.G., Argus, D.F. and Stein, S. (1994), Effect of Recent Revisions to the Geomagnetic Reversal Time-Scale on Estimates of Current Plate Motions, Geophysical research letters 21, 2191-2194.

Dominguez, S., Lallemand, S.E., Malavieille, J. and von Huene, R. (1998), Upper Plate Deformation Associated with Seamount Subduction, Tectonophysics 293, 207-224.

Dominguez, S., Malavieille, J. and Lallemand, S.E. (2000), Deformation of Accretionary Wedges in Response to Seamount Subduction: Insights from Sandbox Experiments, Tectonics 19, 182-196.

Doubrovine, P.V. and Tarduno, J.A. (2008), A Revised Kinematic Model for the Relative Motion between Pacific Oceanic Plates and North America since the Late Cretaceous, Journal of geophysical research 113, B12101, doi:10.1029/2008jb005585.

Espurt, N., Funiciello, F., Martinod, J., Guillaume, B., Regard, V., Faccenna, C. and Brusset, S. (2008), Flat Subduction Dynamics and Deformation of the South American Plate: Insights from Analog Modeling, Tectonics 27, TC3011, doi:10.1029/2007tc002175.

Ferrari, L., Valencia-Moreno, M. and Bryan, S., Magmatism and Tectonics of the Sierra Madre Occidental and Its Relation with the Evolution of the Western Margin of North America, In Geology of México: Celebrating the Centenary of the Geological Society of México: Geological Society of America Special Paper 422 (eds. S.A. Alaniz-Alvarez and A.F. Nieto-Samaniego) (2007) pp. 1-39.

Forsyth, D. and Uyeda, S. (1975), Relative Importance of Driving Forces of Plate Motion, Geophysical Journal of the Royal Astronomical Society 43, 163-200.

Fuis, G.S., Moore, T.E., Plafker, G., Brocher, T.M., Fisher, M.A., Mooney, W.D., Nokleberg, W.J., Page, R.A., Beaudoin, B.C., Christensen, N.I., Levander, A.R., Lutter, W.J., Saltus, R.W. and Ruppert, N.A. (2008), Trans-Alaska Crustal Transect and Continental Evolution Involving Subduction Underplating and Synchronous Foreland Thrusting, Geology 36, 267-270.

Gorbatov, A. and Fukao, Y. (2005), Tomographic Search for Missing Link between the Ancient Farallon Subduction and the Present Cocos Subduction, Geophysical Journal International 160, 849-854.

Grevemeyer, I., Kaul, N., Diaz-Naveas, J.L., Villinger, H.W., Ranero, C.R. and Reichert, C. (2005), Heat Flow and Bending-Related Faulting at Subduction Trenches: Case Studies Offshore of Nicaragua and Central Chile, Earth and Planetary Science Letters 236, 238-248.

Gutscher, M.-A., Spakman, W., Bijwaard, H. and Engdahl, E.R. (2000a), Geodynamics of Flat Subduction: Seismicity and Tomographic Constraints from the Andean Margin, Tectonics 19,

Gutscher, M.A., Malavieille, J., Lallemand, S. and Collot, J.Y. (1999a), Tectonic Segmentation of the North Andean Margin: Impact of the Carnegie Ridge Collision, Earth and Planetary Science Letters 168, 255-270.

Gutscher, M.A., Maury, R., Eissen, J.-P. and Bourdon, E. (2000b), Can Slab Melting Be Caused by Flat Subduction?, Geology 28, 535-538.

Gutscher, M.A., Olivet, J.L., Aslanian, D., Eissen, J.P. and Maury, R. (1999b), The “Lost Inca Plateau”: Cause of Flat Subduction beneath Peru?, Earth and Planetary Science Letters 335-341.

Gutscher, M.A., Spakman, W., Bijwaard, H. and Engdahl, E.R. (2000c), Geodynamics of Flat Subduction: Seismicity and Tomographic Constraints from the Andean Margin, Tectonics 19, 814-833.

Hayes, G.P., Wald, D.J. and Keranen, K. (2009), Advancing Techniques to Constrain the Geometry of the Seismic Rupture Plane on Subduction Interfaces a Priori: Higher-Order Functional Fits, Geochemistry Geophysics Geosystems 10, Q09006, doi:10.1029/2009gc002633.

Husker, A. and Davis, P.M. (2009), Tomography and Thermal State of the Cocos Plate Subduction beneath Mexico City, Journal of geophysical research 114, B04306, doi:10.1029/2008JB006039.

Jarrard, R.D. (1986), Relations among Subduction Parameters, Reviews of Geophysics 24, 217-284.

Johnson, E.R., Wallace, P.J., Delgado Granados, H., Manea, V.C., Kent, A.J.R., Bindeman, I.N. and Donegan, C.S. (2009), Subduction-Related Volatile Recycling and Magma Generation beneath Central Mexico: Insights from Melt Inclusions, Oxygen Isotopes and Geodynamic Models, Journal of Petrology 50, 1729-1764.

Karig, D.E. (1978), Late Cenozoic Subduction and Continental Margin Truncation Along the Northern Middle America Trench, Geological Society of America Bulletin 89, 265-276.

Kay, S.M. and Abbruzzi, J.M. (1996), Magmatic Evidence for Neogene Lithospheric Evolution of the Central Andean "Flat-Slab" between 30°S and 32°S, Tectonophysics 259, 15-28.

Keppie, D.F., 2009. Subduction Erosion Processes with Application to Southern Mexico. PhD Thesis, McGill University, Montreal, 172 pp.

Keppie, D.F., Currie, C.A. and Warren, C. (2009a), Subduction Erosion Modes: Comparing Finite Element Numerical Models with the Geological Record, Earth and Planetary Science Letters 287, 241-254.

Keppie, J.D. (2004), Terranes of Mexico Revisited: A 1.3 Billion Year Odyssey, International Geology Review 46, 765-794.

Keppie, J.D. and Moran-Zenteno, D.J. (2005), Tectonic Implications of Alternative Cenozoic Reconstructions for Southern Mexico and the Chortis Block, International Geology Review 47, 473-491.

Keppie, J.D., Moran-Zenteno, D.J., Martiny, B. and Gonzalez-Torres, E. (2009b), Synchronous 29-19 Ma Arc Hiatus, Exhumation and Subduction of Forearc in Southwestern Mexico, Geological Society, London, Special Publications 328, 169-179.

Kim, Y., Clayton, R.W. and Jackson, J.M. (2010), Geometry and Seismic Properties of the Subducting Cocos Plate in Central Mexico, Journal of geophysical research 115, B06310, doi:10.1029/2009jb006942.

Klitgord, K.D. and Mammerickx, J. (1982), Northern East Pacific Rise - Magnetic Anomaly and Bathymetric Framework, Journal of geophysical research 87, 6725-6750.

Lallemand, S., Heuret, A. and Boutelier, D. (2005), On the Relationships between Slab Dip, Back-Arc Stress, Upper Plate Absolute Motion, and Crustal Nature in Subduction Zones, Geochemistry Geophysics Geosystems 6, Q09006, doi:10.1029/2005GC000917.

Lonsdale, P. (2005), Creation of the Cocos and Nazca Plates by Fission of the Farallon Plate, Tectonophysics 404, 237-264.

Mammerickx, J. and Klitgord, K.D. (1982), Northern East Pacific Rise - Evolution from 25 My Bp to the Present, Journal of geophysical research 87, 6751-6759.

Manea, M., Manea, V.C., Ferrari, L., Kostoglodov, V. and Bandy, W.L. (2005), Tectonic Evolution of the Tehuantepec Ridge, Earth and Planetary Science Letters 238, 64-77.

Manea, V. and Gurnis, M. (2007), Subduction Zone Evolution and Low Viscosity Wedges and Channels, Earth and Planetary Science Letters 264, 22-45.

Martinod, J., Funiciello, F., Faccenna, C., Labanieh, S. and Regard, V. (2005), Dynamical Effects of Subducting Ridges: Insights from 3-D Laboratory Models, Geophysical Journal International 163, 1137-1150.

Menard, H.W. (1978), Fragmentation of Farallon Plate by Pivoting Subduction, Journal of Geology 86, 99-110.

Moran-Zenteno, D., Cerca, M. and Keppie, J.D., The Cenozoic Tectonic and Magmatic Evolution of Southwestern Mexico; Advances and Problems of Interpretation, In Geology of México: Celebrating the Centenary of the Geological Society of México: Geological Society of America Special Paper 422 (eds. S.A. Alaniz-Alvarez and A.F. Nieto-Samaniego) (2007) pp. 71-91.

Moran-Zenteno, D., Corona-Chavez, P. and Tolson, G. (1996), Uplift and Subduction Erosion in Southwestern Mexico since the Oligocene: Pluton Geobarometry Constraints, Earth and Planetary Science Letters 141, 51-65.

Moran-Zenteno, D., Keppie, D.J., Martiny, B. and González-Torres, E. (2009), Reassessment of the Paleogene Position of the Chortis Block Relative to Southern Mexico: Hierarchical Ranking of Data and Features, Revista Mexicana De Ciencias Geologicas 26, 177-188.

MoranZenteno, D.J., CoronaChavez, P. and Tolson, G. (1996), Uplift and Subduction Erosion in Southwestern Mexico since the Oligocene: Pluton Geobarometry Constraints, Earth and Planetary Science Letters 141, 51-65.

Müller, R.D., Sdrolias, M., Gaina, C. and Roest, W.R. (2008), Age, Spreading Rates, and Spreading Asymmetry of the World's Ocean Crust, Geochemistry Geophysics Geosystems 9, Q04006, doi:10.1029/2007gc001743.

Nieto-Samaniego, A.F., Alaniz-Alvarez, S.A., Silva-Romo, G., Eguiza-Castro, M.H. and Mendoza-Rosales, C.C. (2006), Latest Cretaceous to Miocene Deformation Events in the Eastern Sierra Madre Del Sur, Mexico, Inferred from the Geometry and Age of Major Structures, Geological Society of America Bulletin 118, 238-252.

O'Driscoll, L.J., Humphreys, E.D. and Saucier, F. (2009), Subduction Adjacent to Deep Continental Roots: Enhanced Negative Pressure in the Mantle Wedge, Mountain Building and Continental Motion, Earth and Planetary Science Letters 280, 61-70.

Ortega-Gutierrez, F., Solari, L.A., Ortega-Obregon, C., Elias-Herrera, M., Martens, U., Moran-Ical, S., Chiquin, M., Keppie, J.D., De Leon, R.T. and Schaaf, P. (2007), The Maya-Chortis Boundary: A Tectonostratigraphic Approach, International Geology Review 49, 996-1024.

Ortega-Obregon, C., Solari, L.A., Keppie, J.D., Ortega-Gutierrez, F., Sole, J. and Moran-Ical, S. (2008), Middle-Late Ordovician Magmatism and Late Cretaceous Collision in the Southern Maya Block, Rabinal-Salama Area, Central Guatemala: Implications for North America-Caribbean Plate Tectonics, Geological Society of America Bulletin 120, 556-570.

Pardo, M. and Suárez, G. (1993), Steep Subduction Geometry of the Rivera Plate beneath the Jalisco Block in Western Mexico, Geophysical research letters 20, 2391-2394.

Pardo, M. and Suárez, G. (1995), Shape of the Subducted Rivera and Cocos Plates in Southern Mexico: Seismic and Tectonic Implications, Journal of geophysical research 100, 12357-12373.

Parsons, B. and Sclater, J.G. (1977), Analysis of Variation of Ocean-Floor Bathymetry and Heat-Flow with Age, Journal of geophysical research 82, 803-827.

Pérez-Campos, X., Kim, Y., Husker, A., Davis, P.M., Clayton, R.W., Iglesias, A., Pacheco, J.F., Singh, S.K., Manea, V.C. and Gurnis, M. (2008), Horizontal Subduction and Truncation of the Cocos Plate beneath Central Mexico, Geophysical research letters 35, L18303, doi:10.1029/2008gl035127.

Pilger, R.H. (1981), Plate Reconstructions, Aseismic Ridges, and Low-Angle Subduction beneath the Andes, Geological Society of America Bulletin 92, 448-456.

Pindell, J.L., Cande, S.C., Pitman Iii, W.C., Rowley, D.B., Dewey, J.F., Labrecque, J. and Haxby, W. (1988), A Plate-Kinematic Framework for Models of Caribbean Evolution, Tectonophysics 155, 121-138.

Protti, M., Guendel, F. and McNally, K., Correlation between the Age of the Subducting Cocos Plate and the Geometry of the Wadati-Benioff Zone under Nicaragua and Costa Rica, In

Geologic and Tectonic Development of the Caribbean Plate Boundary in Southern Central America. Geological Society of America Special Paper 295 (ed' P. Mann) (1995) pp. 309-326.

Rogers, R.D., Karason, H. and van der Hilst, R.D. (2002), Epeirogenic Uplift above a Detached Slab in Northern Central America, Geology 30, 1031-1034.

Ross, M.I. and Scotese, C.R. (1988), A Hierarchical Tectonic Model of the Gulf of Mexico and Caribbean Region, Tectonophysics 155, 139-168.

Ruff, L.J. (1989), Do Trench Sediments Affect Great Earthquake Occurrence in Subduction Zones, Pure and Applied Geophysics 129, 263-282.

Sak, P.B., Fisher, D.M., Gardner, T.W., Marshall, J.S. and LaFemina, P.C. (2009), Rough Crust Subduction, Forearc Kinematics, and Quaternary Uplift Rates, Costa Rican Segment of the Middle American Trench, Geological Society of America Bulletin 121, 992-1012.

Schaaf, P., Moran-Zenteno, D., Hernandez-Bernal, M.D., Solis-Pichardo, G., Tolson, G. and Kohler, H. (1995), Paleogene Continental Margin Truncation in Southwestern Mexico: Geochronological Evidence, Tectonics 14, 1339-1350.

Singh, S.K. and Pardo, M. (1993), Geometry of the Benioff Zone and State of Stress in the Overriding Plate in Central Mexico, Geophysical research letters 20, 1483-1486.

Solari, L.A., de Leon, R.T., Pineda, G.H., Sole, J., Solis-Pichardo, G. and Hernandez-Trevino, T. (2007), Tectonic Significance of Cretaceous-Tertiary Magmatic and Structural Evolution of the Northern Margin of the Xolapa Complex, Tierra Colorada Area, Southern Mexico, Geological Society of America Bulletin 119, 1265-1279.

Suárez, G., Escobedo, D., Bandy, W. and Pacheco, J.F. (1999), The 11 December, 1995 Earthquake (Mw=6.4): Implications for the Present-Day Relative Motion on the Rivera-Cocos

Plate Boundary, Geophysical research letters 26, 1957-1960.

Tovish, A., Schubert, G. and Luyendyk, B.P. (1978), Mantle Flow Pressure and the Angle of Subduction: Non-Newtonian Corner Flows, Journal of geophysical research 83, 5892-5898.

Turcotte, D.L. and Schubert, G., Geodynamics (Cambridge University Press, New York 2002).

Urrutia-Fucugauchi, J. and Flores-Ruiz, J. (1996), Bouguer Gravity Anomalies and Regional Crustal Structure in Central Mexico, International Geology Review 38, 176 - 194.

van Hunen, J., van den Berg, A.P. and Vlaar, N.J. (2002), On the Role of Subducting Oceanic Plateaus in the Development of Shallow Flat Subduction, Tectonophysics 352, 317-333.

van Hunen, J., van den Berg, A.P. and Vlaar, N.J. (2004), Various Mechanisms to Induce Present-Day Shallow Flat Subduction and Implications for the Younger Earth: A Numerical Parameter Study, Physics of The Earth and Planetary Interiors 146, 179-194.

von Huene, R. and Scholl, D.W. (1991), Observations at Convergent Margins Concerning Sediment Subduction, Subduction Erosion, and the Growth of Continental-Crust, Reviews of Geophysics 29, 279-316.

Watts, A.B. and Ribe, N.M. (1984), On Geoid Heights and Flexure of the Lithosphere at Seamounts, Journal of geophysical research 89, 1152-1170.

Figure Captions

Figure 1

Map of the Pacific seafloor showing the dip of the shallow (less than 125km depth) portion of subducting slabs (Lallemand et al., 2005), and subducting bathymetric highs that have been correlated with zones of shallow subduction (white crosshatched pattern).

Figure 2

Detail view of the shallow slab segment of Japan. Dashed red lines are 20km contour lines of slab depth from model of Hayes et al. (2009). Colored dots are slab dip from Lallemand et al. (2005). The shallow segment appears to correlate with the subduction of the Shikoku basin rather than the two ridges that flank it.

Figure 3

Map of the Pacific seafloor with labeled lithosphere anomalies (white crosshatched regions) that are subducting with no apparent effect on slab dip. Colored dots are slab dip from Lallemand et al. (2005).

Figure 4

Combined receiver function and tomographic image from the MASE transect modified from Pérez-Campos et al. (2008). Vertical axis is kilometers below sea level, horzontal axis is distance along the MASE transect. The location map of Mexico shows the relative location of the MASE transect (black dots) to the TMVB (gray area), offshore bathymetric features, and the dip of the subducted Cocos plate in 20 km contours (Hayes et al., 2009). Plate boundaries from Bird (2003).

Figure 5

Distance of arc magmatism from the trench through time. The blue line is an 0.2 Myr moving average of the distance from the trench. There is a distinct change in the location of the arc starting at 25 Ma that shows the location of active volcanism migrating northward away from the trench then starts a rollback to the south. The inset map shows the extent of the data used (crosses) and the dotted line approximating the trench . Data are from the North American Volcanic Database and Moran-Zenteno et al. (2007).

Figure 6

Average buoyancy at a given age of the crustal columns for four possible types of oceanic lithosphere subducted under Mexico calculated using half space cooling model (Turcotte and Schubert, 2002). Red dotted line is the density of asthenosphere for reference. The modeled lithosphere will resist subduction until it crosses above the asthenosphere line.

The 5Ma time slice of the four models of oceanic lithosphere used in calculating the density variation with age are shown . The models include unaltered normal oceanic lithosphere, 1km of uncompensated thickening to represent the Tehuantepec Ridge, 15% serpentinization if the upper 5km of the oceanic mantle lithosphere, and a 5km isostatic compensated thickening of the oceanic crust to represent seamounts formed on a spreading ridge

Figure 7

A tectonic reconstruction of the Moonless Mountains at 30Ma. Panel A depicts the current location of the Moonless Mountains as red triangles. Blue Triangles show the reconstructed location relative to North America of the hypothetical correlative chain of seamounts on the Farallon plate at 30 Ma in a fixed North America reference frame. Light blue areas are the error ellipses of the rotations given by Doubrovine and Tarduno (2008). Panel B shows the bathymetry of the area around the moonless mountains and the location of the representative bathymetric profile shown to the right. Panel C is a representative profile along the dashed line in panel B. Vertical axis is kilometers below sea level, vertical exaggeration is 100 times.

Figure 8

Panel A shows the Mexican coastline transformed by the rotations of Doubrovine and Tarduno (2008) to show the area of the Pacific plate that is the corrolary to the oceanic lithosphere that was subducting along the southern Mexican margin at 30Ma. The yellow stars are the current and rotated location of Acapulco for reference. There is a small chain of seamounts near what would have been the latitude of Acapulco. The dashed red line is the total 95% confidence area of the error ellipses associated with the rotated points of the coast (solid red line). Panel B shows the bathymetry of the area around the unnamed seamounts and the location of the representative bathymetric profile. Panel C is a representative profile along the dashed line in panel B. Vertical axis is kilometers below sea level, vertical exaggeration is 100 times.

Figure 9

Map of the Pacific seafloor age (Müller et al., 2008), shallow slab segment dips (Lallemand et al., 2005), and subducting bathymetric highs (crosshatched pattern). Not all bathymetric highs are correlated with a zone of shallow subduction. Although there is no direct correlation between the age of the subducting lithosphere and the dip of the slab there appears to be a maximum plate age past which the slab cannot support a flat segment. This explains the subduction of ridges that do not form a shallow slab in the western Pacific.

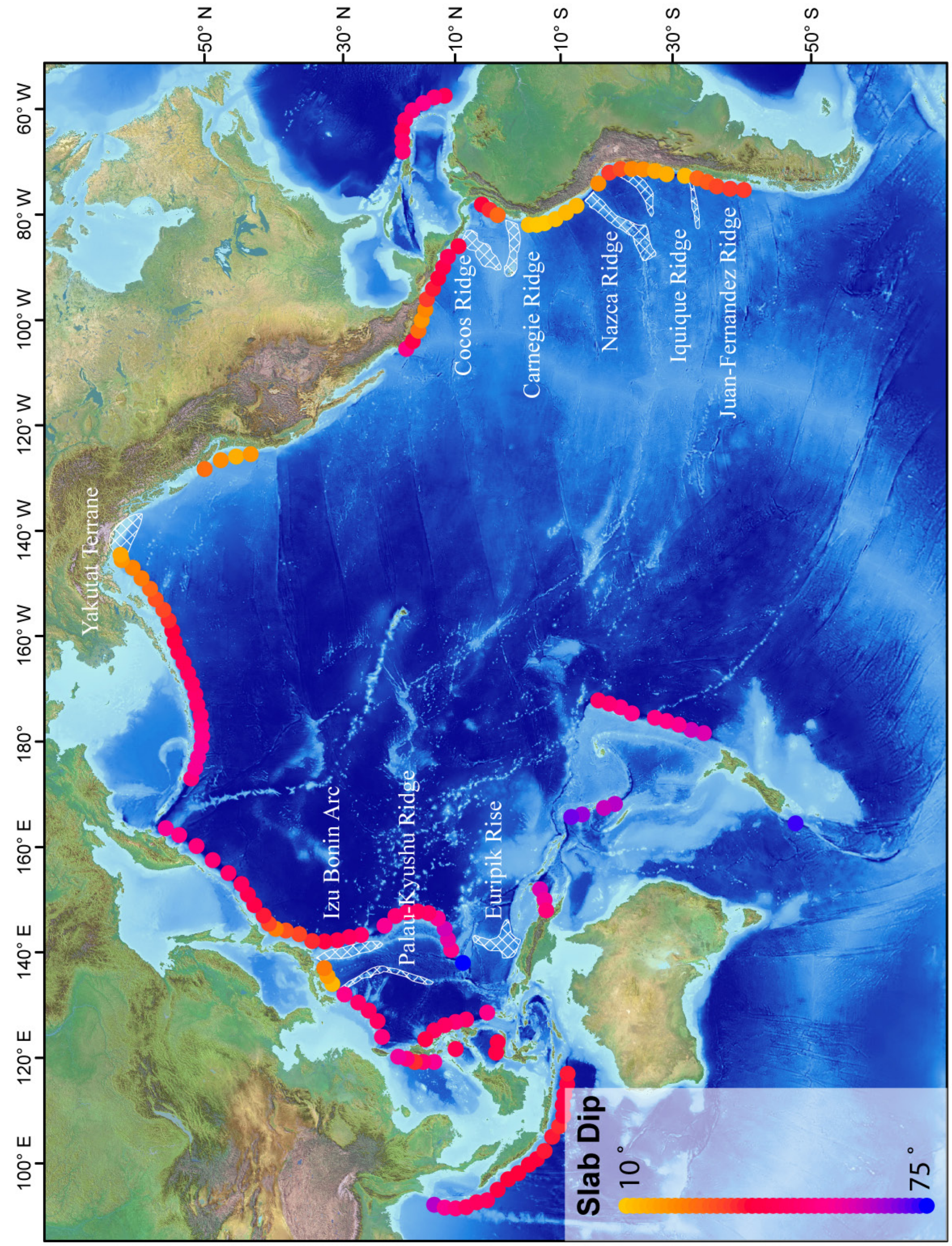

Figure 1. Map of Pacific Basin slab dip

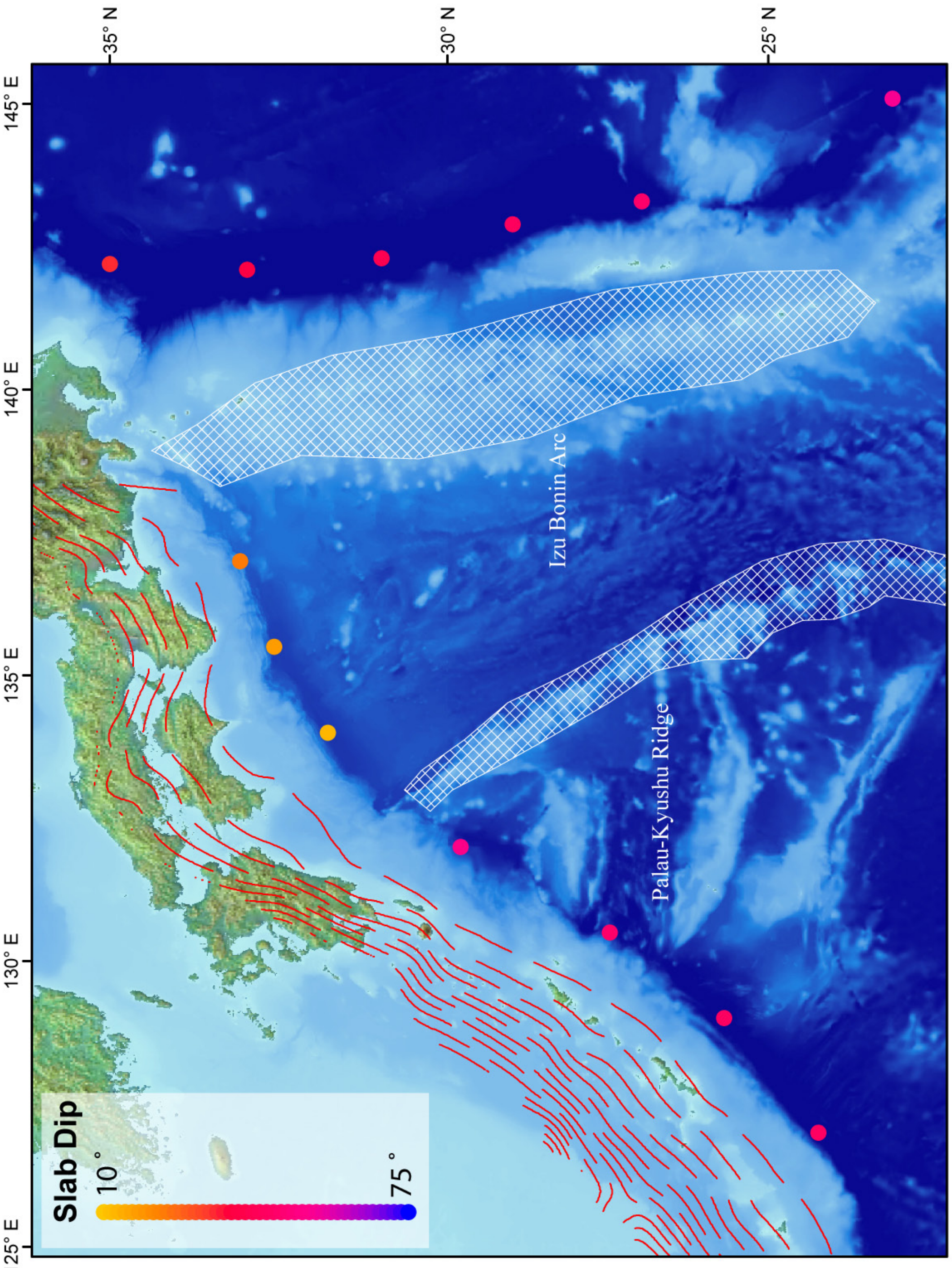

Figure 2. Detail view of the shallow slab segment of Japan

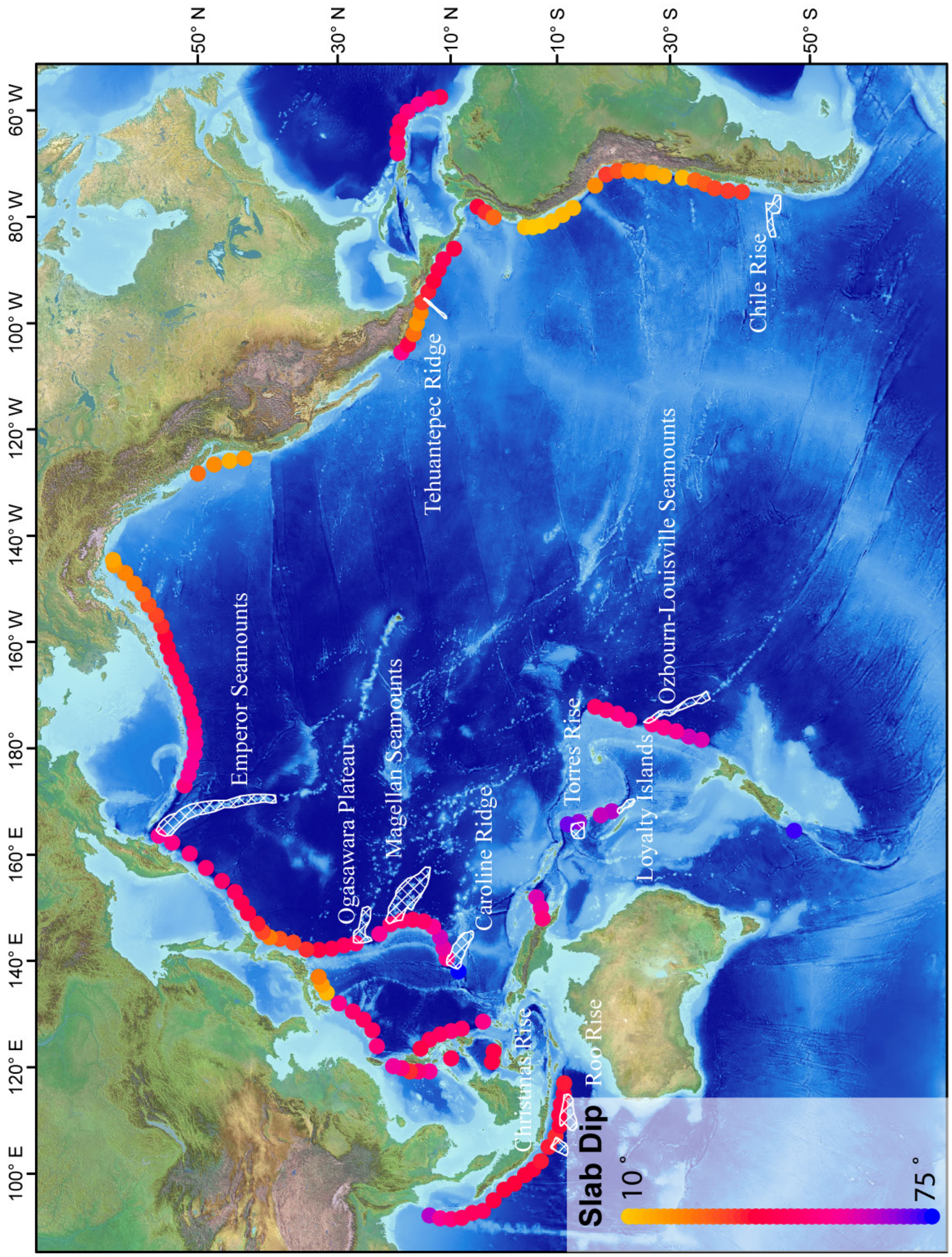

Figure 3. Pacific Basin bathymetric anomalies

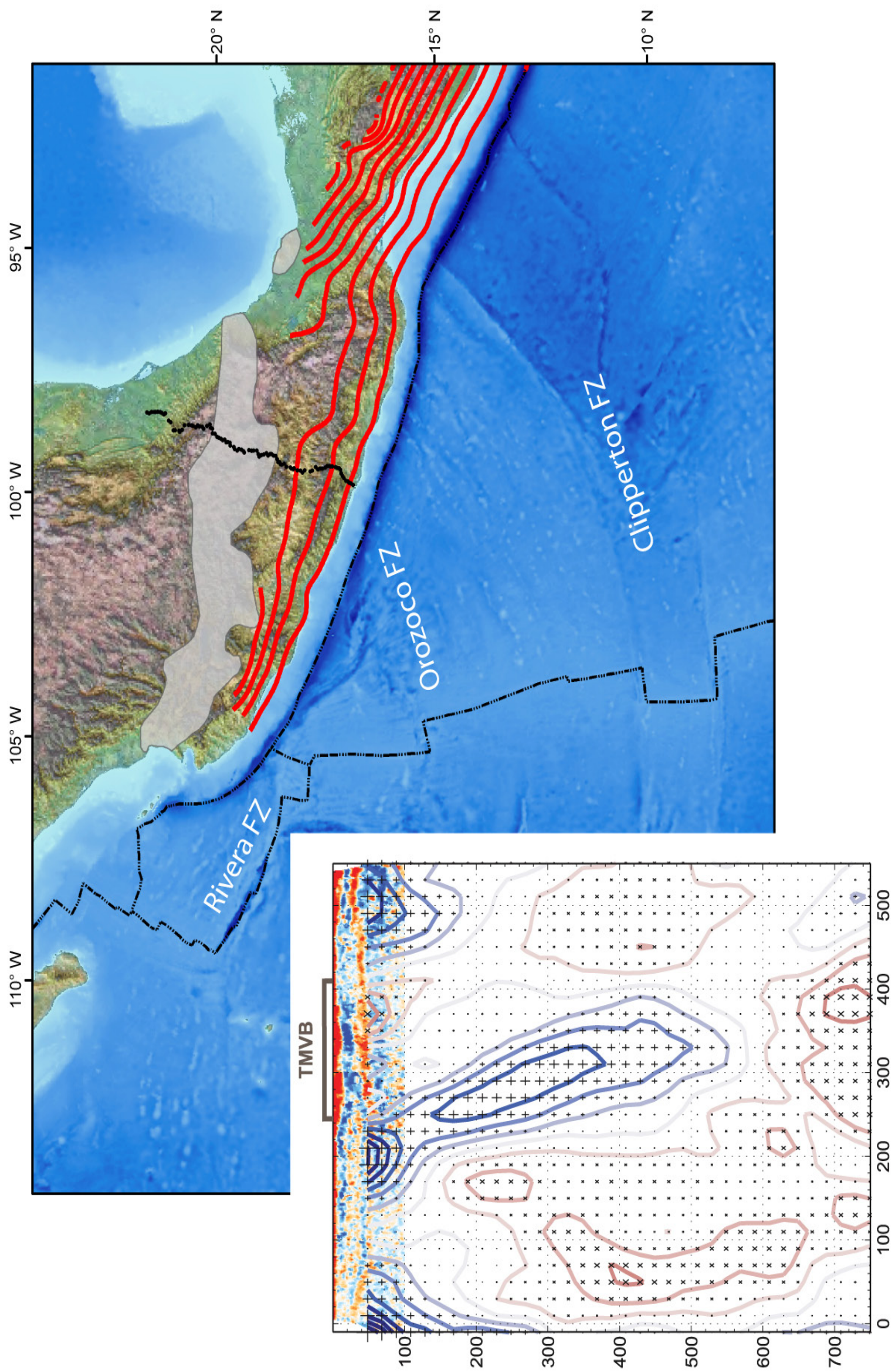

Figure 4. Geometry of the subducting slab

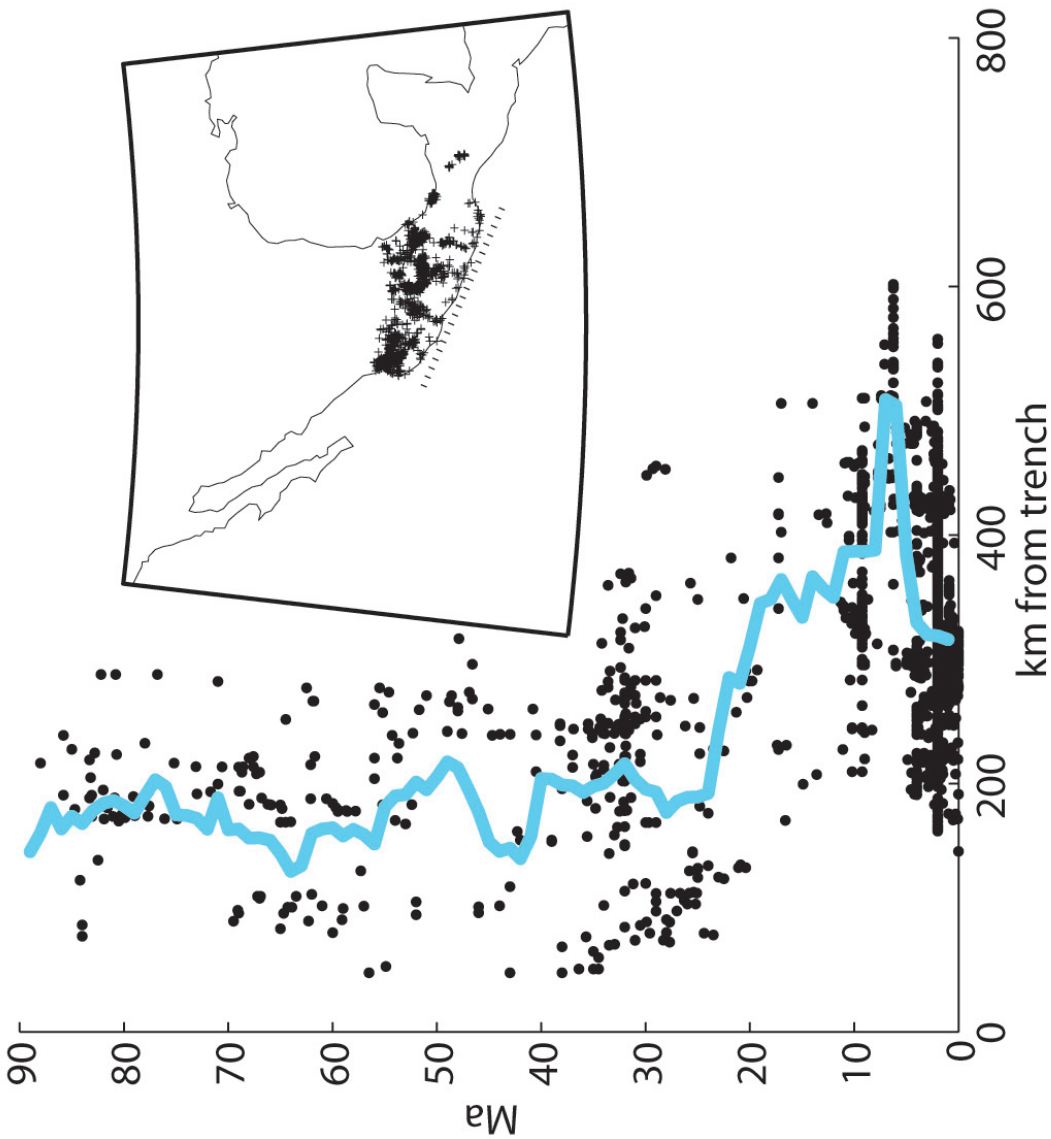

Figure 5. Spatial evolution of TMVB volcanism since 90 Ma

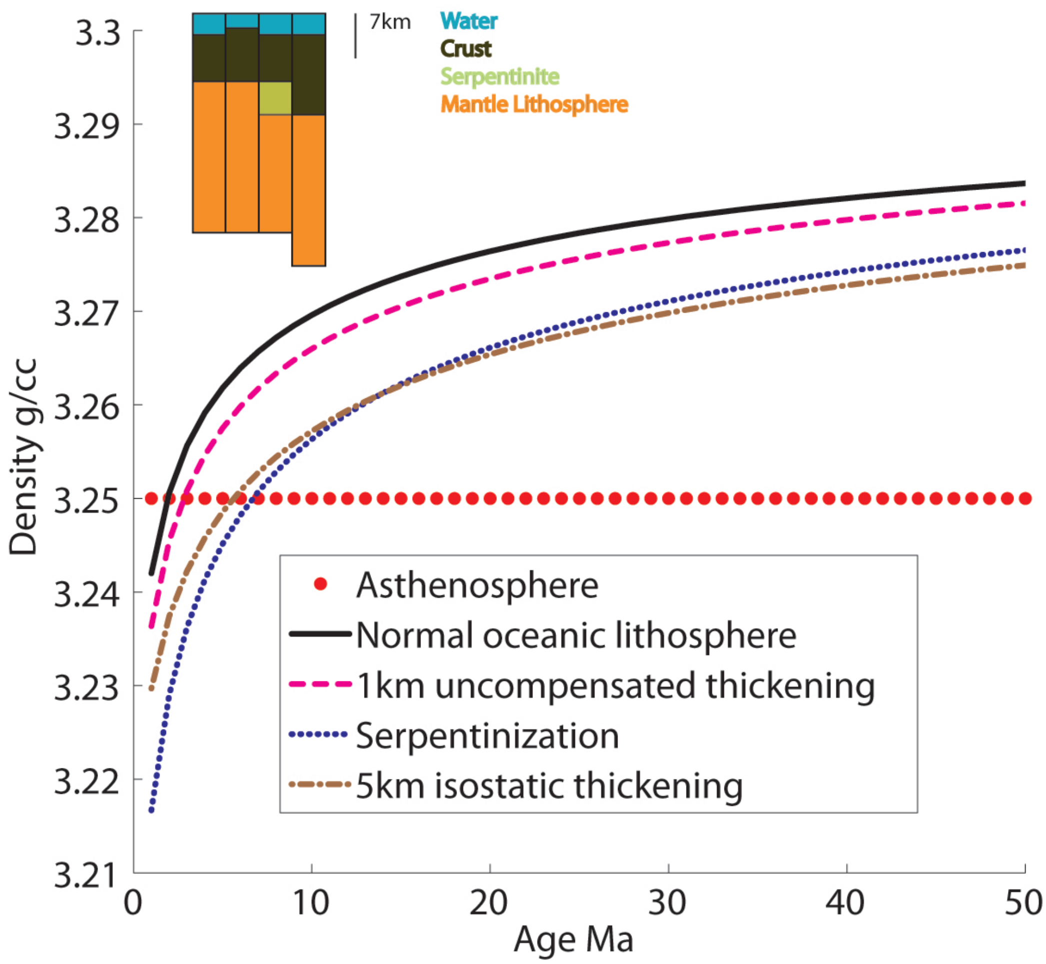

Figure 6. Buoyancy calculations

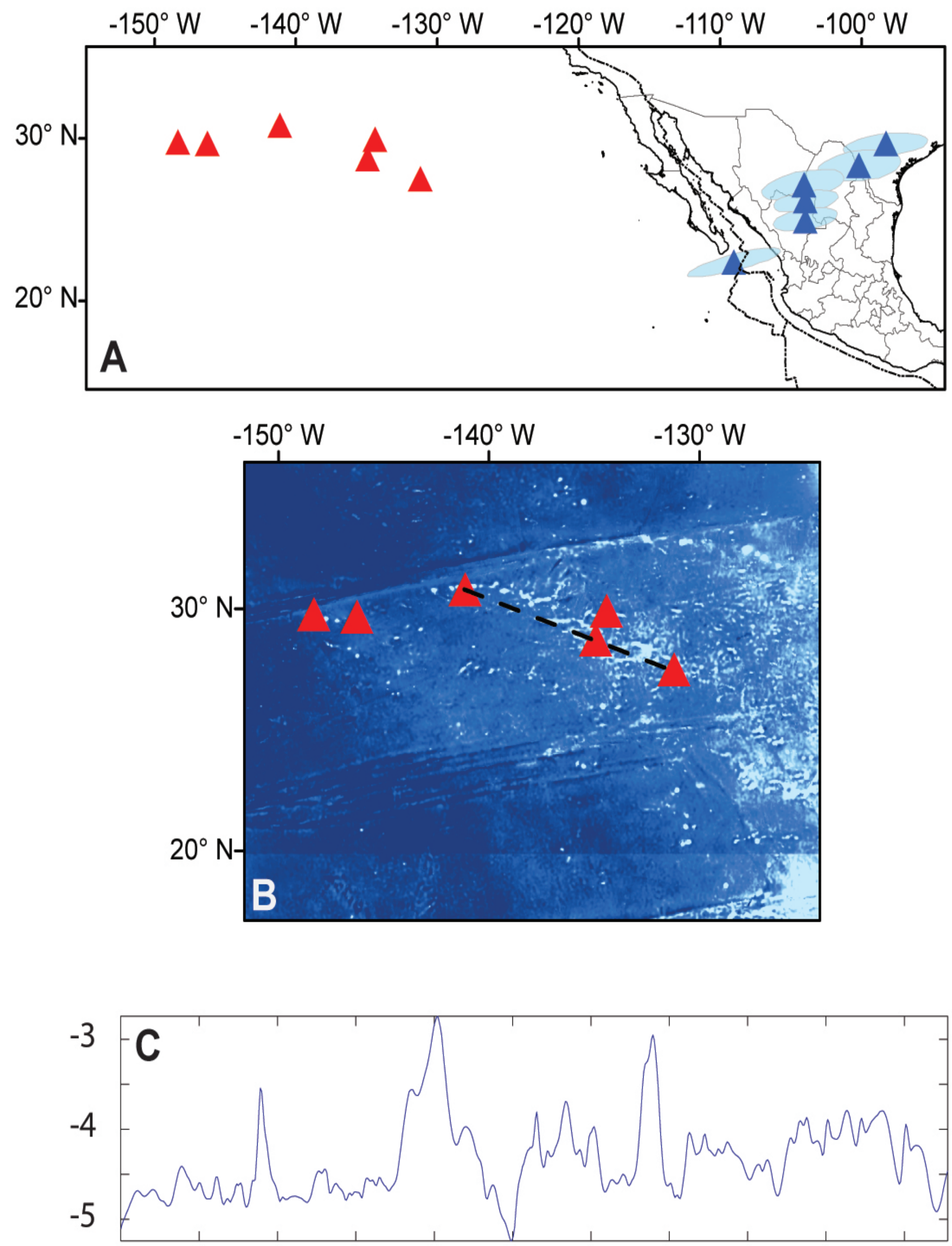

Figure 7. Reconstruction of the Moonless Mountains

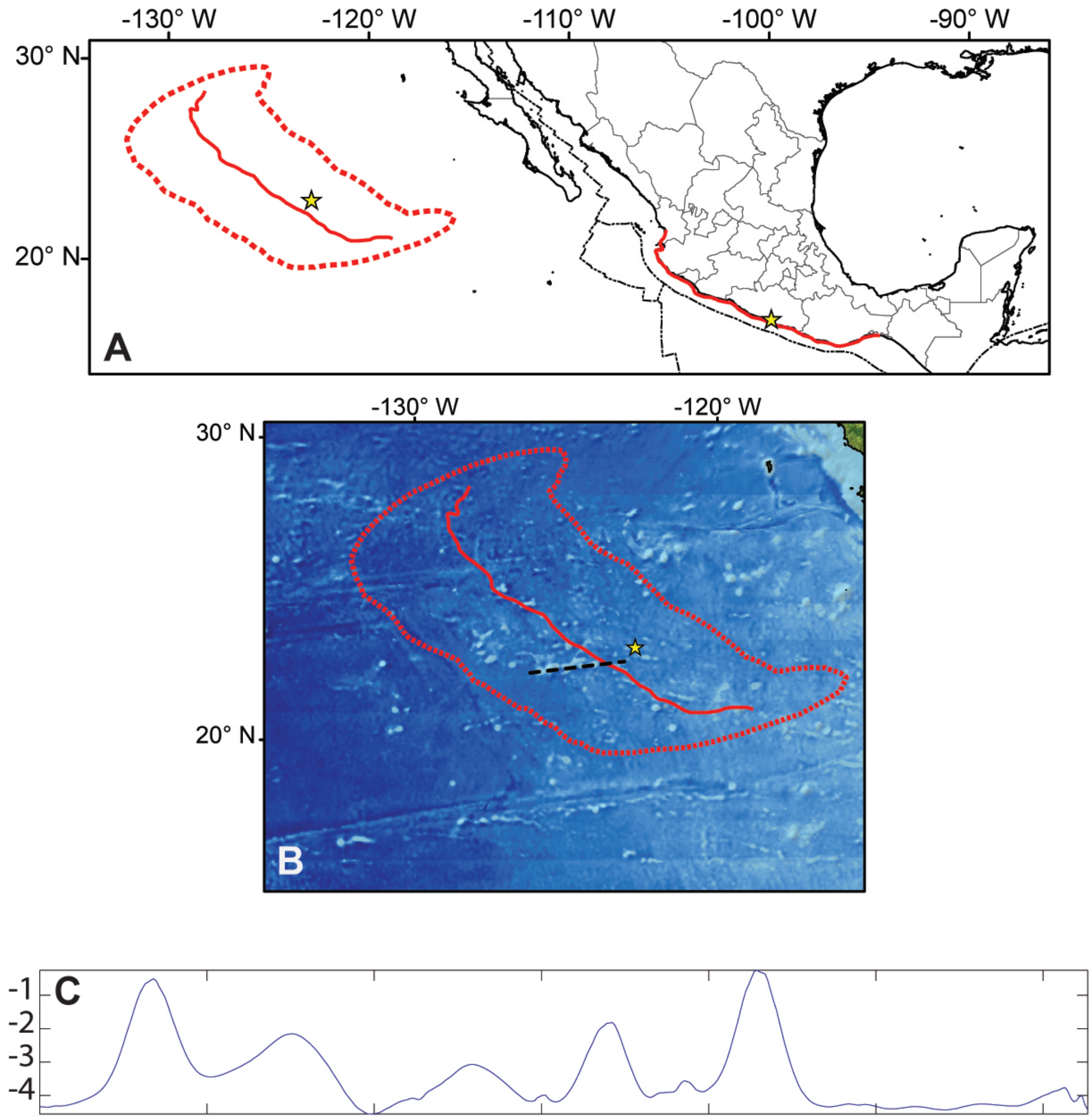

Figure 8. Reconstruction of the Mexican coastline

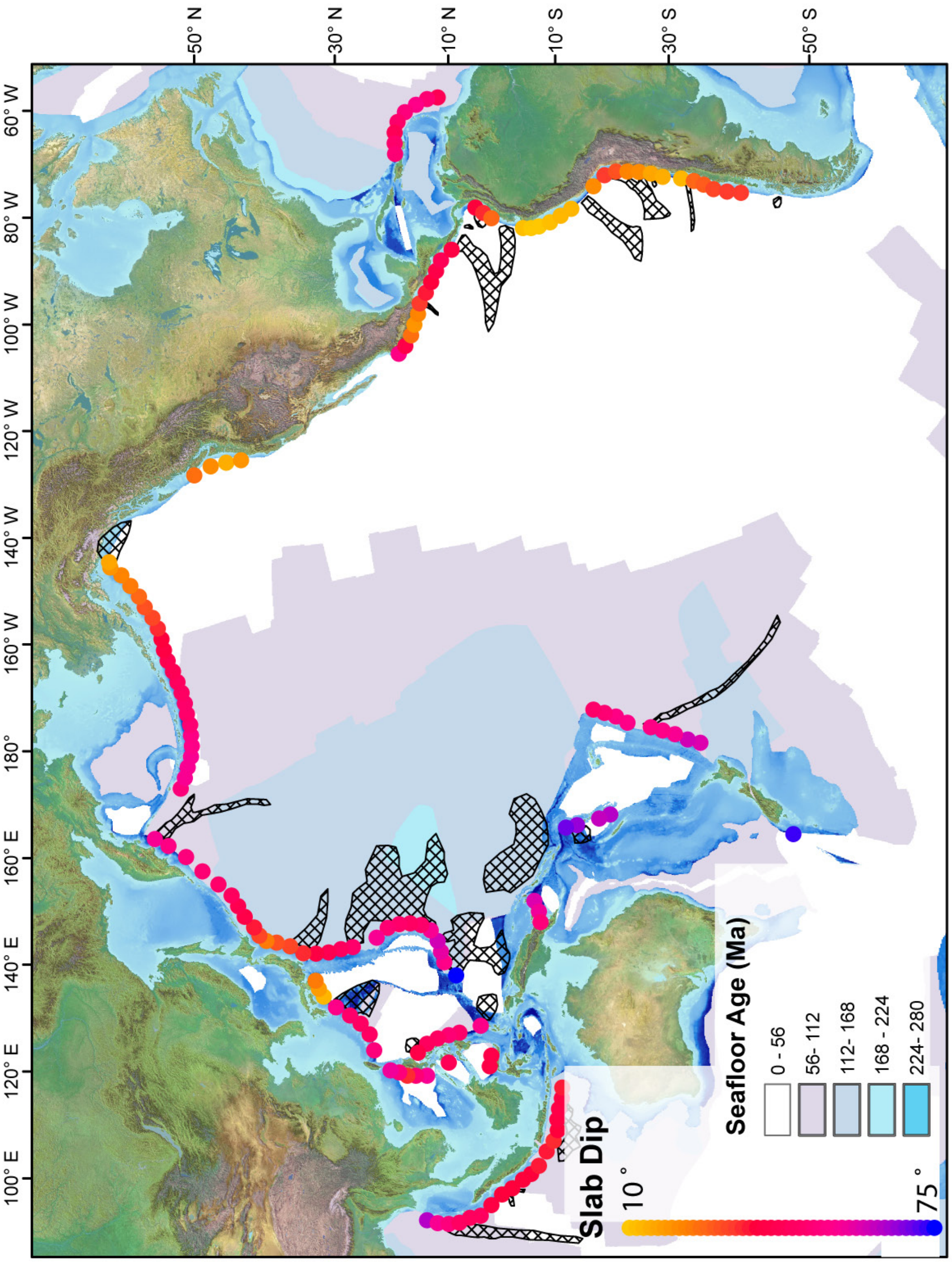

Figure 9. Slab dip, plate age, and bathymetric highs

Chapter 2
The lack of correlation between flat slabs and bathymetric impactors in South America

Originally published in:

Skinner, S. M., & Clayton, R. W. (2013). The lack of correlation between flat slabs and bathymetric impactors in South America. Earth and Planetary Science Letters, 371–372(0), 1-5.

doi: http://dx.doi.org/10.1016/j.epsl.2013.04.013

Abstract

Flat slab subduction has been attributed to various causes including mantle wedge dynamics, overriding by the upper plate, age of the subducting plate, and subduction of anomalously thick oceanic crust. One often favored explanation for flat slabs is the subduction of buoyant features on the oceanic plate in the form of an aseismic-ridge or oceanic plateau. We show through plate tectonic reconstructions of the Marquesas, Tuamotu, and Austral plateau, assuming that features on the conjugate plate can be used as proxies for subducted bathymetric anomalies, that there is very little correlation between the subduction of such anomalies and historic zones of flat subduction in South America. It is apparent that subduction of a bathymetric anomaly need not lead to a flat slab and not all flat slabs are associated with the subduction of a bathymetric anomaly.

Introduction

Approximately 10 percent of present day subduction zones are considered to have flat slabs, which means that their dip angle beyond the seismogenic zone is very shallow (Gutscher et al., 2000). This phenomenon has been shown to exist in the geologic record where cycles of alternating flat and normal-dip subduction are proposed (DeCelles et al., 2009; James and Sacks, 1999; Ramos and Folguera, 2009). Thickened oceanic crust, overriding of the upper plate, and mantle wedge suction are some of the proposed causes of shallow slabs (van Hunen et al., 2004). Perhaps the most frequently invoked explanation for these zones of flat to shallow subduction is excess positive buoyancy related to what we refer to as an impactor, the subduction of a bathymetric anomaly due to locally thickened oceanic crust (Anderson et al., 2007; Cross and Pilger, 1982; Gutscher et al., 1999; Gutscher et al., 2000; Liu et al., 2010; Livaccari et al., 1981; Nur and Ben-Avraham, 1983; Pilger, 1981; Saleeby, 2003). The argument for impactors as the cause of flat slabs is based on visual correlation between subducting features and shallow slabs. One of the clearest examples of this is the subduction of the Juan Fernandez Ridge where flat subduction is occurring in central Chile (Anderson et al., 2007) (Label 12 in Figure 1).

However, the actual increase in buoyancy due to thickening of the oceanic crust in the form of a seamount or oceanic plateau is generally quite small, and decreases rapidly with age of the plate (Cloos, 1993). Other geologic processes such as serpentinization of oceanic mantle lithosphere can create a buoyancy anomaly exceeding that due to thickening of the crust in the form of seamounts, but the overall buoyancy increase remains small (Kopp et al., 2004; Skinner and Clayton, 2011). Geodynamic investigations of the effects of subduction of thick crust (Gerya et al., 2009; van Hunen et al., 2004) indicate that a buoyant impactor is not a sufficient explanation for zones of flat subduction.

Tracking conjugate features

To investigate the correlation of impactors and flat slabs in the past we look for time and space coincidence of these phenomena by plate tectonic reconstructions. There are several island-chains and plateaus on the Pacific plate, and if we assume that these were formed at the East Pacific Rise (EPR) and hence likely had a conjugate on the Farallon (Nazca) Plate (Gutscher et al., 1999), then we can model the time and space interactions of these features with the trench. We reconstruct a set of bathymetric anomalies that mirror the Marquesas, Tuamotu, and Austral seamounts/plateaus. We use the EarthByte plate model (Müller et al., 2008) to reconstruct Pacific plate features to the time and location of their formation on the Pacific-Farallon/Nazca spreading ridge. We then create a feature at the ancient spreading ridge and track its location relative to South America forward in time as it moves as part of the subducting plate. See supplementary Figure1 for more details of the reconstructions. For times older than chron 21 there are no isochrons preserved on the Nazca plate and we must assume symmetric spreading (Seton et al., 2012), in addition any subducted ridge jumps also introduce uncertainty into the reconstructions. Note that the observed ridge jumps in the eastern Pacific are younger than the features we are reconstructing and do not affect our locations based on finite rotations (Cande and Haxby, 1991).

We have confidence in our rotation model and methods based on the agreement of the location of our hypothetical conjugates with observable bathymetric features shown in supplementary Figure 3 and the ability of our reconstructed conjugates to predict the location of observed magnetic isochrons (Figure 2). Our method of reconstruction is an improvement over past studies because we use global plate circuits that allow us to constrain positions relative to South America through time. Additionally the rotation models that we use cover a longer span of time than those used previously and provide finite rotations for a larger number of isochrons, which means the size and orientation of conjugate bathymetric features can evolve based on plate motions instead of being predefined. We have tested the plate rotation model used in our reconstructions (Müller et al., 2008) against four other published rotation models (Mayes et al., 1990; Pardo-Casas and Molnar, 1987; Pilger, 1981; Tebbens and Cande, 1997). See supplementary Tables 1 and 2 for the rotations used. Supplementary Figure 2 shows the close agreement between these models in reconstructing chrons 10 and

13. Note that our reconstruction of the Inca Plateau is 600 kilometers east of the original location proposed by Gutscher et al. (1999). We believe that our reconstructions, that use data from both sides of the spreading ridge, do a better job predicting the location of observable features. A key feature that cannot be accounted for by the half-stage rotation model used in previous reconstructions is the observed asymmetry in spreading along the East Pacific Rise (Müller et al., 2008).

In order to visualize the spatial and temporal relations between our conjugate features and the proposed historic zones of flat subduction, we track points along the centerline of the bathymetric anomalies and calculate the distance from each flat slab. The proximity of the subducting feature is plotted in Figure 3, together with a gray box that represents the spatial and temporal extent of the flat slab as reported by Ramos and Folguera (2009). For one of our conjugate features to be considered as a cause for the flat slab we expect it to intersect the target region near the onset of shallow subduction. The results for each slab are discussed below:

Carnegie Slab (3Ma to Present)

Although the Carnegie slab is a very small target, we track several impactors that arrive at the trench well before the development of the flat slab. The lithosphere currently subducting here is related to Nazca-Cocos spreading that started after 26 Ma and Pacific-Nazca conjugates are not applicable to this flat slab at this point.

Peruvian Slab (11 Ma to 0 Ma)

The Peruvian slab has numerous impactors that reach well into the target zone and can be considered as possible causes of the flat slab. The issue with the Peruvian slab, however, is that there have been impactors for the twenty million years preceding the present day flat slab. If this portion of the South American margin has been consistently seeing bathymetric highs subduct it cannot be the subducting bathymetric high itself that supports the flattening of the slab. As shown in Figure 2, our reconstruction of the conjugate to the Marquesas Plateau is 600 kilometers to the east of the location of Gutscher et al. (1999). This makes it less likely to be the direct cause of the flat slab in Peru.

Altiplano Slab (40-32 Ma to 27-18 Ma)

The Altiplano slab appears to be anti-correlated with impactors. This portion of the margin has seen numerous impactors but they all postdate the flattening of the slab, and the majority of them arrive once the slab has resumed a steep geometry.

Puna Slab (18 Ma to 12 Ma)

The short lived Puna flat slab has no impactors at the onset, but again there are impactors that occur once the slab has ceased to be flat. The impactors that hit after the flat slab are on the larger end of what we have measured, so we cannot use the size of imapactor to explain why some have an effect while others do not.

Pampean Slab (12 Ma to Present)

The Pampean slab has a several impactors once the slab has gone flat. This flat slab is currently explained by the subduction of the Juan Fernandez Ridge, however, this small discontinuous chain of volcanoes was not formed on a spreading ridge so we have no way to constrain the size, shape, or extent of any portion of it that has already been subducted.

Payenia Slab (13 Ma to 5 Ma)

From our analysis there are no conjugate impactors that can be associated with the Payenia flat slab.

Discussion

We have looked at the correlations between flat slabs and impactors more closely with a detailed global data set and have found that the correlations are not as strong as previously thought. In some cases show there is no apparent correlation. Figure 1 represents our assessment of the buoyancy hypothesis at subduction zones around the globe based on the visual correlation of a subducting bathymetric anomaly and a change in slab geometry, as defined by Slab 1.0 (Hayes et al., 2012). Each numbered circle is discussed in the following section. In South America, the along trench width of the Peruvian flat slab is five times greater than the width of the Nazca Ridge which leads us to question the buoyancy of the impactor as the direct cause of the flat slab. While the Carnegie Ridge (8 in Figure 1), Nazca Ridge (10), and Juan Fernandez Ridge (12) coincide with flat flabs, the Iquique Ridge (11) subducts without producing a flat slab and based on our reconstruction of the Inca Plateau there is no subducting anomaly to support the northern Peruvian flat slab (9). In Cascadia (6) and Mexico (7), we have shallow slabs but no indication of an impactor offshore. The Emperor Seamounts (4), Magellan Seamounts (3), Roo Rise (15), and Louisville Ridge (13) all subduct with no apparent change in the geometry of the associated subducting slab. Japan presents some of the best evidence against the buoyancy hypothesis, namely that the shallow slab is anti-correlated with the downgoing bathymetric ridges. The shallow segment of the Nankai subduction zone is centered over the Shikoku basin (2), not the subducting Palau-Kyushu or Izu-Bonin ridges (1). Two extreme examples of locations where buoyancy has changed the subduction zone geometry are the Ontong Java Plateau (14), where the largest igneous province (Neal et al., 1997) has caused a reversal of subduction, and the moderately sized yet anomalously thick Yakutat terrane (5) that has impeded subduction in Alaska (Christeson et al., 2010; Gulick et al., 2007).

The recent compilation of the history of flat slabs in South America through time as defined by Ramos and Folguera (2009) allows us to extend the comparison of impactors and flat slabs back in time in this region. This compilation, plus the fact that this margin only involves two plates for most of its length and history, make this an excellent test of the impactor hypothesis. The present plate geometry in this region has been stable since the 23 Ma creation of the Nazca and Cocos Plates from the Farallon plate (Lonsdale, 2005). We recognize that there are more detailed descriptions of the temporal variations in slab geometry for portions of the South American margin (Kay and Coira, 2009). Our analysis focuses on a more general binary system that classifies a slab as normal or flat. The variation in location and timing of flat slabs as proposed by different authors (Kay and Coira, 2009; Ramos and Folguera, 2009) is less than the discrepancies we find between our reconstructions and target zones and hence does not affect our interpretations.

On the whole the subduction system in South America does not support the hypothesis that flat slabs are solely caused by subducted bathymetric anomalies. The present day connection of the Pampean slab with the Juan Fernandez Ridge, the Peruvian slab with the Nazca

Ridge, and the Carnegie slab with the Carnegie Ridge are the only examples where there is a correlation, out of 15 cases. We argue against these as the cause of the flat slabs based on the fact that the Nazca Ridge is not as wide as the flat slab it creates and that the Juan Fernandez Ridge is a discontinuous structure and neither has large anomalous buoyancy.

We find that there is not a very good correlation between possible subducting anomalies in the past and inferred periods of flat or shallow subducting along the South American margin. The lack of a correlation between subducting anomalies and flat slabs in both the past and present implies that it cannot be the direct cause of flat slab subduction. If we look at the present-day spatially correlated flat slabs and subducting anomalies we can see that the flat slabs are not confined to the location of the subducting anomaly, which further casts doubt on the anomaly as the direct cause. We envision a change in mantle dynamics induced by the subducting anomaly as one possible explanation for flat slabs that persist in the wake of a subducting anomaly. This does not rely on the buoyancy of the subducting anomaly itself.

Based on our analysis of the flat subduction in central Mexico (Skinner and Clayton, 2011) we prefer a model of mantle hydration to induce shallow and flat slabs(Billen and Gurnis, 2001; Manea and Gurnis, 2007). The hydration process may be aided by subduction erosion brought on by the subducting of a bathymetric high in addition to highly altered and hydrated crust or mantle. There is evidence for the hydration process in Mexico in the form of a low viscosity layer that decouples the flat slab and the overriding crust (Kim et al., 2010). Additional evidence for hydration includes mantle xenoliths found in Mexico with water content in excess of 8 wt% (Blatter and Carmichael, 1998).

It appears that there is likely not a single cause of flat slabs. Over geologic time, the mantle can become transiently heterogeneous and it is these anomalies that lead to the diversity of subduction zone geometries that we observe today. The suggestion of orogenic cycles (DeCelles et al., 2009) may be a controlling process, with impactors only having an effect if the subduction is in the part of its cycle where the slab was shallowing. This could explain why in the present day, some zones are unaffected by impactors.

Conclusions

Our plate tectonic reconstructions of the South American margin and potential conjugate bathymetric anomalies when paired with the history of flat slabs compiled by Ramos and Folguera (2009) shows that there is no clear link between a subducting anomaly and zones of flat subduction. We have shown previously that the correlation between current flat slabs and subducting crustal anomalies does not exist and therefore buoyant bathymetric anomalies cannot be the sole cause of flat slabs. With this series of reconstructions we have shown that the correlation between bathymetric anomalies and flat slabs did not exist in the past and that the Inca Plateau was mislocated.

Acknowledgements

We thank J.P. Avouac and J. Stock for discussion and comments on the manuscript. We thank the editor, M.A. Gutscher, and V. Ramos for helpful reviews. This study was supported by the Gordon and Betty Moore Foundation through the Tectonics Observatory at Caltech. This is contribution number 201 from the Caltech Tectonics Observatory.

References

Anderson, M., Alvarado, P., Zandt, G., Beck, S., 2007. Geometry and brittle deformation of the subducting Nazca Plate, Central Chile and Argentina. Geophysical Journal International 171, 419-434.

Billen, M.I., Gurnis, M., 2001. A low viscosity wedge in subduction zones. Earth and Planetary Science Letters 193, 227-236.

Blatter, D.L., Carmichael, I.S.E., 1998. Hornblende peridotite xenoliths from central Mexico reveal the highly oxidized nature of subarc upper mantle. Geology 26, 1035-1038.

Cande, S.C., Haxby, W.F., 1991. Eocene Propagating Rifts in the Southwest Pacific and Their Conjugate Features on the Nazca Plate. J. Geophys. Res. 96, 19609-19622.

Cande, S.C., LaBrecque, J.L., Larson, R.L., Pittman, W.C., Golovchenko, X., Haxby, W.F., 1989. Magnetic lineations of the world's ocean basins, Magnetic lineations of the world's ocean basins. AAPG, Tulsa, OK.

Christeson, G.L., Gulick, S.P.S., van Avendonk, H.J.A., Worthington, L.L., Reece, R.S., Pavlis, T.L., 2010. The Yakutat terrane: Dramatic change in crustal thickness across the Transition fault, Alaska. Geology 38, 895-898.

Cloos, M., 1993. Lithospheric buoyancy and collisional orogenesis; subduction of oceanic plateaus, continental margins, island arcs, spreading ridges, and seamounts. Geological Society of America Bulletin 105, 715-737.

Cross, T.A., Pilger, R.H., 1982. Controls of Subduction Geometry, Location of Magmatic Arcs, and Tectonics of Arc and Back-Arc Regions. Geological Society of America Bulletin 93, 545-562.

DeCelles, P.G., Ducea, M.N., Kapp, P., Zandt, G., 2009. Cyclicity in Cordilleran orogenic systems. Nature Geosci 2, 251-257.

Gerya, T.V., Fossati, D., Cantieni, C., Seward, D., 2009. Dynamic effects of aseismic ridge subduction: numerical modelling. European Journal of Mineralogy 21, 649-661.

Gulick, S.P.S., Lowe, L.A., Pavlis, T.L., Gardner, J.V., Mayer, L.A., 2007. Geophysical insights into the Transition fault debate: Propagating strike slip in response to stalling Yakutat block subduction in the Gulf of Alaska. Geology 35, 763.

Gutscher, M.A., Olivet, J.L., Aslanian, D., Eissen, J.P., Maury, R., 1999. The "lost Inca Plateau": cause of flat subduction beneath Peru? Earth and Planetary Science Letters, 335-341.

Gutscher, M.A., Spakman, W., Bijwaard, H., Engdahl, E.R., 2000. Geodynamics of flat subduction: Seismicity and tomographic constraints from the Andean margin. Tectonics 19, 814-833.

Hayes, G.P., Wald, D.J., Johnson, R.L., 2012. Slab1.0: A three-dimensional model of global subduction zone geometries. Journal of geophysical research 117.

James, D.E., Sacks, I.S., 1999. Cenozoic formation of the central andes; a geophysical perspective. Special Publication (Society of Economic Geologists (U.S.)) 7, 1-25.

Kay, S.M., Coira, B.L., 2009. Shallowing and steepening subduction zones, continental lithospheric loss, magmatism, and crustalflow under the Central Andean Altiplano-Puna Plateau. Backbone of the Americas: shallow subduction, plateau uplift, and ridge and terrane collision, 229.

Kim, Y., Clayton, R.W., Jackson, J.M., 2010. Geometry and seismic properties of the subducting Cocos plate in central Mexico, Journal of Geophysical Research. AGU, p. B06310.

Kopp, H., Flueh, E.R., Papenberg, C., Klaeschen, D., 2004. Seismic investigations of the

O'Higgins Seamount Group and Juan Fernandez Ridge: Aseismic ridge emplacement and lithosphere hydration. Tectonics 23.

Liu, L., Gurnis, M., Seton, M., Saleeby, J., Muller, R.D., Jackson, J.M., 2010. The role of oceanic plateau subduction in the Laramide orogeny. Nature Geosci 3, 353-357.

Livaccari, R.F., Burke, K., Sengor, A.M.C., 1981. Was the Laramide orogeny related to subduction of an oceanic plateau? Nature 289, 276-278.

Lonsdale, P., 2005. Creation of the Cocos and Nazca plates by fission of the Farallon plate. Tectonophysics 404, 237-264.

Manea, V., Gurnis, M., 2007. Subduction zone evolution and low viscosity wedges and channels. Earth and Planetary Science Letters 264, 22-45.

Mayes, C.L., Lawver, L.A., Sandwell, D.T., 1990. Tectonic History and New Isochron Chart of the South Pacific. J. Geophys. Res. 95, 8543-8567.

Müller, R.D., Sdrolias, M., Gaina, C., Roest, W.R., 2008. Age, spreading rates, and spreading asymmetry of the world's ocean crust, Geochemistry Geophysics Geosystems. American Geophysical Union, p. Q04006.

Neal, C.R., Mahoney, J.L., Kroenke, L.W., Duncan, R.A., Petterson, M.G., 1997. The Ontong Java Plateau, in: Mahoney, J.J., Coffin, M. (Eds.), Large Igneous Provinces: Continental, Oceanic, and Planetary Flood Volcanism. American Geophysical Union, pp. 183-216.

Nur, A., Ben-Avraham, Z., 1983. Volcanic gaps due to oblique consumption of aseismic ridges. Tectonophysics 99, 355-362.

Pardo-Casas, F., Molnar, P., 1987. Relative motion of the Nazca (Farallon) and South American Plates since Late Cretaceous time. Tectonics 6, 233-248.

Pilger, R.H., 1981. Plate Reconstructions, Aseismic Ridges, and Low-Angle Subduction beneath the Andes. Geological Society of America Bulletin 92, 448-456.

Ramos, V.A., Folguera, A., 2009. Andean flat-slab subduction through time. Geological Society, London, Special Publications 327, 31-54.

Saleeby, J., 2003. Segmentation of the Laramide Slab, evidence from the southern Sierra Nevada region. Geological Society of America Bulletin 115, 655-668.

Seton, M., Müller, R.D., Zahirovic, S., Gaina, C., Torsvik, T., Shephard, G., Talsma, A., Gurnis, M., Turner, M., Maus, S., Chandler, M., 2012. Global continental and ocean basin reconstructions since 200 Ma. Earth-Science Reviews 113, 212-270.

Skinner, S., Clayton, R., 2011. An Evaluation of Proposed Mechanisms of Slab Flattening in Central Mexico. Pure and Applied Geophysics 168, 1461-1474.

Tebbens, S.F., Cande, S.C., 1997. Southeast Pacific tectonic evolution from early Oligocene to present. Journal of Geophysical Research 102, 12061-12084.

van Hunen, J., van den Berg, A.P., Vlaar, N.J., 2004. Various mechanisms to induce present-day shallow flat subduction and implications for the younger Earth: a numerical parameter study. Physics of The Earth and Planetary Interiors 146, 179-194.

Figure Captions

Figure 1

Map of slab dip for subduction zones around the Pacific basin. Data for subduction zone geometry are from Hayes et al. (2012). Numbered circles represent our interpretation of the validity of the buoyancy hypothesis at each location where we have data constraining changes in the geometry of the subducted slab. Circles are colored red where there is a subducting bathymetric anomaly but no associated flat slab, yellow where there is a flat slab without any apparent subducting bathymetric anomaly, and green where a change in the geometry of the subducting slab and a bathymetric anomaly are coincident. See text for discussion of numbered circles.

Figure 2

Map of present day South America showing the location of our reconstructed magnetic isochrons. . Black dashed lines are 20km slab depth contours from Hayes et al. (2012). Magnetic isochrons are from Cande et al. (1989) , with relevant chrons labeled. Colored circles on the Pacific plate are construction points along magnetic isochrons and are used to reconstruct the location of conjugate features on the Nazca plate. The inset map shows the Marquesas plateau at a larger scale to make the relationship between the plateau and magnetic isochrons clear. The stippled feature is the MM2 reconstruction from figure 2A of Gutscher et al. (1999). Note that our reconstruction of the isochrons that bound the Marquesas plateau require a 600 kilometer eastward shift of the Inca plateau.

Figure 3

Location of Pacific - Farallon/Nazca conjugate features relative to a given flat slab. We have placed points along Pacific plate bathymetric highs, and created conjugate features using standard plate reconstruction techniques and the rotation model of Müller et al. (2008). A plot for each flat slab shows the proximity of a reconstructed point on the bathymetric anomaly to that flat slab, plotted as a function of time. The thickness of the line scales with the crustal volume in a 100 by 200 kilometer box around the Pacific plate conjugate point. The grey box represents the spatial and temporal extent of the flat slab from Ramos and Folguera (2009). We expect impactors to pass through this target zone if the buoyancy hypothesis is the cause of the flat slab. The map shows the location of the flat slabs along the South American margin (Ramos and Folguera, 2009). The black triangles are the point from which our distances are calculated. See Supplementary Table 3 for information about the conjugate points.

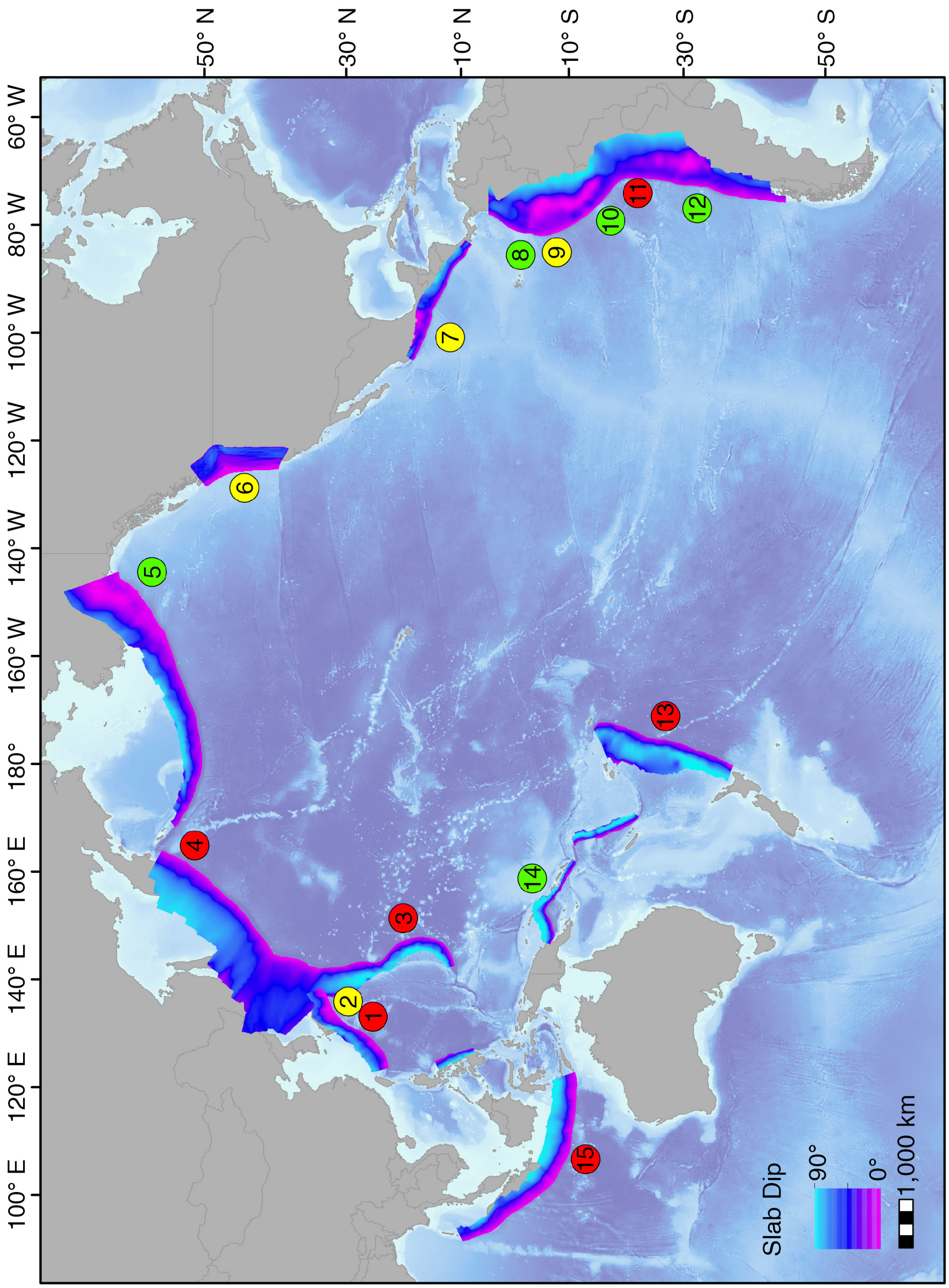

Figure 1. Map of circum-Pacific subduction zone slab dip

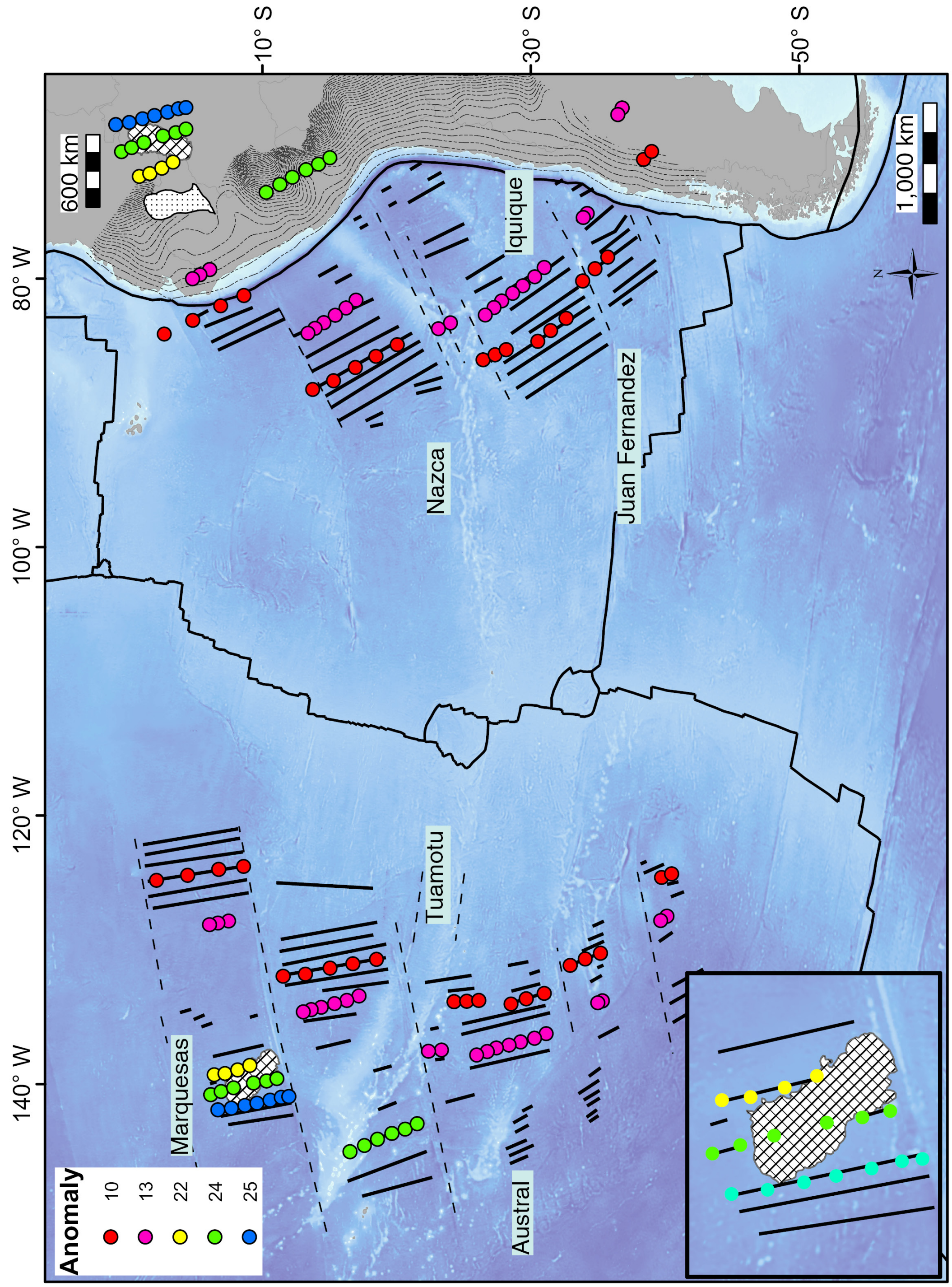

Figure 2. Map of South America and conjugate features

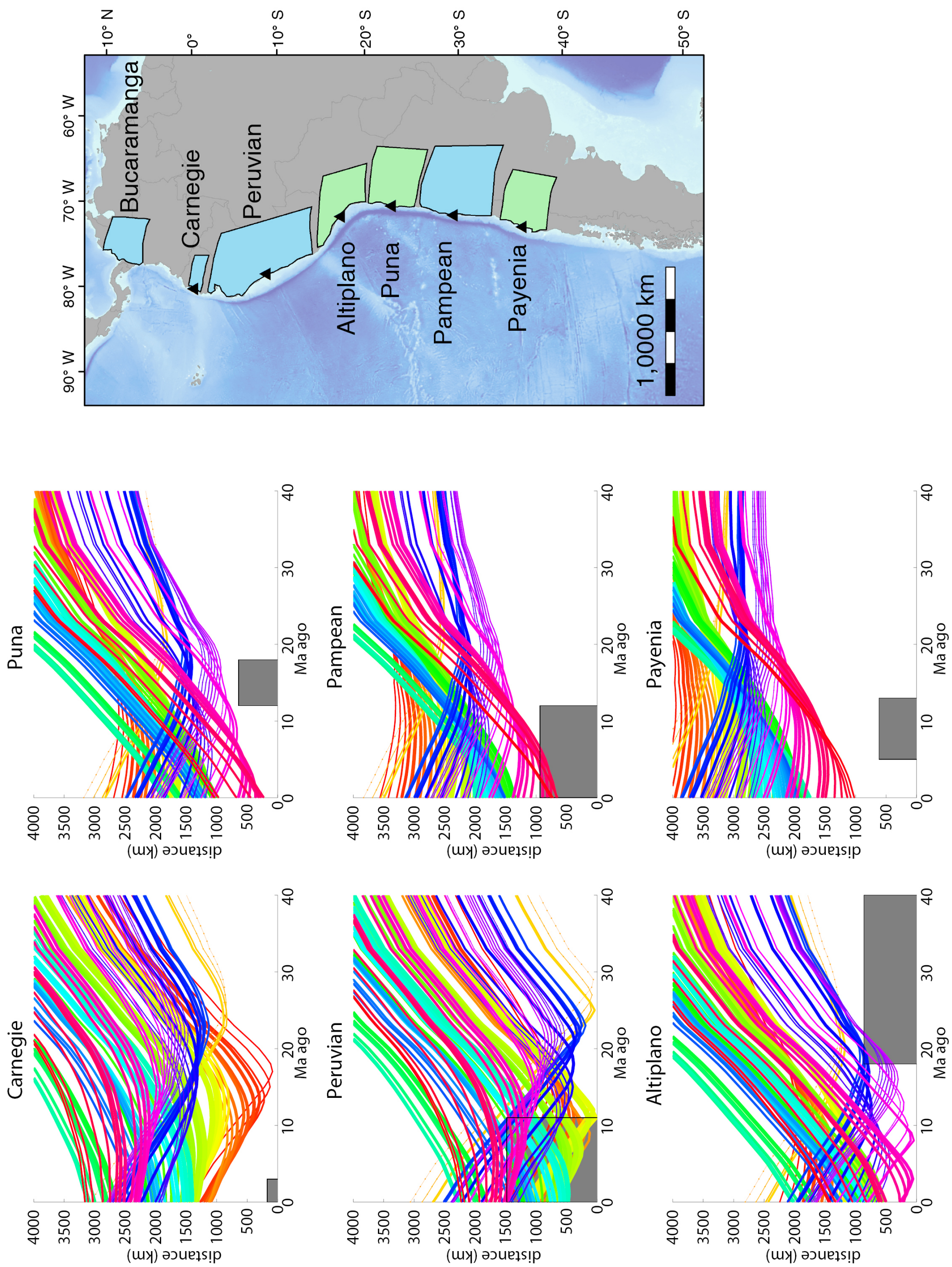

Figure 3. Location of conjugate features relative to a given flat slab

Supplementary Material

Supplementary Figure 1: Conjugate reconstructions

Panel a shows our 92 starting points on the Pacific. The color of the circle is used to match a starting point to a path in Figure 3. The size of the circle is relative to the crustal volume in a 100 km by 200 km swath centered on the starting point. Panel b shows the location of our starting points relative to Pacific bathymetry. Panel c shows our method of distance calculation used in Figure 3. Starting from the reconstucted conjugate point we rotate the point back in time in million year increments. We calculate a linear distance between each reconstructed point(orange circle) and the center of the flat slab (black triangle).

Supplementary Figure 2: Agreement of Reconstructions

This map of the Nazca Plate shows the Pacific points of Figure 2 rotated by five different rotation models . We find that all models do an equally good job of predicting the location of magnetic isochrons as identified by Cande et al. (1989).

Supplementary Figure 3: Agreement of conjugate features

Map of present day South America depicting the agreement of our proposed conjugates with actual bathymetric features. The yellow lines are a mirror image of 1km contours of modern bathymetry on the Pacific plate. The purple lines are 1km contours of modern Nazca Plate bathymetry. Our proposed conjugates match well with the actual bathymetry. Our reconstruction of the Inca Plateau, however, is ~600 km to the east of the original location proposed by Gutscher et al. 1999.

Supplementary Figure 4: Agreement of fracture zones

This map shows syntheic fracture zones produced by the rotation model used in our reconstructions (Müller et al., 2008) in red and fracture zones as mapped by Matthews et al. (2011) in black. While it is unlikely that any model will be able to reproduce all of the complexities of fracture zones, we believe that this model does an excellent job at reprducing the large scale obervable trends.

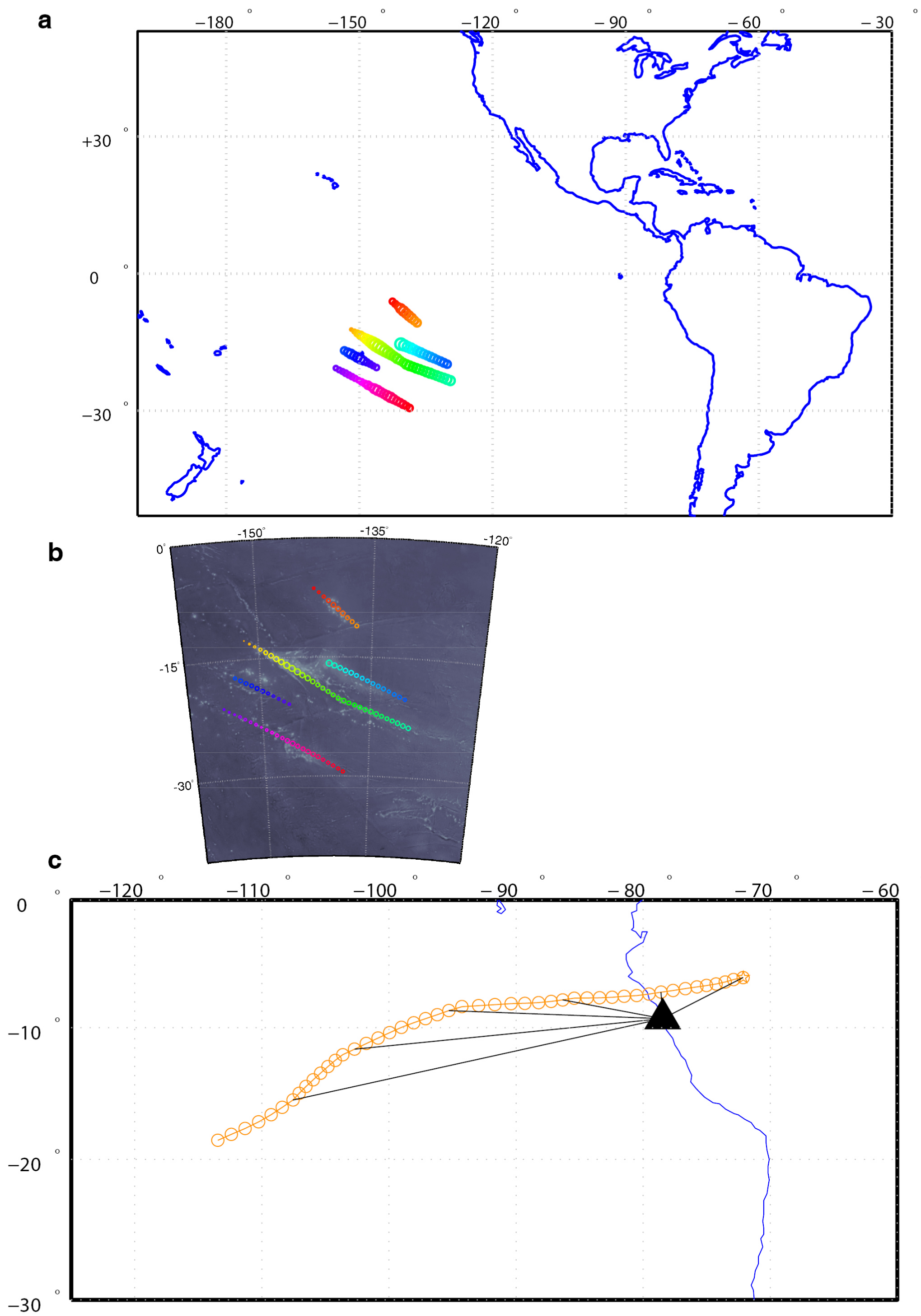

Figure S–1. Conjugate reconstructions

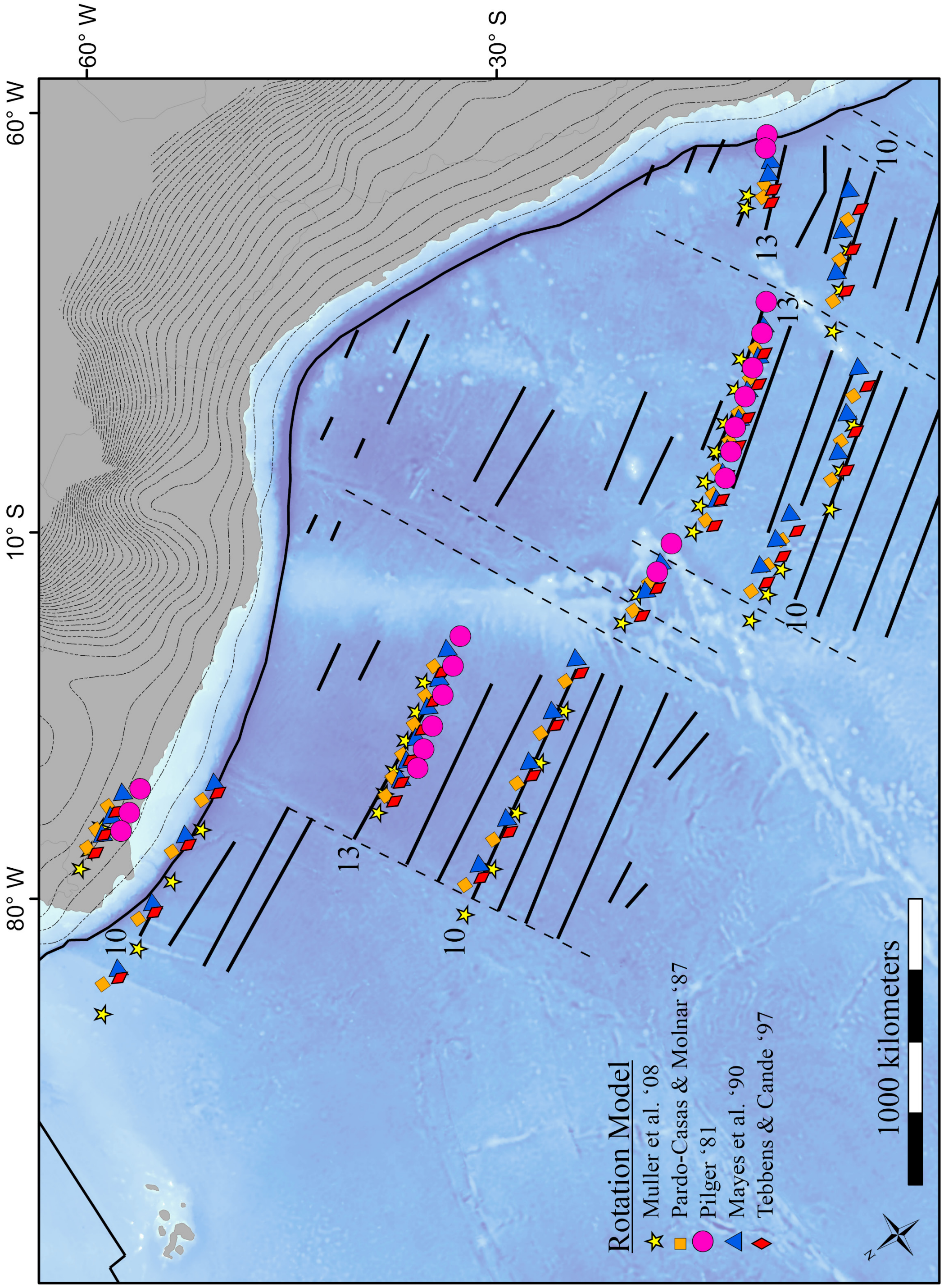

Figure S–2. Agreement of reconstructions

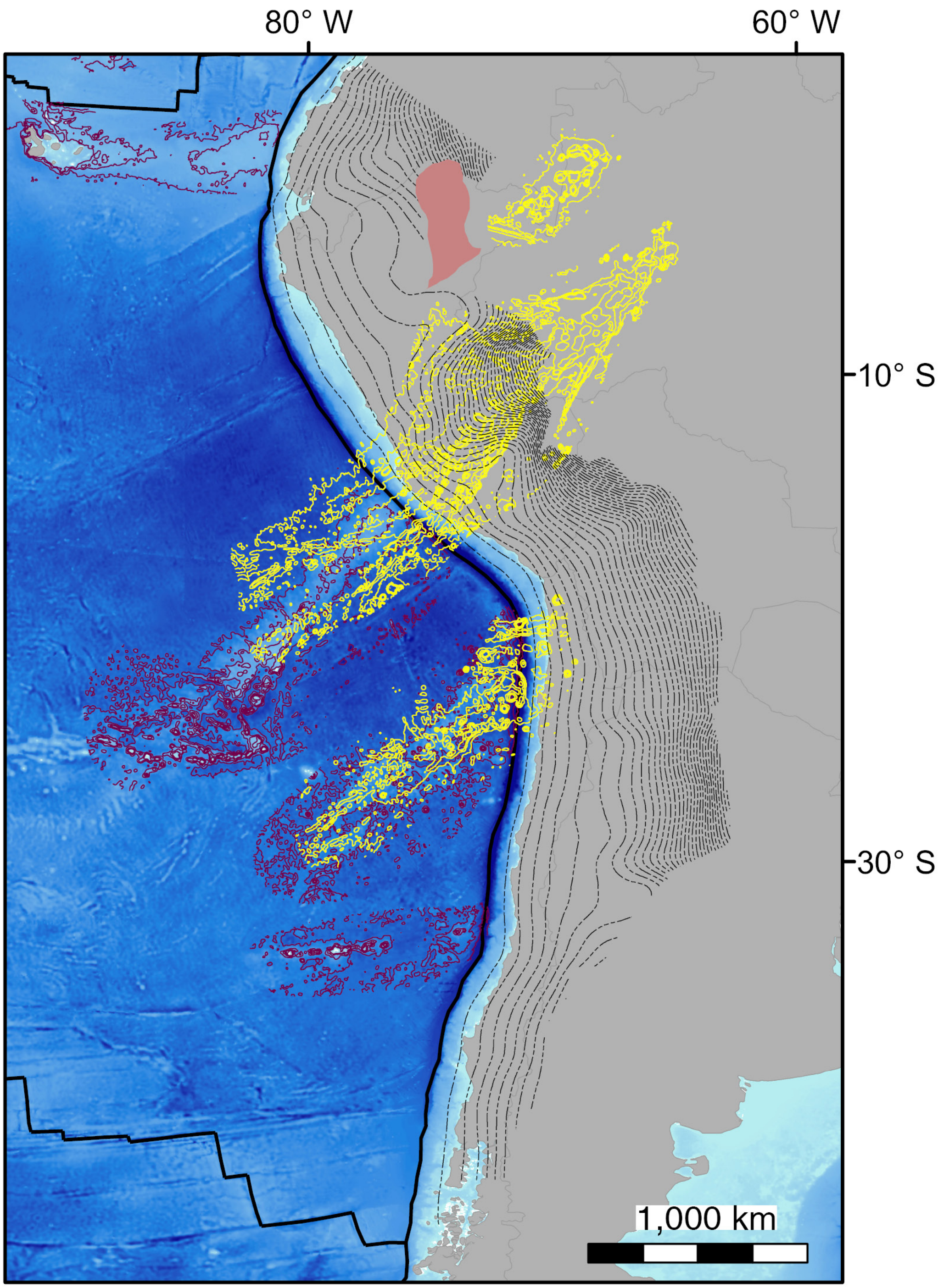

Figure S–3. Agreement of conjugate features

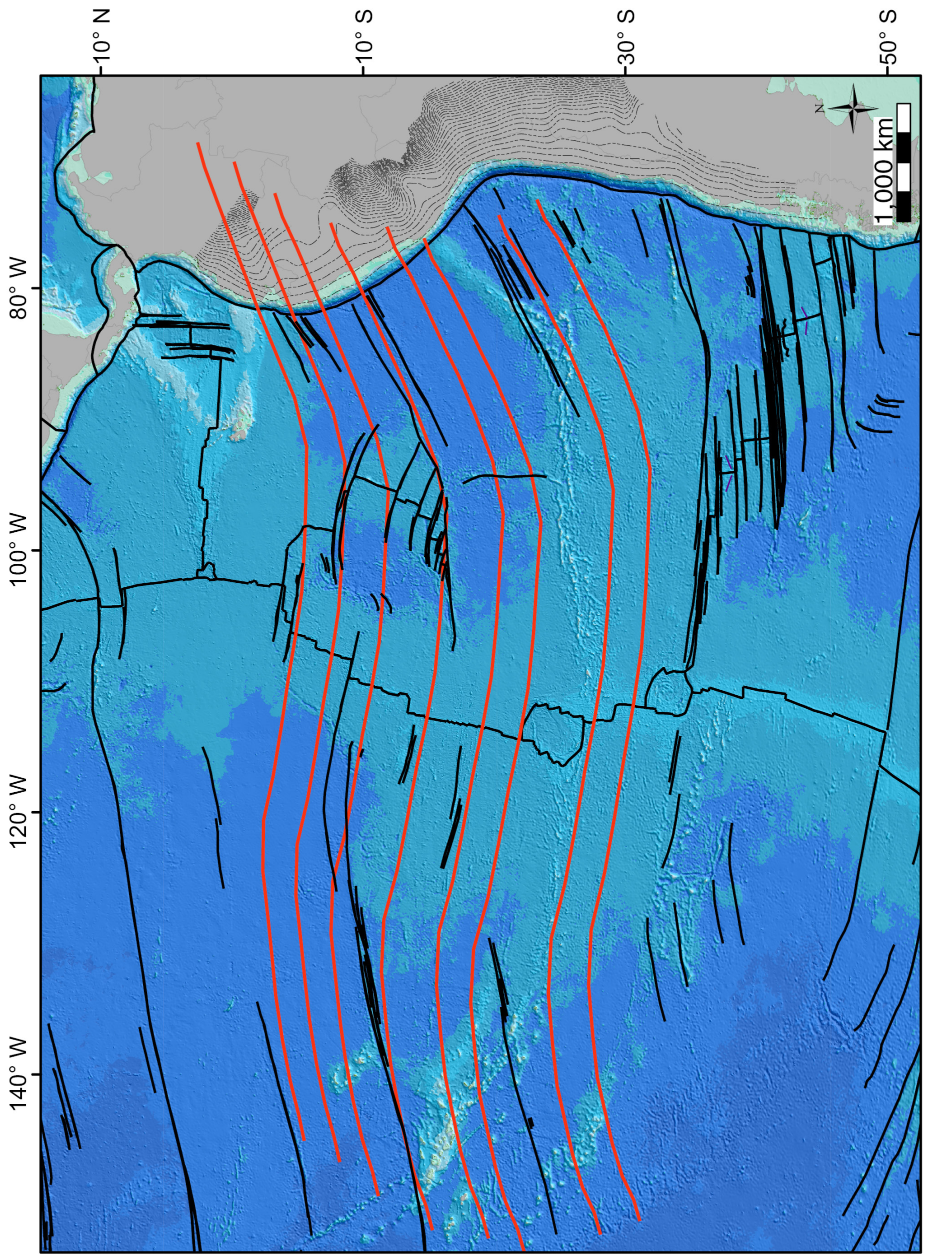

Figure S–4. Agreement of fracture zones

Table 1. Poles of rotation for the Nazca plate relative to the Pacific plate used to test reconstructions of magnetic isochrons.

Chron	**Latitude**	**Longitude**	**Angle**	**Source**
13	68.71	-108.18	-49.44	(Müller et al., 2008)
13	69.85	-106.13	-49.54	(Pardo-Casas and Molnar, 1987)
13	69.04	-104.34	-49.63	(Mayes et al., 1990)
13	69.74	-105.82	-49.24	(Tebbens and Cande, 1997)
13	67.1	-102.4	-49.7	(Pilger, 1981)
10	67.01	-102.46	-43.14	(Müller et al., 2008)
10	67.34	-100.08	-43.77	(Pardo-Casas and Molnar, 1987)
10	66.2	-98.41	-44.05	(Mayes et al., 1990)
10	66.91	-98.3	-43.64	(Tebbens and Cande, 1997)

Table 2. Poles of rotation for the Pacific and Nazca plates relative to the South America plate used in the reconstruction and tracking of conjugate features.

	Nazca/Farallon - South America			**Pacific- South America**		
Age (Ma)	**Latitude**	**Longitude**	**Angle**	**Latitude**	**Longitude**	**Angle**
1	-65.60	78.57	0.79	54.68	-79.97	0.69
2	-63.16	76.35	1.52	57.21	-77.37	1.44
3	62.58	-102.48	-2.28	57.94	-77.99	2.16
4	62.58	-99.95	-3.08	58.23	-79.94	2.82
5	62.56	-98.41	-3.88	58.40	-81.25	3.48
6	64.03	-98.60	-4.82	58.60	-82.11	4.14
7	64.34	-98.66	-5.82	59.44	-82.19	4.74
8	64.57	-98.67	-6.81	60.09	-82.30	5.34
9	64.68	-98.64	-7.81	60.67	-82.38	5.94
10	64.50	-98.21	-8.82	61.55	-82.60	6.52
11	64.25	-96.92	-9.86	62.66	-83.67	7.05
12	64.11	-96.34	-10.86	63.97	-83.70	7.58
13	64.10	-95.60	-11.89	65.02	-84.13	8.08
14	64.12	-94.86	-12.93	65.93	-84.69	8.57
15	64.14	-94.20	-13.97	66.74	-85.24	9.06
16	62.52	-93.88	-15.06	67.47	-85.77	9.55
17	61.12	-93.57	-16.16	68.14	-86.28	10.04
18	60.02	-93.26	-17.34	68.64	-86.92	10.44
19	59.15	-92.95	-18.61	69.02	-87.67	10.78
20	58.40	-92.59	-19.88	69.41	-88.61	11.10
21	59.16	-93.20	-21.14	69.53	-89.12	11.48
22	59.99	-93.89	-22.38	69.59	-89.53	11.86
23	60.73	-94.54	-23.64	69.65	-89.94	12.24
24	61.67	-96.53	-24.56	69.70	-90.34	12.63
25	62.57	-98.59	-25.36	69.56	-90.72	13.15
26	63.39	-100.60	-26.16	69.41	-91.23	13.67
27	64.20	-102.62	-27.00	69.16	-91.84	14.18
28	64.93	-104.89	-27.85	68.80	-91.95	14.67
29	65.49	-107.29	-28.71	68.54	-91.60	15.19
30	65.95	-109.69	-29.57	68.32	-91.13	15.71

Table 2 continued

	Nazca/Farallon - South America			Pacific- South America		
Age (Ma)	**Latitude**	**Longitude**	**Angle**	**Latitude**	**Longitude**	**Angle**
31	66.33	-112.02	-30.44	68.11	-90.73	16.23
32	66.66	-114.29	-31.32	67.91	-90.39	16.75
33	66.92	-116.48	-32.20	67.73	-90.11	17.28
34	67.82	-119.85	-32.69	67.54	-87.92	17.77
35	68.51	-123.49	-33.21	67.49	-84.97	18.23
36	69.10	-127.23	-33.75	67.39	-82.23	18.70
37	69.59	-131.04	-34.31	67.23	-79.67	19.18
38	69.97	-134.88	-34.90	67.04	-77.32	19.67
39	70.25	-138.71	-35.46	66.86	-75.20	20.21
40	70.42	-142.51	-36.00	66.69	-73.30	20.79
41	70.58	-146.13	-36.90	66.49	-72.22	21.28
42	70.66	-149.60	-37.86	66.30	-71.30	21.76
43	70.80	-153.12	-38.91	65.97	-70.90	22.16
44	71.02	-156.70	-40.08	65.52	-71.11	22.44
45	71.23	-159.95	-41.23	65.26	-71.53	22.72
46	71.37	-163.08	-42.39	65.01	-71.96	23.00
47	71.35	-166.21	-43.60	64.57	-72.08	23.29
48	71.25	-169.36	-44.84	64.03	-72.15	23.56
49	71.21	-173.79	-45.93	63.24	-72.73	23.74
50	71.06	-177.97	-47.05	62.46	-73.29	23.93
51	70.84	178.11	-48.19	61.69	-73.84	24.12
52	70.60	174.43	-49.31	61.06	-74.60	24.32
53	70.29	170.95	-50.37	60.52	-75.43	24.60
54	69.66	167.67	-51.42	59.69	-75.85	25.05
55	68.90	164.68	-52.47	58.80	-76.18	25.58
56	68.15	162.15	-53.50	57.98	-76.54	26.12
57	67.62	161.04	-54.02	57.47	-77.10	26.68
58	67.09	160.00	-54.55	56.97	-77.64	27.24
59	66.57	159.04	-55.08	56.50	-78.15	27.80
60	66.05	158.15	-55.61	56.05	-78.64	28.37
61	65.53	157.32	-56.15	55.62	-79.12	28.93
62	64.93	156.69	-56.67	55.20	-79.33	29.58
63	64.33	156.13	-57.19	54.80	-79.52	30.23
64	63.65	155.89	-58.09	53.82	-79.08	30.71

Table 2 continued

	Nazca/Farallon - South America			Pacific- South America		
Age (Ma)	**Latitude**	**Longitude**	**Angle**	**Latitude**	**Longitude**	**Angle**
65	62.99	155.71	-59.05	52.79	-78.63	31.18
66	62.39	155.50	-59.98	51.88	-78.32	31.65
67	61.86	155.25	-60.86	51.11	-78.19	32.10
68	61.35	155.05	-61.79	50.34	-78.06	32.55
69	60.84	154.94	-62.82	49.52	-77.88	33.01
70	60.35	154.83	-63.85	48.72	-77.74	33.48
71	59.87	154.74	-64.88	47.95	-77.62	33.96
72	59.48	154.59	-65.99	47.14	-77.61	34.34
73	59.22	154.36	-67.19	46.28	-77.74	34.56
74	58.96	154.21	-68.27	45.62	-77.84	34.85
75	58.71	154.17	-69.16	45.25	-77.86	35.21
76	58.37	154.09	-70.06	44.83	-77.93	35.66
77	57.87	154.06	-70.74	44.64	-77.99	36.38
78	57.33	154.07	-71.33	44.57	-78.03	37.18
79	56.80	154.09	-71.91	44.52	-78.08	37.99
80	56.31	154.09	-72.40	44.61	-78.21	38.79

Table 3. The starting points on the Pacific plate (Latitude1, Longitude1), seafloor age, crustal volume in a swath centered on the starting point, and our reconstructed conjugate point on the Nazca plate (Latitude2, Longitude2).

Point	Latitude 1	Longitude 1	Age (Ma)	Volume (km^3)	Latitude 2	Longitude 2
1	-6.30	-142.53	60.72	1,896.87	2.07	-65.81
2	-6.83	-141.92	57.63	2,143.89	1.06	-67.33
3	-7.36	-141.31	54.98	2,474.92	-0.02	-68.80
4	-7.89	-140.70	54.20	4,506.24	-0.76	-68.92
5	-8.42	-140.08	52.91	5,118.10	-1.66	-69.51
6	-8.95	-139.47	51.24	4,610.92	-2.70	-70.44
7	-9.47	-138.86	50.71	4,527.80	-3.33	-70.27
8	-10.00	-138.25	48.74	4,410.06	-4.47	-71.42
9	-10.53	-137.63	47.69	3,406.44	-5.30	-71.77
10	-11.06	-137.02	46.86	3,339.93	-6.08	-72.12
11	-12.55	-151.84	90.20	311.42	-0.24	-52.67
12	-12.98	-151.15	87.24	867.60	-0.84	-54.29
13	-13.40	-150.46	84.52	1,971.65	-1.45	-55.69
14	-13.83	-149.77	83.65	3,063.49	-1.97	-55.69
15	-14.25	-149.08	65.43	3,372.65	-5.33	-68.74
16	-14.68	-148.39	64.07	4,516.95	-5.96	-68.96
17	-15.10	-147.71	62.27	5,970.24	-6.68	-69.46
18	-15.53	-147.02	61.99	7,391.30	-7.12	-68.95
19	-15.95	-146.33	59.63	8,192.43	-7.94	-69.81
20	-16.38	-145.64	53.99	8,276.48	-9.73	-73.17
21	-16.80	-144.95	52.95	7,528.97	-10.49	-73.33
22	-17.23	-144.26	51.17	6,676.92	-11.54	-74.08
23	-17.65	-143.57	50.44	5,924.89	-12.16	-73.95
24	-18.08	-142.88	49.73	5,120.90	-12.77	-73.79
25	-18.51	-142.20	47.70	4,416.13	-13.92	-74.74
26	-18.93	-141.51	45.59	4,467.57	-15.22	-76.46
27	-19.36	-140.82	44.04	3,500.96	-16.26	-77.50
28	-19.78	-140.13	42.56	3,400.41	-17.27	-78.44
29	-20.20	-139.44	40.97	4,396.92	-18.33	-79.50
30	-20.51	-138.71	39.66	4,620.93	-19.07	-80.06
31	-20.77	-137.94	39.41	4,176.71	-19.24	-79.47

Table 3 continued

Point	Latitude 1	Longitude 1	Age (Ma)	Volume (km^3)	Latitude 2	Longitude 2
32	-21.04	-137.18	38.74	4,293.07	-19.55	-79.22
33	-21.30	-136.41	30.90	4,371.58	-23.02	-86.12
34	-21.56	-135.65	30.51	4,202.19	-23.26	-85.84
35	-21.83	-134.88	29.90	4,666.64	-23.63	-85.88
36	-22.09	-134.12	28.84	4,791.35	-24.26	-86.55
37	-22.36	-133.35	28.14	4,048.29	-24.68	-86.72
38	-22.62	-132.59	27.70	4,337.69	-24.96	-86.51
39	-22.89	-131.82	26.15	4,328.27	-25.86	-87.89
40	-23.15	-131.06	25.06	4,632.29	-26.50	-88.62
41	-23.42	-130.29	24.64	4,742.64	-26.78	-88.39
42	-23.68	-129.53	24.30	4,816.57	-27.01	-88.04
43	-15.78	-140.66	44.74	7,521.73	-12.38	-77.30
44	-16.06	-139.92	43.51	6,392.49	-13.12	-77.98
45	-16.38	-139.17	42.65	5,453.62	-13.70	-78.21
46	-16.69	-138.42	41.20	5,428.23	-14.58	-79.12
47	-17.01	-137.68	40.31	4,691.05	-15.17	-79.37
48	-17.32	-136.93	37.01	4,368.34	-16.57	-81.51
49	-17.64	-136.19	35.74	4,503.07	-17.17	-81.80
50	-17.96	-135.44	35.45	3,848.80	-17.38	-81.24
51	-18.27	-134.70	34.57	3,859.25	-17.81	-81.18
52	-18.59	-133.95	34.24	4,053.60	-18.03	-80.66
53	-18.90	-133.21	33.15	3,776.03	-18.52	-80.77
54	-19.22	-132.46	31.71	3,292.75	-19.42	-81.91
55	-19.54	-131.72	30.50	3,427.94	-20.20	-82.77
56	-19.85	-130.97	29.72	3,424.29	-20.73	-83.04
57	-20.17	-130.23	28.55	3,199.58	-21.48	-83.85
58	-17.21	-153.38	87.22	2,713.57	-4.85	-56.85
59	-17.57	-152.66	86.81	3,462.03	-5.30	-56.47
60	-17.94	-151.94	83.98	4,228.75	-5.94	-57.76
61	-18.30	-151.22	83.20	3,778.29	-6.42	-57.64
62	-18.67	-150.50	80.54	4,296.81	-7.20	-58.95
63	-19.04	-149.78	75.74	4,449.34	-8.32	-61.84
64	-19.40	-149.05	70.66	3,250.28	-9.55	-64.90
65	-19.77	-148.33	68.12	2,212.25	-10.36	-66.06
66	-20.14	-147.61	66.35	1,807.90	-11.01	-66.53

Table 3 continued

Point	**Latitude 1**	**Longitude 1**	**Age (Ma)**	**Volume (km³)**	**Latitude 2**	**Longitude 2**
67	-20.50	-146.89	63.21	1,509.98	-11.88	-67.83
68	-20.87	-146.17	61.90	1,614.69	-12.44	-67.95
69	-21.01	-155.29	89.66	1,124.26	-8.26	-57.39
70	-21.38	-154.57	88.38	1,339.42	-8.80	-57.58
71	-21.74	-153.84	87.88	1,465.25	-9.27	-57.26
72	-22.11	-153.12	86.30	1,772.32	-9.83	-57.62
73	-22.48	-152.40	85.17	1,732.23	-10.34	-57.69
74	-22.84	-151.68	84.09	1,732.48	-10.84	-57.70
75	-23.21	-150.96	83.12	1,596.97	-11.34	-57.68
76	-23.57	-150.23	78.37	1,244.54	-12.43	-60.44
77	-23.94	-149.51	77.58	1,868.85	-12.94	-60.34
78	-24.31	-148.79	72.84	1,882.21	-14.07	-63.05
79	-24.67	-148.07	69.95	3,268.23	-14.93	-64.41
80	-25.04	-147.35	68.98	2,755.02	-15.46	-64.42
81	-25.40	-146.62	60.46	4,580.50	-17.24	-69.05
82	-25.77	-145.90	58.72	4,748.05	-17.88	-69.40
83	-26.14	-145.18	56.25	4,079.82	-18.64	-70.18
84	-26.50	-144.46	54.10	3,879.73	-19.66	-70.93
85	-26.87	-143.74	49.80	4,638.09	-21.55	-73.10
86	-27.23	-143.02	48.71	4,960.79	-22.22	-73.06
87	-27.60	-142.29	48.09	3,962.24	-22.71	-72.71
88	-27.97	-141.57	45.53	3,253.91	-24.10	-74.60
89	-28.33	-140.85	43.03	3,112.10	-25.51	-76.48
90	-28.70	-140.13	40.01	3,037.82	-27.19	-78.83
91	-29.06	-139.41	38.52	2,380.76	-27.91	-79.12
92	-29.43	-138.68	37.72	2,487.10	-28.37	-78.89

Supplementary References

Cande, S.C., LaBrecque, J.L., Larson, R.L., Pittman, W.C., Golovchenko, X., Haxby, W.F., 1989. Magnetic lineations of the world's ocean basins, Magnetic lineations of the world's ocean basins. AAPG, Tulsa, OK.

Matthews, K.J., Müller, R.D., Wessel, P., Whittaker, J.M., 2011. The tectonic fabric of the ocean basins. Journal of Geophysical Research: Solid Earth 116, B12109.

Mayes, C.L., Lawver, L.A., Sandwell, D.T., 1990. Tectonic History and New Isochron Chart of the South Pacific. J. Geophys. Res. 95, 8543-8567.

Müller, R.D., Sdrolias, M., Gaina, C., Roest, W.R., 2008. Age, spreading rates, and spreading asymmetry of the world's ocean crust, Geochemistry Geophysics Geosystems. American Geophysical Union, p. Q04006.

Pardo-Casas, F., Molnar, P., 1987. Relative motion of the Nazca (Farallon) and South American Plates since Late Cretaceous time. Tectonics 6, 233-248.

Pilger, R.H., 1981. Plate Reconstructions, Aseismic Ridges, and Low-Angle Subduction beneath the Andes. Geological Society of America Bulletin 92, 448-456.

Tebbens, S.F., Cande, S.C., 1997. Southeast Pacific tectonic evolution from early Oligocene to present. Journal of Geophysical Research 102, 12061-12084.

Appendix I

This appendix summarizes two important tests of the buoyant impactor hypothesis that were not included in the published papers.

A set of paired maps is presented for Mexico, South America, and Japan. The top image in each pair is a shaded relief map of the seafloor that can be used to detect subducting crustal anomalies. The lower image is a map of free-air gravity anomalies that is useful for detecting density anomalies in the oceanic plate. The red triangles are locations of Holocene volcanoes. The thin black lines are 20 km depth contours to the top of the subducting slab.

The maps of Mexico demonstrate a complete lack of offshore bathymetric or gravity anomalies to account for the zone of flat subduction. The maps of Japan show that the zone of shallow subduction is centered over the Shikoku basin, and is anti-correlated with the Palau-Kyushu ridge and Izu-Bonin arc. The bathymetric map of South America reveals several bathymetric anomalies. These most notable feature in this set of maps is that the Nazca ridge, which is easily identified in the bathymetric map, is absent from the gravity map. The lack of a gravity anomaly associated with the Nazca ridge implies that the feature is compensated by a dense root, which negates any positive buoyancy due to thickening of the oceanic crust.

If the cause of flat subduction is the positive buoyancy of bathymetric anomalies, then we expect a correlation between the volume of buoyant material subducting and the resulting modification of the subduction zone geometry. We have devised a “subduction number” to test this theory. Using global bathymetry we calculate the volume of additional crust associated with a bathymetric feature relative to surrounding seafloor. We then divide this additional volume by the areal extent of the feature to get the average thickening associated with the feature. The average thickening is multiplied by the length of contact between the trench and anomaly to give us the subduction number. Intuition tells us that a larger subduction number will indicate a greater influence on the subduction geometry. Assuming a feature of constant thickness, an anomaly will have a greater impact when the zone of contact is longer. A longer contact length results in a larger subduction number.

We have plotted the subduction number for eighteen bathymetric anomalies that are visible today. Marked with a yellow circle are features that have been associated with zones of shallow subduction, are the conjugate of a feature proposed to have caused a flat slab, or have clogged a trench. The Ontong-Java Plateau has a large subduction number which is expected based on its great trench modification, however, the Magellan Seamounts have the largest subduction number and have no apparent effect on the slab geometry. There is no clear divide between the anomalies that create flat slabs and those that do not. The lack of any clustering of the shallow subduction zones tells us that the buoyancy from a bathymetric high is not a sufficient condition for predicting a shallow slab.

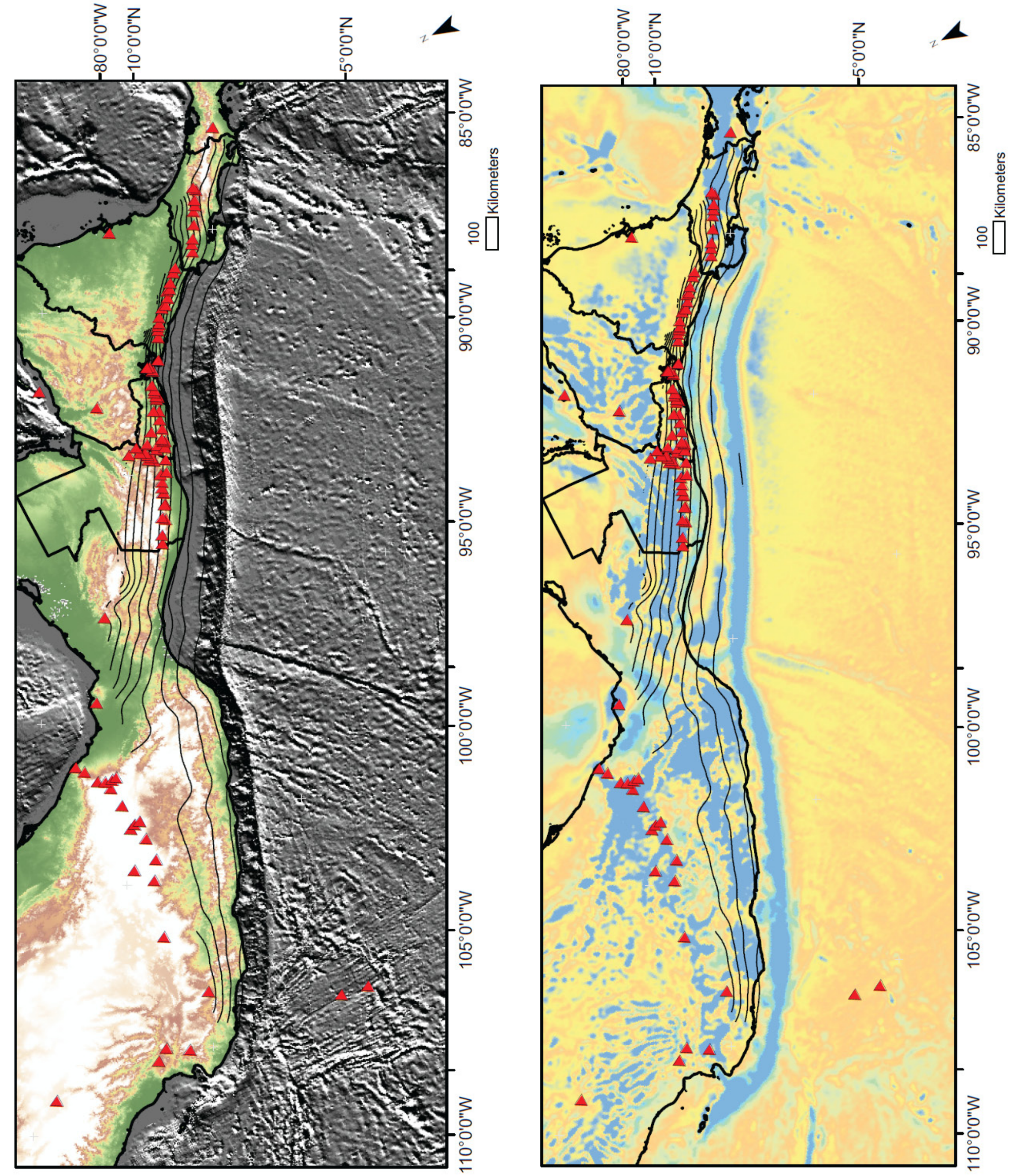

Figure 10. Mexico bathymetry/gravity

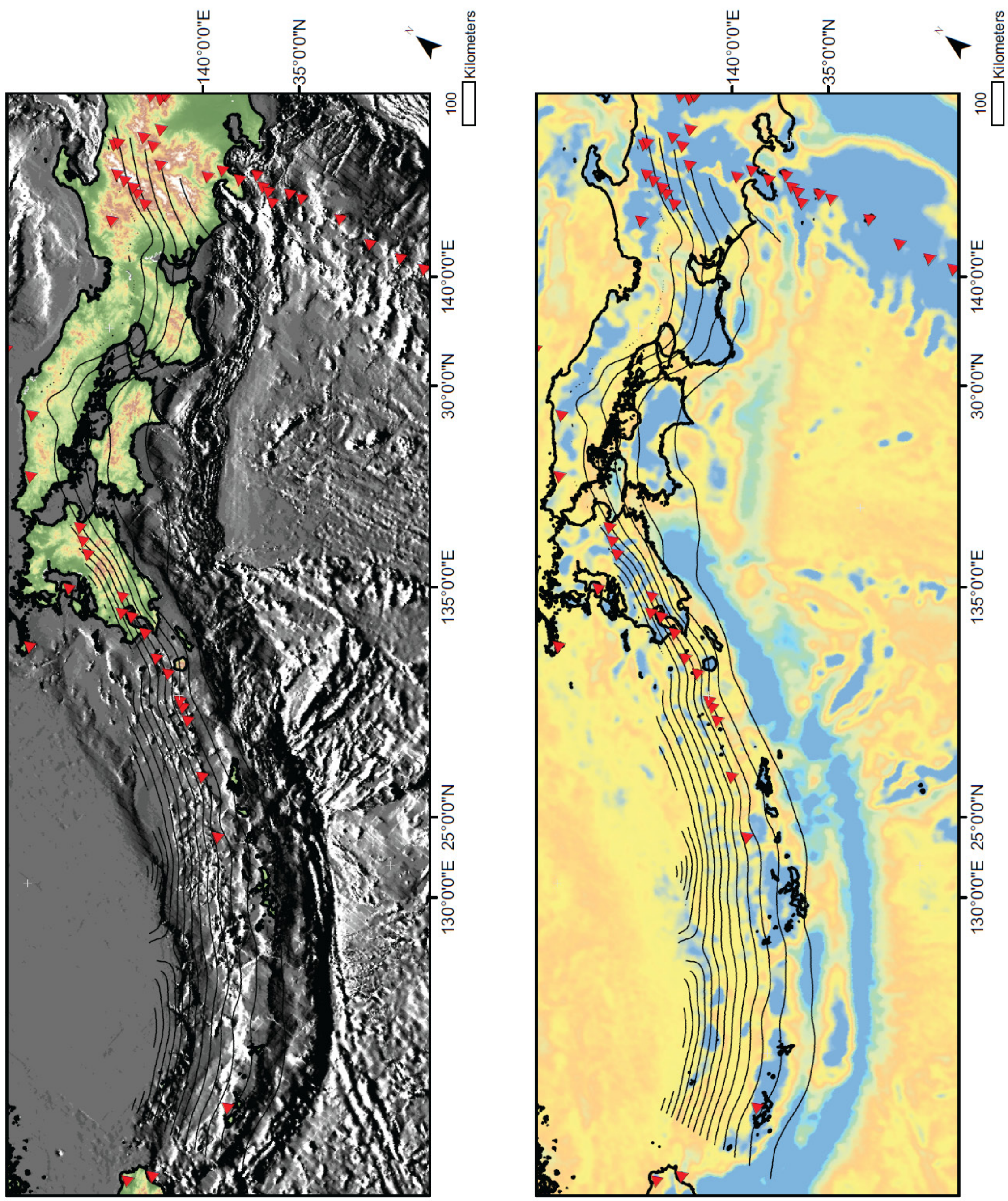

Figure 11. Japan bathymetry/gravity

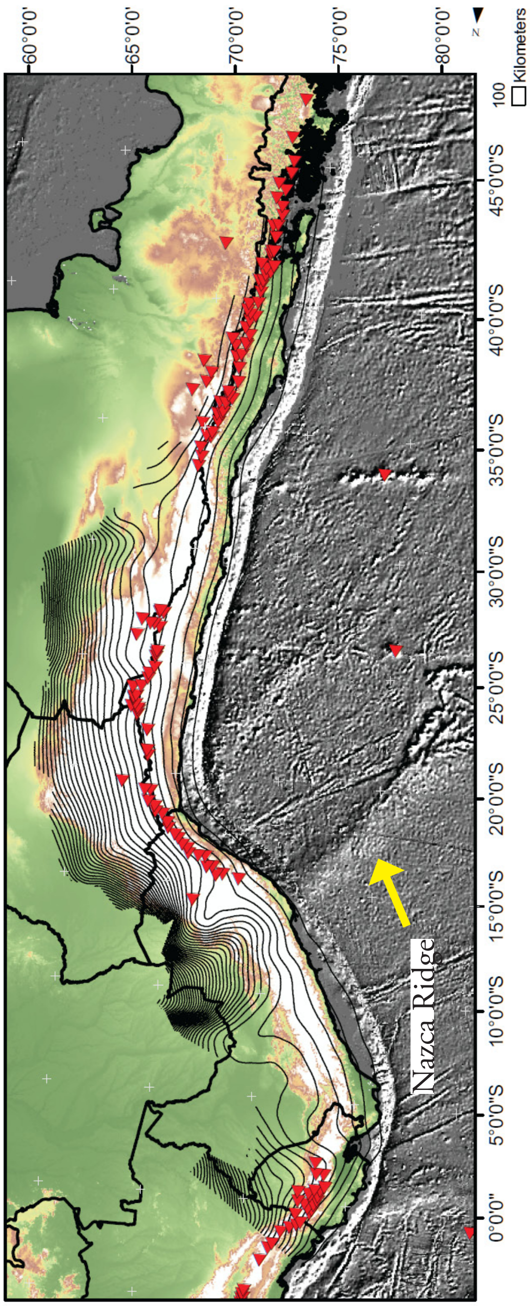

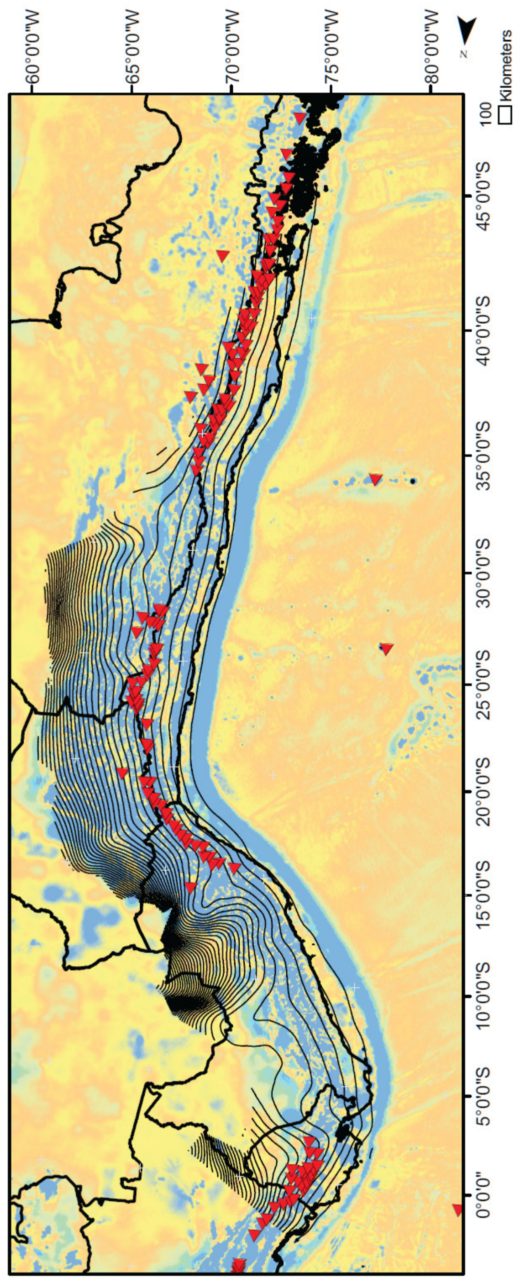

Figure 12. South America bathymetry/gravity

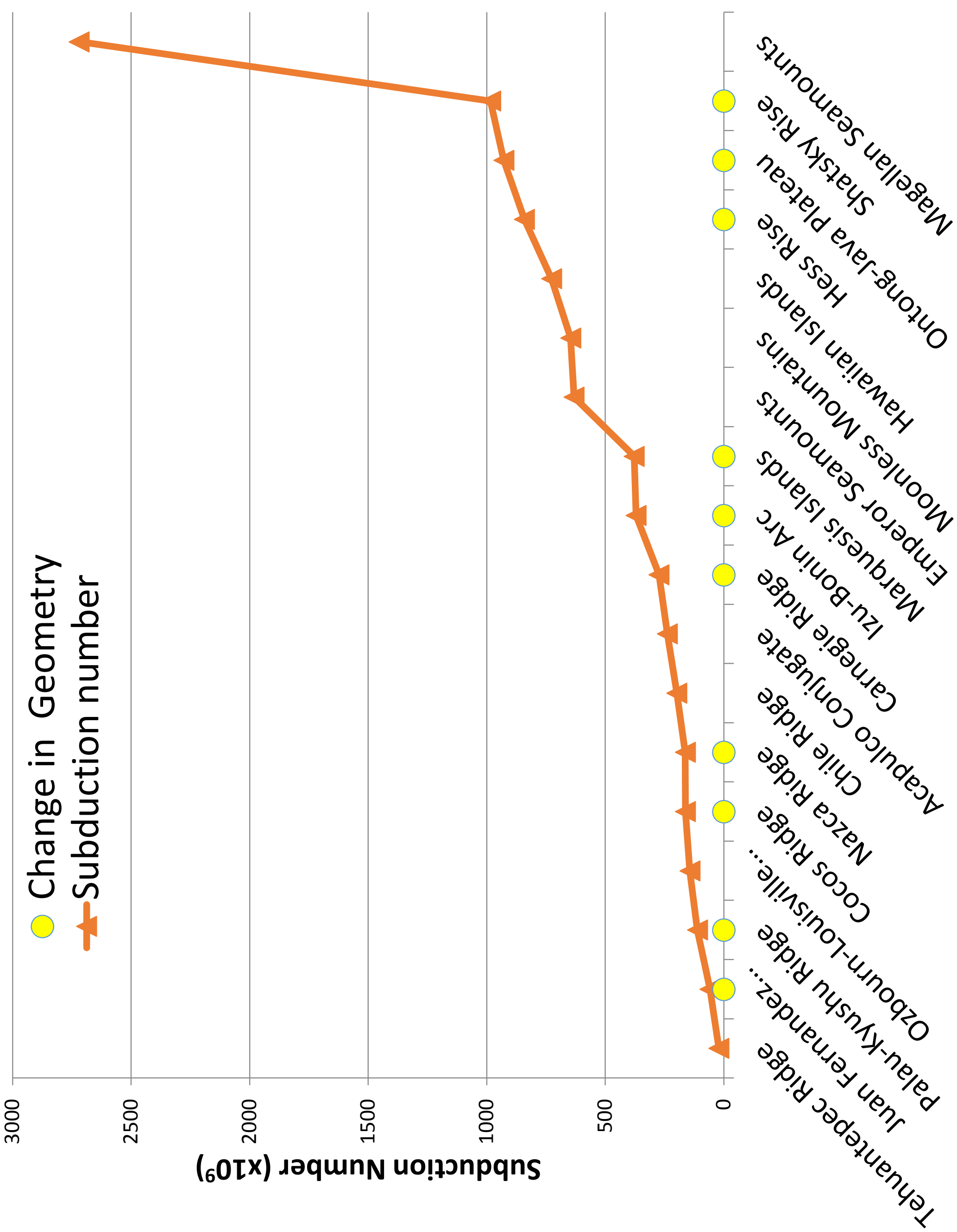

Figure 13. Subduction number

Part II
Paleomagnetic Constraints on Rifting

Chapter 3
Paleomagnetic studies of the Tuff of San Felipe on Isla Angel de La Guarda, Baja California, Mexico

Abstract

Due to its widespread areal extent, the Tuff of San Felipe provides an important datum for reconstructing the rifting process that separated Baja California from the North American plate following the eruption of the tuff. We have located outcrops of this tuff on Isla Angel de la Guarda, in the Gulf of California, and report results from geological field mapping and detailed paleomagnetic and rock magnetic analyses, in an effort to use coherent flow of the tuff as a piercing point to constrain fault offsets. These experiments have both characterized the magnetic mineralogy of the tuff in this new location, and constrained the depositional flow directions. We have determined that the tuff flowed across the island towards the south-west; however, it appears from the high variability in the principal axes of the anisotropy of magnetic susceptibility that the shear exerted on the grains as they were deposited was insufficient to produce a strong lineation fabric, precluding its utility for recognizing channelized flow. However, characteristic remanence directions isolated by principal component analysis reveal vertical-axis rotations of the magnetic remanence vector within the tuff.

Introduction

Rifting of the Baja California Peninsula from the North American plate, and its transfer to the Pacific plate, has been studied extensively over the past few decades in order to provide constraints on the kinematics and dynamics of the rifting process. Studies have focused on the seismically defined structure of the northern Gulf of California and the location of rifting through time (Aragon-Arreola and Martin-Barajas, 2007), motion at the southern end of the

Baja California peninsula (Fletcher et al., 2007; Fletcher and Munguia, 2000), extensional structures along the eastern margin of the Baja California peninsula (Lewis and Stock, 1998a; Nagy, 2000; Nagy et al., 1999), and field mapping of correlative units in Sonora (Bennett, 2013; Oskin and Stock, 2003; Vidal Solano et al., 2008). The Pacific-North America plate boundary in the Gulf of California varies from sea floor spreading in the southernmost extensional basins of the Gulf to distributed continental extension in the Mexicali and Imperial valleys at the northern end of the Gulf of California.

Global plate circuit reconstructions that compare the relative motion of the Pacific and North America plates since 11 Ma imply ~ 634 km of displacement between the Pacific and North American plates (Oskin and Stock, 2003; Oskin et al., 2001; Stock, 2007). Geologic mapping and reconstructions based on the correlation of rock units between the Baja California peninsula, the Sonoran coast, and islands in the Gulf demonstrate that since ~6 Ma there has been ~ 300 km of relative motion accommodated by faults within the Gulf (Oskin and Stock, 2003) . The remaining unaccounted motion suggests that ~300 km of displacement has occurred outside of the Gulf before 6 Ma. Previous workers have suggested that this missing plate motion might have been accommodated by faults on the Pacific coast of the Baja California Peninsula, or in some form of distributed deformation in locations that have yet to be mapped in detail such as Coastal Sonora (Dixon et al., 2000; Fletcher et al., 2007; Fletcher and Munguia, 2000; Marsaglia, 2004; Michaud et al., 2004).

Northern Baja California, Western Sonora, and numerous islands in the Gulf contain a series of Miocene volcanic deposits that have been key to reconstructing deformation and extension in the Gulf of California rift zone. Of these units, the Tuff of San Felipe is the most widespread, and records a distinctive geomagnetic excursion that aids in its unique identification with paleomagnetic techniques (Figure 1) (Lewis and Stock, 1998b; Stock et al., 1999). It has proven invaluable in reconstructing Isla Tiburon to its counterpart on the Baja California Peninsula (Oskin et al., 2001), and constraining the opening of the northern Gulf. Work on locations in the Sierra Libre of Sonora (Vidal-Solano et al., 2005; Vidal Solano et al., 2008) is aimed at locating some of the slip deficit. Work on Isla Angel de la Guarda (Martin-Barajas et al., 2008; Stock et al., 2008) and various mesas around Cataviña (Olguin-Villa, 2010) on the Baja California Peninsula is aimed at placing tighter constraints on the location of offsets due to the rifting process and strike slip plate boundary motions.

The main motivation of this study was to locate and identify positively outcrops of the Tuff of San Felipe, and to use anisotropy of magnetic susceptibility (AMS) to identify the pattern of emplacement with the possibility of detecting channelized flows that could improve offset measurements (Hinz et al., 2009; Lease et al., 2009). In order to understand the AMS fabric in a petrologic sense, exhaustive rock magnetic experiments were performed.

Field expeditions and sample collection

The Tuff of San Felipe was first positively identified on Isla Angel de la Guarda by a field team in 2007 (Martin-Barajas et al., 2008; Stock et al., 2008). Isla Angel de la Guarda is an uninhabited island, part of the Islas del Golfo biological reserve, 75 km long by 20 km wide, located 30 km from the eastern coast of the Baja California Peninsula (29.3° N, 113.4° W).

In 2009 a team went on a reconnaissance sampling trip to Isla Angel de la Guarda. By using satellite images, we chose target localities where we thought we would most likely encounter additional outcrops of the Tuff of San Felipe. During several cross-island hikes and strategic boat landings, we collected 5 oriented block samples for paleomagnetic analysis, from 5 sites within a unit lithologically similar to the Tuff of San Felipe, the identity of which we confirm below.

In 2010, a field team did similar reconnaissance sampling of mesas on the Baja California Peninsula in the area surrounding Cataviña to follow up on a 2008 expedition that identified the Tuff of San Felipe in this region. Again using remote sensing to guide our sampling, we proposed 50 target locations where there were indications of a tuff resembling the Tuff of San Felipe. Some locations turned out to be mesas capped by basalt flows and in one case by a limestone. Due to these remotely misidentified outcrops and vehicle limitations, we were only able to sample 12 locations for paleomagnetic analysis.

In 2011, a team was tasked with further sampling the known extent of the Tuff of San Felipe on Isla Angel de la Guarda to test the utility of AMS as a tool for identifying channelized flows that could then be used as piercing points to determine fault offsets and to help locate the source vent. The motivation of the sample collection pattern was to constrain the three-dimensional flow field with spatially and stratigraphically dense samples (Figure 2). We collected over 362 oriented paleomagnetic cores from 44 sites in addition to 14 oriented block samples. One individual tilted block, roughly 200 meters in diameter, capped by the Tuff of San Felipe, produced six paleomagnetic sample sites distributed around its perimeter.

Field identification of the Tuff of San Felipe is complicated due to the lateral variations in appearance and the incorporation of the underlying substrate. Correlations of the Tuff of San Felipe are based on geochronology, petrology, and most often the unique paleomagnetic signature (Stock et al., 1999). The Tuff of San Felipe records a low inclination and southwest declination due to a geomagnetic excursion (Bennett, 2013; Lewis and Stock, 1998b). This magnetic signature (Declination 212.4°, Inclination -3.0°), in the type locality established by Bennett (2013), is an essential way to identify the Tuff of San Felipe for further study. The thickness of the tuff varies widely. On the island it has a maximum thickness of 12 meters, while exposures up to 180 meters thick can be found in near-vent facies of coastal Baja California (Stock et al., 1999). The tuff is characterized by 3%-15% phenocrysts, with alkali feldspar being the most abundant (Stock et al., 1999). A lack of biotite, however, is probably the most helpful mineralogical constraint in the field. Lithic fragments constitute up to 3% of the tuff (Stock et al., 1999). 40Ar/39Ar analysis of alkali feldspars indicate an age of 12.6 Ma (Stock et al., 1999). Geochemical analysis shows ~75% SiO_2, indicating a rhyolitic composition (Stock et al., 1999; Vidal-Solano et al., 2005).

Geologic setting

Previous studies of the geology of Isla Angel de la Guarda include the 1:250,000 scale reconnaissance map of all of the state of Baja California (the northern half of the peninsula) compiled by Gastil et al. (1975) and lithologic mapping from air photos with ground truthing in 20 coastal locations by Delgado-Argote (2000). We have compiled a geologic map of the Los Machos region (29.63° N, 113.43° W) of the island focused on the Tuff of San Felipe and the units directly above and below it (Figure 3).

The stratigraphy in the Los Machos area targeted in this study is as follows. Dacite lavas form the base of the section relative to this investigation. The dacite is overlain depositionally by a volcaniclastic conglomerate. The base of the conglomerate is clast-supported with poorly sorted sub-angular clasts ranging in size from pebble to cobble. The conglomerate unit grades up into a matrix-supported deposit with concentrated lenses of pebbles. The Tuff of San Felipe sits depositionally on top of the volcaniclastic conglomerate, with a maximum thickness exposed on the island of ~ 12 meters. The top of the fluvial unit does not appear to be altered by the emplacement of the tuff, however, samples were not collected below the tuff so this cannot be confirmed with a baked contact test. On the island, the tuff is of moderate grade (Branney and Kokelaar, 1992) having both welded and unwelded zones. There is no macroscopic eutaxitic foliation, lithophysae, or rheomorphic structures as are common in the tuff in other localities where it is thicker (Oskin and Stock, 2003; Stock et al., 1999). The tuff on the island also differs from other exposures in that it is phenocryst poor < 10% and lacks a basal vitrophyre. The base of the tuff is a 0.8 meter thick white, poorly-welded pyroclastic-density current deposit with ~1% pebble-sized angular lithic fragments. This grades upward into a 1.3 meter thick very pale orange to grayish orange deposit, accompanied by an increase in the size and abundance (~3%) of the lithic fragments. The degree of welding then increases upward in the tuff, and the color changes to light brown. There is then a 6 meter thick strongly welded zone that is blackish red to light purple. Above this zone, there is a ~ 1 meter thick welded moderate brown zone that grades upward into a ~1 meter thick unwelded moderate yellowish brown friable zone. In most of the locations where it is exposed the unwelded friable zone of the tuff forms the caprock of the mesa. In a few areas there is a clast-supported volcaniclastic conglomerate, up to six meters thick, preserved above the tuff. A two-meter thick cap of vesicular basalt forms the top of the mesa in a few locations (Figure 3), and preserves the easily erodible conglomerate.

The tuff is exposed across a series of moderately-tilted, westward-dipping blocks. A series of roughly north-striking, high-angle normal faults displaces it with an east side down sense of motion. We hypothesize a low-angle structure, which predates the high-angle faults, that cuts out the lower volcaniclastic conglomerate and puts the tuff in fault contact with the dacite lavas (Figure 4; Appendix II). This low angle structure is also well exposed in an area where it places tuff on tuff, resulting in an unknown thickness of missing section (Figure 5). This structure could produce erroneous stratigraphic locations for the collected samples, if this apparent cooling boundary has had translational motion that cuts out section.

Methods

Measurement of the characteristic paleomagnetic remanence direction (ChRM) is the most expedient and cost effective method of confirming a lithologic unit characterized by an unusual magnetic direction, such as the Tuff of San Felipe. In addition to the simple diagnostic utility of measuring the ChRM, we can use the paleomagnetic measurements and an undeformed reference site (Bennett, 2013) to detect tectonic motion about a vertical axis (Lewis and Stock, 1998b). AMS is a relatively rapid but most importantly nondestructive method of measuring the magnetic fabric of a rock. In order to interpret the petrologic or tectonic origin of the magnetic fabric, the magnetic mineralogy of the sample must be well characterized. We have performed exhaustive rockmagnetic experiments to determine the magnetic mineralogy of our samples. We have utilized techniques that exploit the characteristic responses of magnetization and susceptibility as a function of field strength, temperature, and frequency to determine the chemical nature and grain size of the magnetic minerals present in our samples.

Sample collection and preparation

Spatially oriented samples were collected either as oriented, hand-size blocks or as 2.5-cm-diameter core samples drilled with a modified chain-saw motor fitted with a non-magnetic diamond-tipped bit. Cooling and lubrication for the field drilling process were provided by sea water. Cores were oriented in the field with a Pomeroy™ orienting fixture. For redundancy, both a magnetic compass and sun compass were used, when possible, using standard techniques. All core measurements were taken with respect to magnetic north. Block samples were oriented by drawing a strike line and an orthogonal line in the dip direction on an exposed planar surface. The dip of the surface was measured with an inclinometer and the strike direction was again recorded with a magnetic compass and a sun compass, when possible. Care was taken to avoid obvious lightning strikes by examining each sampling site for local magnetic anomalies with the compass of a pocket transit. Tilt corrections were determined using the basal contact of the tuff or from the foliation. All bedding measurements were taken with respect to geographic north on a magnetic compass set to a declination of 13°. When possible, the stratigraphic height of cores was measured. Measurements were transformed into the magnetic north coordinate system for data processing. All stratigraphic height measurements reported are meters above the base of the tuff. Where the base of the tuff was exposed, the height of the core was directly measured. In locations where the base of the tuff was not exposed, we used the red to purple color change (Figure 5a) of the densely welded section of the tuff as a datum 4 meters above the base of the tuff (as measured at site 2) and measurements were made relative to that level. Block samples were cored at the California Institute of Technology on a drill press fitted with a non-magnetic diamond-tipped coring bit. Following this, the field positions were reoriented in space using a sand box, and the 2.5 cm cores were reoriented to the same convention used for the samples drilled in the field.

Cores were cut into 2.2 cm long specimens to produce an aspect ratio that minimizes the influence of the shape anisotropy of the specimen itself (Porath et al., 1966). Cores produced between one and six specimens suitable for AMS measurement. The diameter and length of each specimen were measured with a set of digital calipers. A digital balance was used to measure the mass of each specimen. Specimens were cut in half for paleomagnetic remanence measurements.

AMS (Anisotropy of Magnetic Susceptibility)

Magnetic susceptibility is an intrinsic property of all materials independent of whether they are diamagnetic, paramagnetic, or ferromagnetic. Volumetric magnetic susceptibility (K) is a dimensionless (in SI units) constant of a material that relates the strength of an induced magnetization (M) [A/m] to an applied magnetic field (H) [A/m]. Susceptibility is a function of the magnitude of the applied field, frequency of the applied field, temperature of the sample, orientation of the sample with respect to the applied field, and the composition of the sample. If the induced magnetization varies as a function of the orientation of the applied field the material possesses anisotropic magnetic susceptibility. AMS is a symmetric second rank tensor that can be represented as a triaxial ellipsoid with the principal axes K1 (max), K2 (intermediate), and K3 (minimum) corresponding to the three eigenvectors of the AMS tensor.

All specimens discussed here were measured on the AGICO MFK1-FA at the California Institute of Technology using the Windows-based software SAFYR4W version 4.0.4. Measurements were made at room temperature with an applied field intensity of 200 A/m at a frequency of 976 Hz. At these settings the instrument has a field homogeneity of 0.5%, sensitivity of 2x10-8, and an accuracy of 0.1% (AGICO, 2009). Before measuring samples, the coils were allowed to stabilize for ten minutes, a standard was measured to calibrate the instrument, and a holder correction was measured. The measurement process involves placing the specimen in the rotating holder in 3 orthogonal positions. The susceptibility is measured while rotating the specimen about the three orthogonal axes. A final measurement of the bulk susceptibility is made without rotating the specimen. Before and after each insertion of the specimen into the coils, the empty coils are measured.

Paleomagnetic remanence

Components of the characteristic remanent magnetization (ChRM) were measured by incrementally erasing the natural remanent magnetization (NRM) of a specimen though low-temperature cycling, alternating field (AF), or thermal demagnetization. The progressive destruction of overprinting magnetic vectors reveals components with progressively higher coercivity or Curie temperature eventually revealing the most resistant, stable magnetization, most likely recorded when the rock was formed.

All remanence measurements were made at the California Institute of Technology on one of two 2G Enterprises™ SQuID magnetometer using the RAPID consortium automatic sample changer (Kirschvink et al., 2008), housed in a magnetically –shielded room (one of μ-metal, and the other of soft steel as described by Scott and Frohlich (1985)). After measuring AMS on all of the specimens, one specimen was selected from each core and cut into two smaller specimens. For both of these, demagnetization started with measurements of the NRM followed by two low-temperature thermal-cycling steps. These involved immersion and thermal equilibration to 77K in liquid nitrogen for ~15 minutes. The samples were warmed back to room temperature before being measured. This cycling below the Verwey transition (~120K) removes overprints from multi-domain magnetite (Özdemir et al., 2002; Ozima et al., 1964; Schmidt, 1993). Half of each split specimen was then demagnetized using progressive 3-axis AF demagnetization, while the other half was treated with low-field AF followed by thermal techniques. The AF demagnetization was carried out at steps of 1 mT from 1 to 10 mT, 2 mT from 10 to 50 mT, and 5 mT from 50 to 100 mT, using waveforms synthesized by a digital/analogue conversion system (Wack and Gilder, 2012). Thermal demagnetization began with a low-AF cleaning in steps of 1 mT from 1 to 6 mT, largely to remove any effects from undetected lightning strikes or accidental exposure to moderate fields during sampling and laboratory preparation. The specimens were heated in magnetically shielded computer-controlled ovens (residual fields <10 nT) under a gentle flow of N_2 gas to minimize oxidation, in 20°C steps from 60°C to 700°C. The step size was reduced to 10°C from 560°C to 600°C, near the Curie temperature of magnetite ~585°C. Principal component analysis was done using the techniques of Kirschvink (1980) as implemented by Jones (2002).

Rockmag

For the AF demagnetized sub-sample, rock magnetic experiments aimed at determining the coercivity distribution of grains holding the NRM, compared with the total population of magnetic carriers in the rock, were carried out at the California Institute of Technology using the 2G™ SQuID magnetometer following the RAPID consortium protocol of Kirschvink et al. (2008). The acquisition and demagnetization of the NRM, anhysteretic remanent magnetization (ARM), isothermal remanent magnetization (IRM), and backfield IRM allow us to calculate several ratios that are diagnostic of grain size and magnetic mineralogy. The Lowrie-Fuller test compares the AF demagnetization of an ARM to that of an IRM (Lowrie and Fuller, 1971; Xu and Dunlop, 1995). A median destructive field (MDF) of the ARM that is greater than the MDF of IRM is indicative of single domain magnetite and an MDF of ARM less than the MDF of IRM indicates multi-domain magnetite. The ratio of the demagnetization of the NRM or ARM to the demagnetization of the IRM is a measure of the efficiency of the magnetization and informs us of the mechanism imparting the ChRM (Cisowski et al., 1990; Fuller et al., 2002). The intersection of the IRM acquisition and IRM demagnetization curves gives us information about the interacting fields in the sample (Cisowski, 1981).

Specifically, the coercivity distribution of grains that held the NRM of samples was determined by the progressive, 3-axis AF demagnetization in 44 steps, in peak fields of up to 110 mT. Next, the coercivity distribution of the ferromagnetic minerals present (irrespective of whether or not they recorded part of the NRM) was determined by comparing magnetizations gained/lost with the techniques of ARM and IRM. An ARM acquisition experiment (to measure ARM susceptibility) was conducted first on the samples in a peak axial AF field of 100 mT, in 11 steps with a DC biasing field from 0 to 1 mT. To determine the ARM coercivity spectrum the peak ARM was then erased by a series of 20 log-distributed AF steps in the axial direction up to 300 mT, the limit of the axial AF coil. To measure the IRM coercivity spectrum below 100 mT, the samples were next given a 100 mT isothermal remanent magnetization (IRM) in the positive axial direction and then erased by AF demagnetization in the same step sequence used for the ARM. To extend this to higher field levels, IRM acquisition series was imparted progressively using the same log-distributed series up to 870 mT, the limit of the pulse magnetizer. This saturation isothermal remanent magnetization (SIRM) was then erased by axial AF demagnetization to a peak field of 300 mT. Finally, the back-field IRM properties were measured by giving the samples a single IRM pulse of 870mT in the positive axial direction, followed by opposing this with progressively increasing IRM pulses in the negative direction in steps up to 750 mT. This series involved approximately 180 discrete remanence measurements per sample and was run on a suite of 32 samples.

Thermal susceptibility

The variation of magnetic susceptibility as a function of temperature provides another diagnostic tool for determining and characterizing magnetic mineralogy. The Verwey transition, a large increase in susceptibility above ~120K, associated with the change from monoclinic to cubic symmetry, is indicative of magnetite. The Morin transition of hematite shows a large increase in susceptibility above ~262K, due to a canting in the antiferromagnetic alignment of Bohr magnetons. The Hopkinson peak, an increase in susceptibility below the Curie temperature, is more pronounced in single and pseudo-single-domain (PSD) grains than in multidomain grains. Thermal variation of susceptibility also allows calculation of the Curie temperature of a sample.

Thermal variation of magnetic susceptibility curves were measured at the California Institute of Technology using an AGICO MFK1_FA Kappabridge with a CS4 high temperature furnace and a CSL low temperature cryostat controlled by the SUFYTE5W software version

5.0.1. Samples were initially crushed with a Plattner's mortar and pestle, made from hardened alloy tool steel. The sample was then reduced to a fine powder using an agate mortar and pestle. Samples of approximately 0.3 grams were weighed out and placed in a quartz glass tube with a platinum thermocouple. Low temperature measurements were made first to avoid high temperature alteration of the samples. The samples were then placed in the cryostat apparatus and cooled to -194°C by slowly adding liquid nitrogen to the cryostat jacket. Once the samples reached the desired temperature the liquid nitrogen was expelled with high pressure argon gas. The samples were continuously measured as they warmed back to room temperature through the automated insertion and removal of the apparatus into the measurement coils. High-temperature measurements were made from room temperature to 700°C (heating curve). Samples were heated at a rate of 6.5°C per minute and held at the maximum temperature for five minutes. The samples were then cooled back down to room temperature as additional measurements were made (cooling curve). An inert atmosphere is provided by a 100 ml/minute flow of argon into the quartz glass test tube.

Emplacement temperature

The temperature of emplacement of a pyroclastic density current deposit will decrease radially as a function of distance from the source. The ability to measure this for different outcrops of the Tuff of San Felipe would place another constraint on the paleogeography and the magnitude of tectonic offsets. Hrouda et al. (2003) developed a method for determining this temperature that is based on the observation that the cooling and heating curves of a thermal susceptibility measurement are usually quite different; however, when the sample is reheated to the same temperature, the heating curve follows the cooling curve of the previous experiment. If a sample is progressively cycled to higher temperatures, the temperature at which the heating and cooling curves begin to diverge should indicate the temperature that the rock cooled from in nature or the highest temperature of alteration that it has experienced.

We used this technique to estimate emplacement temperatures on selected samples of the Tuff of San Felipe. Emplacement temperatures were estimated by cycling samples through heating and cooling cycles to progressively higher maximum temperatures. A standard thermal susceptibility powdered sample of 0.3 grams was loaded into the CS4 furnace. The sample was initially heated to 100 °C and then heated in 75 °C increments up to a maximum of 700°C. The A40 alteration index of Hrouda (2003) is used to quantify the deviation of the heating and cooling curves at 40°C.

Vibrating sample magnetometer (VSM) hysteresis

Hysteresis loops are the standard method for determining the grain size and composition of magnetic particles (Day et al., 1977). Four parameters can be used to summarize a hysteresis loop: saturation remanent magnetization (Mr), saturation magnetization (Ms), coercivity (Hc), and coercivity of remanence (Hcr). The ratios of Mr/Ms and Hcr/Hc are diagnostic of domain state.

Hysteresis loops were measured at the Institute for Rock Magnetism at the University of Minnesota using a Princeton Measurements Corporation vibrating sample magnetometer. Room temperature measurements were measured on standard 2.3 cm cylindrical specimens as well as on smaller sample chips. The samples were securely attached to a vibrating sample holder and centered within the pickup coils. Hysteresis loops were measured in a maximum field of 1.5 T in increments of 0.01 T. Measurements made with an averaging time of one second produced an excellent signal to noise ratio. Backfield coercivity measurements were also made.

VSM magnetization as a function of temperature

Magnetization as a function of temperature is the standard method of determining Curie temperatures for paleomagnetic samples.

Temperature dependent magnetization was measured at the Institute for Rock Magnetism at the University of Minnesota using a Princeton Measurements Corporation vibrating sample magnetometer with a high-temperature furnace assembly. A millimeter sized sample chip was attached to a sample holder using a ceramic cement, attached to the vibration head, and lowered into the furnace that was already centered on the pickup coils. Samples were heated to 1000 K in a helium atmosphere and an applied field of 1.5 T.

Frequency dependence of susceptibility

The measured magnetic susceptibility of a sample depends on the timescale of observation. The frequency of an applied field can be used as proxy for the relaxation time of a magnetic particle (Butler, 1992; Tauxe et al., 2010). Superparamagnetic particles can be detected by measuring the magnetic susceptibility of a specimen at a range of frequencies since the susceptibility of superparamagnetic particles decreases with increasing frequency (Carter-Stiglitz et al., 2006).

The frequency dependence of susceptibility was measured at the Institute for Rock Magnetism at the University of Minnesota using a Magnon GmbH variable frequency susceptibility bridge. Specimens were measured in a 300 A/m field at 100, 200, 500, 1000, 2000, 5000, and 10000 Hz. The measurement protocol was to select a frequency, measure the empty chamber, place the specimen on the plunger and lower it into the coils, measure the susceptibility with the specimen present, remove the sample and measure the empty chamber for a second time.

Magnetic Properties Measurement System (MPMS)

The size and composition of magnetic particles determine their magnetic response to frequency, field, and temperature. A magnetic property measurement system (MPMS) is designed to make high fidelity measurements of a samples magnetization while varying the temperature and applied field.

Two sets of experiments were run at the Institute for Rock Magnetism at the University of Minnesota using a Quantum Design MPMS, following the protocol of Moskowitz et al. (1993). The first experiment imparted an IRM on the sample at 300 K and then measured the magnetization as the sample was cooled to 2 K in zero field. An IRM was given to the sample at 2 K and the magnetization was measured as the sample was rewarmed to 300 K in zero field. The second experiment measured the susceptibility of the sample while varying temperature from 2 – 300 K at seven different frequencies (1, 3, 10, 30, 100, 300, 1000 Hz). Samples were prepared as rock chips or powers contained in gelcaps. The sample was fixed inside a plastic drinking straw that was then attached to a sample rod that was lowered into the MPSM through an airlock.

FORCs

Classical hysteresis loops measure the bulk response of a sample to an applied field. First-order reversal curves (FORCs) probe the inside of a hysteresis loop revealing information about the distribution of characteristics of particles within a sample (Mayergoyz, 1986; Pike et al., 1999; Roberts et al., 2000). FORCs are measured by first saturating the sample in a positive field. The applied field is then reduced to a given reversal field (Ha) and the magnetization of the sample is measured as the field (Hb) is ramped back up to the saturating field. This process is repeated for progressively lower reversal fields. The end result of these measurements is the magnetization as a function of applied field, M(Ha,Hb). The FORC distribution is defined as the mixed second derivative of this magnetization (Pike et al., 1999). A FORC diagram transforms the data into a new set of coordinates with Hc on the x-axis and Hu on the y-axis, where 2Hc=Hb-Ha and 2Hu=Ha+Hb. In this new coordinate space the x-axis is equivalent to coercivity and the y-axis is a measure of interaction between particles.

FORCs were measured for several samples at the Institute for Rock Magnetism at the University of Minnesota using a Princeton Measurements VSM. Measurements were made on both standard 2.5 cm cylindrical specimens and specimen chips. Samples were saturated with a 1.5 T field. Measurements were made with Hu varying from -0.1 to 0.1 T and Hc varying from 0 to 0.1 T. FORC data was processed with the FORCinel software of Harrison and Feinberg (2008).

Anisotropy of Anhysteretic Remanent Magnetization

While AMS provides a relatively quick and nondestructive method to measure and describe the magnetic fabric of a specimen, it uses susceptibility which is a property of all materials. Therefore, the AMS of a specimen is the result of the average susceptibility of all mineral constituents of the specimen. One way to isolate the magnetic fabric due to only the ferromagnetic minerals is to measure the anisotropy of anhysteretic remanent magnetization

(AARM) (Jackson, 1991; Jackson and Tauxe, 1991; Potter, 2004).

AARM was measured on nine specimens at the Institute for Rock Magnetism at the University of Minnesota using a 2G SQuID magnetometer and an ASC Scientific static alternating field demagnetizer. Each specimen was manually AF demagnetized along three orthogonal axes. The demagnetized specimen was measured manually on the SRM in six directions. An ARM was given to the specimen along one axis in a peak alternating field of 0.2 T with a 0.005 T biasing field along the axis. The specimen was measured on the SRM in six directions. The specimen was then AF demagnetized along the axis that was previously given an ARM. This process was repeated for between six and ten axes of the specimen.

Thermal enhancement of AMS

The samples of TSF have an average percent anisotropy of 4%. This weak anisotropy can cause transposition of the measured susceptibility axes and can increase the uncertainty, both of which make it more difficult to identify the principal directions and corresponding petrofabric. In order to combat this issue, we have experimented with the thermal enhancement of susceptibility (Borradaile and Lagroix, 2000; Jeleńska and Kądziałko-Hofmokl, 1990). Heating a sample increases the bulk susceptibility by the growth of iron oxides (Dunlop, 1974). If this new mineral growth occurs in void spaces or as an overgrowth on already present phases, the original anisotropy will be retained and increased.

Two 2.5 cm cores were drilled from an oriented block sample. Each core was cut into 7 specimens 2.2 cm long. The AMS of samples was measured in a 200 A/m field with the spinning mode of the AGICO MFK1-FA Kappabridge. An initial measurement was made at the standard frequency of 976 Hz. This measurement was duplicated to test the reproducibility of the measurements. Two more measurements were made at 3,904 Hz and 15,616 Hz. The specimens were then left to rest for twelve hours in a μ-metal cylinder inside of the μ-metal shielded room. After the 12 hours in near zero field, the specimens were again measured at the three different frequencies. The specimens were then immersed in liquid nitrogen for 30 minutes in the μ-metal shielded room and warmed back to room temperature. From this step onward the AMS after each treatment was only measured at a frequency of 976 Hz. A second low-temperature step was performed on all of the samples during which two of the specimens were measured while still frozen at -196°C. The specimens were given a low alternating field demagnetization of 2.3, 4.6, and 6.9 mT. The specimens were then heated in a shielded oven in an air atmosphere to 50°C for one hour, 90°C for one hour, and 115°C for one hour. After these initial thermal steps the specimens were split into two groups, one that continued the heating process in air and the other in a controlled nitrogen atmosphere. The specimens were then heated for 30 minutes to temperatures of 150°C, 220°C, 260°C, 300°C, 400°C, 470°C, 540°C, 610°C, 680°C, and 700°C.

Data Analysis

AMS

The samples show anisotropy typical for a welded tuff (Ellwood, 1982; Hillhouse and Wells, 1991; Knight et al., 1986; MacDonald and Palmer, 1990; Palmer et al., 1996; Palmer et al., 1991; Seaman et al., 1991; Thomas et al., 1992). The anisotropy of all measured specimens ranges from 0.7 – 7.3% with a mean of 4% and a standard deviation of 1.7%. Such a weak anisotropy is not unusual for a tuff that does not exhibit a macroscopic fabric.

The AMS tensors of the samples exhibit a well-defined foliation and a more poorly defined lineation. Almost all of the samples lie in the oblate sector of a Flinn diagram (Flinn, 1962) (Figure 6). There is only one specimen that exhibits a relatively large degree of anisotropy and has a prolate shape.

The mean susceptibility (in 10-6 SI) ranges from 374 – 7949 with an average of 2764 ± 1613 (1σ). The mean susceptibility does not correlate with the density of the specimens, which is assumed to be due to differential compaction of the tuff (Figure 7). Assuming the magnetic particles were uniformly distributed in the pyroclastic flow, the compaction process would increase the volume fraction of high susceptibility particles and consequently the mean susceptibility. The fact that mean susceptibility and specimen density are not correlated tells us that either the fraction of high susceptibility particles varies for other reasons such as differing composition, varying concentration of lithic clasts, or that the welding process is not effective at concentrating magnetic minerals.

There is no strong correlation between the mean susceptibility and the size of the error ellipses on individual AMS axes, which means the errors are not due to the measurement of weak samples. The sites show both well-defined tri-axial and girdle distributions of K2 and K3. There is no clear correlation between the mean Jelinek anisotropy factor (Jelinek, 1981) and the clustering of K1 and K3. The lack of a correlation between the degree of anisotropy and the precision of the K1 axis indicates that the variations in the lineation direction are not an artifact of measuring samples with a low degree of anisotropy. The overall weakly-defined lineation and large variation in the declination of K1 within a single site indicate poor alignment of the magnetic grains.

The flow direction, as defined by the plunge direction of the K3 axis and by the azimuth

180 degrees away from the K1 axis, is consistent for the vast majority of sites (Figure 8). The general flow direction defined by the AMS fabric for all sites is to the South – Southwest, although there is significant variation between sites. Notably, the small tilted block, containing sites 1 through 6, contains the largest variation in flow directions.

Thermal enhancement

The thermal enhancement experiment proved unsuccessful in providing tighter constraints on the principal axes of the AMS fabric. While the treatments increased the degree of anisotropy in all specimens, the magnitude of the change was not uniform (Figure 9). The thermal treatments produced a clockwise rotation of the declination of K1 (Figure 10). The angular dispersion of the declinations did not improve with progressive heating. The bulk susceptibility shows some very interesting variation with differing treatments (Figure 11). It decreases with increasing frequency, indicating a superparamagnetic component (Carter-Stiglitz et al., 2006). The duplicate measurements at frequency 1 are almost indistinguishable. Resting the samples in zero field decreases the susceptibility. There is a large increase in susceptibility after the specimens have been cooled to 77 Kelvin and warmed back to room temperature. The susceptibility remains elevated when the specimens are measured while still frozen. While the decrease in susceptibility with frequency indicates very small superparamagnetic grains, the increase in susceptibility with low-temperature cycling indicates the presence of larger multi-domain grains (Özdemir et al., 2002; Ozima et al., 1964; Schmidt, 1993).

After a low-AF treatment the susceptibility returns to the pre low-temperature cycle values. Once the samples have been heated above the Curie temperature of magnetite, the bulk susceptibility drops off rapidly. The decrease in susceptibility past the magnetite Curie temperature is puzzling. Demagnetization should not permanently alter the bulk susceptibility unless there is alteration or creation of new phases, such as titanomagnetite from magnetite (Jackson et al., 1998). The susceptibility altering does not appear to be influenced by heating in the presence of air or a controlled nitrogen atmosphere.

Remanence

Thermal and AF demagnetization techniques produce mean tilt corrected directions of ChRM that are statistically indistinguishable (Figure 12). AF demagnetization results in Fisher mean declination of 235.5 and an inclination of -5.3 with an $\alpha 95$ of 4.7. Thermal demagnetization results in a Fisher mean declination of 232.9 and an inclination of -6.8 with an $\alpha 95$ of 4.7. This consistency between the two methods allows us to use the much faster and less user-intensive AF demagnetization procedures for the bulk of our samples.

The samples show clear demagnetization paths that cleanly head toward the origin (Figure 13). The specimens show consistent demagnetization patterns with a few exceptions. Most specimens lose the bulk of their magnetization around 580°C, the Curie temperature of magnetite (Figure 14). Some specimens start to demagnetize at lower temperatures, most likely indicating a higher titanium content (titanomagnetite). A few specimens retain up to 10% of their magnetization past 600°C indicating the presence of an antiferromagnetic phase like hematite. One specimen from site 3 shows an increase in magnetization most likely due to the removal of an overprint that is anti-parallel to the ChRM. Most specimens demagnetize in the range of 10s of mT, indicating magnetite (Figure 15). Five specimens (2a, 2r, 5k, 24e, 31e) retain more than 25% of their initial magnetization at a field of 90mT indicating a high coercivity phase such as hematite, or perhaps elongate magnetite needles exsolved within feldspars.

Rockmag

The Lowrie-Fuller test shows that most samples have a median destructive field (MDF) of SIRM greater than the MDF of ARM, indicating single domain particles (Figure 16). The shape of the demagnetization curves are more often S-shaped than exponential, indicating a pseudo-single-domain grain size (Dunlop and Özdemir, 2001). The crossover in the IRM plot, correlative to the coercivity of remanence, is in the range of 20-30 mT, again indicating magnetite (Cisowski, 1981) (Figure 17). The crossover does not always occur at half of the SIRM indicating that there is interaction of the magnetic particles (Cisowski, 1981). The backfield IRMs are all in the range of 30mT, also consistent with the coercivity of magnetite (Dunlop and Özdemir, 2001) (Figure 18).

Thermal susceptibility

All of the thermal susceptibility curves (Figure 19) indicate that the dominant magnetic phase is magnetite. There is a peak near the 120K Verwey transition of magnetite and a Hopkinson peak followed by a sharp decrease in susceptibility near the 580°C Curie temperature of magnetite. Most samples exhibit a type three relationship where the cooling curve is much lower than the heating curve but of a similar shape, caused by an unknown alteration of the magnetic phases (Hrouda, 2003). Some samples show a type two relationship, where the cooling curve is higher than the heating curve indicating the production of magnetite from less magnetic phases (Hrouda, 1994). A few samples produce a cooling curve of a different shape than the heating curve (Figure 20). This indicates the creation of two separate phases, perhaps with different concentrations of titanium.

Emplacement temperature

Repeated heating experiments on six samples gave inconclusive results, partially hampered by a software error that halted the measurement procedure. The largest A40 anomaly that we have measured is 15% and indicates a temperature of 700°C (Figure 21). This anomaly is nowhere near the 500% anomaly that Hrouda et al. (2003) observed when they first described the technique. Most of the variation seen is only on the order of a few percent, insufficient to constrain the emplacement temperature of the tuff. However, we can determine from these experiments that the tuff has not undergone significant thermal alteration.

Hysteresis

Plotting the results of all measured hysteresis loops on a Day plot (Dunlop, 2002), the ratio of coercivity of remanence to coercivity versus the ratio of saturation remanent magnetization to saturation magnetization, indicates that all our samples are in the (PSD) grain region (Figure 22). This result can mean either that our samples are actually in the PSD size range or that we have a population of multidomain and a population of single-domain grains and what we have measured is a mixing line of the two populations. The shape of the hysteresis loops, relatively steep and narrow without constriction near the origin, indicate PSD grains (Roberts et al., 1995; Tauxe et al., 1996). The largest variation that we observe between samples is in the paramagnetic component (Figure 23). Large variations in the paramagnetic content of the matrix can be a contributing factor to the variations that we measure in the AMS ellipsoid (Richter and van der Pluijm, 1994).

VSM thermal

The majority of samples examined for the variation of magnetization at high temperature show a clear magnetite signal with a Curie temperature of 850 K (Figure 24). Ssample 6g shows evidence of a secondary component of hematite with a Curie temperature of 950 K (Figure 24). Some samples show a slight change in slope around 550 K, possibly indicating a phase with an increased titanium content.

Frequency dependence of susceptibility

All 88 specimens measured show a clear decrease in susceptibility with increasing frequency of the applied field (Figure 25). This behavior is a clear sign of the presence of a superparamagnetic fraction of grains in the sample (Carter-Stiglitz et al., 2006).

MPMS

The results from the room temperature SIRM remanence on cooling and low-temperature SIRM remanence on warming show three different patterns. One pattern shows a minor change in moment at 120K, the Verwey transition in magnetite (Figure 26). Another pattern has a larger change in remanence at 100K, a possible depression of the Verwey transition due to non-stoichiometric magnetite or the partial oxidation to maghemite (Kosterov, 2002). The final pattern has the 100K transition as well as a change in remanence at 160K of unknown origin.

The experiments of the frequency and temperature dependence of susceptibility confirm that the major magnetic phase in the samples is magnetite. The peak of in-phase susceptibility at 120K and the peak of out-of-phase susceptibility at 50K are diagnostic of magnetite (Figure 27). The MPMS experiments also show a frequency dependence of susceptibility, indicating the presence of superparamagnetic grains.

FORCs

In FORC distribution space, a ridge along the Hu=0 axis indicates uniaxial non-interacting single-domain particles, a ridge along the Ha=0 axis indicates multidomain particles, while dispersion about the Hu=0 axis indicates interaction of single-domain particles or pseudo-single-domain particles (Carvallo et al., 2003; Dunlop et al., 1990; Harrison and Feinberg, 2008; Heslop and Muxworthy, 2005; Muxworthy and Williams, 2005; Muxworthy et al., 2005; Pike et al., 1999; Pike et al., 2001; Roberts et al., 2000). All of the samples exhibit pseudo-single-domain behavior or are a mixture of interacting single-domain particles and multidomain particles (Figure 28).

AARM

The degree of anisotropy of the ARM varies from 4 – 19% with a mostly oblate fabric (Figure 29). While the AARM produces the same northeast – southwest oriented fabric as the AMS, the bearing of motion implied by the inclination of K3 is in the opposite direction. Although the mean plunge of the K3 axes suggests flow directed to the northwest, the error ellipses are quite large and do not exclude flow to the southeast. The error ellipses around K3 range from 5 – 37 degrees while the error ellipses around K1 range from 17 – 70 degrees. The AARM fabric is consistent with the AMS fabric, but needs measurements in more directions to be statistically significant.

Discussion

The results of exhaustive rock magnetic experiments indicate that the main carrier of the magnetization, in the Tuff of San Felipe on Isla Angel de la Guarda, is titanomagnetite with a pseudo-single-domain grain size. Some samples contain minor components of a higher coercivity phase such as hematite and larger multidomain grains. Pseudo-single-domain titanomagnetite allows the interpretation of the AMS fabric as a normal fabric. The agreement of the AARM fabric with the AMS fabric also gives us confidence that we do not have a reverse fabric.

The excellent agreement between the mean direction produced by the paired AF and thermal demagnetization of split test specimens justifies our use of AF demagnetization. From AF demagnetization of additional samples, we can calculate the rotation of coherent blocks relative to a stable Tuff of San Felipe reference site on the Baja California Peninsula defined by Bennett (2013). Individual measured rotations vary from the reference site by 20 degrees counterclockwise to 62 degrees clockwise, with an average rotation of 34 degrees in a clockwise direction (Figure 30).

The azimuth of the K3 axis defines a general flow direction to the south-southwest, although there is large scatter even within the directions given by cores at an individual site. We can try and correct for the scatter in the AMS principal axis at individual sites by performing a vertical axis rotation correction (Hillhouse and Wells, 1991). Using the rotations determined for each specimen to correct for the rotation of the remanent magnetization, we rotated the three AMS axis into a tectonic reference frame (Figure 31). The tectonic correction factor does not dramatically reduce the scatter at individual sites (Figure 32), though the mean declinations of the principal AMS axes are slightly enhanced (Figure 33). We have also performed an inclination correction, relative to the reference site, about a horizontal axis perpendicular to the trend of the K3 axis. This correction also fails to reduce the intra-site scatter of the principal AMS axes. If the scatter in the AMS is the result of post-depositional rotations, the vertical axis rotation correction based on the Tuff of San Felipe reference vector direction should greatly reduce the scatter. Because this correction has failed to reduce the scatter we can conclude it is not due to a structural rotation of the blocks. The most likely remaining explanation for the dispersion in the AMS axes is turbulent flow of the ignimbrite during deposition. Non-laminar flow during deposition reduces the alignment of the long axes of the magnetic grains which could account for the weak lineation fabric that we have measured as well as the dispersion that we observe at individual sites. Because the AMS fabric is so sensitive to the local conditions around the location of deposition, it is not a useful tool for recognizing small-scale coherent flow. Our sampling on the 200 meter wide tilted block poses a significant challenge when trying to determine coherent flow simply on the scale of tens of meters.

The small tilted block was sampled intensely due to the fact that it was interpreted in the field to be a single coherent block that was accessible from all directions. These samples produced the most directional scatter in ChRM of all our locations. The exhaustive rock magnetic experiments were designed to find a mineralogical explanation for the dispersion in the AMS fabrics here; however, we found no significant difference in the mineralogy of the specimens to account for the significant variation we observe. Additionally, there are no observed rheomorphic textures in the field and we do not find a correlation between the density of the specimens, a proxy for degree of welding, or the degree of anisotropy and the anomalous directions of the K1 and K3 axes. We have, however, found a correlation between the approximate stratigraphic height of a specimen and a rotation in the remanence direction (Figure 34). In order to test the strength of this correlation, we performed a test to determine whether or not the Fisher means of the upper and lower specimens at site 2, which covers the entire stratigraphy on the tilted block, were statistically distinct (Fisher et al., 1987). The Fisher mean direction of the site 2 specimens in the lower four meters of the section is statistically different from the mean of the specimens found above four meters, at the 99.95 confidence level (N=28 and N=19, χ^2=2.56x10^{-34}). Therefore, the rotation of the top of the unit relative to the bottom is a real signal.

Possible causes for this change in remanence direction were examined. We have ruled out misorientation of the cores due to a spurious local magnetic field by checking all of our magnetic compass measurements against the corresponding sun compass measurements. The average difference between the strike as measured by the sun compass and the magnetic compass is less than three degrees. We have also checked the least squares analysis of the demagnetization data and find no reason to doubt our fitting procedure; we have an average maximum angular deviation (MAD values) of 1.8 degrees and the Fisher means from a thermal demagnetization dataset are indistinguishable from that of the AF demagnetized dataset.

Having ruled out sampling and processing artefacts, we are left to determine a physical explanation for the rotation of the magnetic remanence within the unit. There are four possible physical ways to explain the rotation we observe: 1) the Earth's magnetic field may have shifted while the tuff was cooling, 2) the tuff deformed ductilely after it had cooled below its Curie temperature, 3) alteration of the tuff by devitrification of vapor phase alteration has given the upper section of the tuff a chemical remanent magnetization (CRM) at a time after deposition when the Earth's magnetic field has shifted, or 4) a low-angle fault or slump has rotated the top of the unit.

The Earth's magnetic field has been shown to change at a rate of up to 1° per week during a reversal (Bogue and Glen, 2010). In order to record the 27° magnetic remanence rotation that we observe, the top of the tuff would have to have cooled below the Curie temperature of magnetite 189 days after the base. Such a temporal cooling differential is not expected for a single 12 meter ignimbrite deposit (Keating, 2005; Wallace et al., 2003). Numerical modeling indicates that the entire deposit would have cooled below the curie temperature of magnetite within seven months (Riehle et al., 1995). In addition, this would not produce the rotation pattern that we observe. If the Earth's magnetic field were to change while the tuff was cooling, it is the middle of the unit that will cool the most slowly and thus record a different remanent magnetization vector. Variation in the Earth's magnetic field cannot explain the changing ChRM that we observe.

The minimum temperature for welding in a rhyolitic tuff has been estimated to be between 500°C and 625°C (Sheridan and Wang, 2005), however, this temperature can also exceed 900°C at high water content and low lithostatic pressure (Grunder et al., 2005). If we use the conservative estimate of 500°C, there is only an 85°C window where the remanence vector will be locked into the magnetic mineralogy and welding can continue. The lack of rheomorphic deformation in the outcrops of the tuff in this location cast doubt on the idea of ductile deformation post emplacement.

Devitrification and vapor-phase alteration have been show to produce magnetite (Stimac et al., 1996), however, we do not see any significant variation in the magnetic mineralogy or grain size. This requires the post-depositional chemical precipitation of magnetic phases of the same composition and size as those produced through magmatic processes. The location of the zone of alteration would have to be highly localized. There is no apparent difference between the cores in the rotated section and the outcrops on the rest of the island. Experimental results have shown that magnetite precipitates with its easy axis aligned with the applied field (Pick and Tauxe, 1991). This makes the prediction that the ChRM due to a magnetite chemical remanent magnetization (CRM) will align with the K1 axis of the AMS ellipsoid. A test of the correlation between the ChRM declination and the AMS lineation direction casts doubt on the idea that we have measured a CRM (Figure 35). A Fuller test also shows that we have measured a TRM (Figure 36) (Cisowski et al., 1990; Fuller et al., 1988; Fuller et al., 2002).

We have not recognized a low-angle structure in the outcrops where we observe the rotation of remanence. However, elsewhere on the island, we have mapped a low-angle planar feature within the tuff (Appendix II). However, this model has another problem, since where we have sampled across the mapped low-angle structure, we do not see any vertical-axis rotation (Figure 37). For the low-angle fault model to hold true, this structure would have to be moving independently from the one observed in the other outcrops, or it may have some structural variability.

Conclusion

We have determined through extensive rock magnetic studies that the main magnetic carrier in the Tuff of San Felipe on Isla Angel de la Guarda is pseudo-single-domain magnetite. This fact allows us to interpret the principal axes of the AMS fabric in terms of an emplacement flow direction. We have determined that the Tuff of San Felipe flowed across Isla Angel de la Guarda from the northeast to southwest. An average of 30° of clockwise vertical-axis rotation of the Tuff of San Felipe outcrops has been determined by comparing the characteristic remanent magnetization on the island to a stable reference site on the Baja California peninsula. We have attempted to reduce the scatter in the AMS measurements by correcting the principal axes directions for vertical-axis tectonic evidenced by the rotation of the remanent magnetization. This tectonic correction failed to improve the clustering of the principal AMS axes and suggests that the observed scatter in the AMS measurements is a primary feature of turbulent flow at the time of deposition. The deflection of AMS axes by highly localized processes limits its function as a method of recognizing offset channelized flow. Our thorough magnetic sampling has revealed previously unrecognized, rotations within the tuff. Though not definitive, the current best explanation for the differential rotation is a low-angle structure. Our work provides testable hypothesis and a direction for future work elucidating the cause of the observed rotation.

References:

AGICO, 2009, MFK1-FA/CS4/CSL Users's Guide Ver. 4: Brno, Czech Republic, Advanced Geoscience Instruments Company.

Aragon-Arreola, M., and Martin-Barajas, A., 2007, Westward migration of extension in the northern Gulf of California, Mexico: Geology, v. 35, no. 6, p. 571-574.

Bennett, S., 2013, The Role of Rift Obliquity in Formation of the Gulf of California [PhD: University of California, Davis, 205 p.

Bogue, S. W., and Glen, J. M. G., 2010, Very rapid geomagnetic field change recorded by the partial remagnetization of a lava flow: Geophysical Research Letters, v. 37, no. 21, p. L21308.

Borradaile, G. J., and Lagroix, F., 2000, Thermal Enhancement of Magnetic Fabrics in High Grade Gneisses: Geophysical Research Letters, v. 27, no. 16, p. 2413-2416.

Branney, M., and Kokelaar, P., 1992, A reappraisal of ignimbrite emplacement: progressive aggradation and changes from particulate to non-particulate flow during emplacement of high-grade ignimbrite: Bulletin of Volcanology, v. 54, no. 6, p. 504-520.

Butler, R. F., 1992, Paleomagnetism: magnetic domains to geologic terranes, Blackwell Scientific Publications Boston.

Carter-Stiglitz, B., Solheid, P., Egli, R., and Chen, A., 2006, Tiva Canyon Tuff (II): IRM Q, v. 16, no. 1, p. 1.

Carvallo, C., Muxworthy, A. R., Dunlop, D. J., and Williams, W., 2003, Micromagnetic modeling of first-order reversal curve (FORC) diagrams for single-domain and pseudo-single-domain magnetite: Earth and Planetary Science Letters, v. 213, no. 3–4, p. 375-390.

Cisowski, S., 1981, Interacting vs. non-interacting single domain behavior in natural and synthetic samples: Physics of the Earth and Planetary Interiors, v. 26, no. 1–2, p. 56-62.

Cisowski, S. M., Dunn, J. R., Fuller, M., and Wasilewski, P. J., 1990, NRM: IRM(s) demagnetization plots of intrusive rocks and the origin of their NRM: Tectonophysics, v. 184, no. 1, p. 35-54.

Day, R., Fuller, M., and Schmidt, V. A., 1977, Hysteresis properties of titanomagnetites: Grain-size and compositional dependence: Physics of the Earth and Planetary Interiors, v. 13, no. 4, p. 260-267.

Delgado-Argote, L. A., 2000, Evolución tectónica y magmatismo Neógeno de la margen oriental de Baja California central [PhD: Universidad Nacional Autónoma de México.

Dixon, T., Farina, F., DeMets, C., Suarez-Vidal, F., Fletcher, J., Marquez-Azua, B., Miller, M., Sanchez, O., and Umhoefer, P., 2000, New kinematic models for Pacific-North America Motion from 3 Ma to Present, II: Evidence for a "Baja California Shear Zone": Geophysical Research Letters, v. 27, no. 23, p. 3961-3964.

Dunlop, D., 1974, Thermal enhancement of magnetic susceptibility: J. Geophys, v. 40, p. 439-451.

Dunlop, D. J., 2002, Theory and application of the Day plot (Mrs/Ms versus Hcr/Hc) 1. Theoretical curves and tests using titanomagnetite data: Journal of Geophysical Research: Solid Earth, v. 107, no. B3, p. EPM 4-1-EPM 4-22.

Dunlop, D. J., and Özdemir, Ö., 2001, Rock magnetism: fundamentals and frontiers, Cambridge University Press.

Dunlop, D. J., Westcott-Lewis, M. F., and Bailey, M. E., 1990, Preisach diagrams and anhysteresis: do they measure interactions?: Physics of the Earth and Planetary Interiors, v. 65, no. 1–2, p. 62-77.

Ellwood, B. B., 1982, Estimates of flow direction for calc-alkaline welded tuffs and paleomagnetic data reliability from anisotropy of magnetic susceptibility measurements: Central San Juan Mountains, southwest Colorado: Earth and Planetary Science Letters, v. 59, no. 2, p. 303-314.

Fisher, N. I., Lewis, T., and Embleton, B. J., 1987, Statistical analysis of spherical data, Cambridge University Press.

Fletcher, J. M., Grove, M., Kimbrough, D., Lovera, O., and Gehrels, G. E., 2007, Ridge-trench interactions and the Neogene tectonic evolution of the Magdalena shelf and southern Gulf of California: Insights from detrital zircon U-Pb ages from the Magdalena fan and adjacent areas: Geological Society of America Bulletin, v. 119, no. 11-12, p. 1313-1336.

Fletcher, J. M., and Munguia, L., 2000, Active continental rifting in southern Baja California, Mexico: Implications for plate motion partitioning and the transition to seafloor spreading in the Gulf of California: Tectonics, v. 19.

Flinn, D., 1962, On folding during three-dimensional progressive deformation: Quarterly Journal of the Geological Society, v. 118, no. 1-4, p. 385-428.

Fuller, M., Cisowski, S., Hart, M., Haston, R., Schmidtke, E., and Jarrard, R., 1988, NRM: IRM(S) demagnetization plots; An aid to the interpretation of natural remanent magnetization: Geophysical Research Letters, v. 15, no. 5, p. 518-521.

Fuller, M., Kidane, T., and Ali, J., 2002, AF demagnetization characteristics of NRM, compared with anhysteretic and saturation isothermal remanence: an aid in the interpretation of NRM: Physics and Chemistry of the Earth, Parts A/B/C, v. 27, no. 25–31, p. 1169-1177.

Gastil, R. G., Phillips, R. P., and Allison, E. C., 1975, Reconnaissance geology of the state of Baja California, Geological Society of America, Geological Society of America Memoir.

Grunder, A., Grunder, D., Laporte, T., and Druitt, 2005, Experimental and textural investigation of welding: effects of compaction, sintering, and vapor-phase crystallization in the rhyolitic Rattlesnake Tuff: Journal of volcanology and geothermal research, v. 142, no. 1, p. 89-104.

Harrison, R. J., and Feinberg, J. M., 2008, FORCinel: An improved algorithm for calculating first-order reversal curve distributions using locally weighted regression smoothing: Geochemistry, Geophysics, Geosystems, v. 9, no. 5.

Heslop, D., and Muxworthy, A. R., 2005, Aspects of calculating first-order reversal curve distributions: Journal of Magnetism and Magnetic Materials, v. 288, no. 0, p. 155-167.

Hillhouse, J. W., and Wells, R. E., 1991, Magnetic fabric, flow directions, and source area of the Lower Miocene Peach Springs Tuff in Arizona, California, and Nevada: Journal of Geophysical Research: Solid Earth, v. 96, no. B7, p. 12443-12460.

Hinz, N. H., Faulds, J. E., and Henry, C. D., 2009, Tertiary volcanic stratigraphy and paleotopography of the Diamond and Fort Sage Mountains: Constraining slip along the Honey Lake fault zone in the northern Walker Lane, northeastern California and western Nevada: Geological Society of America Special Papers, v. 447, p. 101-131.

Hrouda, F., 1994, A technique for the measurement of thermal changes of magnetic susceptibility of weakly magnetic rocks by the CS-2 apparatus and KLY-2 Kappabridge: Geophysical Journal International, v. 118, no. 3, p. 604-612.

-, 2003, Indices for Numerical Characterization of the Alteration Processes of Magnetic Minerals Taking Place During Investigation of Temperature Variation of Magnetic Susceptibility: Studia Geophysica et Geodaetica, v. 47, no. 4, p. 847-861.

Hrouda, F., Müller, P., and Hanák, J., 2003, Repeated progressive heating in susceptibility vs.

temperature investigation: a new palaeotemperature indicator?: Physics and Chemistry of the Earth, Parts A/B/C, v. 28, no. 16–19, p. 653-657.

Jackson, M., 1991, Anisotropy of magnetic remanence: a brief review of mineralogical sources, physical origins, and geological applications, and comparison with susceptibility anisotropy: Pure and Applied Geophysics, v. 136, no. 1, p. 1-28.

Jackson, M., Moskowitz, B., Rosenbaum, J., and Kissel, C., 1998, Field-dependence of AC susceptibility in titanomagnetites: Earth and Planetary Science Letters, v. 157, no. 3–4, p. 129-139.

Jackson, M., and Tauxe, L., 1991, Anisotropy of magnetic susceptibility and remanence: developments in the characterization of tectonic, sedimentary, and igneous fabric: Reviews of Geophysics, v. 29, p. 371-376.

Jeleńska, M., and Kądziałko-Hofmokl, M., 1990, Dependence of anisotropy of magnetic susceptibility of rocks on temperature: Physics of the Earth and Planetary Interiors, v. 62, no. 1–2, p. 19-31.

Jelinek, V., 1981, Characterization of the magnetic fabric of rocks: Tectonophysics, v. 79, no. 3–4, p. T63-T67.

Jones, C. H., 2002, User-driven integrated software lives:"PaleoMag" paleomagnetics analysis on the Macintosh: Computers & Geosciences, v. 28, no. 10, p. 1145-1151.

Keating, G. N., 2005, The role of water in cooling ignimbrites: Journal of Volcanology and Geothermal Research, v. 142, no. 1–2, p. 145-171.

Kirschvink, J. L., 1980, The least-squares line and plane and the analysis of palaeomagnetic data: Geophysical Journal International, v. 62, no. 3, p. 699-718.

Kirschvink, J. L., Kopp, R. E., Raub, T. D., Baumgartner, C. T., and Holt, J. W., 2008, Rapid, precise, and high-sensitivity acquisition of paleomagnetic and rock-magnetic data: Development of a low-noise automatic sample changing system for superconducting rock magnetometers: Geochemistry, Geophysics, Geosystems, v. 9, no. 5, p. Q05Y01.

Knight, M. D., Walker, G. P. L., Ellwood, B. B., and Diehl, J. F., 1986, Stratigraphy, paleomagnetism, and magnetic fabric of the Toba Tuffs: Constraints on the sources and eruptive styles: Journal of Geophysical Research: Solid Earth, v. 91, no. B10, p. 10355-10382.

Kosterov, A., 2002, Low-temperature magnetic hysteresis properties of partially oxidized magnetite: Geophysical Journal International, v. 149, no. 3, p. 796-804.

Lease, R. O., McQuarrie, N., Oskin, M., and Leier, A., 2009, Quantifying Dextral Shear on the Bristol-Granite Mountains Fault Zone: Successful Geologic Prediction from Kinematic Compatibility of the Eastern California Shear Zone: The Journal of Geology, v. 117, no. 1, p. 37-53.

Lewis, C. J., and Stock, J. M., 1998a, Late Miocene to Recent transtensional tectonics in the Sierra San Fermín, northeastern Baja California, Mexico: Journal of Structural Geology, v. 20, no. 8, p. 1043-1063.

-, 1998b, Paleomagnetic evidence of localized vertical axis rotation during Neogene extension, Sierra San Fermín, northeastern Baja California, Mexico: Journal of Geophysical Research: Solid Earth, v. 103, no. B2, p. 2455-2470.

Lowrie, W., and Fuller, M., 1971, On the alternating field demagnetization characteristics of multidomain thermoremanent magnetization in magnetite: Journal of Geophysical Research, v. 76, no. 26, p. 6339-6349.

MacDonald, W. D., and Palmer, H. C., 1990, Flow directions in ash-flow tuffs: a comparison of geological and magnetic susceptibility measurements, Tshirege member (upper Bandelier

Tuff), Valles caldera, New Mexico, USA: Bulletin of Volcanology, v. 53, no. 1, p. 45-59.

Marsaglia, K. M., 2004, Sandstone detrital modes support Magdalena Fan displacement from the mouth of the Gulf of California: Geology, v. 32, no. 1, p. 45-48.

Martin-Barajas, A., Stock, J. M., Lopez-Martinez, M., and Chapman, A., Estratigraphia volcanica del Neogeno en la mitad norte de Isla Angel de la Guarda, in Proceedings 1er congreso sobre la evolucion geologica y ecologica del noroeste de Mexico, Hermosillo, Sonora, 2008.

Mayergoyz, I. D., 1986, Mathematical models of hysteresis: Magnetics, IEEE Transactions on, v. 22, no. 5, p. 603-608.

Michaud, F., Sosson, M., Royer, J. Y., Chabert, A., Bourgois, J., Calmus, T., Mortera, C., Bigot-Cormier, F., Bandy, W., Dyment, J., Pontoise, B., and Sichler, B., 2004, Motion partitioning between the Pacific plate, Baja California and the North America plate: The Tosco-Abreojos fault revisited: Geophys. Res. Lett., v. 31.

Moskowitz, B. M., Frankel, R. B., and Bazylinski, D. A., 1993, Rock magnetic criteria for the detection of biogenic magnetite: Earth and Planetary Science Letters, v. 120, no. 3, p. 283-300.

Muxworthy, A., and Williams, W., 2005, Magnetostatic interaction fields in first-order-reversal-curve diagrams: Journal of Applied Physics, v. 97, no. 6.

Muxworthy, A. R., King, J. G., and Heslop, D., 2005, Assessing the ability of first-order reversal curve (FORC) diagrams to unravel complex magnetic signals: Journal of Geophysical Research: Solid Earth, v. 110, no. B1, p. B01105.

Nagy, E. A., 2000, Extensional deformation and paleomagnetism at the western margin of the Gulf extensional province, Puertecitos Volcanic Province, northeastern Baja California, Mexico: Geological Society of America Bulletin, v. 112, no. 6, p. 857-870.

Nagy, E. A., Grove, M., and Stock, J. M., 1999, Age and stratigraphic relationships of pre- and syn-rift volcanic deposits in the northern Puertecitos Volcanic Province, Baja California, Mexico: Journal of Volcanology and Geothermal Research, v. 93, no. 1-2, p. 1-30.

Olguin-Villa, A. E., 2010, Estudio fisico y quimico del volcanismo hiperalcalino en la region de Catavina, Baja California [Tesis de Licenciatura: Universidad de Sonora, 87 p.

Oskin, M., and Stock, J., 2003, Pacific-North America plate motion and opening of the Upper Delfin basin, northern Gulf of California, Mexico: Geological Society of America Bulletin, v. 115, no. 10, p. 1173-1190.

Oskin, M., Stock, J., and Martin-Barajas, A., 2001, Rapid localization of Pacific-North America plate motion in the Gulf of California: Geology, v. 29, no. 5, p. 459-462.

Özdemir, Ö., Dunlop, D. J., and Moskowitz, B. M., 2002, Changes in remanence, coercivity and domain state at low temperature in magnetite: Earth and Planetary Science Letters, v. 194, no. 3–4, p. 343-358.

Ozima, M., Ozima, M., and Nagata, T., 1964, Low Temperature Treatment as an Effective Means of Magnetic Cleaning of Natural Remanent Magnetization: Journal of geomagnetism and geoelectricity, v. 16, no. 1, p. 37-40.

Palmer, H. C., MacDonald, W. D., Gromme, C. S., and Ellwood, B. B., 1996, Magnetic properties and emplacement of the Bishop tuff, California: Bulletin of Volcanology, v. 58, no. 2-3, p. 101-116.

Palmer, H. C., MacDonald, W. D., and Hayatsu, A., 1991, Magnetic, structural and geochronologic evidence bearing on volcanic sources and Oligocene Deformation of Ash Flow Tuffs, northeast Nevada: Journal of Geophysical Research: Solid Earth, v. 96, no. B2, p. 2185-2202.

Pick, T., and Tauxe, L., 1991, Chemical remanent magnetization in synthetic magnetite: Journal of Geophysical Research: Solid Earth (1978–2012), v. 96, no. B6, p. 9925-9936.

Pike, C. R., Roberts, A. P., and Verosub, K. L., 1999, Characterizing interactions in fine magnetic particle systems using first order reversal curves: Journal of Applied Physics, v. 85, no. 9, p. 6660-6667.

Pike, C. R., Roberts, A. P., and Verosub, K. L., 2001, First order reversal curve diagrams and thermal relaxation effects in magnetic particles: Geophysical Journal International, v. 145, no. 3, p. 721-730.

Porath, H., Stacey, F. D., and Cheam, A. S., 1966, The choice of specimen shape for magnetic anisotropy measurements on rocks: Earth and Planetary Science Letters, v. 1, no. 2, p. 92.

Potter, D. K., 2004, A comparison of anisotropy of magnetic remanence methods—a user's guide for application to palaeomagnetism and magnetic fabric studies: Geological Society, London, Special Publications, v. 238, no. 1, p. 21-35.

Richter, C., and van der Pluijm, B. A., 1994, Separation of paramagnetic and ferrimagnetic susceptibilities using low temperature magnetic susceptibilities and comparison with high field methods: Physics of the earth and planetary interiors, v. 82, no. 2, p. 113-123.

Riehle, J., Miller, T., and Bailey, R., 1995, Cooling, degassing and compaction of rhyolitic ash flow tuffs: a computational model: Bulletin of Volcanology, v. 57, no. 5, p. 319-336.

Roberts, A. P., Cui, Y., and Verosub, K. L., 1995, Wasp-waisted hysteresis loops: Mineral magnetic characteristics and discrimination of components in mixed magnetic systems: Journal of Geophysical Research, v. 100, no. B9, p. 17909-17917,17924.

Roberts, A. P., Pike, C. R., and Verosub, K. L., 2000, First-order reversal curve diagrams: A new tool for characterizing the magnetic properties of natural samples: Journal of Geophysical Research: Solid Earth (1978–2012), v. 105, no. B12, p. 28461-28475.

Schmidt, P. W., 1993, Palaeomagnetic cleaning strategies: Physics of the Earth and Planetary Interiors, v. 76, no. 1–2, p. 169-178.

Scott, G. R., and Frohlich, C., 1985, Large-volume, magnetically shielded room: A new design and material, in Kirschvink, J. L., Jones, D. S., and McFadden, B., eds., Magnetite Biomineralization and Magnetoreception in Organisms: A New Biomagnetism: New York & London, Plenum Press, p. 197-222.

Seaman, S., McIntosh, W., Geissman, J., Williams, M., and Elston, W., 1991, Magnetic fabrics of the Bloodgood Canyon and Shelley Peak Tuffs, southwestern New Mexico: implications for emplacement and alteration processes: Bulletin of Volcanology, v. 53, no. 6, p. 460-476.

Sheridan, M. F., and Wang, Y., 2005, Cooling and welding history of the Bishop Tuff in Adobe Valley and Chidago canyon, California: Journal of volcanology and geothermal research, v. 142, no. 1, p. 119-144.

Stimac, J., Hickmott, D., Abell, R., Larocque, A. C. L., Broxton, D., Gardner, J., Chipera, S., Wolff, J., and Gauerke, E., 1996, Redistribution of Pb and other volatile trace metals during eruption, devitrification, and vapor-phase crystallization of the Bandelier Tuff, New Mexico: Journal of Volcanology and Geothermal Research, v. 73, no. 3–4, p. 245-266.

Stock, J., Martín, A., Chapman, A., and López-Martínez, M., Net Slip across the Ballenas Transform Fault Measured from Offset Ignimbrite Deposits, in Proceedings AGU Fall Meeting Abstracts2008, Volume 1, p. 1853.

Stock, J. M., 2007, The kinematic puzzle of the Gulf of California rift system: Eos, v. 88, no. 23, Suppl., p. S31A-01.

Stock, J. M., Lewis, C. J., and Nagy, E. A., 1999, The Tuff of San Felipe: an extensive middle

Miocene pyroclastic flow deposit in Baja California, Mexico: Journal of Volcanology and Geothermal Research, v. 93, no. 1-2, p. 53-74.

Tauxe, L., Butler, R. F., Van der Voo, R., and Banerjee, S. K., 2010, Essentials of paleomagnetism, University of California Press.

Tauxe, L., Mullender, T., and Pick, T., 1996, Potbellies, wasp-waists, and superparamagnetism in magnetic hysteresis: Journal of Geophysical Research: Solid Earth (1978–2012), v. 101, no. B1, p. 571-583.

Thomas, I. M., Moyer, T. C., and Wikswo, J. P., 1992, High resolution magnetic susceptibility imaging of geological thin sections: Pilot study of a pyroclastic sample from the Bishop Tuff, California, U.S.A: Geophysical Research Letters, v. 19, no. 21, p. 2139-2142.

Vidal-Solano, J., Paz-Moreno, F. A., Iriondo, A., Demant, A., and Cochemé, J.-J., 2005, Middle Miocene peralkaline ignimbrites in the Hermosillo region (Sonora, Mexico): Geodynamic implications: Comptes Rendus Geosciences, v. 337, no. 16, p. 1421-1430.

Vidal Solano, J. R., Lapierre, H., Stock, J. M., Demant, A., Paz Moreno, F. A., Bosch, D., Brunet, P., and Amortegui, A., 2008, Isotope geochemistry and petrogenesis of peralkaline Middle Miocene ignimbrites from central Sonora: relationship with continental break-up and the birth of the Gulf of California: Bulletin de la Societe Geologique de France, v. 179, no. 5, p. 453-464.

Wack, M. R., and Gilder, S. A., 2012, The SushiBar: An automated system for paleomagnetic investigations: Geochemistry, Geophysics, Geosystems, v. 13, no. 3, p. Q12Z38.

Wallace, P. J., Dufek, J., Anderson, A. T., and Zhang, Y., 2003, Cooling rates of Plinian-fall and pyroclastic-flow deposits in the Bishop Tuff: inferences from water speciation in quartz-hosted glass inclusions: Bulletin of volcanology, v. 65, no. 2-3, p. 105-123.

Xu, S., and Dunlop, D. J., 1995, Toward a better understanding of the Lowrie-Fuller test: Journal of Geophysical Research: Solid Earth, v. 100, no. B11, p. 22533-22542.

Figure Captions

Figure 1

Regional map showing locations of Tuff of San Felipe outcrops. Black diamonds are samples studied by previous authors. Red squares are samples collected near Cataviña. Green triangles are samples collected on Isla Angel de la Guarda.

Figure 2

Paleomagnetic sample locations on Isla Angel de la Guarda.

Figure 3

Geologic map of the Los Machos area. A key relationship to note is the nature of the contact between the Tuff of San Felipe and lower units. The tuff sits depositionally on the conglomerate but is in possible fault contact with the dacite lavas.

Figure 4

Fault contact, small-scale view. Panel A shows a possibly sheared fine-grained zone between two welded zones of the tuff. Panel B shows an upper welded zone of the tuff in contact with the dacite lavas.

Figure 5

Proposed fault contact, large-scale view. Possible fault trace marked by yellow arrows. Panel A shows the location where the planar structure was originally identified as a cooling feature. Panel B shows the location where the planar feature was first recognized to have motion across it due to the presence of a damage zone and missing stratigraphy. Person is 1.5 meters for scale. The red arrow points to the red to purple change in the welded zone that was used as a datum (4 meters) for stratigraphic height measurements when the base of the tuff was not exposed.

Figure 6

Flinn and Jelinek plots. Panel A is a Flinn plot showing the relationship between the foliation and lineation fabrics. The 1:1 line divides the space into prolate (cigar shaped) and oblate (pancake shaped) domains. Most of the samples have an oblate fabric. Panel B is a Jelinek plot of the shape parameter (T) versus the Jelinek degree of anisotropy (Pj). Most of the samples have a positive shape parameter indicating an oblate fabric. As the samples become more anisotropic the oblate fabric is accentuated.

Figure 7

Specimen density versus mean susceptibility. There is no clear correlation between the specimen density (a proxy for welding) and the mean susceptibility. Compaction welding should increase the quantity of magnetic minerals in a given volume. We see no correlation and conclude that the magnetic minerals must not have been evenly distributed in the original deposit.

Figure 8

AMS flow field. This map shows azimuth of the minimum (blue lines) and maximum (red lines) axes of the AMS ellipsoids of all specimens. The flow azimuth can be interpreted as along the trend defined by the maximum axis K1 (lineation) and in the direction of the trend of the minimum axis K3 (foliation).

Figure 9

Thermal enhancement effects on degree of anisotropy. The degree of anisotropy is increase by the thermal treatments, however, the changes are not uniform across all specimens. Each color represents one core drilled from a single block sample. The square symbol is the specimen heated in a nitrogen atmosphere.

Figure 10

Thermal enhancement of the K1 declination. The thermal treatments produce a clockwise rotation of the maximum axis. The thermal treatments fail to reduce the spread in declination, in fact, the dispersion increases. Each color represents one core drilled from a single block sample. The square symbol is the specimen heated in a nitrogen atmosphere.

Figure 11

Thermal enhancement of bulk susceptibility. The bulk susceptibility shows a varied response to the treatments. We can see a frequency dependence indicating superparamagnetic grains. The duplicated measurements agree very well giving us confidence that the changes we are seeing are not instrument noise. Low-temperature cycling produces an increase in bulk susceptibility. The bulk susceptibility drops off once the specimen is heated past the Curie temperature of magnetite. Each color represents one core drilled from a single block sample. The square symbol is the specimen heated in a nitrogen atmosphere.

Figure 12

Fisher means of AF and thermal demagnetization. A lower hemisphere equal-area stereonet plot of the characteristic remanent magnetization of split samples determined by thermal demagnetization (red squares) and AF demagnetization (blue circles). The Fisher mean of each dataset is marked with a blue star (AF) or a red star (thermal).

Figure 13

Orthographic demagnetization plots. A sample of representative demagnetization diagrams. While the thermal demagnetization diagrams are noisier than the AF, both head towards the origin and produce excellent fits.

Figure 14

Thermal J/Jo. Magnetization relative to the NRM as a function of thermal cleaning temperature. Most of the specimens demagnetize in the range of 585°C, the Curie temperature of magnetite. Demagnetization at lower temperatures indicates an increasing titanium content.

Figure 15

AF J/Jo. Magnetization relative to NRM as a function of the AF demagnetizing field. Most samples have demagnetized by 40 mT, indicating magnetite. A few samples contain a hematite component and do not demagnetize fully even at 90 mT.

Figure 16

Lowrie-Fuller test. Figure A shows an exponential curve indicating a multidomain response yet the median destructive field (MDF) of ARM is higher than the MDF of IRM indicating a single-domain response. Figure B shows an s-shaped curve indicating single-domain particles and the MDF of IRM is higher than the MDF of ARM, indicating multi-domain particles. These plots confirm the pseudo-single-domain nature of our samples.

Figure 17

IRM crossover. This plot shows the acquisition and AF demagnetization of an IRM. The fact that the point where the two curves cross deviates from half of the SIRM indicates that there are interactions between the magnetic particles.

Figure 18

Backfield IRM. The point where the backfield IRM crosses the x-axis indicates the coercivity. In this case a value of 30 mT is indicative of magnetite. The magnetization level where the curves turn horizontal can also determine the SIRM.

Figure 19

Two representative plots of the thermal variation of susceptibility. Red lines indicate susceptibility measured on warming, blue lines are susceptibility measured on cooling. The Verwey transition at -153°C and a Hopkinson peak at 585°C indicate magnetite.

Figure 20

Abnormal thermal variation of susceptibility. One of a few specimens that show the creation of two separate phases upon cooling. Two possible explanations for this pattern are the oxidation of magnetite to maghemite due to insufficient argon flow or the exsolution of titanomagnetite.

Figure 21

Paleotemperature estimates. Panel A shows the raw progressive heating and cooling curves. Panel B shows the susceptibility at 40°C measured on the heating (red star) and cooling curve (blue circle) of each temperature cycle. Panel C shows the A40 index, the difference between the heating and cooling susceptibility measured at 40°C. A large increase in the A40 index indicates that the sample has been heated beyond temperatures that it experienced in-situ.

Figure 22

Day plot. The day plot can be used to determine the grain size based on the ratio of hysteresis parameters. The different boundaries correspond to those determined by Day (thin lines) and Dunlop (thick lines). All of the specimens plot in the pseudo-single-domain range.

Figure 23

Hysteresis loops. Two examples of representative hysteresis loops. The red lines are the raw measurements of moment. The blue lines are corrected for the paramagnetic slope at high fields. There is a large difference in the paramagnetic component in these two samples, which could provide an explanation for the scatter in the AMS data.

Figure 24

Magnetization as a function of temperature. Panel A shows a cooling curve above the heating curve. Panel B shows a cooling curve below the heating curve, in addition to changes in magnetization at 950 K.

Figure 25

Frequency dependent susceptibility. This plot shows a clear decrease in the susceptibility with increasing frequency of the applied field. This is a clear indication of superparamagnetic grains.

Figure 26

Low-temperature magnetization cycling. The left column shows the magnetization as a function of temperature for both a room temperature SIRM on cooling (black squares) and a low-temperature SIRM on warming (red squares). The right column shows the derivative of the magnetization, which emphasizes the changes in slope around the Verwey transition.

Figure 27

Susceptibility as a function of temperature and frequency. The in-phase component shows a peak at the magnetite Verwey transition. The out-of-phase component of susceptibility has a peak at 50K, diagnostic of magnetite.

Figure 28

Forc Diagrams. A representative sampling of FORC distribution diagrams showing the multidomain and pseudo-single-domain nature of the sasmples.

Figure 29

AARM. Flinn and Jelinek plots show the shape and degree of anisotropy of the samples. A lower-hemishpere equal area stereonet shows the K1 (red) and K3 (blue) axes of the AARM ellipsoid. The rose diagram shows the azimuthal distribution of the K1 (red) and K3 (blue) axes. The inclination of the K3 axes indicated flow to the northeast.

Figure 30

ChRM rotation. Maps showing the mean characteristic remanent magnetization declination (white arrow) for all specimens relative to the reference site declination (black arrow). The red arrows indicate the¸ 95 confidence limits on the mean direction. The amount of rotation across the island is highly variable.

Figure 31

Tectonic correction of flow directions. The K1 and K3 declinations of the AMS ellipsoid are rotated by the angle between the TSF reference declination and the ChRM of the specimen. The tectonic correction does not reduce the scatter.

Figure 32

Tectonic correction of foliation. This map shows the vertical-axis rotation correction applied to K3 relative to the uncorrected K3. The correction does not reduce the scatter in the directions at individual sites.

Figure 33

Tectonic correction for all sites. Lower-hemisphere equal-area stereonets showing the ChRM vectors and the AMS axes for all sites. A red symbol indicates a point on the upper hemisphere. Rose diagrams showing the azimuthal distribution of the ChRM and the AMS principal axes. We can see that the tectonic vertical-axis rotation correction does not remove all of the scatter in the AMS directions,

Figure 34

Stratigraphic ChRM rotation. This plot shows the ChRM of all specimens relative to their stratigraphic height. There is a clear clockwise rotation of the ChRM with increasing stratigraphic height in some locations. The colored symbols represent the six sites on the little mesa. The black symbols are all other sites on the island. Site 2 (yellow) samples the greatest stratigraphic range and clearly shows a statistically significant change in mean direction.

Figure 35

AMS lineation versus ChRM declination. Theory predicts that a magnetite CRM will produce an AMS fabric with the maximum axis aligned with the applied field at the time of formation. Our data from site 2 does not fall on the 1:1 line and implies that we have not measured a CRM.

Figure 36

A Fuller plot showing the relationship between the ARM (red circles), NRM (blue squares), and IRM coercivity spectra. TRMs have been shown to plot along the 1:100 line. One of our samples has an elevated NRM moment but matches the other samples in ARM space, most likely due to an IRM overprint from lightning.

Figure 37

Faulted stratigraphic ChRM rotation. This plot shows the lack of rotation of the ChRM across a known (blue) and inferred (red) fault cutting through the tuff.

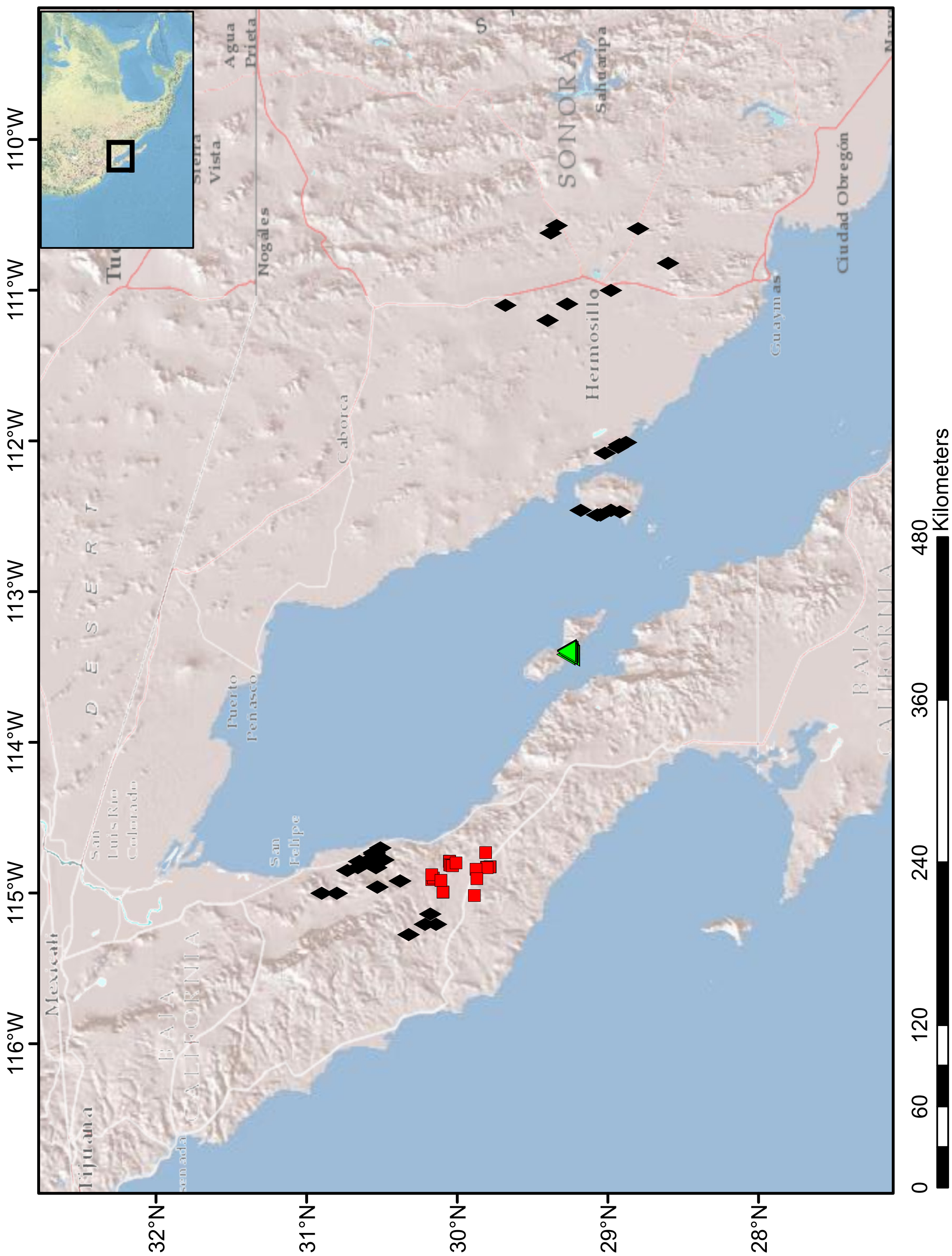

Figure 1. Tuff of San Felipe outcrops

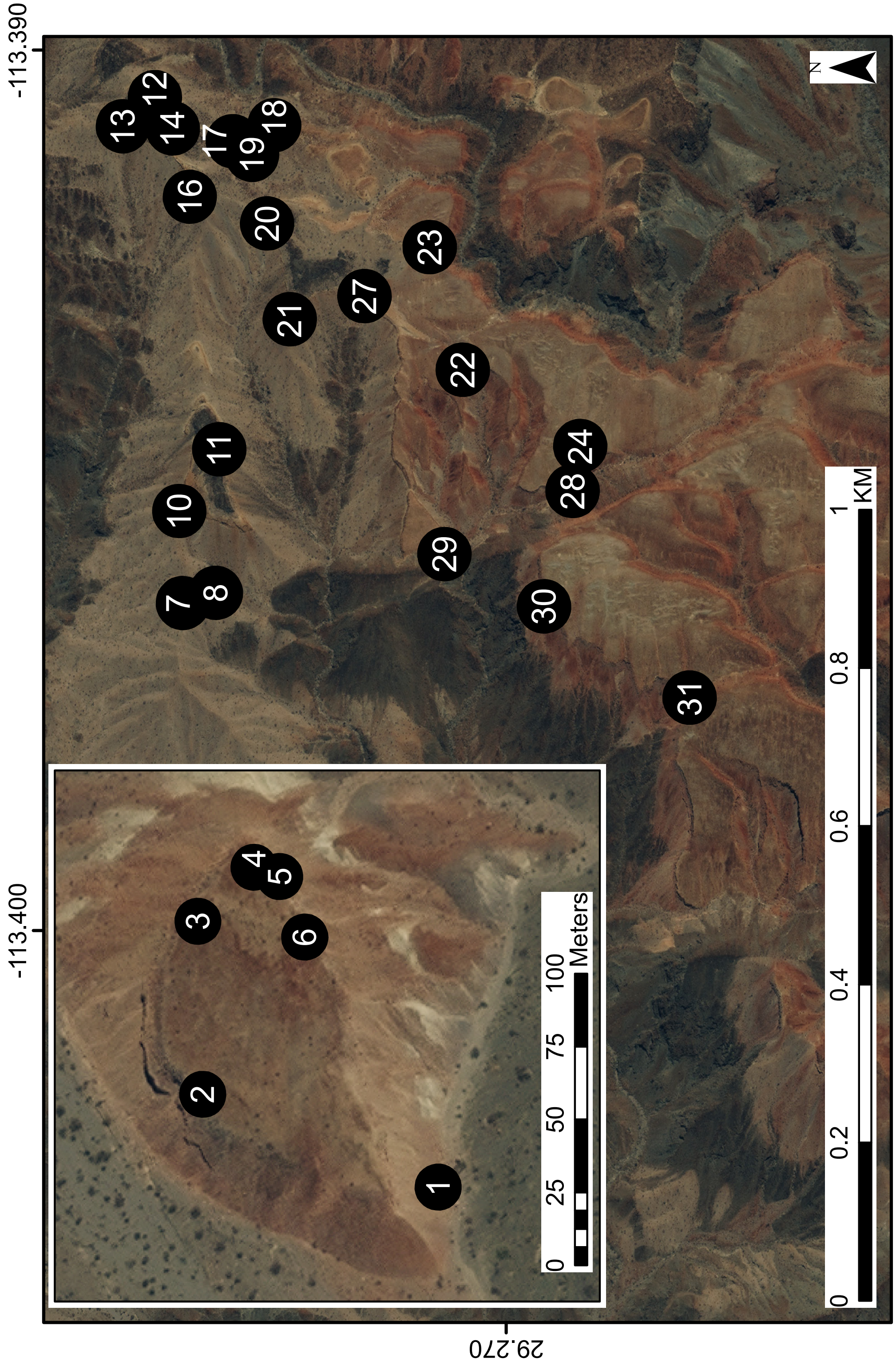

Figure 2. Paleomagnetic sampling sites

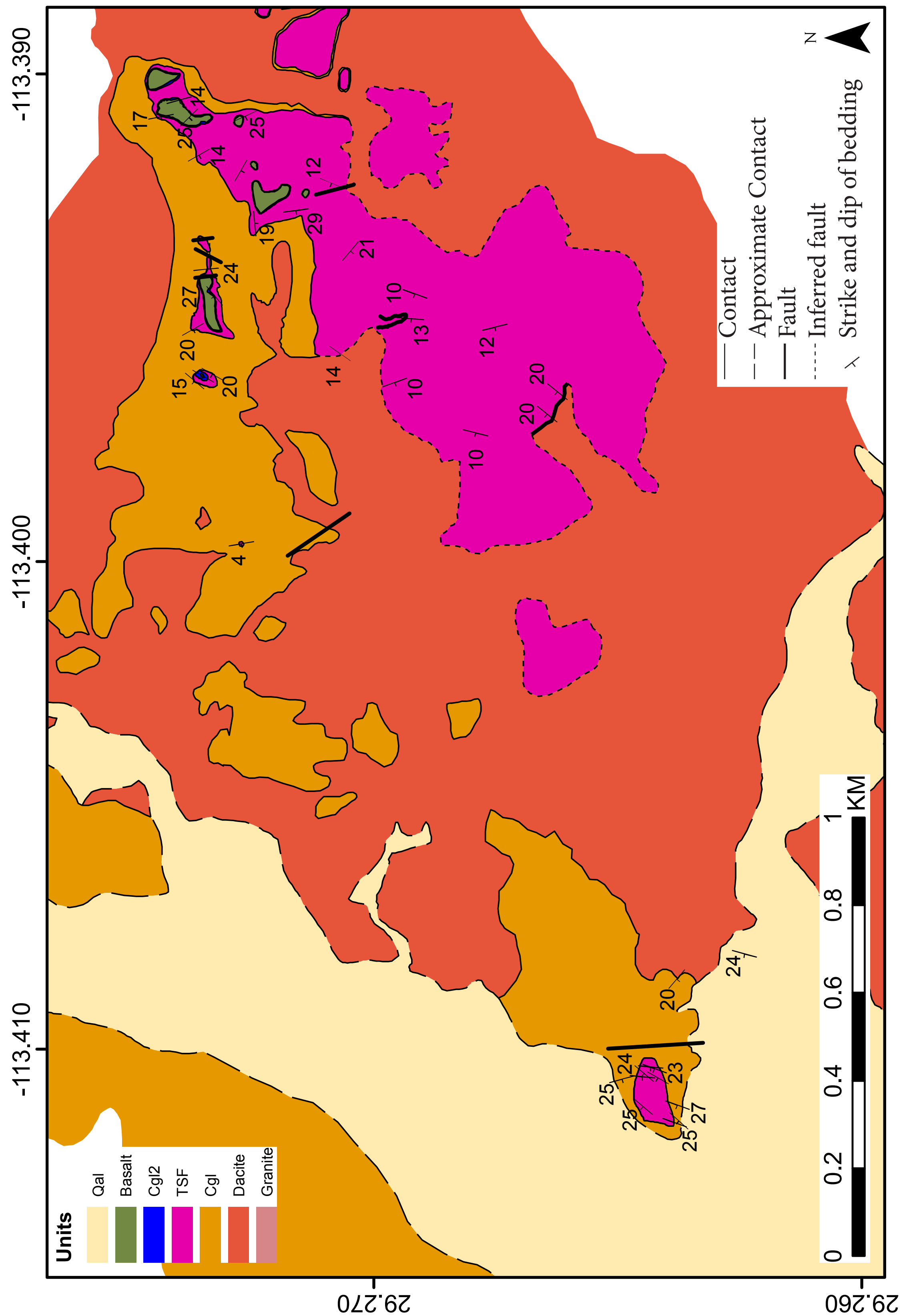

Figure 3. Geologic map

Figure 4. Close-up of fault contacts

Figure 5. Outcrop scale fault contacts

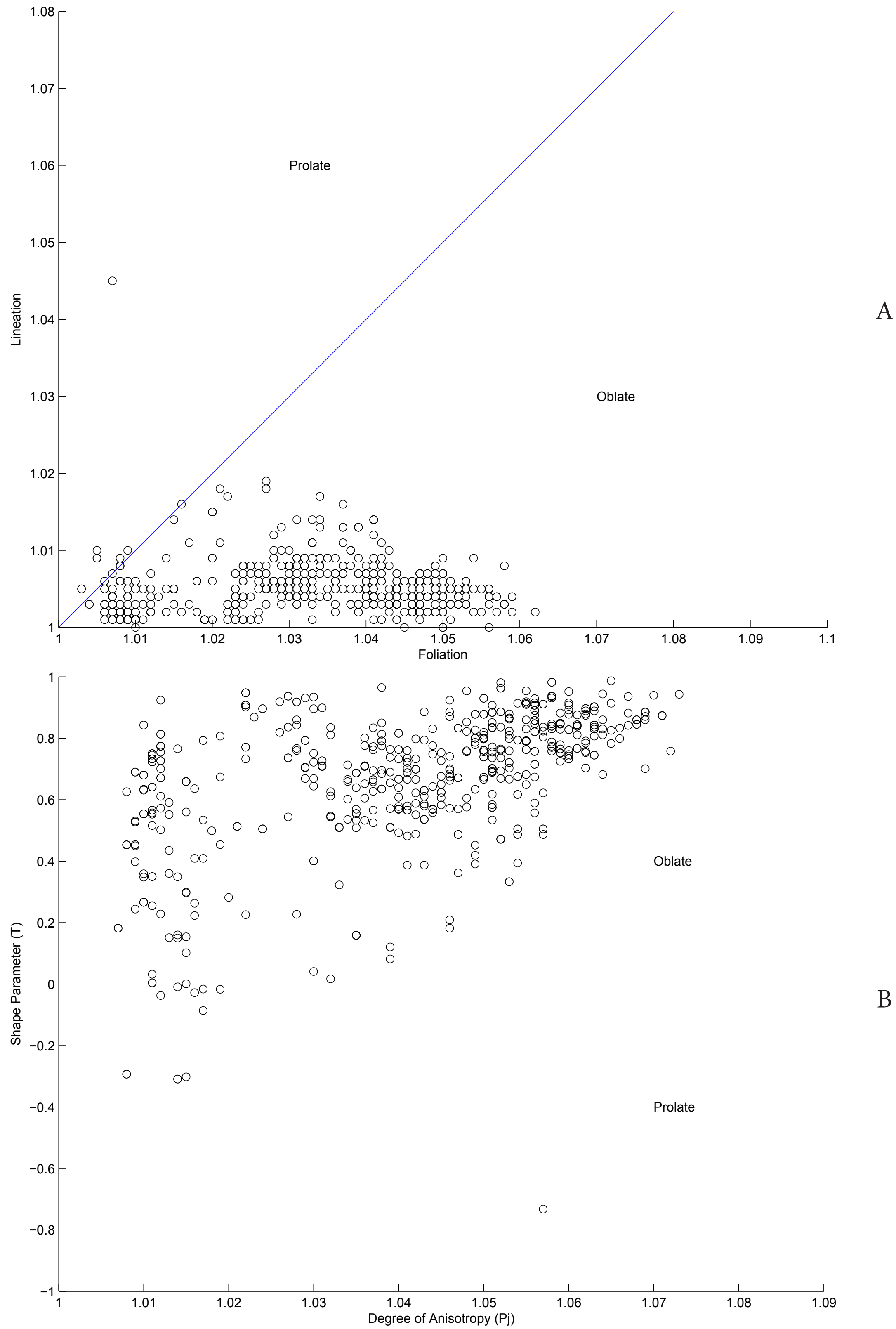

Figure 6. Anisotropy parameters

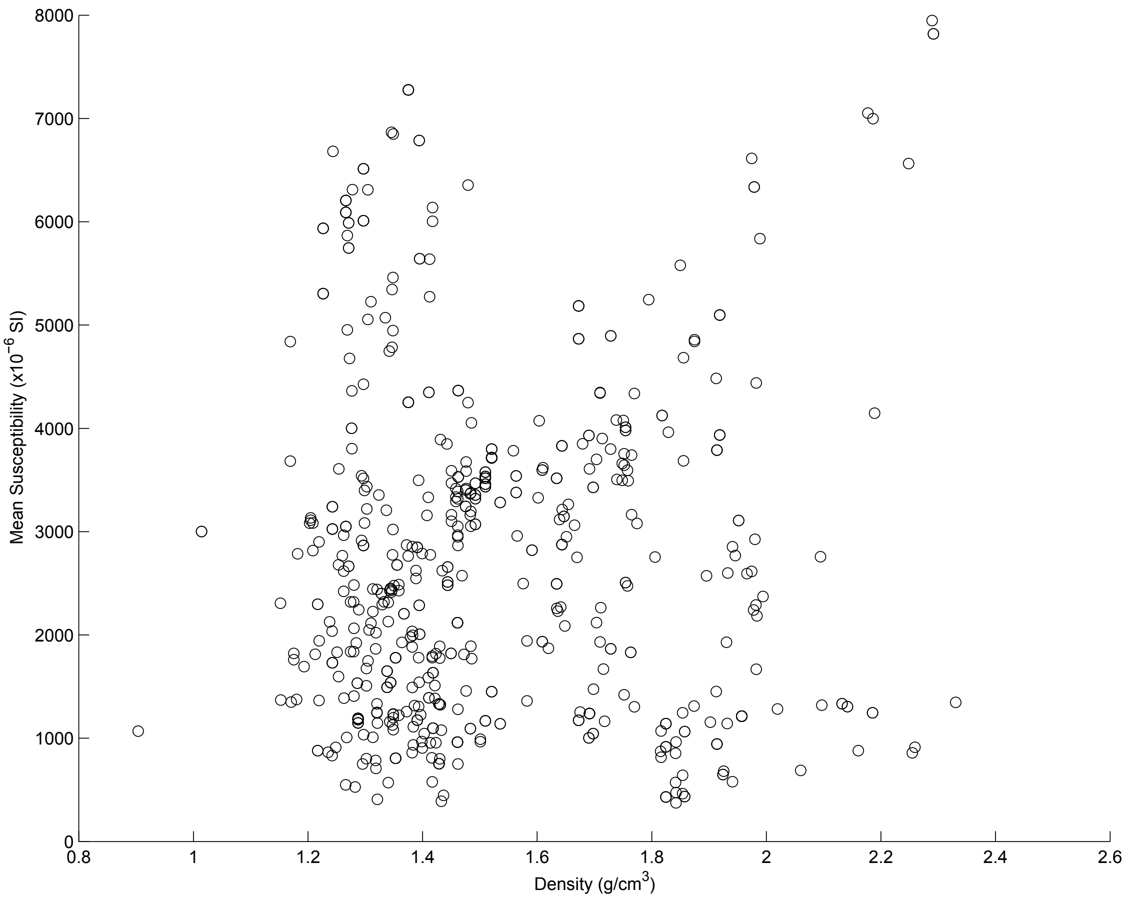

Figure 7. Sample density vs mean susceptibility

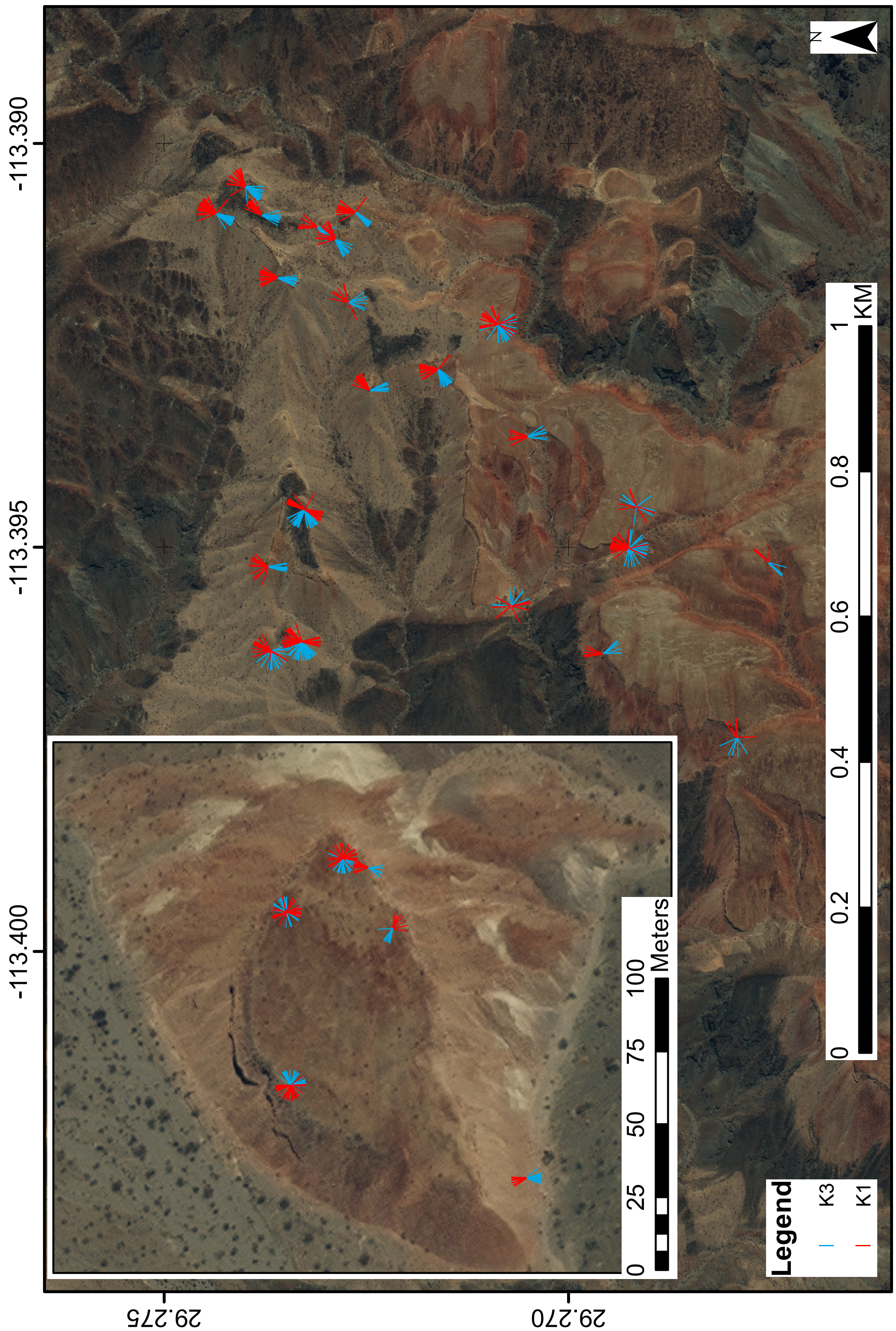

Figure 8. AMS flow field

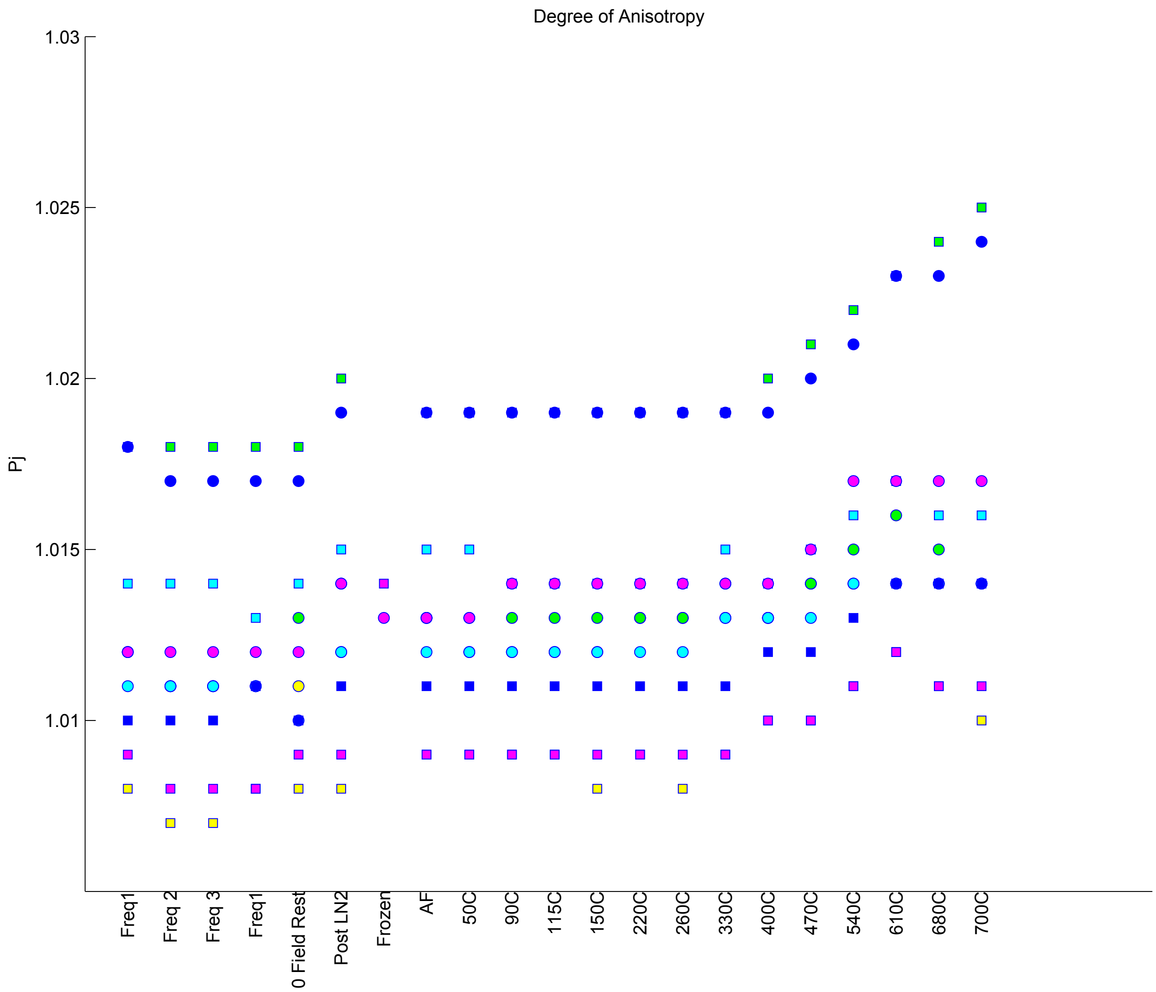

Figure 9. Thermal enhancement effects on degree of anisotropy

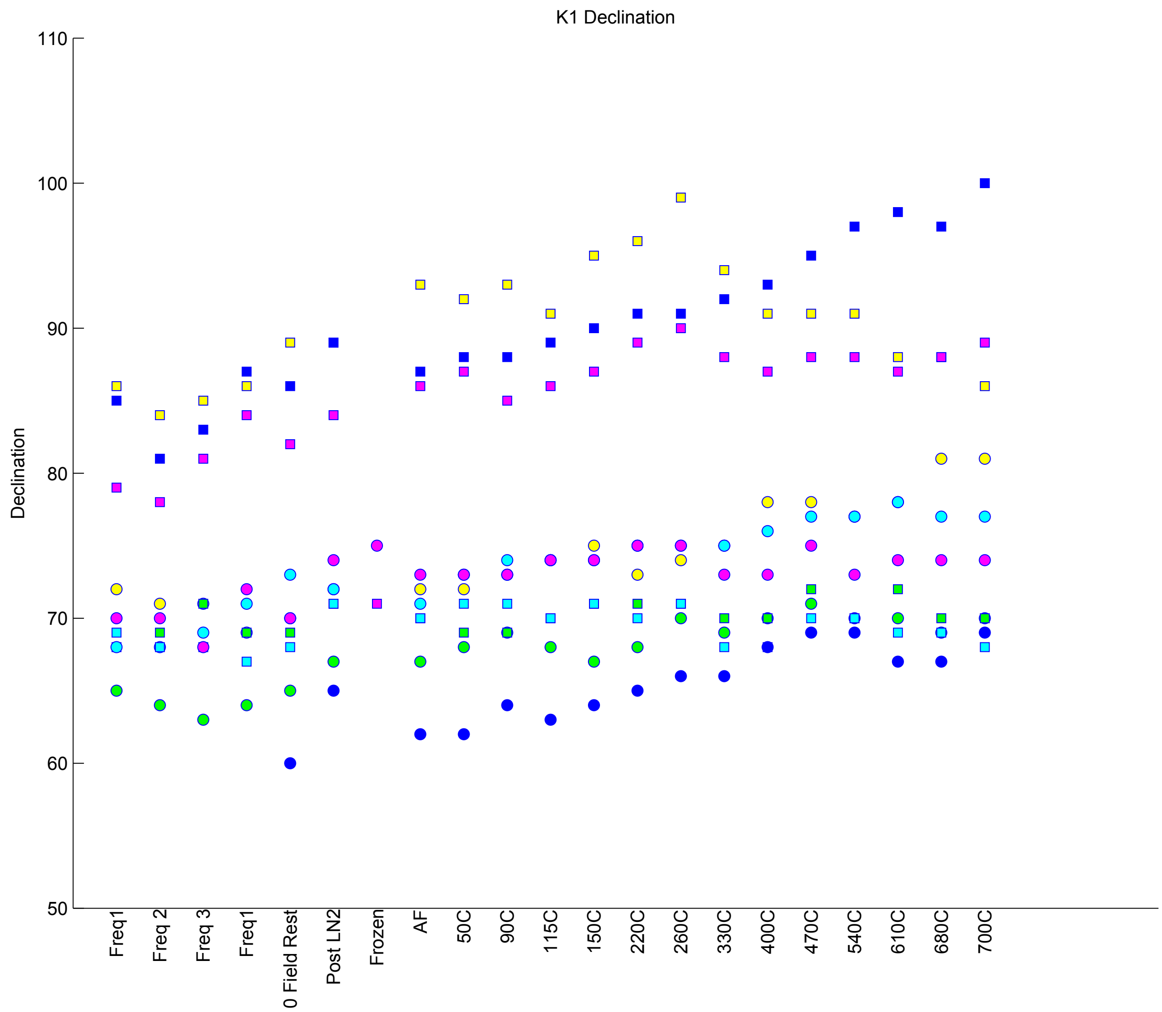

Figure 10. Thermal enhancement of the K1 declination

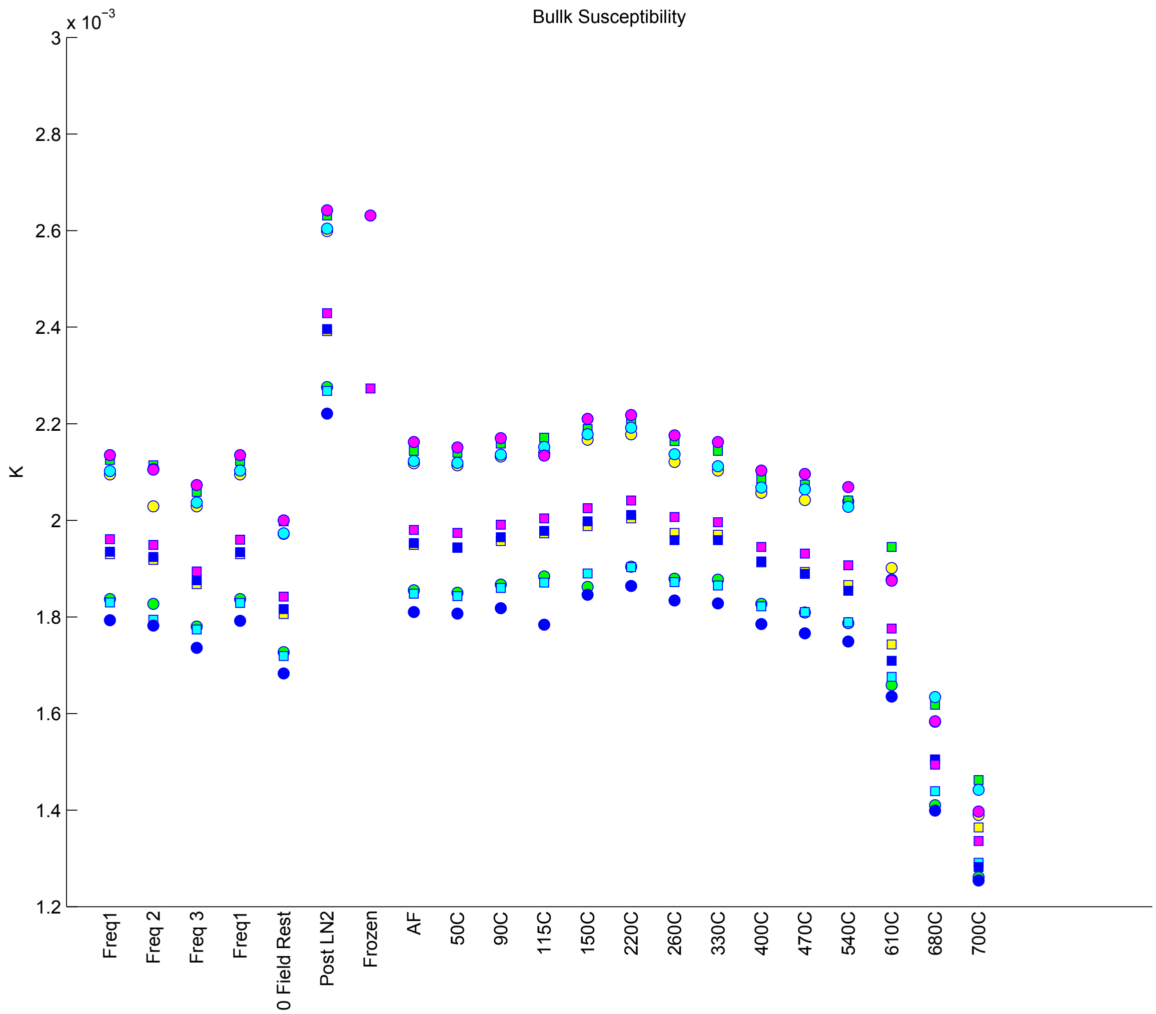

Figure 11. Thermal enhancement of bulk susceptibility

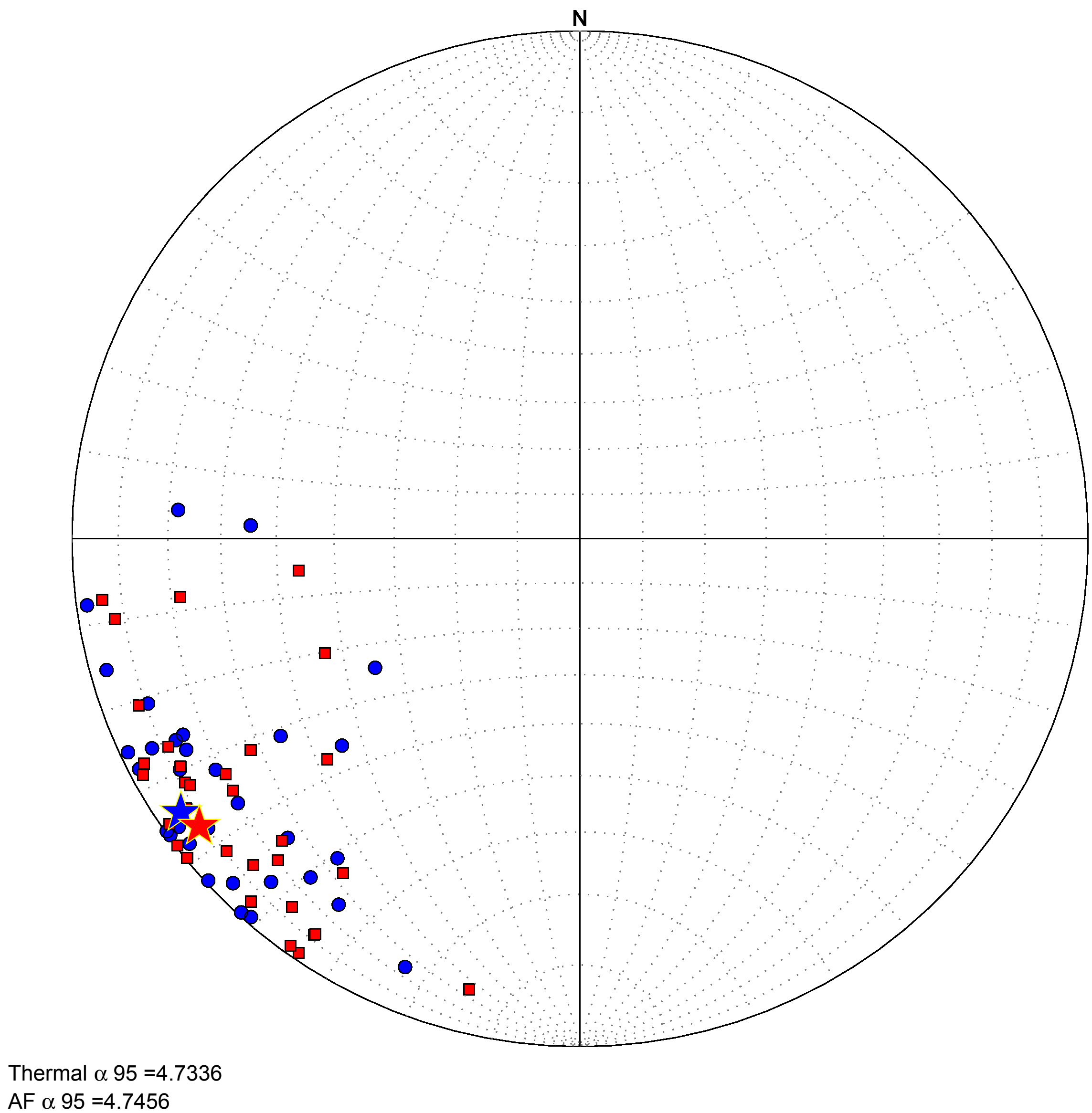

Figure 12. Fisher means of AF and thermal demagnetization

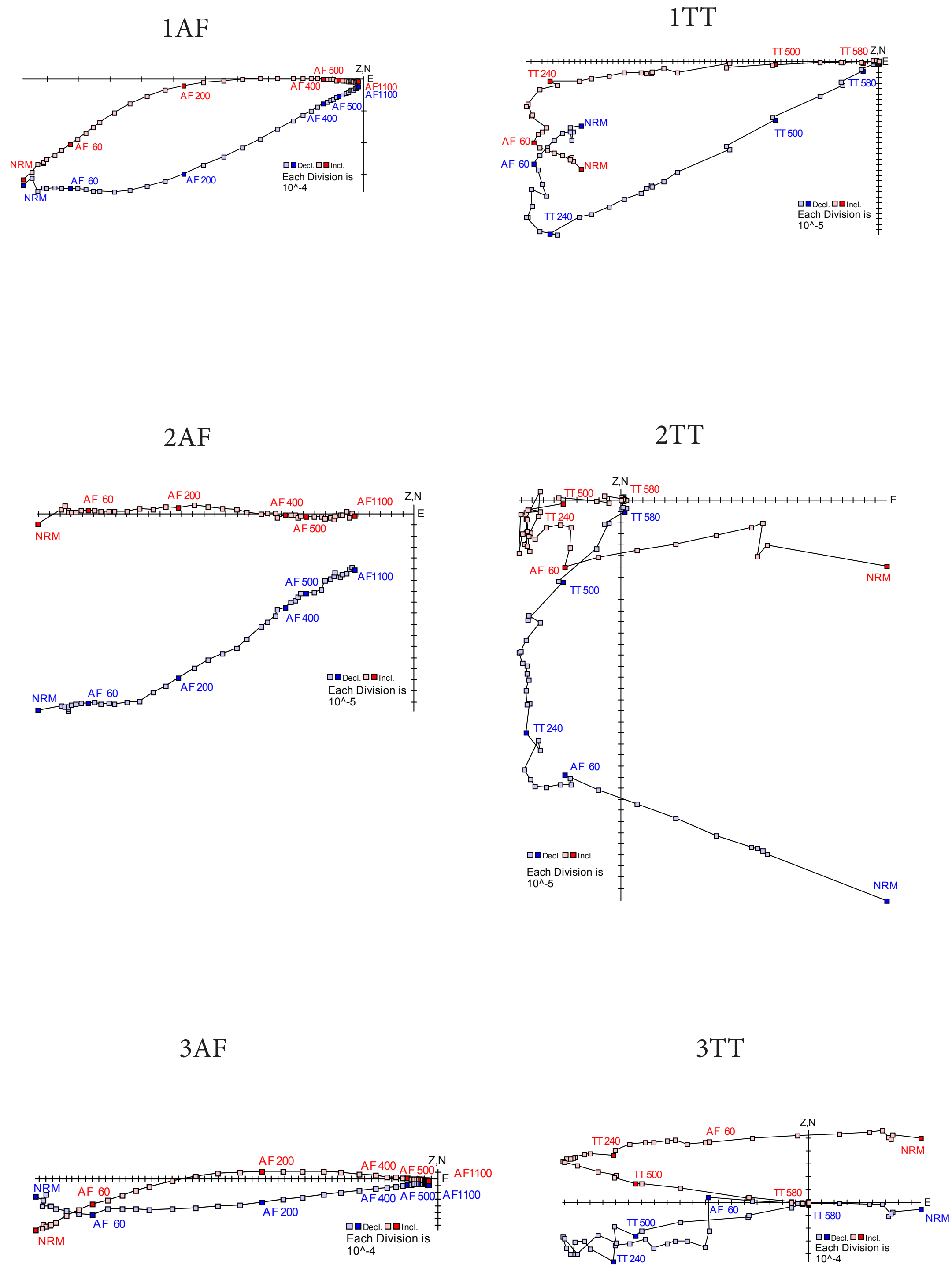

Figure 13. Orthographic demagnetization plots.

4AF

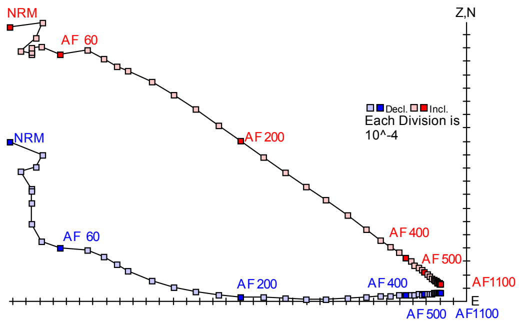

4TT

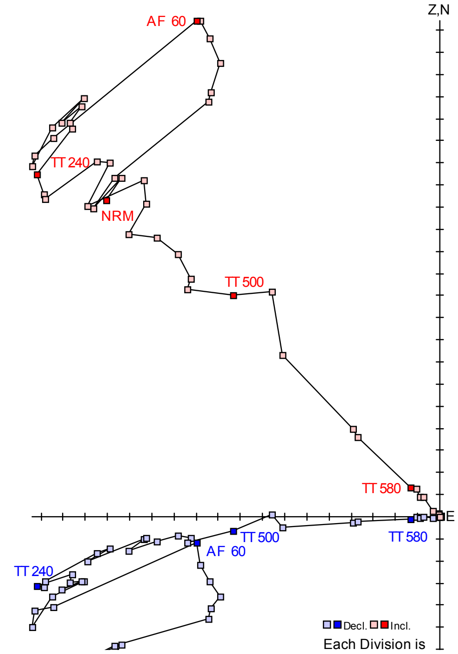

5AF

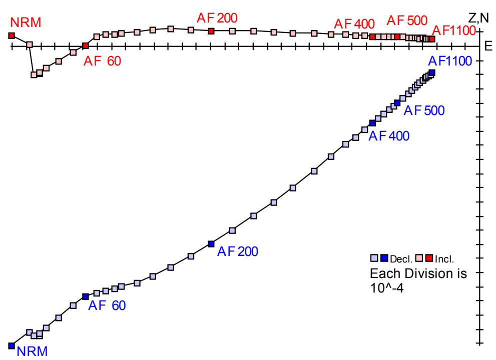

5TT

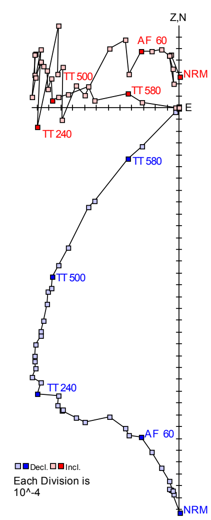

6AF

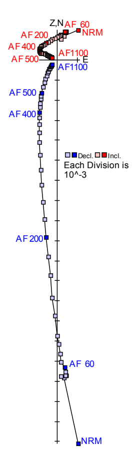

6TT

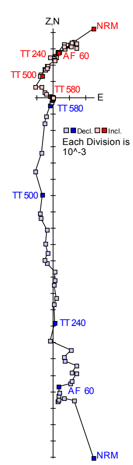

Orthographic demagnetization plots (continued)

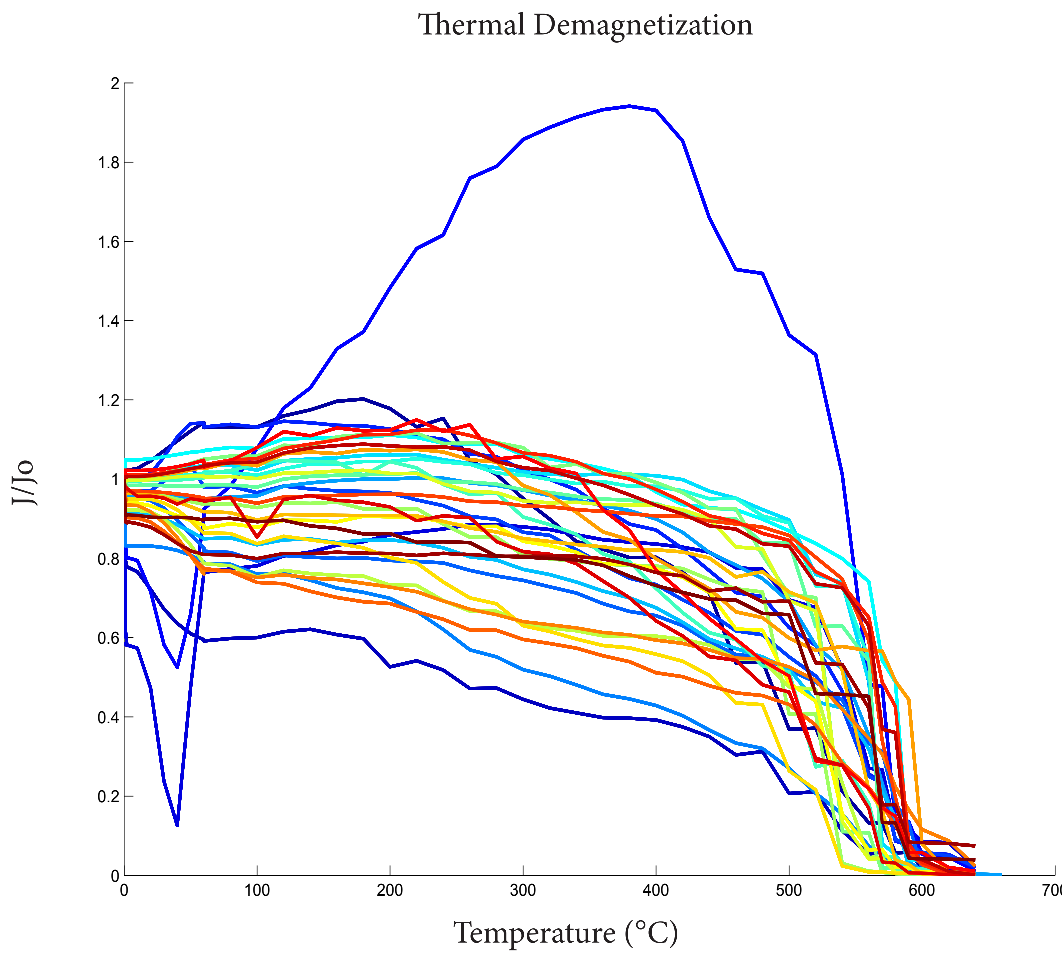

Figure 14. Thermal J/Jo

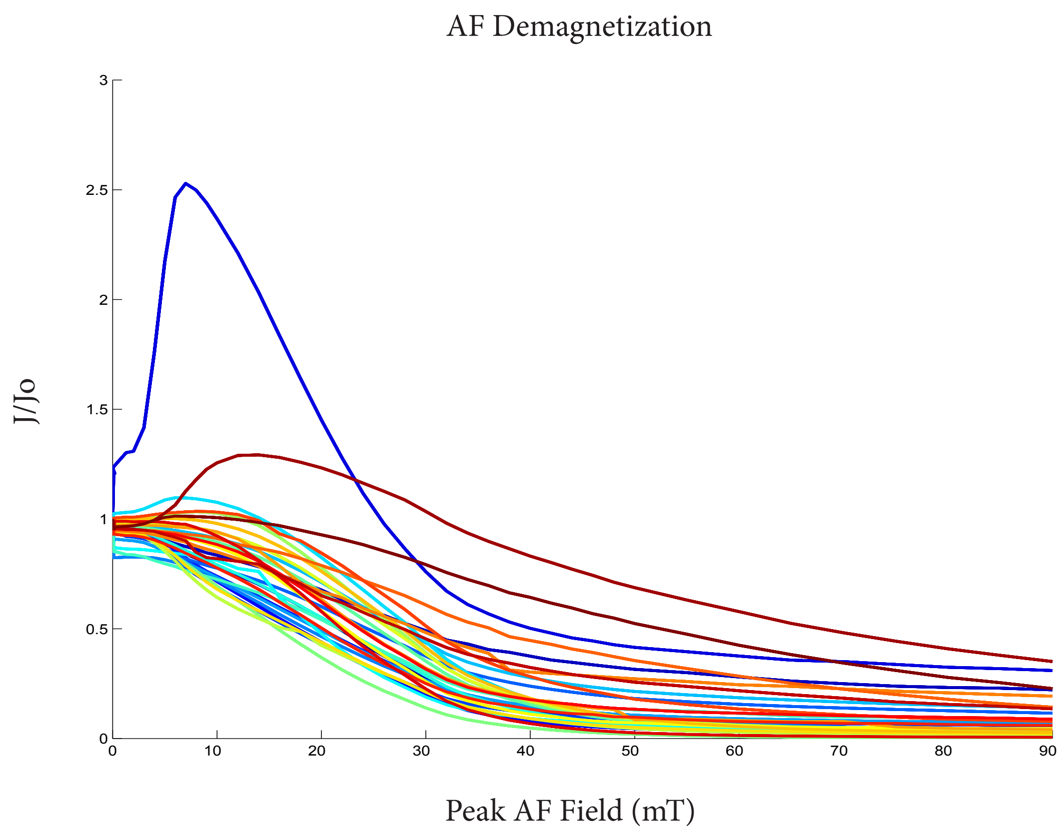

Figure 15. AF J/Jo

A

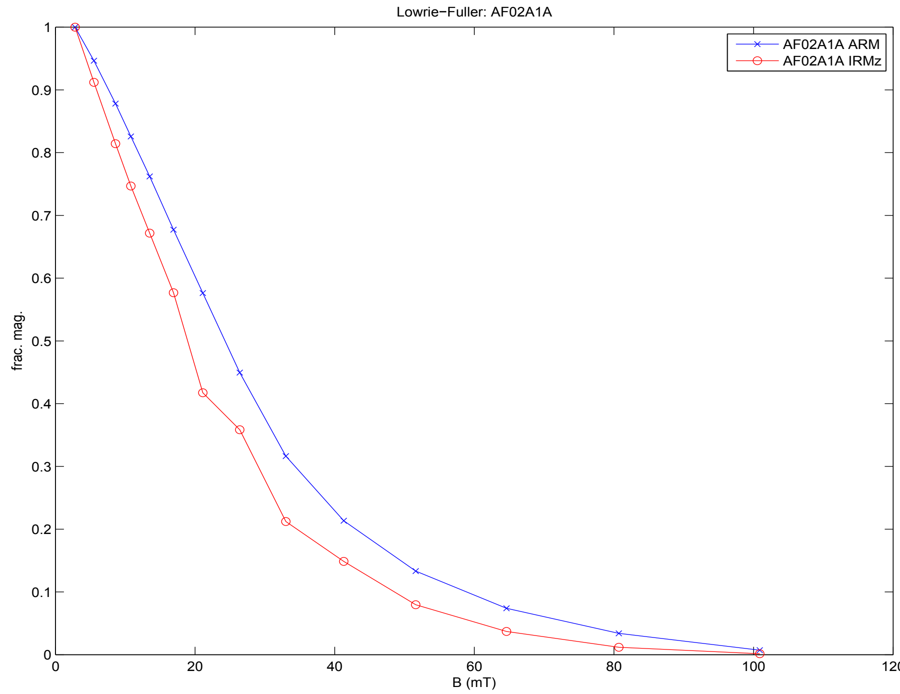

B

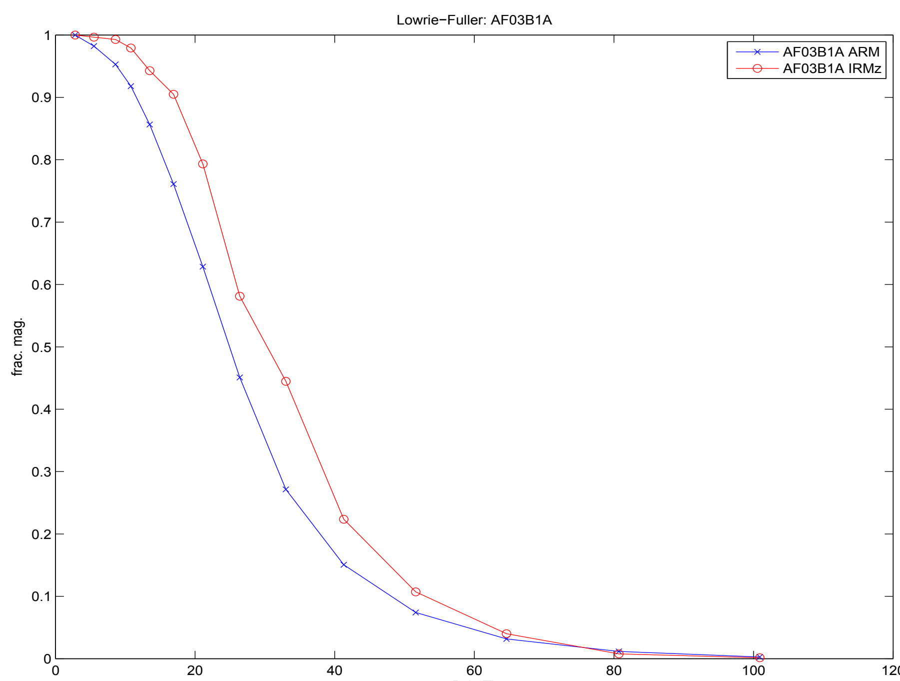

Figure 16. Lowrie-Fuller test

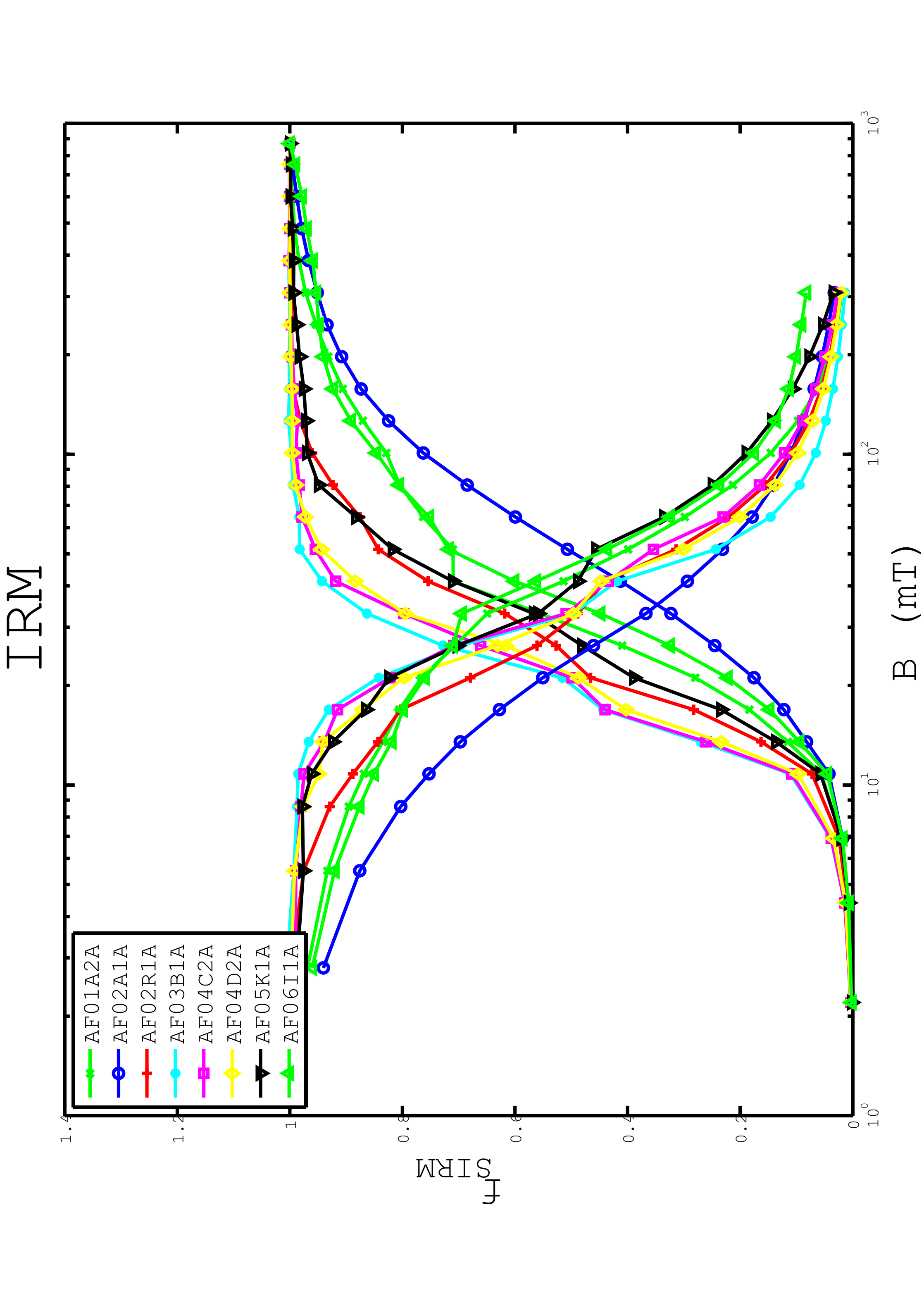

Figure 17. IRM crossover

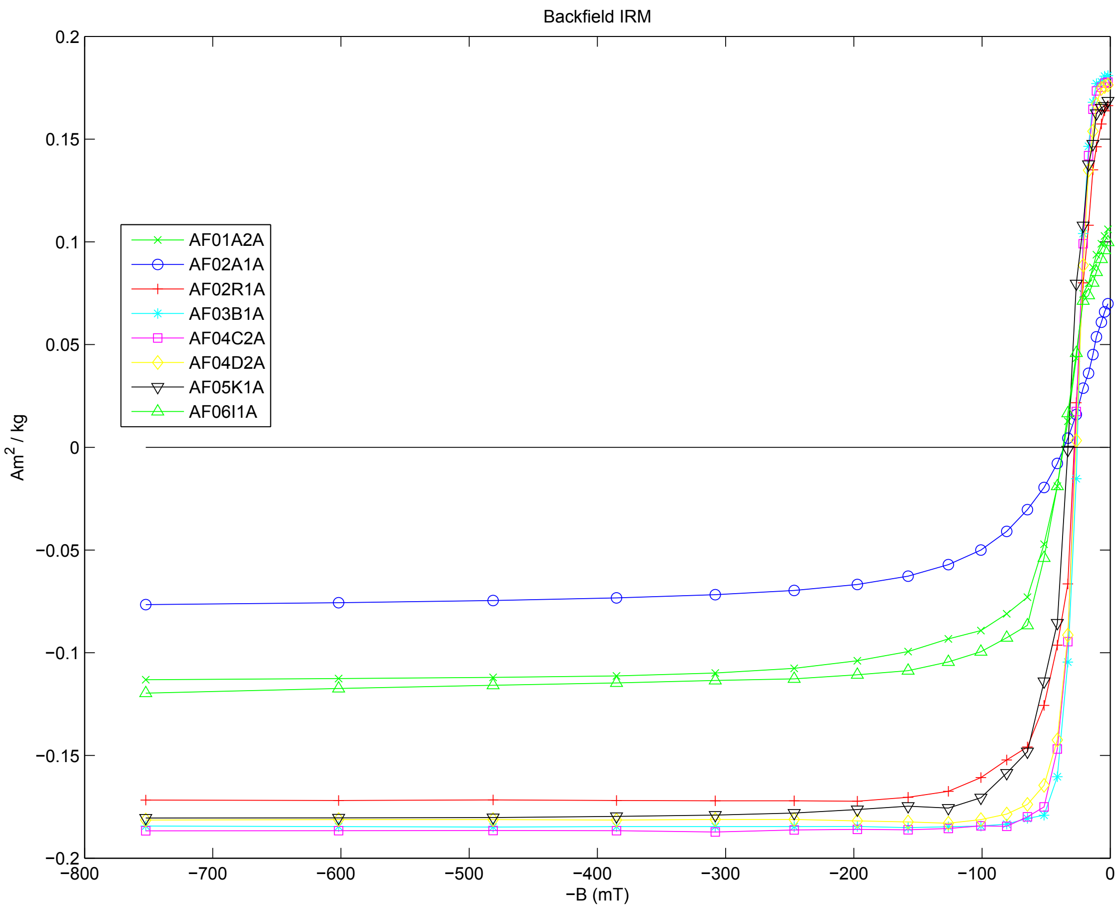

Figure 18. Backfield IRM

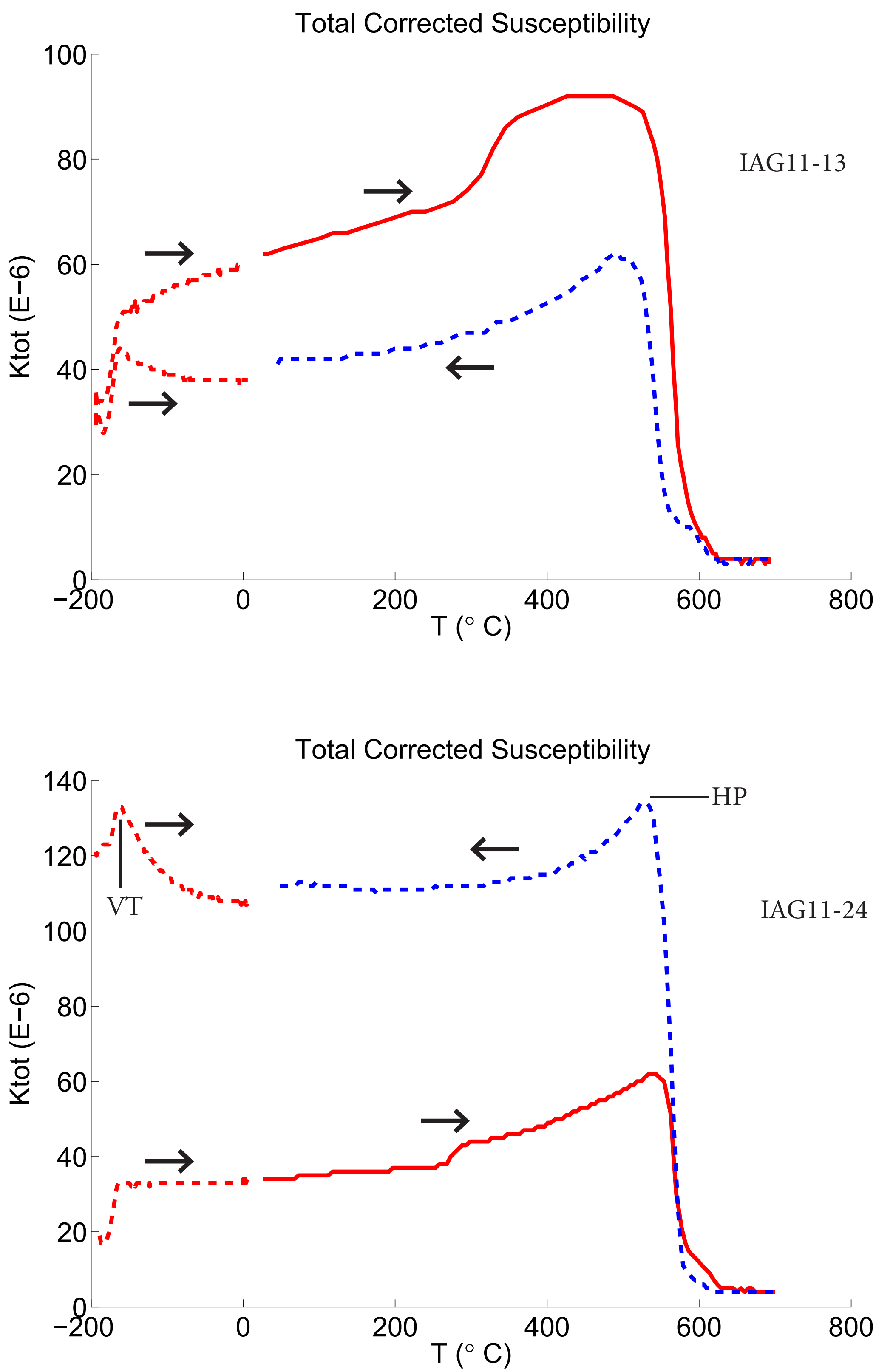

Figure 19. Representative thermal variation of susceptibility

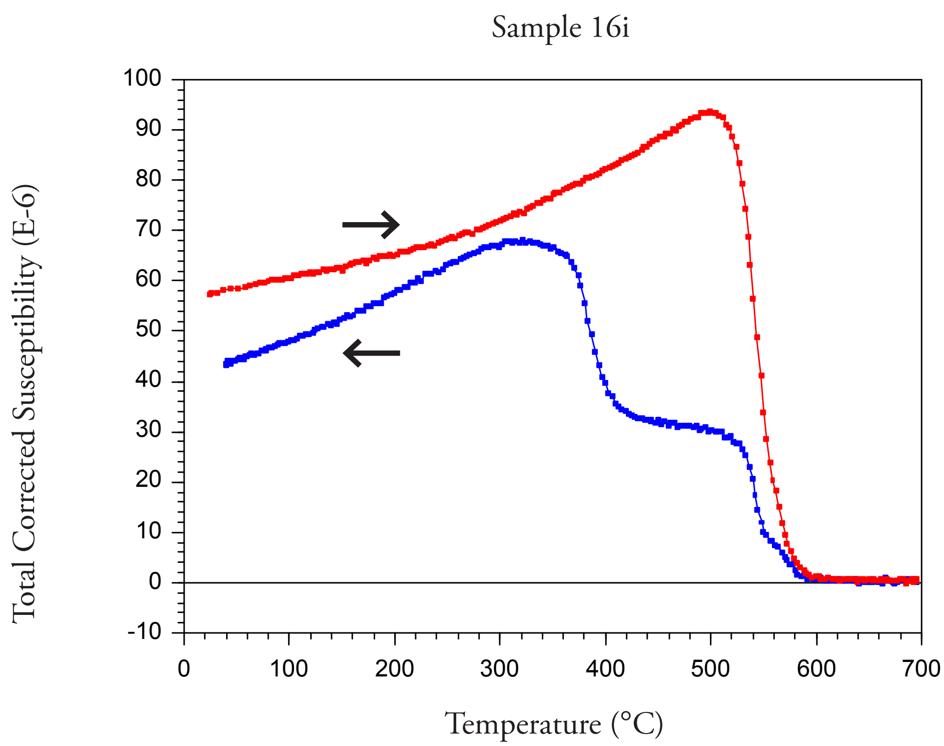

Figure 20. Abnormal thermal variation of susceptibility

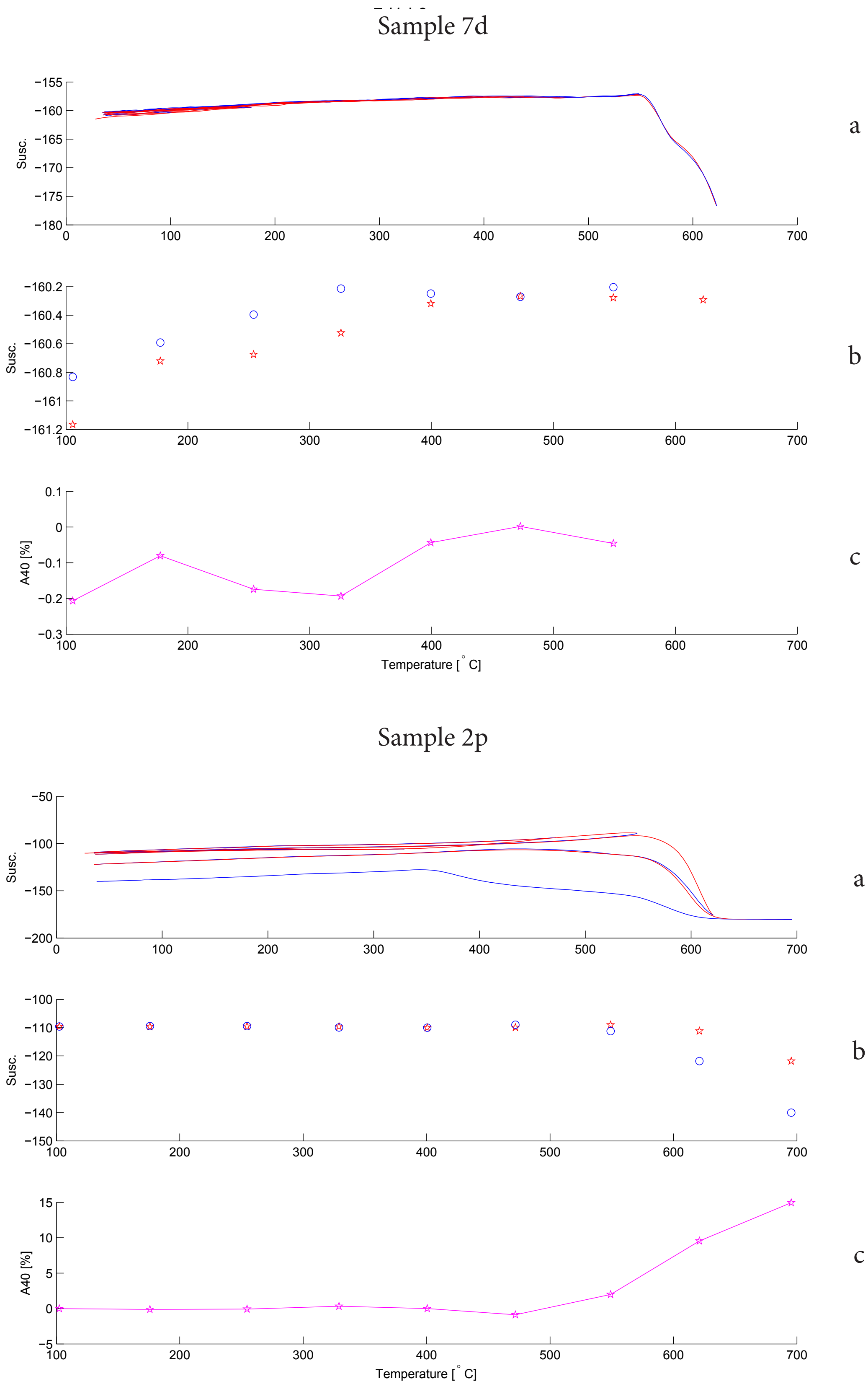

Figure 21. Paleotemperature estimates

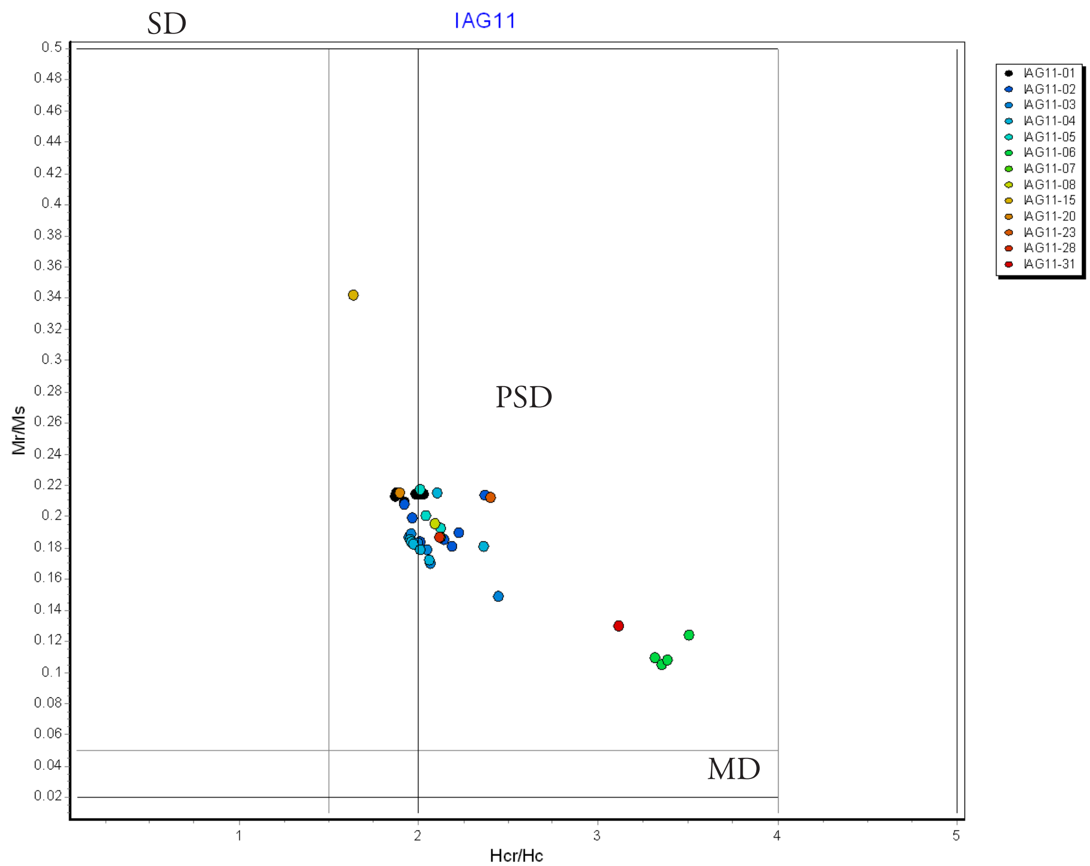

Figure 22. Day plot

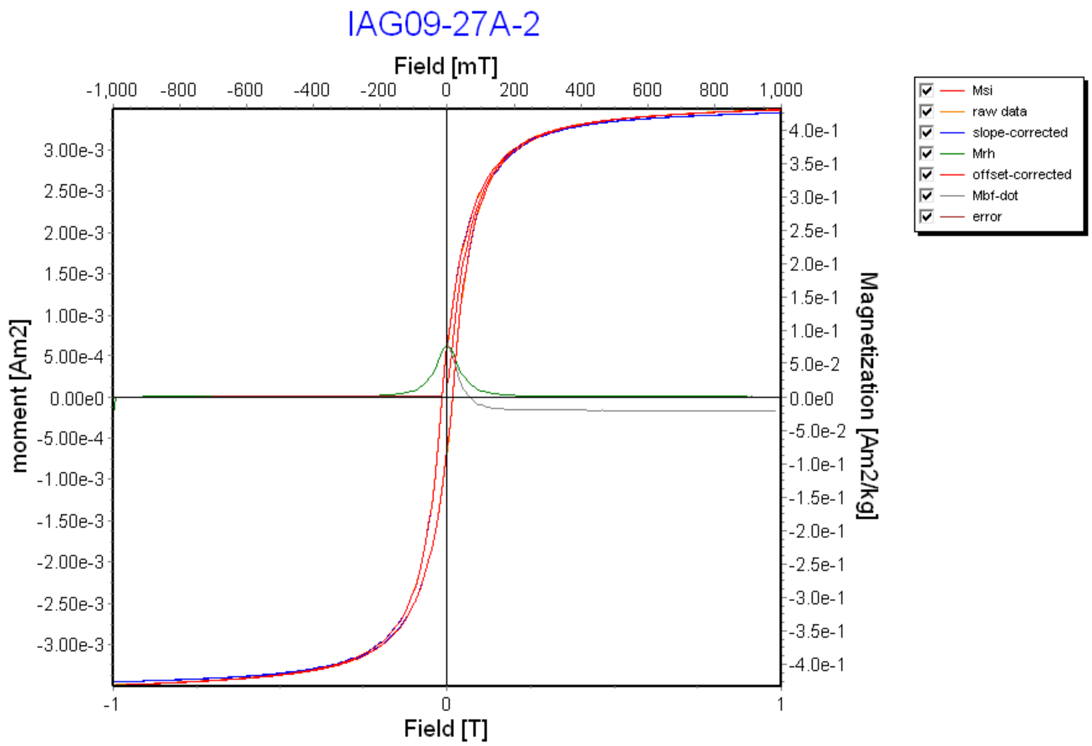

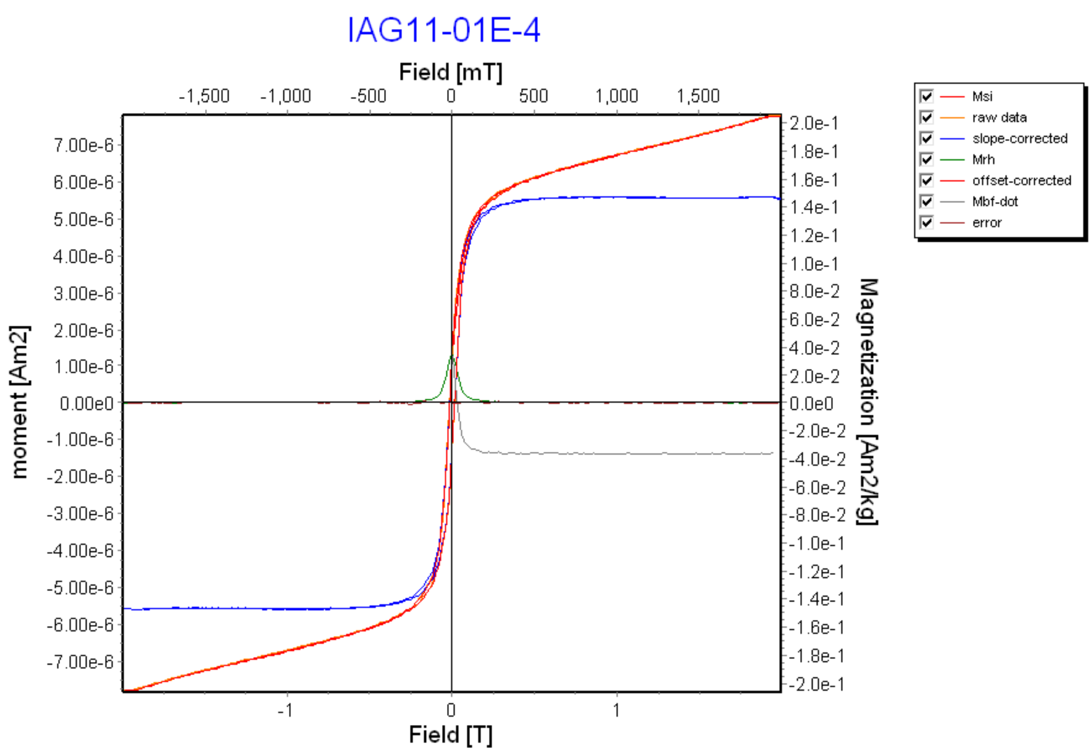

Figure 23. Hysteresis loops

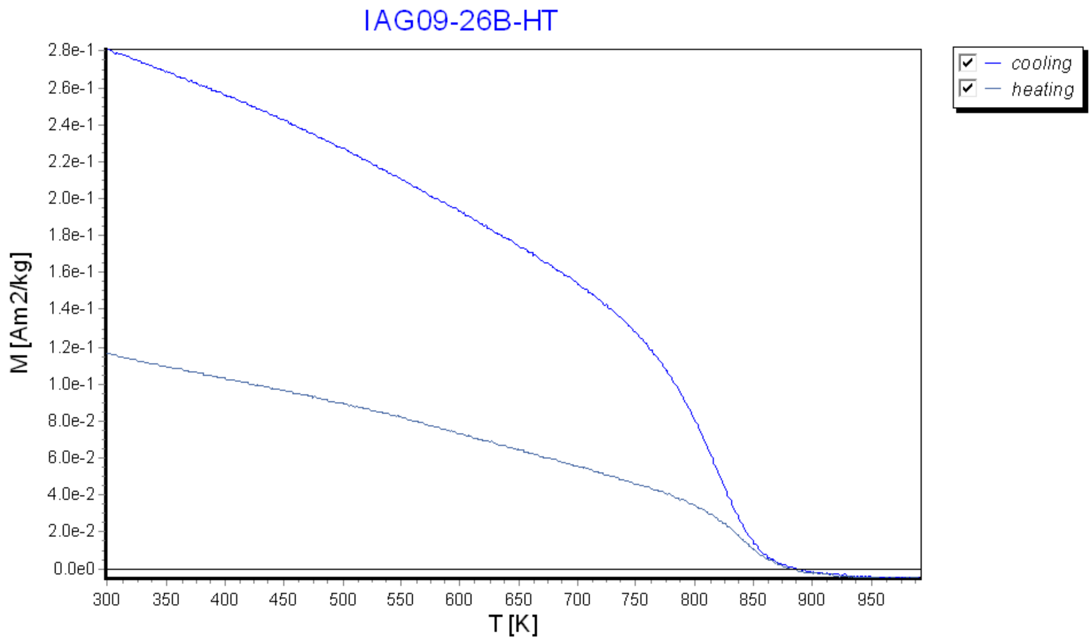

A

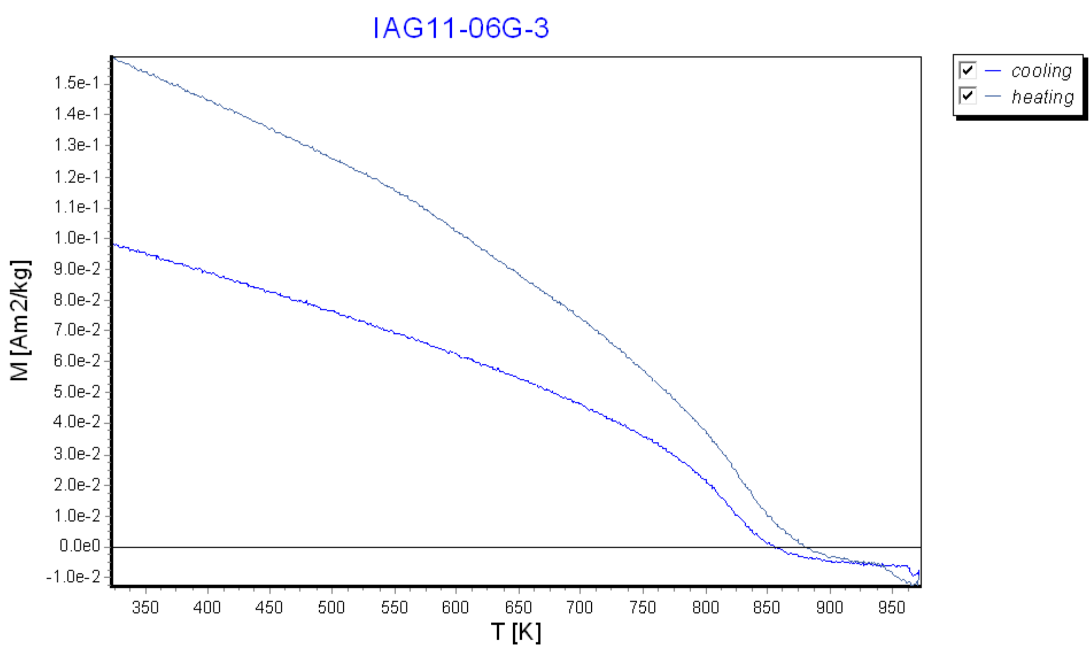

B

Figure 24. Magnetization as a function of temperature

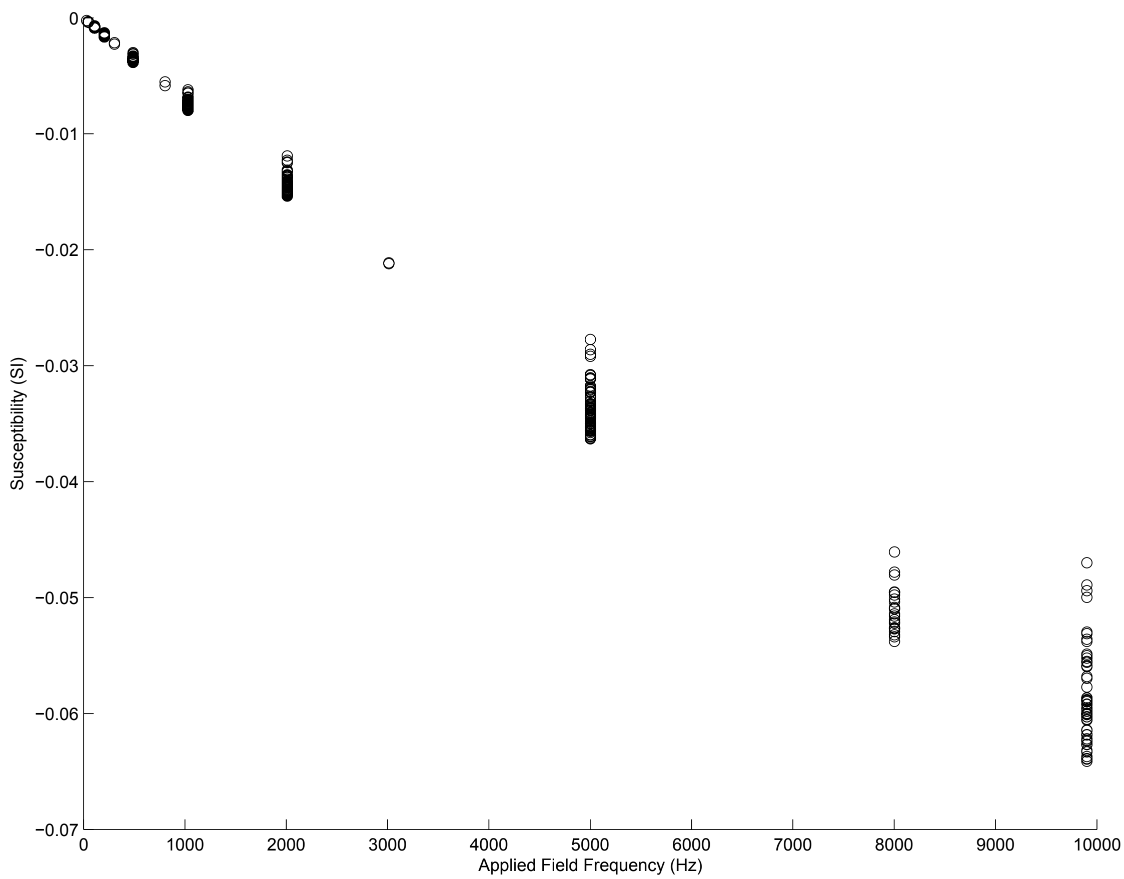

Figure 25. Frequency dependent susceptibility

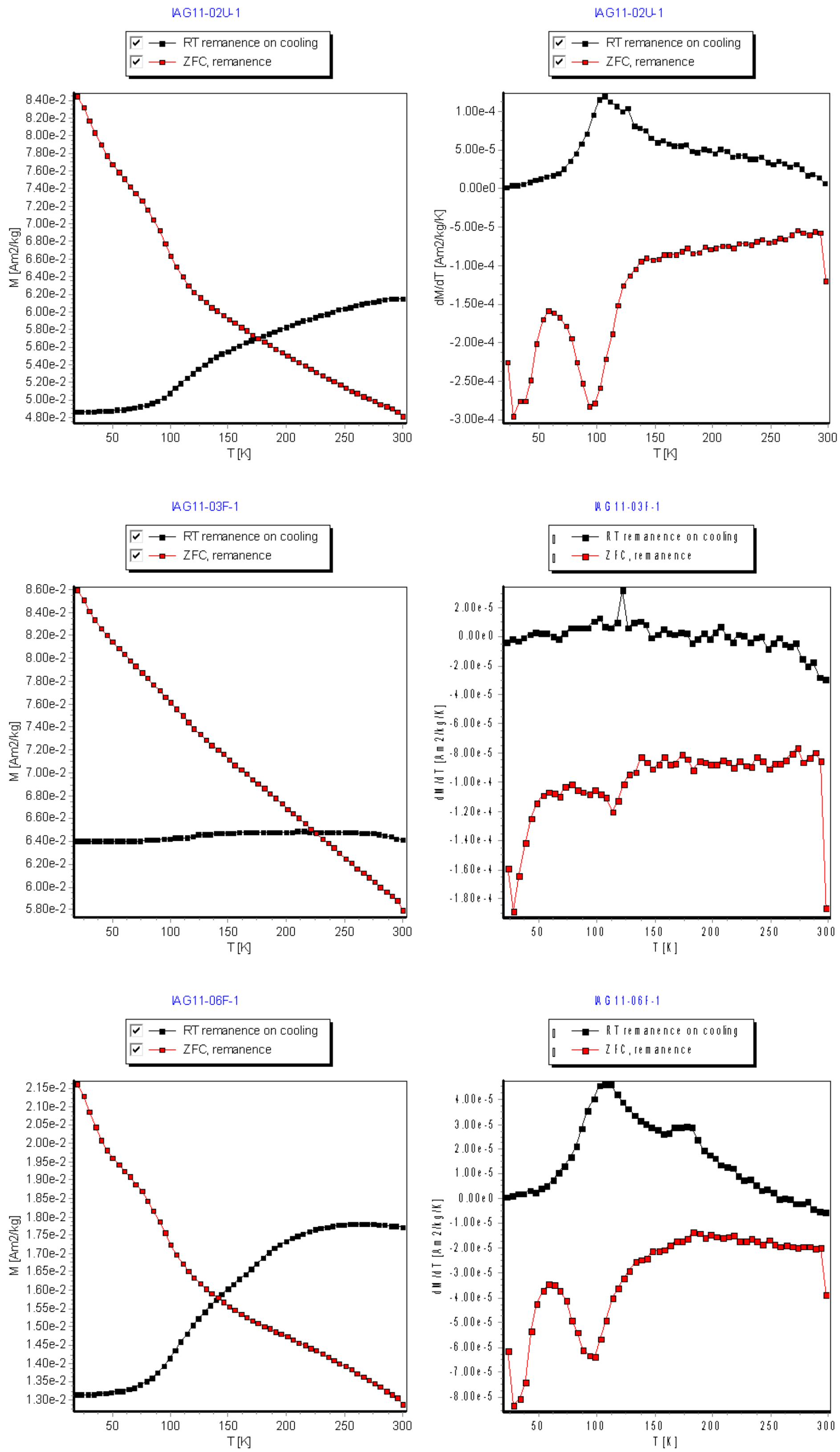

Figure 26. Low-temperature magnetization cycling

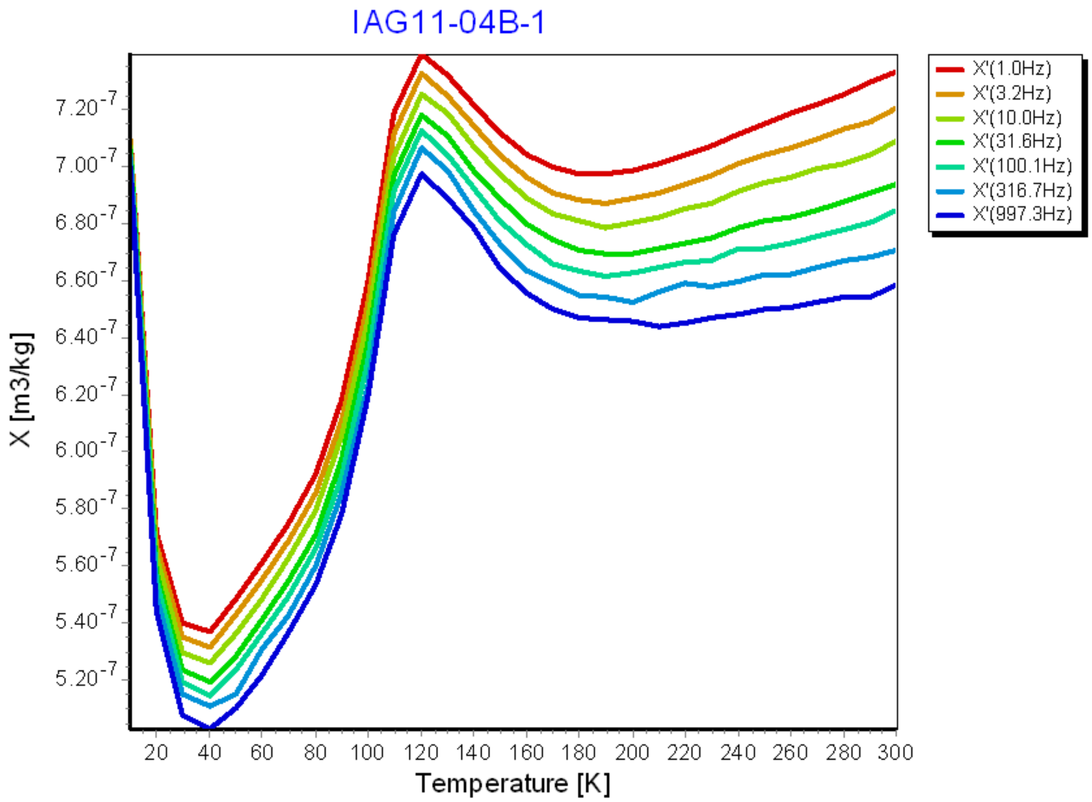

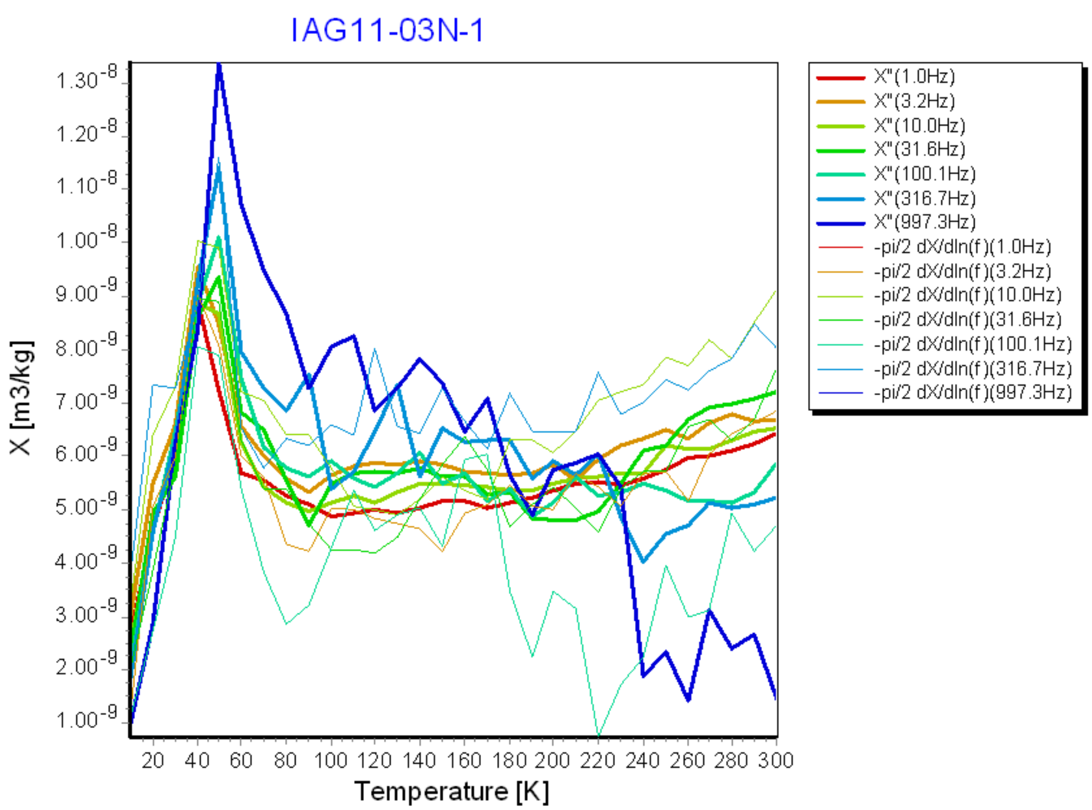

Figure 27. Susceptibility as a function of temperature and frequency

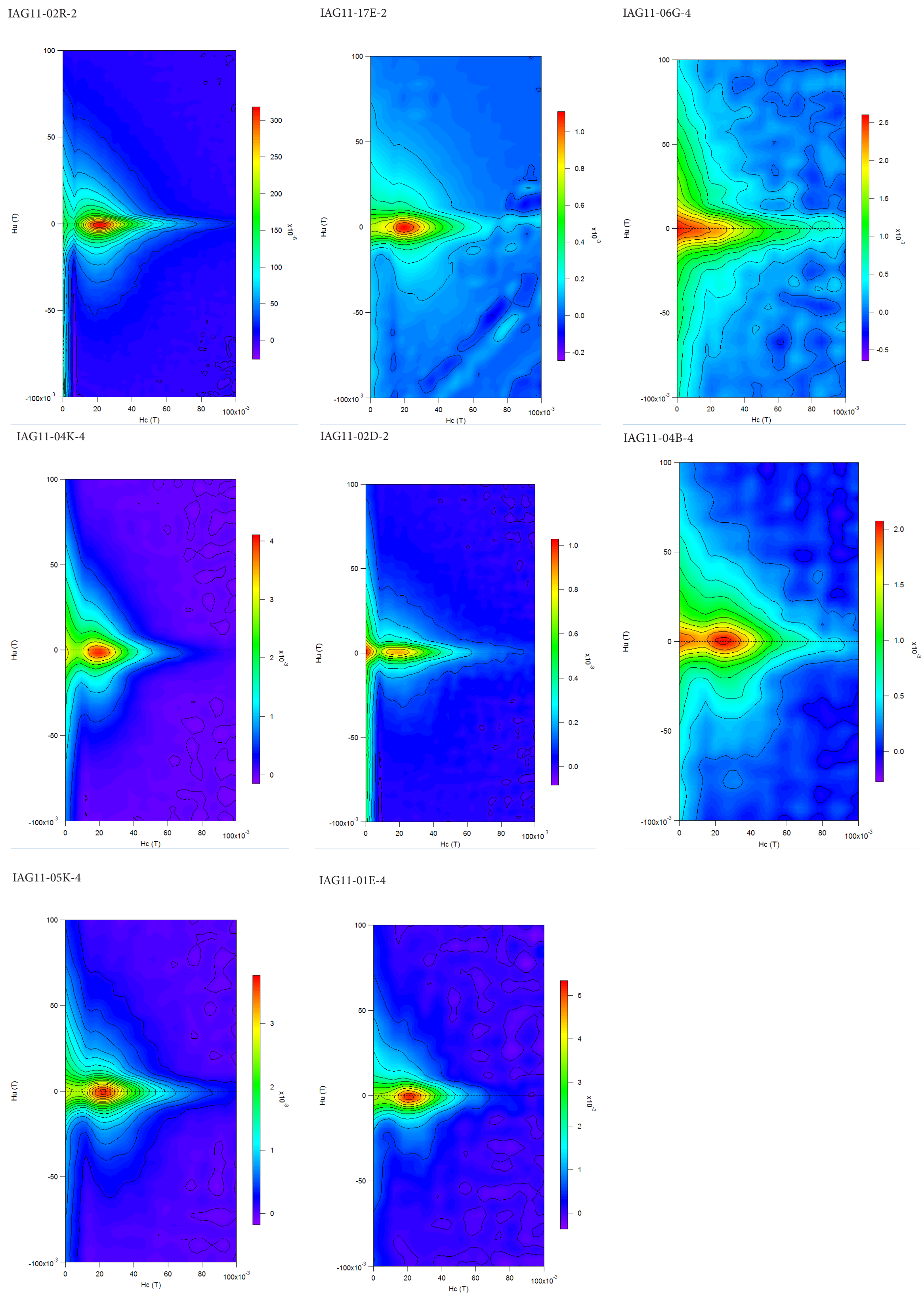

Figure 28. FORC diagrams

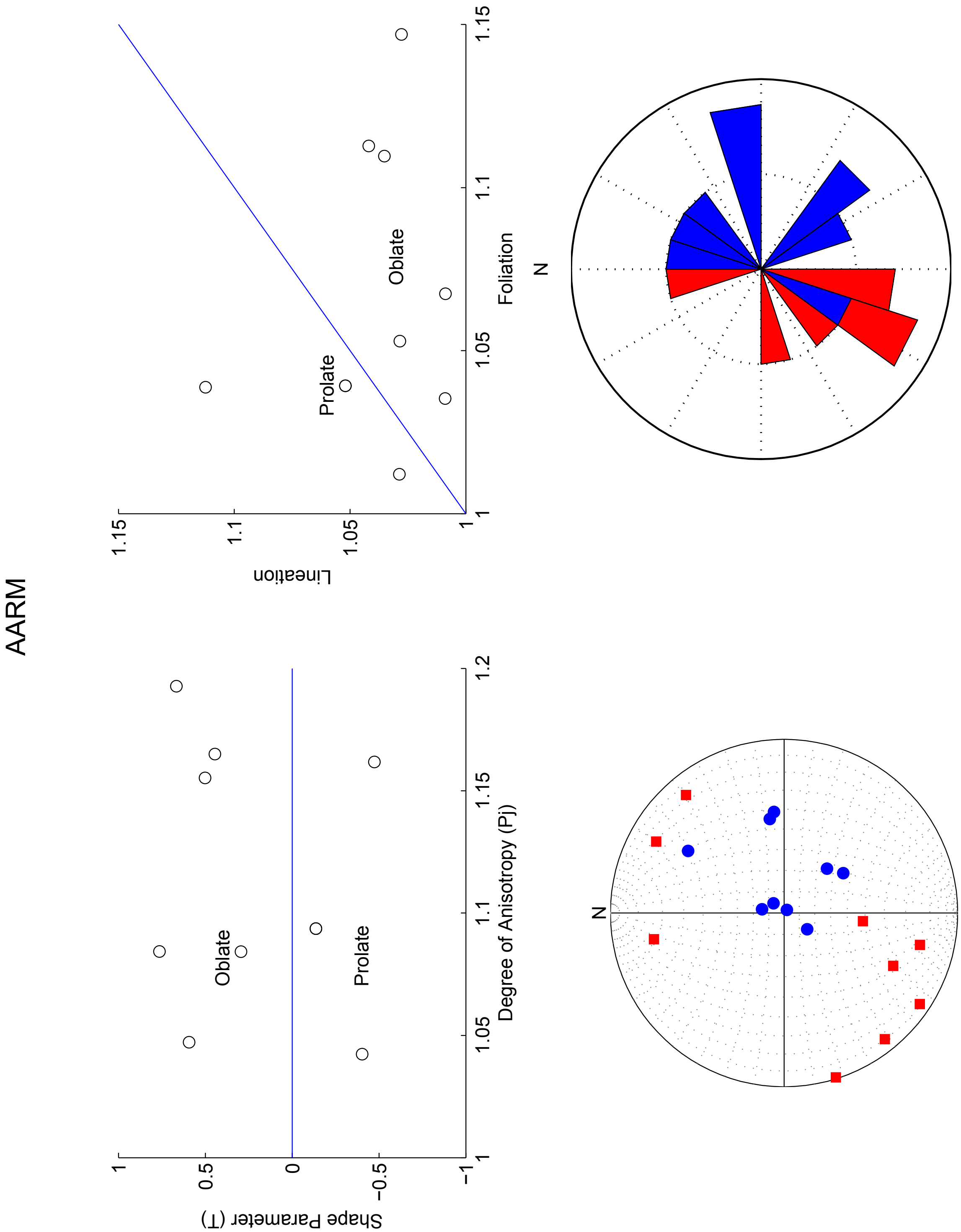

Figure 29. AARM

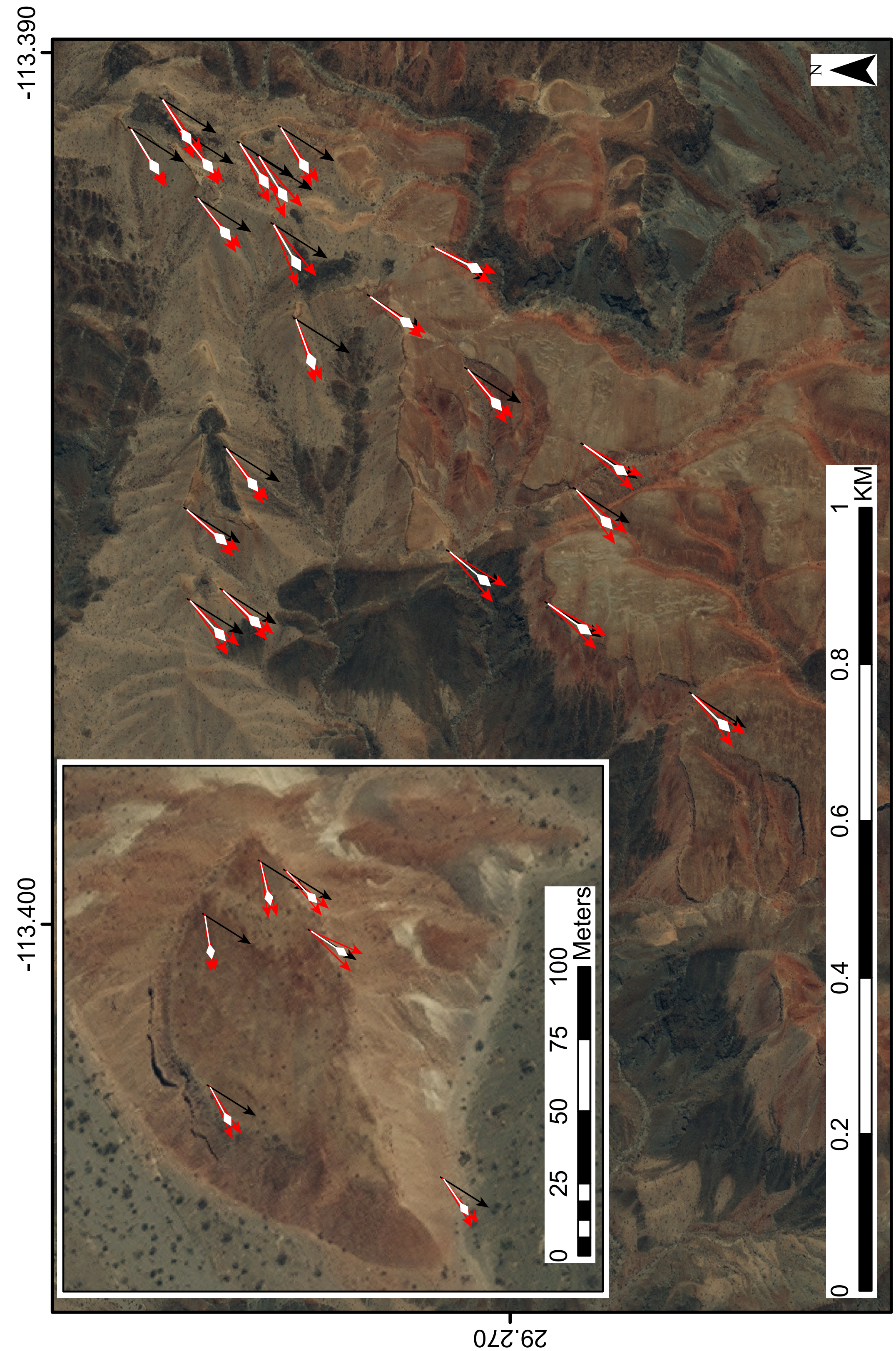

Figure 30. ChRM rotation

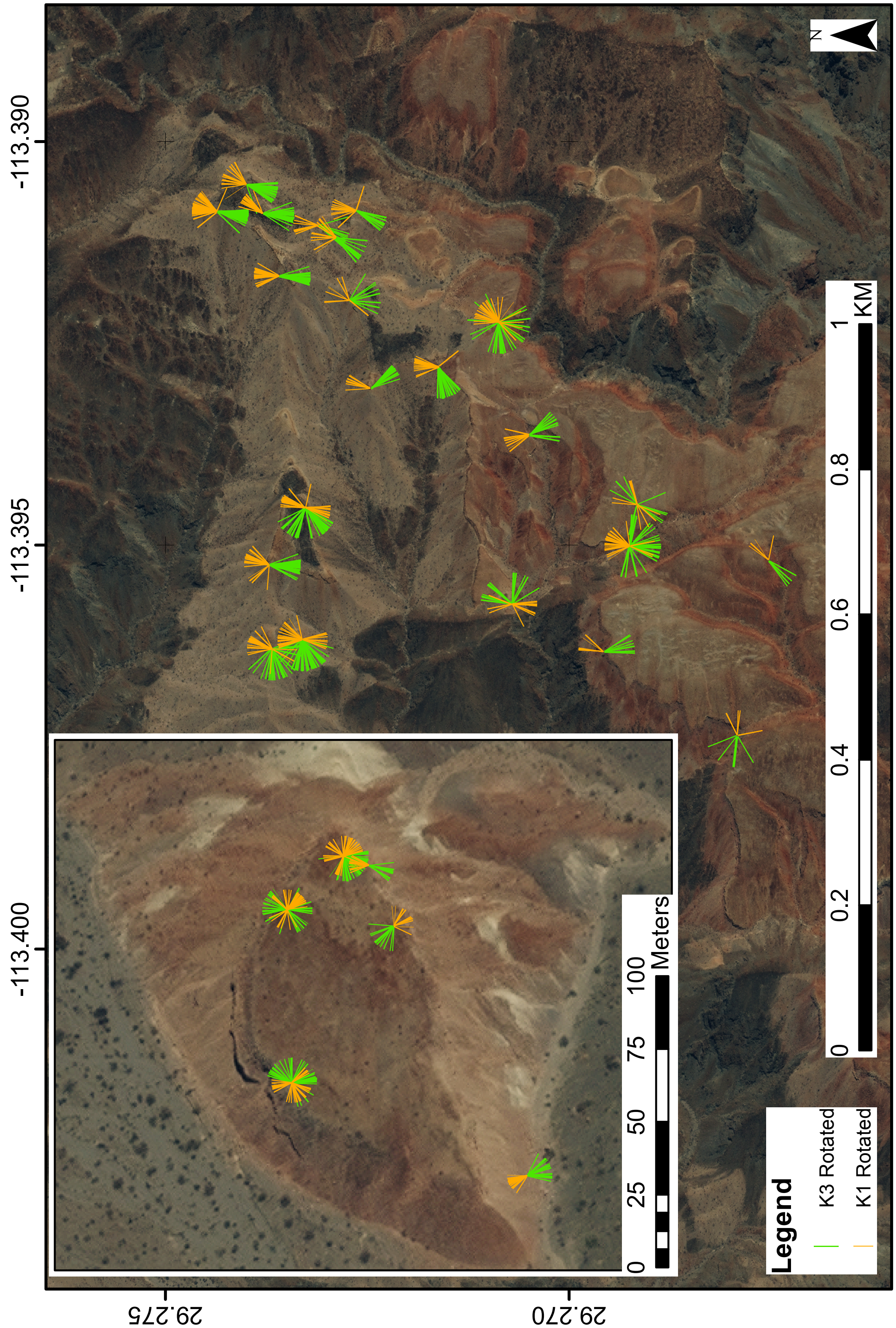

Figure 31. Tectonic correction of flow directions

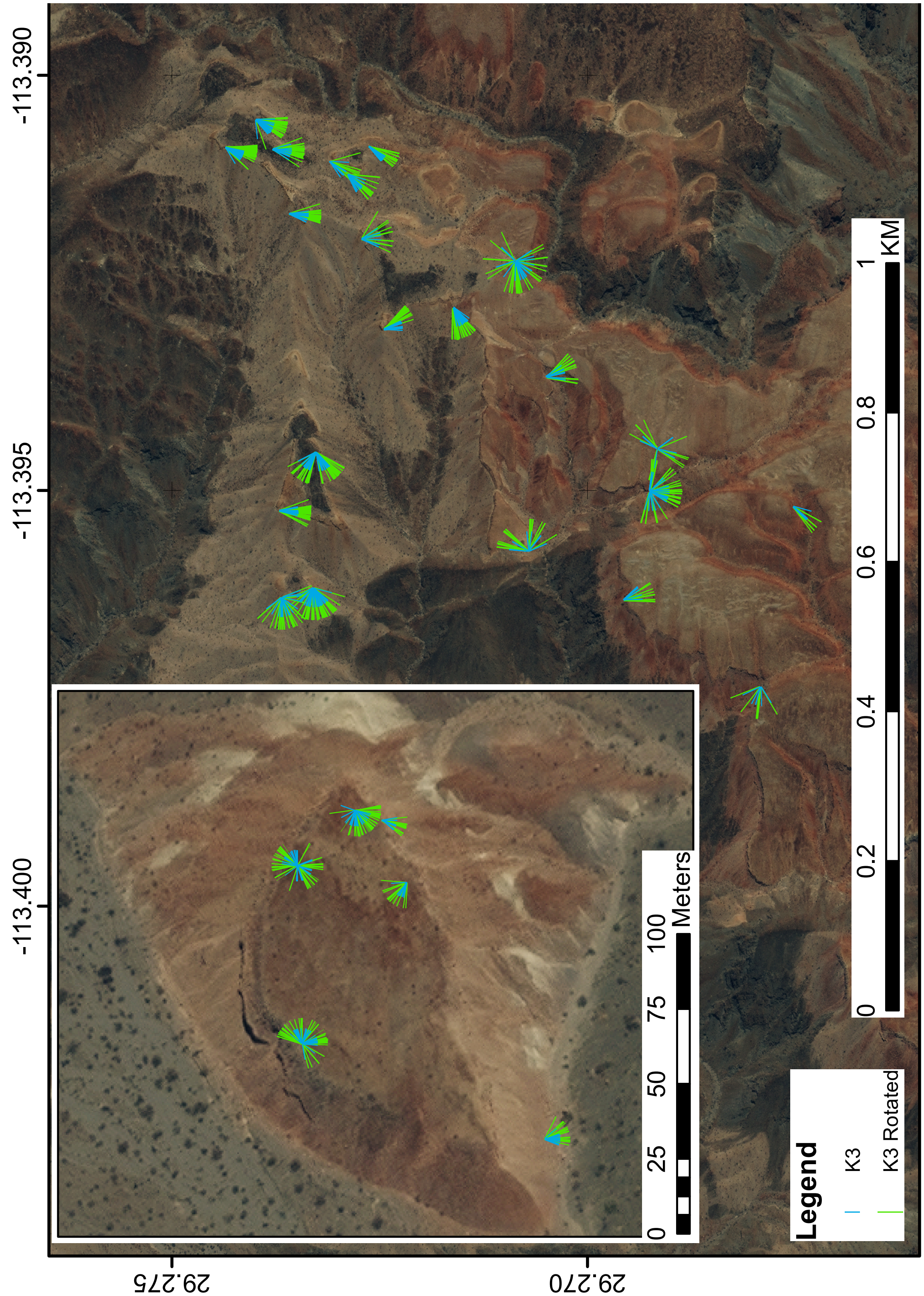

Figure 32. Tectonic correction of foliation

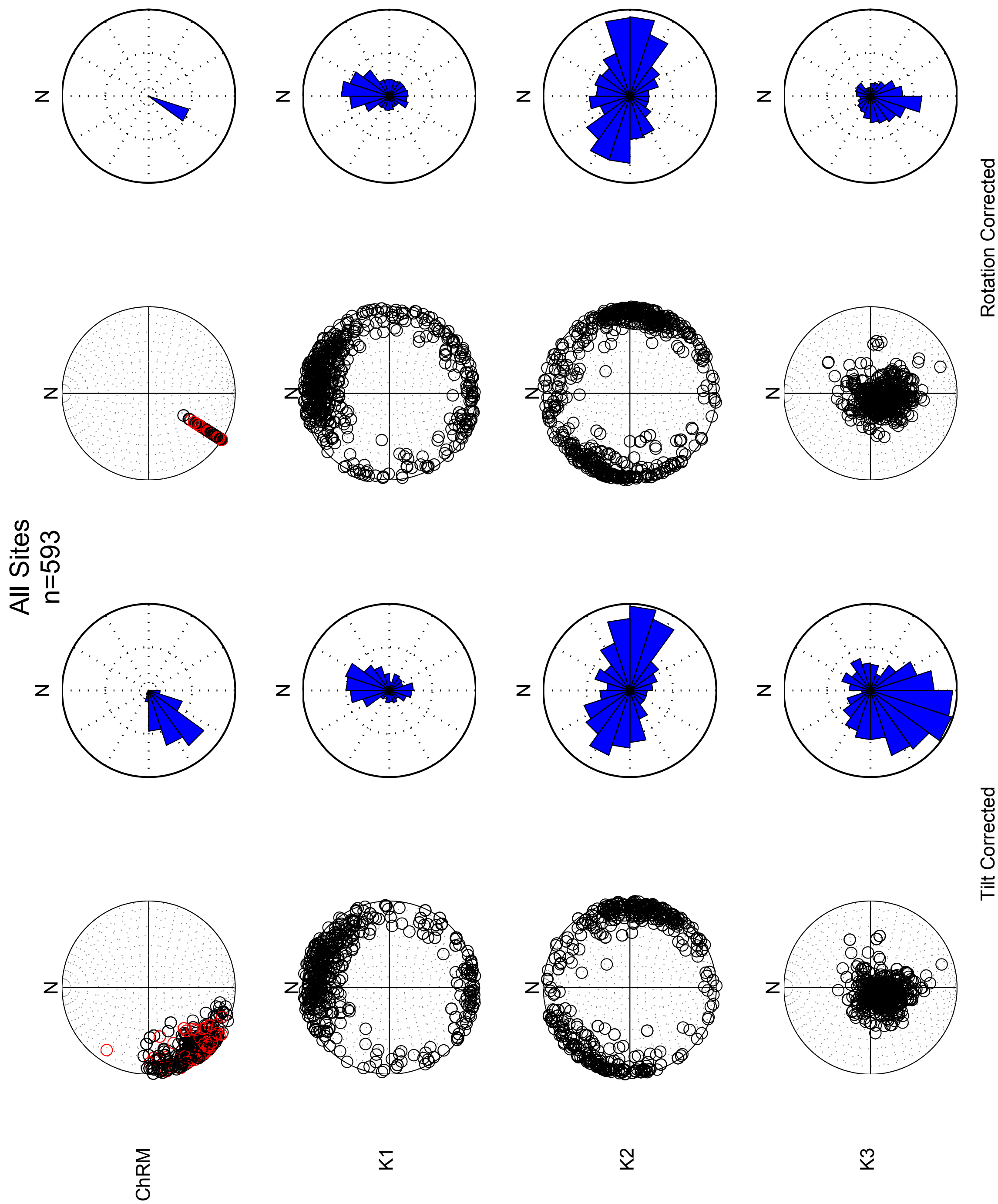

Figure 33. Tectonic correction for all sites

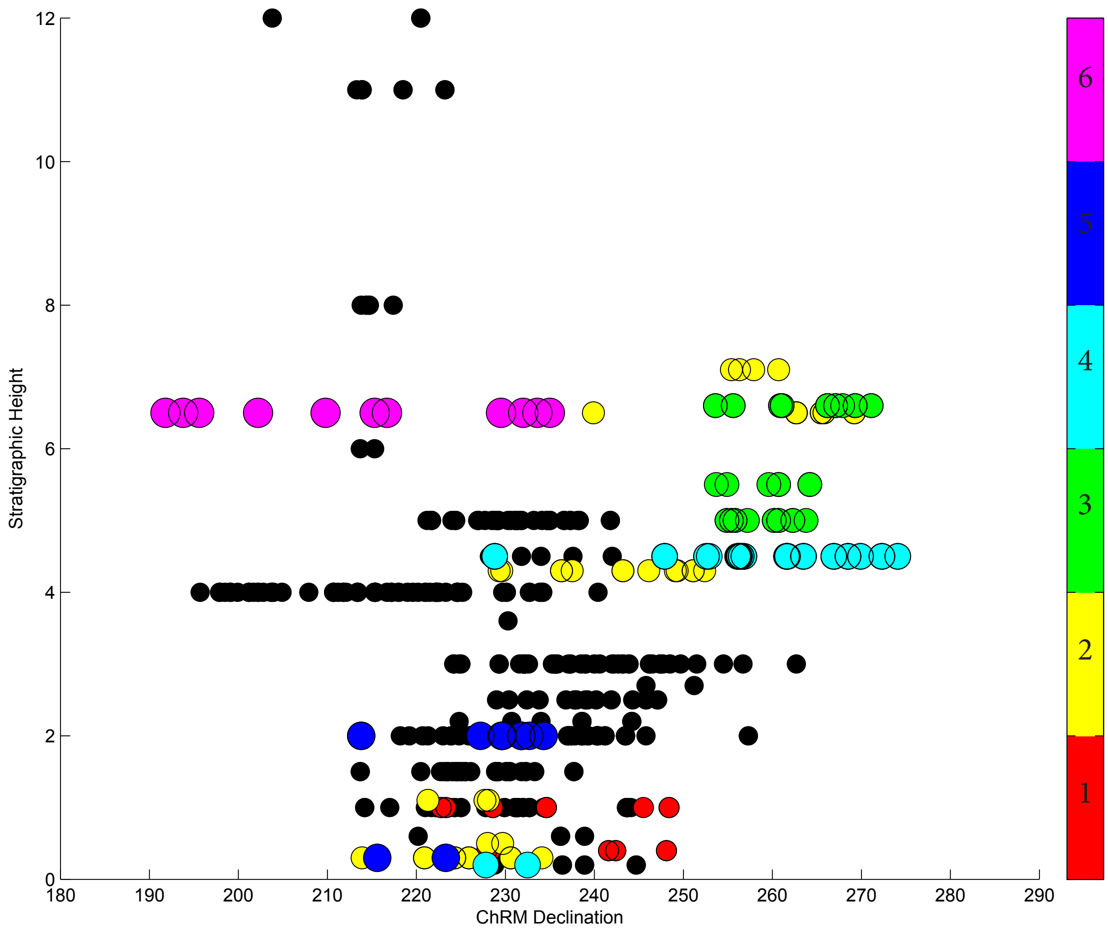

Figure 34. Stratigraphic ChRM rotation

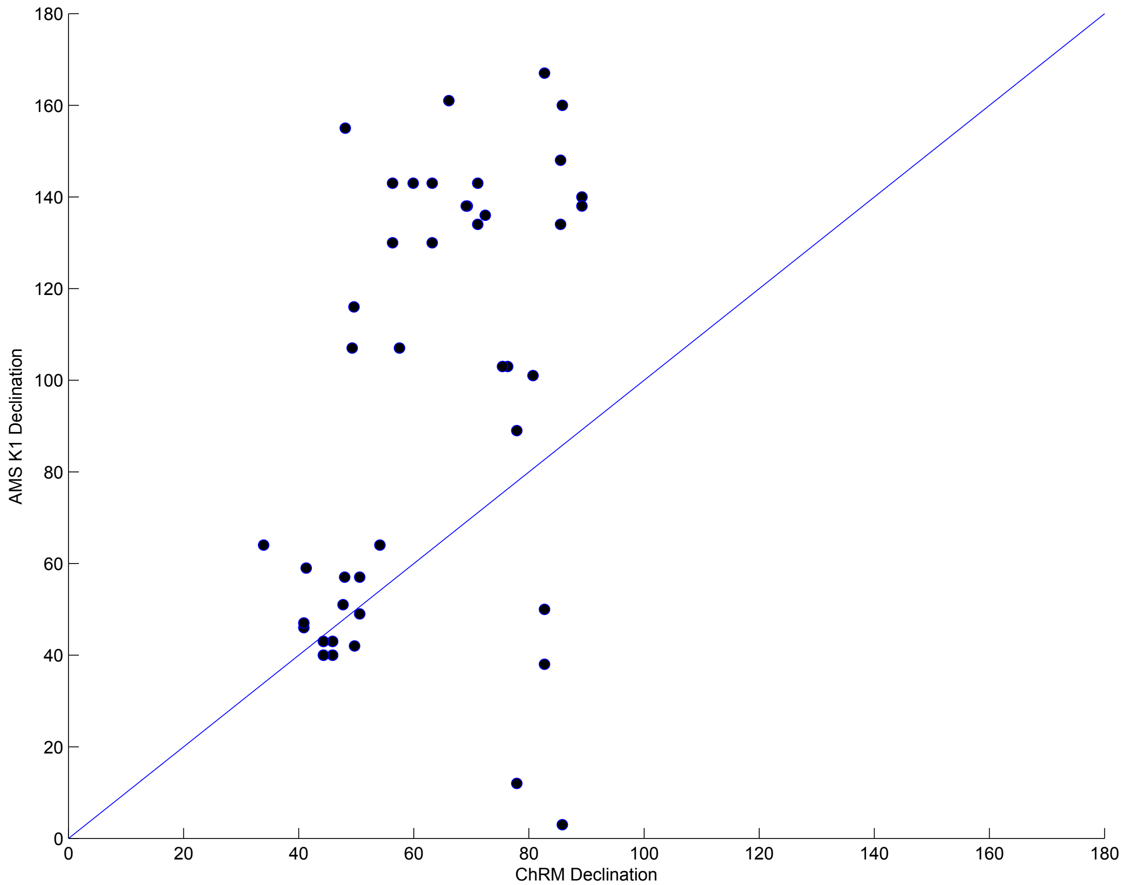

Figure 35. AMS lineation vs ChRM

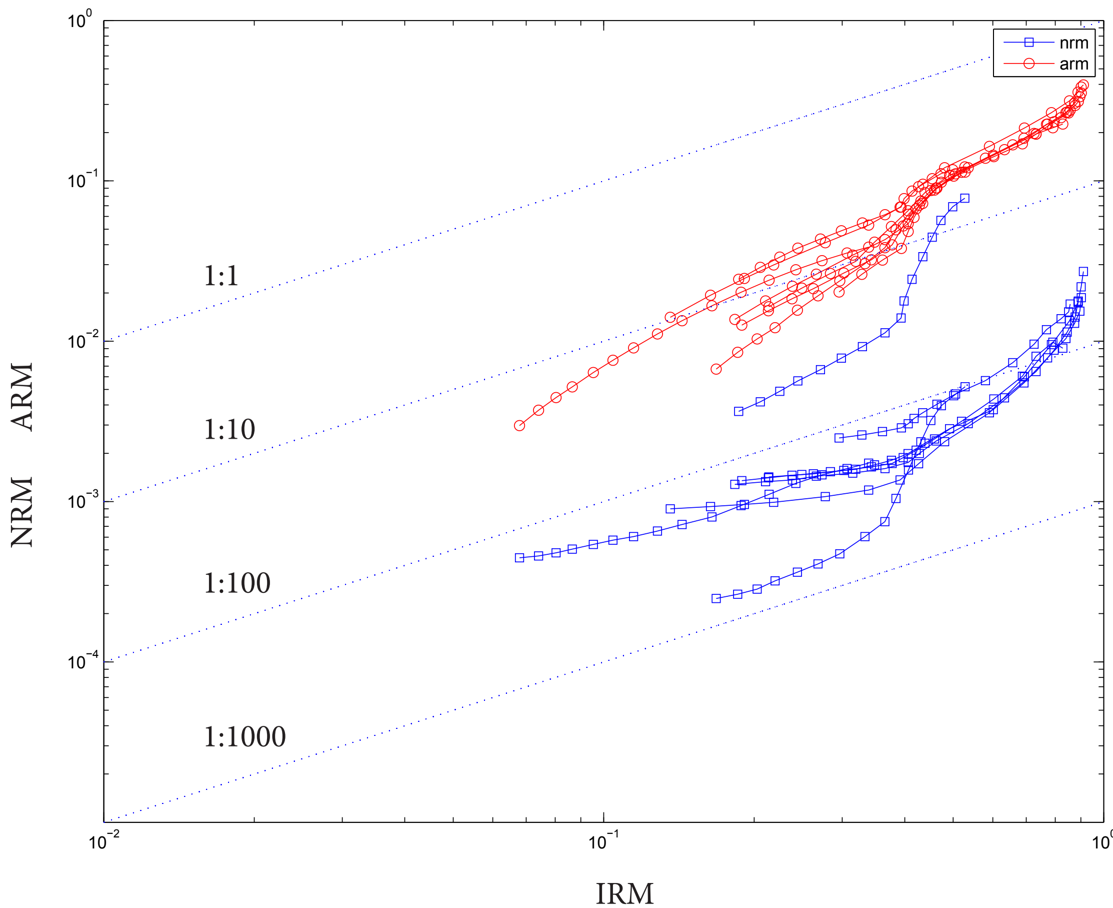

Figure 36. Fuller plot

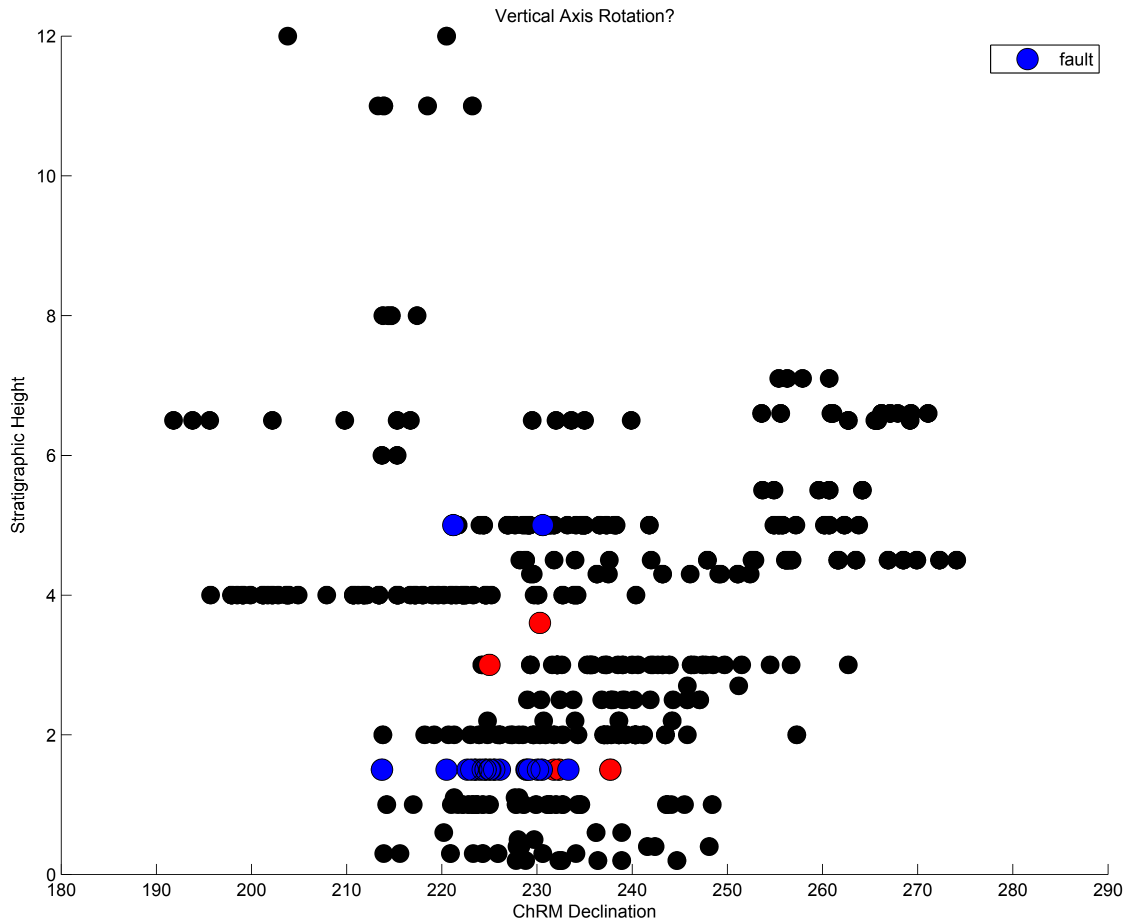

Figure 37. Faulted stratigraphic ChRM rotation

Appendix II

This appendix summarizes the evidence for a low-angle structure with motion across it. We have observed a planar low-angle structure within the tuff. In some outcrops this feature resembles a cooling break while in others it has features that indicate motion. Regardless of the nature of this structure, its occurrence is highly variable. Not all outcrops of the tuff show evidence of a cooling break, and not all outcrops where we have identified the break have clear indication of motion. Without further study, we cannot determine the exact nature of this structure. Sampling of the fracture filling material is needed to determine if it is cataclastic (gouge) or a chemical precipitate (caliche). Baked contact tests across this structure will give us information about the temperature gradient across the boundary.

Figure 1

Here we can see a planar feature, confined within the tuff, cutting down through the section. Note the distance between the grey to red transition and the planar feature. There is a possibly sheared fine grained layer that varies in size with a maximum thickness of 5 inches. (29.2694 N, 113.3951 W)

Figure 2

This photo shows what was originally identified as a cooling boundary, but is now interpreted as part of the low-angle structure. Motion may have localized along a prexisting cooling boundary. (29.2704 N, 113.3934 W)

Figure 3

These photos show a section of the tuff that is ~150 meters away from the locations shown in Figures 1 and 2. Panel A shows the lateral continuity of the section. Panel B is a zoomed in view of the same section and shows that there if no sub-horizontal feature cutting through this outcrop. This section shows no evidence of a cooling boundary. (29.2703 N, 113.3955 W)

Figure 4

This photo shows brecciation along the interface shown in Figure 1. The breccia includes clasts from the tuff above and below the contact. (29.2694 N, 113.3951 W)

Figure 5

This photo shows a welded upper layer of the tuff in contact with the dacite lavas. The contact between the units includes breccia from both the tuff and dacite. There is no basal vitrophyre or other evidence of cooling at the contact. The tuff is welded all the way to the contact. The dacite does not appear heavily thermally altered. (29.2665 N, 113.3969 W)

Figure 6

Panel A (29.2665 N, 113.3969 W) shows the comingling of breccia clasts from above and below the planar structure. Panel B (29.2647 N, 113.4112 W) shows a depositional contact where there only clasts are blocks plucked from the underlying conglomerate. The circles direct the readers attention to the diagnotic clasts.

Figure 7

Panel A shows the small tilted block. The arrow marks the location of site 2. Panel B is a close-up of site 2. The exposed cliff-forming white base of the tuff does not appear to continue past the gully, indicated by the white arrow. (29.2647 N, 113.4112 W)

Figure 8

Location map of the previous photos. Scalebar is 600 meters.

Figure 14. Possible fault

Figure 15. Possible cooling boundary

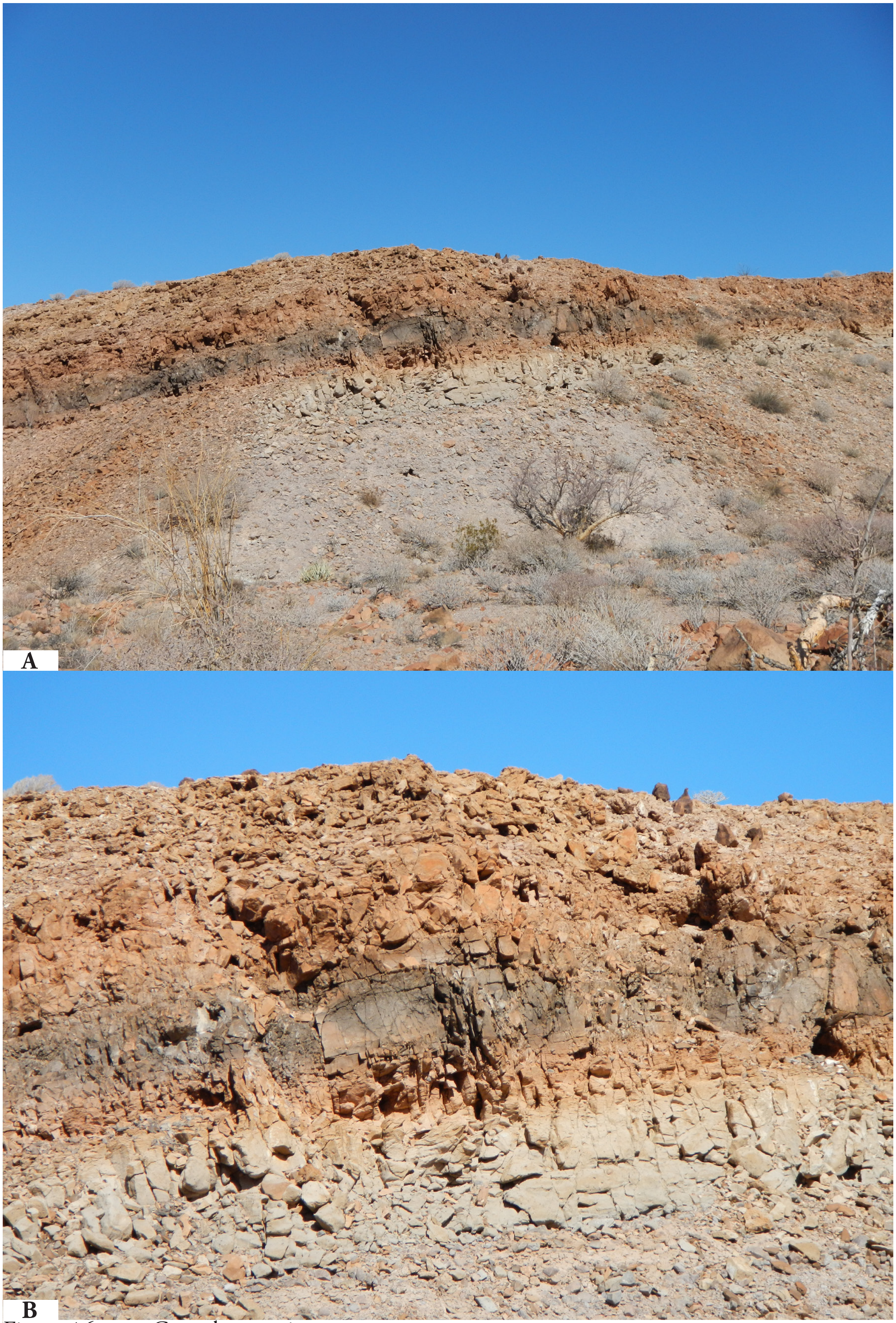

Figure 16. Complete section

Figure 17.	Breccia within tuff

Figure 18.	Brecciated contact

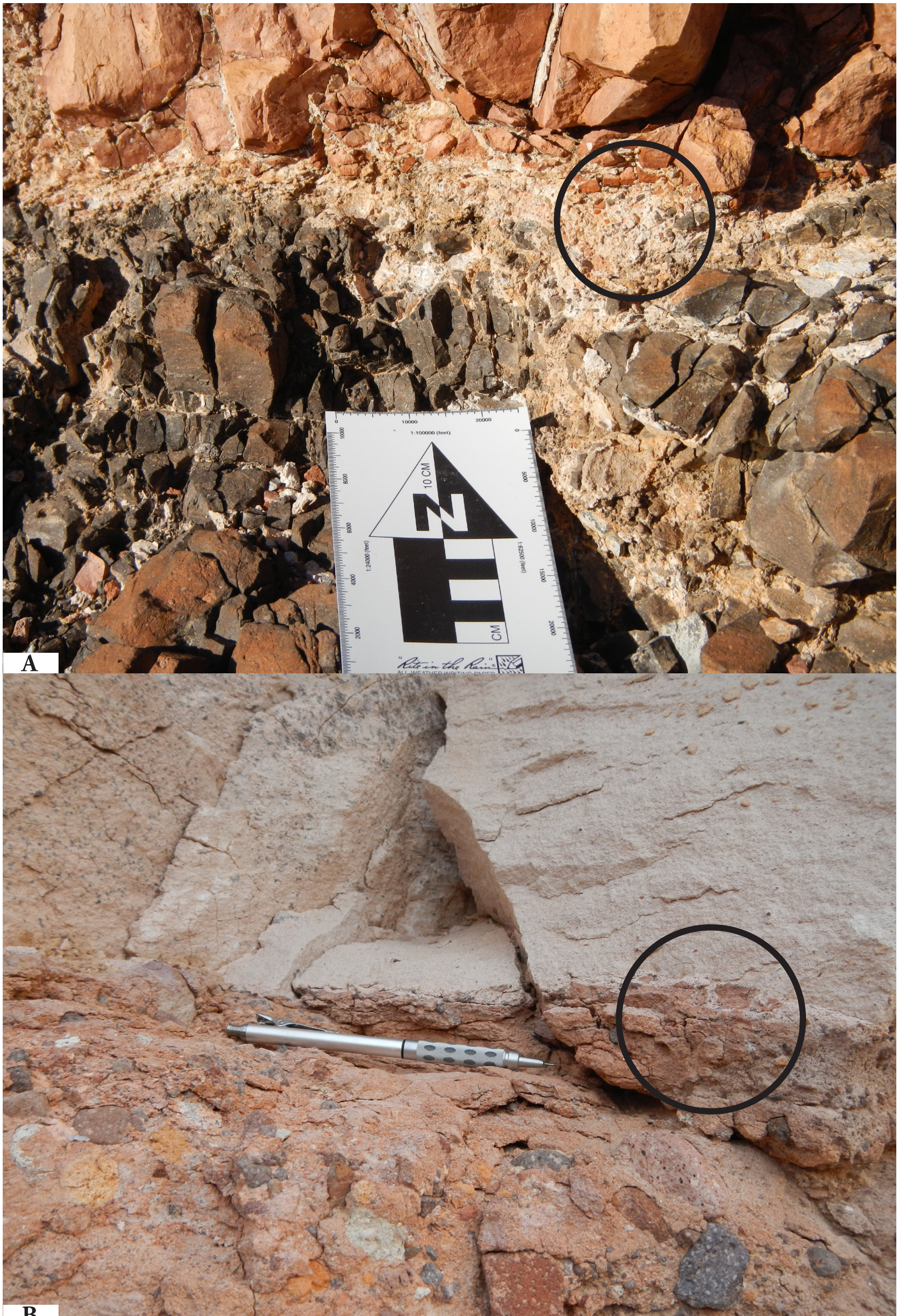

Figure 19. Fault vs depositional contact

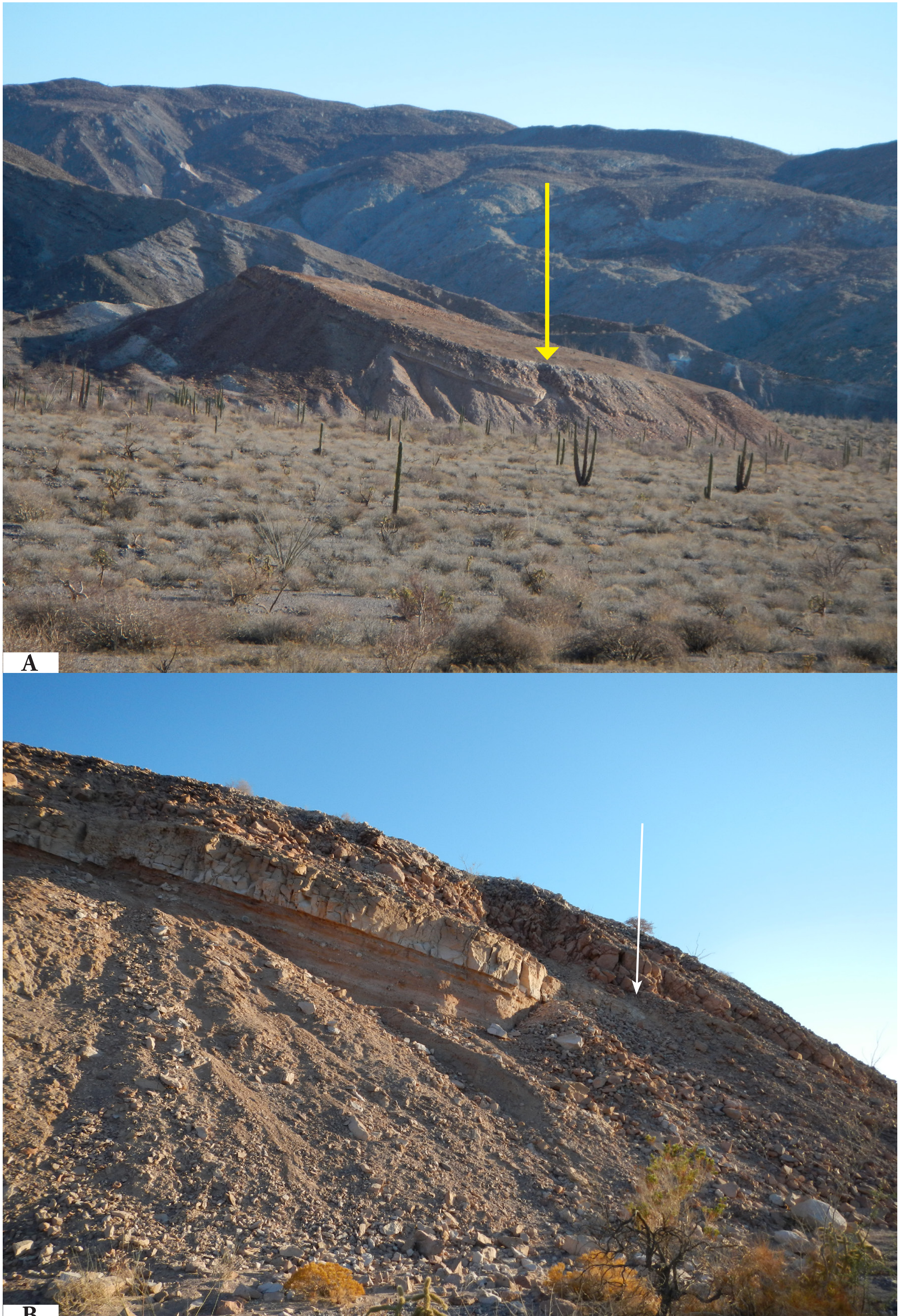

Figure 20. Site 2

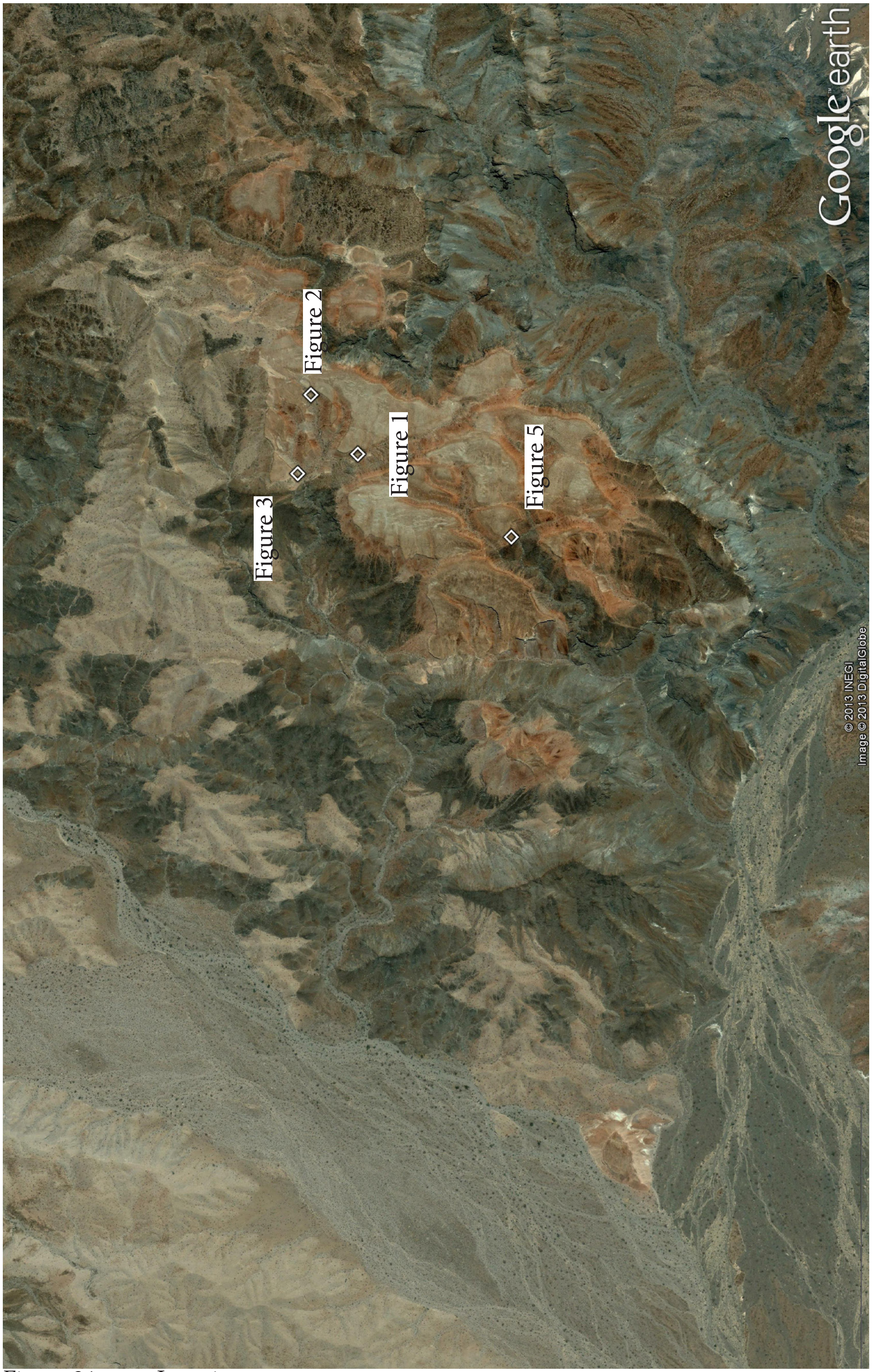

Figure 21. Location map

Paleomagnetic data tables and plots

Sample collection data

Core name (Sample), site latitude (Latitude), site longitude (Longitude), core plate strike relative to magnetic north (Dec), core plate dip using right-hand rule (Inc), sun compass declination (Sun), time of sun compass measurement in UTC (UTC), stratigraphic height of sample (Height), date of collection (Date).

AMS Results

Specimen name (Specimen), lineation (L), foliation (F), degree of anisotropy (Pj), maximum axis declination (D1), intermediate axis declination (D2), minimum axis declination (D3), maximum axis inclination (I1), intermediate axis inclination (I2), minimum axis inclination (I3), mean susceptibility in the order of 10^{-6} SI (Norm), all declination and inclination measurements in a tili-corrected geographic reference frame. See site figures for explanation of how to interpret these values.

IRM Measurement History

IRM_VSM Low-T = room temperature hysteresis loops, IRM_Sartoris = sample mass, IRM_Magnon = frequency dependence of susceptibility, IRM_VSM High-T = magnetization as a function of temperature, IRM_SRM = AARM, IRM_MPSM-5S = magnetization as a function of temperature and thermal and frequency dependence of susceptibility.

ChRM Site Means

Site number (Site), site latitude (Latitude), site longitude (Longitude), Tilt corrected Fisher mean declination (Dt), Tilt corrected Fisher mean inclination (It), cone of 95% confidence about the mean (Alpha95), Fisher precision parameter (Kappa), number of samples (N), Strike of bedding for tilt correction (Strike), Dip of bedding used for tilt correction, using right-hand rule (Dip), all declination and inclination measurements in a tili-corrected geographic reference frame.

AMS Site Means

Site number (Site), maximum axis declination (K1d), maximum axis inclination (K1i), first 95% confidence angle of maximum axis (C1a), second 95% confidence angle of maximum axis (C1b) , intermediate axis declination (K2d), intermediate axis inclination (K2i), first 95% confidence angle of intermediate axis (C2a), second 95% confidence angle of intermediate axis (C2b) , minimum axis declination (K3d), minimum axis inclination (K3i), first 95% confidence angle of minimum axis (C3a), second 95% confidence angle of minimum axis (C3b), number of samples (N), all declination and inclination measurements in a tili-corrected geographic reference frame.

ChRM and AMS by Site

The tilt corrected ChRM and three principal AMS axes are plotted on lower hemisphere equal area stereonets (red points indicate upper hemisphere) and on normalized rose diagrams. For each specimen we have calculated the vertical axis rotation that aligns the ChRM with the reference declination of the Tuff of San Felipe. We use this same rotation to perform a structural correction of the data. The rotation corrected data are plotted on lower hemisphere equal area stereonets and on normalized rose diagrams. The number next to the rose diagram indicates the number of specimens in the largest grouping. All declination and inclination measurements in geographic reference frame. The flow direction can be interpreted as being 180° away from the declination of the K1 axis or in the direction of the K3 axis declination. The flow direction can be read directly from the tilt corrected rose diagrams of K1 and K3. Because our samples have a much stronger foliation we prefer the K3 declination as an indicator of flow direction, however, for most of our both methods produce similar results. Site 1 for example, has a flow direction of 175° measured by either the K1 or K3 declinations.

Mean ChRM

Fisher mean and 95% confidence cone of the ChRM for each site. All declination and inclination measurements in a tilt corrected geographic reference frame.

Table 1. Sample collection data

Sample	Latitude	Longitude	Dec	Inc	Sun	UTC	Height (m)	Date
IAG11-01B	29.26374516	-113.4114716	146	89	119	21:42	0.4	19-Nov-11
IAG11-01C	29.26374516	-113.4114716	148	88		21:50	0.4	19-Nov-11
IAG11-01D	29.26374516	-113.4114716	83	92	50	21:55	0.4	19-Nov-11
IAG11-01E	29.26374516	-113.4114716	130	85	100	22:00	1	19-Nov-11
IAG11-01F	29.26374516	-113.4114716	135	88		22:04	1	19-Nov-11
IAG11-01G	29.26374516	-113.4114716	137	89		22:05	1	19-Nov-11
IAG11-01A	29.26374516	-113.4114716	145	93	119	21:32	0.4	19-Nov-11
IAG11-02AA	29.26447984	-113.4111614	162	105			7.1	20-Nov-11
IAG11-02Q	29.26447984	-113.4111614	325	97			4.3	19-Nov-11
IAG11-02R	29.26447984	-113.4111614	317	97			4.3	19-Nov-11
IAG11-02S	29.26447984	-113.4111614	188	59			6.5	19-Nov-11
IAG11-02T	29.26447984	-113.4111614					6.5	19-Nov-11
IAG11-02U	29.26447984	-113.4111614	189	57			6.5	19-Nov-11
IAG11-02V	29.26447984	-113.4111614	177	67			6.5	19-Nov-11
IAG11-02W	29.26447984	-113.4111614	189	66			6.5	20-Nov-11
IAG11-02X	29.26447984	-113.4111614	177	68			6.5	20-Nov-11
IAG11-02O	29.26447984	-113.4111614	300	91			4.3	19-Nov-11
IAG11-02Z	29.26447984	-113.4111614	188	108			7.1	20-Nov-11
IAG11-02N	29.26447984	-113.4111614	297	85			4.3	19-Nov-11
IAG11-02BB	29.26447984	-113.4111614	190	115			7.1	20-Nov-11
IAG11-02Y	29.26447984	-113.4111614	188	104			7.1	20-Nov-11
IAG11-02F	29.26447984	-113.4111614	193	97			0.5	19-Nov-11
IAG11-02A	29.26447984	-113.4111614	162	101		22:37	0.3	19-Nov-11
IAG11-02B	29.26447984	-113.4111614	165	97			0.3	19-Nov-11
IAG11-02C	29.26447984	-113.4111614	162	101			0.3	19-Nov-11

Sample	Latitude	Longitude	Dec	Inc	Sun	UTC	Height (m)	Date
IAG11-02P	29.26447984	-113.4111614	315	94			4.3	19-Nov-11
IAG11-02E	29.26447984	-113.4111614	191	97			0.5	19-Nov-11
IAG11-02G	29.26447984	-113.4111614	204	102			1.1	19-Nov-11
IAG11-02H	29.26447984	-113.4111614	192	95			1.1	19-Nov-11
IAG11-02I	29.26447984	-113.4111614	182	94			1.1	19-Nov-11
IAG11-02J	29.26447984	-113.4111614	178	92			1.1	19-Nov-11
IAG11-02K	29.26447984	-113.4111614	275	65			4.3	19-Nov-11
IAG11-02L	29.26447984	-113.4111614	286	86			4.3	19-Nov-11
IAG11-02M	29.26447984	-113.4111614	295	81			4.3	19-Nov-11
IAG11-02D	29.26447984	-113.4111614	164	103			0.3	19-Nov-11
IAG11-03L	29.26450565	-113.4105505	319	80	338	18:45	6.6	20-Nov-11
IAG11-03O	29.26450565	-113.4105505	329	82	346	18:51	6.6	20-Nov-11
IAG11-03H	29.26450565	-113.4105505	334	86			5.5	20-Nov-11
IAG11-03M	29.26450565	-113.4105505	320	82	337	18:49	6.6	20-Nov-11
IAG11-03K	29.26450565	-113.4105505	320	79	341	18:44	6.6	20-Nov-11
IAG11-03J	29.26450565	-113.4105505	328	88			6.6	20-Nov-11
IAG11-03I	29.26450565	-113.4105505	333	89			5.5	20-Nov-11
IAG11-03F	29.26450565	-113.4105505	309	71	336	18:22	5.5	20-Nov-11
IAG11-03E	29.26450565	-113.4105505	307	70	334	18:21	5.5	20-Nov-11
IAG11-03D	29.26450565	-113.4105505	309	66			5	20-Nov-11
IAG11-03N	29.26450565	-113.4105505	327	83	345	18:48	6.6	20-Nov-11
IAG11-03C	29.26450565	-113.4105505	343	53			5	20-Nov-11
IAG11-03B	29.26450565	-113.4105505	323	45			5	20-Nov-11
IAG11-03A	29.26450565	-113.4105505	317	56			5	20-Nov-11
IAG11-03G	29.26450565	-113.4105505	311	79	338	18:24	5.5	20-Nov-11
IAG11-04D	29.26433542	-113.4103563	42	80	52	19:05	4.5	20-Nov-11
IAG11-04L	29.26433542	-113.4103563	37	71	48	19:15	4.5	20-Nov-11

Sample	Latitude	Longitude	Dec	Inc	Sun	UTC	Height (m)	Date
IAG11-04K	29.26433542	-113.4103563	40	72	50	19:15	4.5	20-Nov-11
IAG11-04J	29.26433542	-113.4103563	35	72	46	19:14	4.5	20-Nov-11
IAG11-04I	29.26433542	-113.4103563	39	68	51	19:12	4.5	20-Nov-11
IAG11-04H	29.26433542	-113.4103563	38	66	50	19:11	4.5	20-Nov-11
IAG11-04G	29.26433542	-113.4103563	30	73	43	19:10	4.5	20-Nov-11
IAG11-04E	29.26433542	-113.4103563	37	72	52	19:07	4.5	20-Nov-11
IAG11-04C	29.26433542	-113.4103563	41	81	55	19:04	4.5	20-Nov-11
IAG11-04B	29.26433542	-113.4103563	344	79	358	19:01	0.2	20-Nov-11
IAG11-04A	29.26433542	-113.4103563	353	64	4	19:00	0.2	20-Nov-11
IAG11-04F	29.26433542	-113.4103563	38	74	53	19:08	4.5	20-Nov-11
IAG11-05F	29.2642552	-113.4103873	6	81	11	19:30	2	20-Nov-11
IAG11-05J	29.2642552	-113.4103873	9	74	9	19:34	2	20-Nov-11
IAG11-05I	29.2642552	-113.4103873	10	79	9	19:33	2	20-Nov-11
IAG11-05K	29.2642552	-113.4103873	2	72	5	19:35	2	20-Nov-11
IAG11-05G	29.2642552	-113.4103873	13	80	19	19:31	2	20-Nov-11
IAG11-05D	29.2642552	-113.4103873	10	72	17	19:26	1	20-Nov-11
IAG11-05C	29.2642552	-113.4103873	16	72	24	19:25	0.3	20-Nov-11
IAG11-05B	29.2642552	-113.4103873	15	75	19	19:24	0.3	20-Nov-11
IAG11-05A	29.2642552	-113.4103873	12	78	20	19:23	0.3	20-Nov-11
IAG11-05H	29.2642552	-113.4103873	5	71	10	19:31	2	20-Nov-11
IAG11-05E	29.2642552	-113.4103873	359	75	6	19:28	1	20-Nov-11
IAG11-06G	29.2641744	-113.410599	64	78	66	19:50	6.5	20-Nov-11
IAG11-06M	29.2641744	-113.410599	66	77	65	19:56	6.5	20-Nov-11
IAG11-06L	29.2641744	-113.410599	68	79	70	19:55	6.5	20-Nov-11
IAG11-06K	29.2641744	-113.410599	68	72	67	19:54	6.5	20-Nov-11
IAG11-06J	29.2641744	-113.410599	64	74	65	19:53	6.5	20-Nov-11
IAG11-06H	29.2641744	-113.410599	67	80	69	19:51	6.5	20-Nov-11

Sample	Latitude	Longitude	Dec	Inc	Sun	UTC	Height (m)	Date
IAG11-06F	29.2641744	-113.410599	67	74	69	19:48	6.5	20-Nov-11
IAG11-06E	29.2641744	-113.410599	67	77	70	19:46	6.5	20-Nov-11
IAG11-06D	29.2641744	-113.410599	66	81	68	19:45	6.5	20-Nov-11
IAG11-06C	29.2641744	-113.410599	67	73	70	19:44	6.5	20-Nov-11
IAG11-06B	29.2641744	-113.410599	66	76	70	19:43	6.5	20-Nov-11
IAG11-06A	29.2641744	-113.410599	66	78	70	19:43	6.5	20-Nov-11
IAG11-06I	29.2641744	-113.410599	66	78	67	19:52	6.5	20-Nov-11
IAG11-07H	29.27367722	-113.396284	270	85			2	21-Nov-11
IAG11-07Q	29.27367722	-113.396284	185	87	185	19:57	2	21-Nov-11
IAG11-07P	29.27367722	-113.396284	184	83	185	19:56	2	21-Nov-11
IAG11-07O	29.27367722	-113.396284	175	85			2	21-Nov-11
IAG11-07N	29.27367722	-113.396284	181	83			2	21-Nov-11
IAG11-07M	29.27367722	-113.396284	178	84	182	19:50	2	21-Nov-11
IAG11-07L	29.27367722	-113.396284	270	75			2	21-Nov-11
IAG11-07K	29.27367722	-113.396284	277	78	281	19:39	2	21-Nov-11
IAG11-07B	29.27367722	-113.396284	180	93	196	19:06	2	21-Nov-11
IAG11-07A	29.27367722	-113.396284	178	97	196	19:04	2	21-Nov-11
IAG11-07C	29.27367722	-113.396284	175	96	191	19:07	2	21-Nov-11
IAG11-07D	29.27367722	-113.396284	185	85			2	21-Nov-11
IAG11-07E	29.27367722	-113.396284	181	90			2	21-Nov-11
IAG11-07F	29.27367722	-113.396284	265	76			2	21-Nov-11
IAG11-07G	29.27367722	-113.396284	267	89			2	21-Nov-11
IAG11-07I	29.27367722	-113.396284	271	84			2	21-Nov-11
IAG11-07J	29.27367722	-113.396284	278	83			2	21-Nov-11
IAG11-08L	29.27330154	-113.3961665	85	19	76	20:30		21-Nov-11
IAG11-08J	29.27330154	-113.3961665	22	83	19	20:20	1	21-Nov-11
IAG11-08R	29.27330154	-113.3961665	58	35	43	20:41		21-Nov-11

Sample	Latitude	Longitude	Dec	Inc	Sun	UTC	Height (m)	Date
IAG11-08Q	29.27330154	-113.3961665	59	41	47	20:39		21-Nov-11
IAG11-08P	29.27330154	-113.3961665	60	36	52	20:37		21-Nov-11
IAG11-08O	29.27330154	-113.3961665	59	42	52	20:35		21-Nov-11
IAG11-08M	29.27330154	-113.3961665	73	22	62	20:33		21-Nov-11
IAG11-08K	29.27330154	-113.3961665	12	83	3	20:21	1	21-Nov-11
IAG11-08H	29.27330154	-113.3961665	15	86			1	21-Nov-11
IAG11-08G	29.27330154	-113.3961665	19	85			1	21-Nov-11
IAG11-08A	29.27330154	-113.3961665	16	76			1	21-Nov-11
IAG11-08F	29.27330154	-113.3961665	22	87			1	21-Nov-11
IAG11-08E	29.27330154	-113.3961665	19	86			1	21-Nov-11
IAG11-08D	29.27330154	-113.3961665	15	91			1	21-Nov-11
IAG11-08C	29.27330154	-113.3961665	18	90			1	21-Nov-11
IAG11-08B	29.27330154	-113.3961665	22	72			1	21-Nov-11
IAG11-08I	29.27330154	-113.3961665	13	87			1	21-Nov-11
IAG11-08N	29.27330154	-113.3961665	59	35	40	20:42		21-Nov-11
IAG11-09B	29.27349164	-113.396204	181	98	166	20:49	0.4	21-Nov-11
IAG11-09H	29.27349164	-113.396204	186	82	163	21:00	0.4	21-Nov-11
IAG11-09G	29.27349164	-113.396204	184	83	163	20:58	0.4	21-Nov-11
IAG11-09F	29.27349164	-113.396204					0.4	21-Nov-11
IAG11-09E	29.27349164	-113.396204	168	91	151	20:55	0.4	21-Nov-11
IAG11-09C	29.27349164	-113.396204	184	97	168	20:51	0.4	21-Nov-11
IAG11-09A	29.27349164	-113.396204	183	102	168	20:48	0.4	21-Nov-11
IAG11-09D	29.27349164	-113.396204	166	89	149	20:53	0.4	21-Nov-11
IAG11-10I	29.27371544	-113.3952386	272	66			0.6	21-Nov-11
IAG11-10O	29.27371544	-113.3952386	145	33	100	23:24	4	21-Nov-11
IAG11-10L	29.27371544	-113.3952386	102	31	57	23:20	4	21-Nov-11
IAG11-10M	29.27371544	-113.3952386	140	22	95	23:22	4	21-Nov-11

Sample	Latitude	Longitude	Dec	Inc	Sun	UTC	Height (m)	Date
IAG11-10P	29.27371544	-113.3952386	145	28	101	23:24	4	21-Nov-11
IAG11-10K	29.27371544	-113.3952386	135	20	90	23:19	4	21-Nov-11
IAG11-10J	29.27371544	-113.3952386	131	31	87	23:17	4	21-Nov-11
IAG11-10A	29.27371544	-113.3952386	344	65			0.6	21-Nov-11
IAG11-10N	29.27371544	-113.3952386	144	18	99	23:23	4	21-Nov-11
IAG11-10B	29.27371544	-113.3952386	352	60			0.6	21-Nov-11
IAG11-10C	29.27371544	-113.3952386	354	68			0.6	21-Nov-11
IAG11-10D	29.27371544	-113.3952386	300	38			0.6	21-Nov-11
IAG11-10E	29.27371544	-113.3952386	330	52			0.6	21-Nov-11
IAG11-10F	29.27371544	-113.3952386	285	43			0.6	21-Nov-11
IAG11-10G	29.27371544	-113.3952386	310	33			0.6	21-Nov-11
IAG11-10H	29.27371544	-113.3952386	305	55			0.6	21-Nov-11
IAG11-11H	29.27326097	-113.3945364	4	86	13	19:18	5	22-Nov-11
IAG11-11K	29.27326097	-113.3945364	15	88	23	19:20	5	22-Nov-11
IAG11-11Q	29.27326097	-113.3945364	0	79	7	19:24	5	22-Nov-11
IAG11-11P	29.27326097	-113.3945364	0	80	9	19:23	5	22-Nov-11
IAG11-11O	29.27326097	-113.3945364	7	80	10	19:23	5	22-Nov-11
IAG11-11N	29.27326097	-113.3945364					5	22-Nov-11
IAG11-11M	29.27326097	-113.3945364	0	70	8	19:22	5	22-Nov-11
IAG11-11L	29.27326097	-113.3945364	1	82	10	19:21	5	22-Nov-11
IAG11-11I	29.27326097	-113.3945364	7	96	17	19:19	5	22-Nov-11
IAG11-11G	29.27326097	-113.3945364	10	92	21	19:16	5	22-Nov-11
IAG11-11F	29.27326097	-113.3945364	27	85	41	19:06	1	22-Nov-11
IAG11-11E	29.27326097	-113.3945364	27	84	40	19:05	1	22-Nov-11
IAG11-11D	29.27326097	-113.3945364	21	81	36	19:04	1	22-Nov-11
IAG11-11C	29.27326097	-113.3945364	25	84	40	19:03	1	22-Nov-11
IAG11-11A	29.27326097	-113.3945364	18	63	34	19:00	1	22-Nov-11

Sample	Latitude	Longitude	Dec	Inc	Sun	UTC	Height (m)	Date
IAG11-11B	29.27326097	-113.3945364	23	68	38	19:02	1	22-Nov-11
IAG11-11J	29.27326097	-113.3945364	6	89	16	19:19	5	22-Nov-11
IAG11-12I	29.27399145	-113.3905336	10	32	338	21:56	2.2	22-Nov-11
IAG11-12A	29.27399145	-113.3905336	33	25	8	21:30	0.2	22-Nov-11
IAG11-12M	29.27399145	-113.3905336	358	26	323	22:12	2.2	22-Nov-11
IAG11-12L	29.27399145	-113.3905336	0	26	325	22:06	2.2	22-Nov-11
IAG11-12K	29.27399145	-113.3905336	22	18	348	21:59	2.2	22-Nov-11
IAG11-12J	29.27399145	-113.3905336	16	16	344	21:57	2.2	22-Nov-11
IAG11-12G	29.27399145	-113.3905336	2	80	334	21:39	0.2	22-Nov-11
IAG11-12F	29.27399145	-113.3905336	6	77	339	21:37	0.2	22-Nov-11
IAG11-12E	29.27399145	-113.3905336	4	89	336	21:35	0.2	22-Nov-11
IAG11-12D	29.27399145	-113.3905336	359	88	332	21:34	0.2	22-Nov-11
IAG11-12B	29.27399145	-113.3905336	20	25	354	21:31	0.2	22-Nov-11
IAG11-12H	29.27399145	-113.3905336	5	31	333	21:54	2.2	22-Nov-11
IAG11-12C	29.27399145	-113.3905336	2	93	335	21:32	0.2	22-Nov-11
IAG11-13D	29.27435691	-113.3908698	347	75			2	22-Nov-11
IAG11-13H	29.27435691	-113.3908698	338	94			2	22-Nov-11
IAG11-13G	29.27435691	-113.3908698	345	86			2	22-Nov-11
IAG11-13F	29.27435691	-113.3908698	349	86			2	22-Nov-11
IAG11-13E	29.27435691	-113.3908698	350	83			2	22-Nov-11
IAG11-13C	29.27435691	-113.3908698	354	86			2	22-Nov-11
IAG11-13B	29.27435691	-113.3908698	355	82			2	22-Nov-11
IAG11-13A	29.27435691	-113.3908698	355	78			2	22-Nov-11
IAG11-14A	29.27379071	-113.3908903	87	88	46	22:46	3	22-Nov-11
IAG11-14B	29.27379071	-113.3908903	83	86	53	22:47	3	22-Nov-11
IAG11-14C	29.27379071	-113.3908903	89	82	48	22:48	3	22-Nov-11
IAG11-14D	29.27379071	-113.3908903	83	85	43	22:49	3	22-Nov-11

Sample	Latitude	Longitude	Dec	Inc	Sun	UTC	Height (m)	Date
IAG11-14E	29.27379071	-113.3908903	86	89	45	22:50	3	22-Nov-11
IAG11-14F	29.27379071	-113.3908903	82	82	41	22:51	3	22-Nov-11
IAG11-15B	29.2738213	-113.3910857	23	90	339	22:58		22-Nov-11
IAG11-15C	29.2738213	-113.3910857	23	89	338	22:59		22-Nov-11
IAG11-15A	29.2738213	-113.3910857	23	89	338	22:57		22-Nov-11
IAG11-16G	29.27359097	-113.3916657	194	94	214	18:58	5	23-Nov-11
IAG11-16K	29.27359097	-113.3916657	170	90	186	19:04	5	23-Nov-11
IAG11-16J	29.27359097	-113.3916657	176	90	198	19:02	5	23-Nov-11
IAG11-16H	29.27359097	-113.3916657	185	89	204	18:59	5	23-Nov-11
IAG11-16F	29.27359097	-113.3916657	170	86	190	18:57	5	23-Nov-11
IAG11-16E	29.27359097	-113.3916657	179	89	198	18:56	5	23-Nov-11
IAG11-16D	29.27359097	-113.3916657	174	87	194	18:55	5	23-Nov-11
IAG11-16C	29.27359097	-113.3916657	174	91	195	18:54	5	23-Nov-11
IAG11-16B	29.27359097	-113.3916657	175	85	204	18:52	5	23-Nov-11
IAG11-16A	29.27359097	-113.3916657	178	87	200	18:51	5	23-Nov-11
IAG11-16I	29.27359097	-113.3916657	188	80	206	19:01	5	23-Nov-11
IAG11-17H	29.27310607	-113.3910375	278	63	266	20:39	4.5	23-Nov-11
IAG11-17G	29.27310607	-113.3910375	250	66	243	20:25	2.5	23-Nov-11
IAG11-17M	29.27310607	-113.3910375	275	60	262	20:43	4.5	23-Nov-11
IAG11-17L	29.27310607	-113.3910375	276	59	264	20:42	4.5	23-Nov-11
IAG11-17K	29.27310607	-113.3910375	290	61	276	20:42	4.5	23-Nov-11
IAG11-17I	29.27310607	-113.3910375	284	62	271	20:40	4.5	23-Nov-11
IAG11-17A	29.27310607	-113.3910375	254	31	248	20:18	2.5	23-Nov-11
IAG11-17E	29.27310607	-113.3910375	261	42	254	20:21	2.5	23-Nov-11
IAG11-17D	29.27310607	-113.3910375	258	32	251	20:21	2.5	23-Nov-11
IAG11-17C	29.27310607	-113.3910375	257	30	251	20:20	2.5	23-Nov-11
IAG11-17B	29.27310607	-113.3910375	255	39	250	20:19	2.5	23-Nov-11

Sample	Latitude	Longitude	Dec	Inc	Sun	UTC	Height (m)	Date
IAG11-17J	29.27310607	-113.3910375	286	63	274	20:41	4.5	23-Nov-11
IAG11-17F	29.27310607	-113.3910375	261	31	255	20:23	2.5	23-Nov-11
IAG11-18E	29.2726361	-113.3908552	351	71	333	20:56	3	23-Nov-11
IAG11-18J	29.2726361	-113.3908552	3	51	344	20:59	3	23-Nov-11
IAG11-18I	29.2726361	-113.3908552	340	63	321	20:59	3	23-Nov-11
IAG11-18H	29.2726361	-113.3908552	2	70	344	20:59	3	23-Nov-11
IAG11-18F	29.2726361	-113.3908552	350	80	332	20:57	3	23-Nov-11
IAG11-18D	29.2726361	-113.3908552	349	67	330	20:56	3	23-Nov-11
IAG11-18C	29.2726361	-113.3908552	6	68	348	20:55	3	23-Nov-11
IAG11-18B	29.2726361	-113.3908552	5	66	347	20:54	3	23-Nov-11
IAG11-18A	29.2726361	-113.3908552	4	50	346	20:54	3	23-Nov-11
IAG11-18G	29.2726361	-113.3908552	1	67	342	20:58	3	23-Nov-11
IAG11-19I	29.27288756	-113.3911896	256	82	234	21:21	2.5	23-Nov-11
IAG11-19J	29.27288756	-113.3911896	231	81	210	21:22	2.5	23-Nov-11
IAG11-19B	29.27288756	-113.3911896	247	84	226	21:18	2.5	23-Nov-11
IAG11-19O	29.27288756	-113.3911896	178	76	154	21:32	2.5	23-Nov-11
IAG11-19N	29.27288756	-113.3911896	177	81	151	21:31	2.5	23-Nov-11
IAG11-19M	29.27288756	-113.3911896	193	81	166	21:30	2.5	23-Nov-11
IAG11-19K	29.27288756	-113.3911896	172	81	148	21:28	2.5	23-Nov-11
IAG11-19A	29.27288756	-113.3911896	243	84	222	21:17	2.5	23-Nov-11
IAG11-19G	29.27288756	-113.3911896					2.5	23-Nov-11
IAG11-19L	29.27288756	-113.3911896	180	79	155	21:29	2.5	23-Nov-11
IAG11-19F	29.27288756	-113.3911896	259	81	239	21:20	2.5	23-Nov-11
IAG11-19E	29.27288756	-113.3911896	249	80	229	21:19	2.5	23-Nov-11
IAG11-19D	29.27288756	-113.3911896	241	82	220	21:19	2.5	23-Nov-11
IAG11-19H	29.27288756	-113.3911896	245	81	225	21:21	2.5	23-Nov-11
IAG11-19C	29.27288756	-113.3911896	258	87	237	21:18	2.5	23-Nov-11

Sample	Latitude	Longitude	Dec	Inc	Sun	UTC	Height (m)	Date
IAG11-20H	29.27271749	-113.3919684	240	74	195	23:23	3	23-Nov-11
IAG11-20P	29.27271749	-113.3919684	232	66	186	23:29	3	23-Nov-11
IAG11-20O	29.27271749	-113.3919684	242	58	194	23:33	3	23-Nov-11
IAG11-20N	29.27271749	-113.3919684	247	54	199	23:32	3	23-Nov-11
IAG11-20M	29.27271749	-113.3919684	232	66	186	23:28	3	23-Nov-11
IAG11-20L	29.27271749	-113.3919684	232	70	186	23:27	3	23-Nov-11
IAG11-20K	29.27271749	-113.3919684	233	71	188	23:26	3	23-Nov-11
IAG11-20I	29.27271749	-113.3919684	240	77	194	23:24	3	23-Nov-11
IAG11-20Q	29.27271749	-113.3919684	230	69	184	23:31	3	23-Nov-11
IAG11-20G	29.27271749	-113.3919684	178	72	131	23:22	3	23-Nov-11
IAG11-20F	29.27271749	-113.3919684	163	63	112	23:21	3	23-Nov-11
IAG11-20E	29.27271749	-113.3919684	174	69	129	23:19	3	23-Nov-11
IAG11-20D	29.27271749	-113.3919684	221	90	179	23:06	2.7	23-Nov-11
IAG11-20C	29.27271749	-113.3919684	226	84	184	23:05	2.7	23-Nov-11
IAG11-20B	29.27271749	-113.3919684	232	79	190	23:04	2.7	23-Nov-11
IAG11-20A	29.27271749	-113.3919684	222	80	180	23:03	2.7	23-Nov-11
IAG11-20J	29.27271749	-113.3919684	240	74	195	23:25	3	23-Nov-11
IAG11-21K	29.27246008	-113.3930588	315	67			3	24-Nov-11
IAG11-21L	29.27246008	-113.3930588	314	64			3	24-Nov-11
IAG11-21J	29.27246008	-113.3930588	318	72			3	24-Nov-11
IAG11-21I	29.27246008	-113.3930588	241	82			3	24-Nov-11
IAG11-21H	29.27246008	-113.3930588	334	73			3	24-Nov-11
IAG11-21F	29.27246008	-113.3930588	225	75	245	18:56	3	24-Nov-11
IAG11-21E	29.27246008	-113.3930588	221	95			3	24-Nov-11
IAG11-21D	29.27246008	-113.3930588	222	99			3	24-Nov-11
IAG11-21C	29.27246008	-113.3930588	220	98			3	24-Nov-11
IAG11-21A	29.27246008	-113.3930588	233	68			3	24-Nov-11

Sample	Latitude	Longitude	Dec	Inc	Sun	UTC	Height (m)	Date
IAG11-21G	29.27246008	-113.3930588	334	78			3	24-Nov-11
IAG11-21B	29.27246008	-113.3930588	222	95			3	24-Nov-11
IAG11-22B	29.27049411	-113.3936322	0	70	358	19:54	3.6	24-Nov-11
IAG11-22G	29.27049411	-113.3936322	37	97	31	20:13	1.5	24-Nov-11
IAG11-22F	29.27049411	-113.3936322	50	66	44	20:13	1.5	24-Nov-11
IAG11-22E	29.27049411	-113.3936322	73	95	68	20:12	1.5	24-Nov-11
IAG11-22C	29.27049411	-113.3936322	12	69	11	19:56	3	24-Nov-11
IAG11-22A	29.27049411	-113.3936322	3	83	2	19:53	4	24-Nov-11
IAG11-22D	29.27049411	-113.3936322	55	115	50	20:11	3	24-Nov-11
IAG11-23E	29.27086978	-113.3922368	198	36	168	21:59	4	24-Nov-11
IAG11-23F	29.27086978	-113.3922368	183	32	153	22:01	4	24-Nov-11
IAG11-23G	29.27086978	-113.3922368	203	49	172	22:02	4	24-Nov-11
IAG11-23I	29.27086978	-113.3922368	195	24	163	22:03	4	24-Nov-11
IAG11-23C	29.27086978	-113.3922368	211	30	181	21:57	4	24-Nov-11
IAG11-23B	29.27086978	-113.3922368	8	26	338	21:54	4	24-Nov-11
IAG11-23A	29.27086978	-113.3922368	341	45	310	21:52	4	24-Nov-11
IAG11-23D	29.27086978	-113.3922368	188	33	158	21:58	4	24-Nov-11
IAG11-23H	29.27086978	-113.3922368	170	33	140	22:03	4	24-Nov-11
IAG11-24E	29.26915878	-113.3944991	121	19			4	24-Nov-11
IAG11-24A	29.26915878	-113.3944991	127	21			4	24-Nov-11
IAG11-24B	29.26915878	-113.3944991	108	80			4	24-Nov-11
IAG11-24C	29.26915878	-113.3944991	122	29			4	24-Nov-11
IAG11-24D	29.26915878	-113.3944991	197	25			4	24-Nov-11
IAG11-25BLOCK	29.27872019	-113.416737	229	76	198	21:50		25-Nov-11
IAG11-26BLOCK	29.26491888	-113.4106195	262	70	217	23:12		25-Nov-11
IAG11-27I	29.27161099	-113.3927938	160	25	174	19:20	12	26-Nov-11
IAG11-27H	29.27161099	-113.3927938	163	90	180	19:18	11	26-Nov-11

Sample	Latitude	Longitude	Dec	Inc	Sun	UTC	Height (m)	Date
IAG11-27Q	29.27161099	-113.3927938	146	89	155	19:32	8	26-Nov-11
IAG11-27P	29.27161099	-113.3927938	146	75	155	19:31	8	26-Nov-11
IAG11-27O	29.27161099	-113.3927938	154	88	163	19:30	8	26-Nov-11
IAG11-27N	29.27161099	-113.3927938	170	92	180	19:29	8	26-Nov-11
IAG11-27M	29.27161099	-113.3927938	170	92	180	19:29	8	26-Nov-11
IAG11-27L	29.27161099	-113.3927938	162	89	171	19:28	8	26-Nov-11
IAG11-27K	29.27161099	-113.3927938	148	34	160	19:25	12	26-Nov-11
IAG11-27G	29.27161099	-113.3927938	164	94	179	19:17	11	26-Nov-11
IAG11-27F	29.27161099	-113.3927938	166	94	179	19:17	11	26-Nov-11
IAG11-27E	29.27161099	-113.3927938	167	96	180	19:16	11	26-Nov-11
IAG11-27D	29.27161099	-113.3927938	166	78	180	19:15	11	26-Nov-11
IAG11-27C	29.27161099	-113.3927938	118	31	134	19:12	6	26-Nov-11
IAG11-27B	29.27161099	-113.3927938	128	26	143	19:10	6	26-Nov-11
IAG11-27A	29.27161099	-113.3927938	175	76	182	19:09	6	26-Nov-11
IAG11-27J	29.27161099	-113.3927938	150	32	164	19:23	12	26-Nov-11
IAG11-27AA	29.27161099	-113.3927938	119	37	136	19:07	4.5	26-Nov-11
IAG11-28X	29.26924604	-113.3950119	345	55			1.5	26-Nov-11
IAG11-28N	29.26924604	-113.3950119	265	30			1.5	26-Nov-11
IAG11-28O	29.26924604	-113.3950119	274	23			1.5	26-Nov-11
IAG11-28P	29.26924604	-113.3950119	291	20			1.5	26-Nov-11
IAG11-28Q	29.26924604	-113.3950119	344	29			1.5	26-Nov-11
IAG11-28Y	29.26924604	-113.3950119	46	77			1.5	26-Nov-11
IAG11-28S	29.26924604	-113.3950119	336	89			1.5	26-Nov-11
IAG11-28U	29.26924604	-113.3950119	346	96			1.5	26-Nov-11
IAG11-28W	29.26924604	-113.3950119	344	54			1.5	26-Nov-11
IAG11-28R	29.26924604	-113.3950119	356	27			1.5	26-Nov-11
IAG11-28M	29.26924604	-113.3950119	327	41			1.5	26-Nov-11

Sample	Latitude	Longitude	Dec	Inc	Sun	UTC	Height (m)	Date
IAG11-28V	29.26924604	-113.3950119	343	29			1.5	26-Nov-11
IAG11-28D	29.26924604	-113.3950119	207	83			1.5	26-Nov-11
IAG11-28L	29.26924604	-113.3950119	185	57			1.5	26-Nov-11
IAG11-28T	29.26924604	-113.3950119	340	83			1.5	26-Nov-11
IAG11-28A	29.26924604	-113.3950119	181	21	151	21:58	5	26-Nov-11
IAG11-28C	29.26924604	-113.3950119	204	84			1.5	26-Nov-11
IAG11-28E	29.26924604	-113.3950119	205	81			1.5	26-Nov-11
IAG11-28F	29.26924604	-113.3950119	204	81			1.5	26-Nov-11
IAG11-28G	29.26924604	-113.3950119	189	84			1.5	26-Nov-11
IAG11-28H	29.26924604	-113.3950119	191	86			1.5	26-Nov-11
IAG11-28I	29.26924604	-113.3950119	190	89			1.5	26-Nov-11
IAG11-28J	29.26924604	-113.3950119	186	63			1.5	26-Nov-11
IAG11-28K	29.26924604	-113.3950119	193	60			1.5	26-Nov-11
IAG11-28B	29.26924604	-113.3950119	123	71	91	22:06	5	26-Nov-11
IAG11-29A	29.27070156	-113.3957262	359	74	19	19:06	4	27-Nov-11
IAG11-29H	29.27070156	-113.3957262	61	92	67	19:32	4	27-Nov-11
IAG11-29K	29.27070156	-113.3957262	63	87	68	19:35	4	27-Nov-11
IAG11-29J	29.27070156	-113.3957262	61	87	66	19:34	4	27-Nov-11
IAG11-29I	29.27070156	-113.3957262	60	88	67	19:33	4	27-Nov-11
IAG11-29G	29.27070156	-113.3957262					4	27-Nov-11
IAG11-29F	29.27070156	-113.3957262	149	96	172	19:13	4	27-Nov-11
IAG11-29E	29.27070156	-113.3957262	142	93	166	19:13	4	27-Nov-11
IAG11-29D	29.27070156	-113.3957262	15	84	32	19:09	4	27-Nov-11
IAG11-29B	29.27070156	-113.3957262	358	77	18	19:07	4	27-Nov-11
IAG11-29C	29.27070156	-113.3957262	33	67	54	19:08	4	27-Nov-11
IAG11-30D	29.26957285	-113.3963192	183	55	158	21:40	4	27-Nov-11
IAG11-30E	29.26957285	-113.3963192	252	62	226	21:41	4	27-Nov-11

Sample	Latitude	Longitude	Dec	Inc	Sun	UTC	Height (m)	Date
IAG11-30B	29.26957285	-113.3963192	216	99	191	21:37	4	27-Nov-11
IAG11-30A	29.26957285	-113.3963192	202	85	178	21:35	4	27-Nov-11
IAG11-30C	29.26957285	-113.3963192	189	58	164	21:38	4	27-Nov-11
IAG11-31B	29.26791684	-113.3973573	235	40	202	22:17		27-Nov-11
IAG11-31C	29.26791684	-113.3973573	239	32	205	22:19		27-Nov-11
IAG11-31D	29.26791684	-113.3973573	240	39	205	22:20		27-Nov-11
IAG11-31E	29.26791684	-113.3973573	183	19	149	22:21		27-Nov-11
IAG11-31F	29.26791684	-113.3973573	186	25	152	22:23		27-Nov-11
IAG11-31G	29.26791684	-113.3973573	190	87	156	22:23		27-Nov-11
IAG11-31A	29.26791684	-113.3973573	244	33	210	22:16		27-Nov-11
IAG11-32E	29.2675244	-113.3951887	166	67	123	23:11		27-Nov-11
IAG11-32F	29.2675244	-113.3951887	169	59	126	23:13		27-Nov-11
IAG11-32C	29.2675244	-113.3951887	175	84	134	23:08		27-Nov-11
IAG11-32B	29.2675244	-113.3951887	166	11	125	23:07		27-Nov-11
IAG11-32A	29.2675244	-113.3951887	151	63	118	23:06		27-Nov-11
IAG11-32D	29.2675244	-113.3951887	166	83	124	23:10		27-Nov-11
IAG11-33BLOCK	29.26382731	-113.4085349						28-Nov-11
IAG11-34BLOCK	29.26382731	-113.4085349						28-Nov-11
IAG11-35BLOCK	29.25832886	-113.3981805	336	40				28-Nov-11
IAG11-36BLOCK	29.25843	-113.40449						28-Nov-11
IAG11-37BLOCK	29.25486395	-113.4155592						28-Nov-11
IAG11-38BLOCK	29.24890065	-113.4238805						28-Nov-11
IAG11-39BLOCK	29.27267038	-113.3864199	140	40	132	19:48		26-Nov-11
IAG11-40BLOCK	29.27240912	-113.386494	22	69	10	20:01		26-Nov-11
IAG11-41BLOCK	29.26757477	-113.3953397	70	82	25	22:08		27-Nov-11
IAG11-42BLOCK	29.26622805	-113.3965043	163	63	110	22:27		27-Nov-11
IAG11-43BLOCK	29.26643995	-113.3969621	167	84	114	22:51		27-Nov-11

Sample	Latitude	Longitude	Dec	Inc	Sun	UTC	Height (m)	Date
IAG11-44BLOCK	29.26643961	-113.3969605						27-Nov-11

Table 2. AMS Results

Specimen	L	F	Pj	D1	D2	D3	I1	I2	I3	Norm
1B1	1.008	1.04	1.052	230	51	321	42	48	1	1541
1C1	1.005	1.039	1.049	248	40	141	49	37	14	1681.1
1A1	1.01	1.038	1.051	224	65	323	38	50	10	1096.9
1F2	1.003	1.036	1.044	236	64	329	39	50	4	2866.4
1A2	1.007	1.039	1.05	223	50	315	35	54	4	1633.2
1D1	1.014	1.031	1.047	162	71	341	58	1	32	1385.7
1D2	1.017	1.022	1.039	167	67	335	62	5	28	1510.4
1E1	1.007	1.04	1.051	230	58	323	35	55	4	2118
1F1	1.004	1.035	1.044	229	76	323	21	67	10	1280.7
1G1	1.006	1.032	1.041	220	44	312	38	52	2	905.4
1E2	1.011	1.033	1.047	228	34	136	21	68	5	961.99
1F3	1.007	1.031	1.04	228	56	319	20	70	3	751.02
2J1	1.006	1.032	1.041	59	314	151	6	67	23	3078.8
2E1	1.009	1.031	1.042	57	290	154	18	61	21	1770.6
2B1	1.014	1.034	1.049	49	309	139	2	78	12	1111.2
2N1	1.002	1.008	1.01	143	321	53	19	71	1	5638.3
2BB2	1.005	1.011	1.016	89	345	183	8	58	31	2546.3
2BB1	1.002	1.009	1.012	12	266	171	59	9	29	2624
2W2	1.004	1.009	1.013	340	76	177	34	8	54	5343.9
2X1	1.004	1.007	1.012	38	300	173	22	19	60	4947
2R1	1.001	1.01	1.012	138	300	45	26	63	8	4000.6
2K1	1.002	1.006	1.009	116	357	231	31	40	35	6866.6
2C1	1.014	1.033	1.049	226	19	134	11	77	6	1078.6
2O1	1.005	1.006	1.011	143	295	26	82	8	4	5642
2A1	1.017	1.034	1.053	244	80	335	14	75	4	1093.1

Specimen	L	F	Pj	D1	D2	D3	I1	I2	I3	Norm
2W1	1.002	1.01	1.013	3	270	175	35	4	55	4784.3
2D1	1.014	1.041	1.057	220	34	130	15	75	2	1330.9
2Y1	1.009	1.005	1.014	103	1	210	15	37	49	2678
2N2	1.002	1.007	1.009	134	321	226	31	58	3	5274.6
2U1	1.003	1.009	1.012	320	52	157	20	6	69	4363.1
2X2	1.003	1.007	1.01	50	310	154	12	40	48	5460.1
2S1	1.004	1.009	1.013	328	61	182	16	10	71	4426.1
2Z1	1.002	1.009	1.012	101	354	199	12	54	34	1927.2
2Q1	1.002	1.006	1.009	161	65	251	1	78	11	3157.7
2H1	1.002	1.047	1.056	51	290	148	15	61	24	2574.2
2B2	1.011	1.042	1.056	237	0	145	8	76	12	934.57
2X3	1.003	1.011	1.015	347	79	179	24	4	66	3021
2D1	1.013	1.039	1.054	223	48	313	7	83	1	753.91
2S2	1.001	1.011	1.014	314	47	181	13	14	71	3515.3
2M1	1.003	1.006	1.009	136	17	238	20	53	30	3354.5
2U2	1.003	1.012	1.016	318	52	185	15	16	68	3804
2O2	1.003	1.004	1.007	130	275	28	34	50	18	2007.1
2I1	1.045	1.007	1.057	335	197	88	44	38	22	4072.8
2P1	1.002	1.007	1.01	287	122	18	11	79	3	1532.6
2C2	1.012	1.041	1.056	227	29	137	5	85	2	389.76
2F1	1.008	1.025	1.035	42	268	139	20	62	18	1307.2
2V1	1.005	1.009	1.015	323	233	143	38	0	52	4748.3
3L2	1.008	1.008	1.015	278	128	14	26	60	13	1776.1
3J1	1.006	1.008	1.014	277	178	13	8	50	39	2774.7
3L1	1.006	1.006	1.011	254	144	3	21	42	41	1889.9
3A1	1.004	1.007	1.011	78	317	180	21	52	30	6786.8
3F1	1.001	1.01	1.012	300	59	205	12	67	20	5226.8

Specimen	L	F	Pj	D1	D2	D3	I1	I2	I3	Norm
3B1	1.004	1.007	1.01	85	324	199	31	40	34	7276.2
3H1	1.004	1.009	1.014	267	106	6	41	47	10	2871.1
3O1	1.006	1.008	1.015	264	134	9	28	50	26	1347.5
3D1	1.001	1.009	1.011	108	276	13	40	49	6	6682.1
3C1	1.002	1.009	1.012	83	289	187	44	43	13	6848.7
3E1	1.003	1.01	1.013	96	283	186	3	87	0	4677.1
3M1	1.005	1.01	1.015	265	129	6	27	55	21	1817.8
3K2	1.005	1.007	1.013	283	116	20	46	43	7	1794.6
3I1	1.003	1.008	1.011	247	128	15	41	29	35	2788.4
3N1	1.002	1.012	1.015	260	126	6	32	48	24	1778.5
3K1	1.006	1.008	1.014	263	109	12	57	31	12	1780
3G1	1.01	1.005	1.015	280	149	26	31	48	25	5071.8
3B2	1.001	1.01	1.012	37	296	199	51	9	37	4252.3
3M2	1.008	1.008	1.017	268	117	15	49	38	15	956.03
3L3	1.01	1.009	1.019	249	113	0	39	41	24	799.74
3H2	1.007	1.007	1.014	278	179	13	7	53	37	1258
3K3	1.006	1.006	1.012	268	147	16	27	45	33	576.52
3N2	1.015	1.02	1.035	268	80	177	21	69	3	805.71
3J2	1.006	1.009	1.015	263	131	13	35	44	26	954.75
3A2	1.005	1.003	1.008	87	346	184	9	50	39	2286.2
3F2	1.005	1.012	1.017	297	81	202	20	66	13	2113.1
4K2	1.002	1.008	1.01	285	83	182	49	39	11	4248.5
4J2	1.001	1.009	1.011	312	91	183	75	12	10	6009.6
4I2	1.002	1.007	1.009	269	38	170	21	58	22	6309.4
4G1	1.002	1.008	1.011	72	262	164	26	64	4	5866.5
4F2	1.001	1.006	1.008	70	277	169	34	53	13	6138.1
4J1	1.002	1.008	1.01	72	280	178	48	39	14	6512.5

Specimen	L	F	Pj	D1	D2	D3	I1	I2	I3	Norm
4L1	1.002	1.006	1.009	77	334	168	2	79	10	3683.1
4D1	1.002	1.006	1.008	80	252	344	59	31	3	5935.7
4E2	1.002	1.01	1.012	86	277	185	66	24	4	5988.9
4I1	1.003	1.006	1.009	270	39	168	25	54	25	5054.3
4C1	1.003	1.007	1.011	92	288	195	66	23	6	6205.8
4K1	1.006	1.01	1.016	344	95	190	61	11	26	6355.3
4G2	1.002	1.008	1.011	67	245	337	16	74	1	4952.8
4H1	1	1.01	1.012	250	12	153	16	62	23	6310.9
4F1	1.001	1.008	1.01	61	265	172	67	21	9	6004.1
4E1	1.002	1.008	1.011	91	272	182	78	12	0	5745.6
4D2	1.002	1.009	1.011	80	251	342	78	12	2	5303.8
4J3	1.002	1.009	1.012	51	262	167	63	24	13	2865.9
4E3	1.001	1.007	1.009	283	107	14	43	47	2	2664.6
4L2	1.003	1.006	1.01	80	343	171	3	68	22	4839.9
4B1	1.011	1.037	1.051	293	105	203	12	78	2	446.03
4A1	1.018	1.027	1.046	297	46	206	4	78	11	527.36
4C2	1.001	1.009	1.011	95	282	192	68	21	2	6091.3
4C3	1.001	1.008	1.011	94	261	4	6	84	1	3049.2
5K1	1.006	1.047	1.059	105	226	15	2	87	3	3931.2
5B1	1.008	1.043	1.056	134	255	37	16	61	23	1163.1
5H2	1.004	1.049	1.059	288	108	198	18	72	0	2506.5
5H3	1.006	1.04	1.05	283	86	193	7	83	2	4010.1
5J1	1.003	1.046	1.055	111	280	20	22	68	4	3062.6
5A1	1.016	1.037	1.054	126	265	29	23	61	17	990.46
5A2	1.019	1.027	1.046	124	252	29	15	67	17	966.39
5H1	1.004	1.044	1.053	289	113	20	12	78	1	3980
5I1	1.001	1.051	1.06	283	112	16	29	60	4	3902

Specimen	L	F	Pj	D1	D2	D3	I1	I2	I3	Norm
5G1	1.006	1.048	1.06	277	124	10	18	70	8	2263.6
5K2	1.006	1.046	1.058	288	118	18	5	85	1	1002.9
6C1	1.002	1.025	1.029	113	259	4	45	39	18	1135.2
6H1	1.003	1.021	1.026	30	282	187	62	9	26	3101.1
6G1	1.001	1.02	1.023	293	73	183	41	41	21	2756.9
6I1	1.003	1.022	1.027	297	84	181	61	25	14	3107.4
6L1	1.003	1.02	1.025	90	346	190	12	49	38	2120.8
6F1	1.001	1.022	1.026	297	70	176	48	32	25	2289.6
6A1	1.014	1.015	1.03	284	72	187	26	60	14	1928.9
6J1	1.002	1.023	1.028	55	284	180	50	28	25	2768
6K1	1.001	1.026	1.031	331	81	177	59	11	28	2926.4
6B1	1.001	1.025	1.03	28	265	171	70	11	17	2371.6
6E1	1.003	1.023	1.028	282	72	183	33	54	14	2184
6M1	1.006	1.024	1.032	280	47	151	52	26	26	2241.6
6D1	1.002	1.022	1.027	290	79	180	52	34	15	1871.4
7K1	1.008	1.058	1.072	42	287	191	62	12	24	3642.8
7C1	1.003	1.05	1.06	77	289	169	12	75	7	3849.6
7N1	1.002	1.043	1.051	259	28	167	10	74	12	3264.4
7A1	1.004	1.034	1.042	31	259	167	79	8	8	2957.8
7O1	1.003	1.044	1.053	272	64	172	34	52	14	3214.2
7H1	1.004	1.033	1.041	83	289	179	26	61	11	3618.2
7L1	1.01	1.038	1.051	50	286	189	61	17	23	3117.7
7G2	1.003	1.043	1.051	79	278	184	61	27	8	2493.6
7B1	1.004	1.048	1.059	80	339	170	1	86	4	3327.2
7J1	1.003	1.051	1.061	74	278	185	68	20	8	2750.8
7F1	1.002	1.049	1.058	82	301	191	40	42	21	2230.4
7G1	1.005	1.044	1.054	63	274	177	58	28	14	3516.5

Specimen	L	F	Pj	D1	D2	D3	I1	I2	I3	Norm
7D2	1.006	1.04	1.05	265	32	169	15	66	18	1361.6
7D1	1.005	1.041	1.051	270	56	172	28	58	15	1942.4
7Q2	1.006	1.044	1.055	266	66	174	20	68	7	1934.7
7Q1	1.003	1.044	1.053	278	79	184	27	62	8	3595.9
7E1	1.016	1.016	1.032	263	51	165	29	57	14	2497
8B1	1.005	1.043	1.053	96	278	186	19	71	1	3699
8D1	1.006	1.049	1.061	92	260	359	29	60	5	3427.8
8Q1	1.003	1.029	1.036	107	358	212	18	47	38	1831.8
8F1	1.006	1.053	1.066	104	257	3	39	48	14	3505.1
8K1	1.005	1.052	1.063	96	231	6	3	86	3	3753
8C1	1.005	1.051	1.063	100	246	4	23	62	13	3789.7
8E1	1.006	1.05	1.062	95	255	360	29	59	9	3607.6
8J2	1.003	1.053	1.063	84	235	353	10	78	6	3660.5
8J1	1.003	1.053	1.063	88	259	355	37	53	5	3496.8
8A1	1.003	1.051	1.062	90	306	180	8	81	6	3798.9
8G2	1.004	1.053	1.064	89	218	358	5	82	6	3741.5
8O1	1.008	1.026	1.036	87	342	204	22	34	48	2021.1
8H1	1.005	1.054	1.066	272	150	2	2	87	3	3594.5
8M1	1.006	1.024	1.032	98	4	215	11	20	67	1978.5
8P1	1.006	1.027	1.035	98	352	223	26	28	50	1921.4
8G1	1.005	1.053	1.065	86	252	355	18	71	4	3163.7
8H2	1.005	1.052	1.064	102	244	10	10	78	7	2474.8
8N1	1.005	1.027	1.034	81	332	192	21	39	43	1865.3
8K2	1.007	1.048	1.06	92	265	2	12	78	1	1420.3
8I1	1.009	1.05	1.064	102	253	10	14	74	7	1669.8
8B2	1.008	1.032	1.043	277	157	7	2	87	3	2118.9
8E2	1.007	1.049	1.062	104	259	7	31	56	11	1238.2

Specimen	L	F	Pj	D1	D2	D3	I1	I2	I3	Norm
8E2	1.008	1.049	1.062	103	257	6	30	57	12	1238.3
8D2	1.007	1.05	1.063	103	257	8	25	63	10	1044.6
8N2	1.006	1.028	1.037	86	343	188	13	46	42	783.84
8O2	1.006	1.028	1.036	90	347	203	18	35	49	707.76
8C2	1.007	1.047	1.06	103	238	7	19	64	17	942.92
9B1	1.001	1.002	1.003	334	243	150	29	1	61	6082.6
9G1	1	1.002	1.002	238	113	3	45	30	30	5532.1
9D1	1.001	1.001	1.002	120	229	10	21	40	42	8799.7
9E1	1.002	1.002	1.003	110	202	9	4	20	69	5782.5
10J1	1.004	1.043	1.052	324	55	159	19	5	70	1253.4
10N1	1.006	1.042	1.052	340	249	137	7	3	82	3783.8
10O2	1.003	1.039	1.047	303	39	155	24	13	62	3539.4
10P2	1.004	1.041	1.05	308	41	143	25	6	64	3716.7
10P2	1.003	1.041	1.049	305	39	146	24	8	65	3714.4
10L1	1.006	1.036	1.046	35	297	158	17	24	60	2257.6
10P1	1.007	1.04	1.051	327	58	156	24	4	65	3799
10D1	1.005	1.028	1.036	354	91	242	13	28	59	961.62
10O1	1.007	1.042	1.053	333	64	161	22	3	68	3378.1
10C1	1.018	1.021	1.039	110	320	207	26	61	13	1083.3
10G1	1.011	1.017	1.028	80	336	197	21	32	50	967.15
10A1	1.013	1.029	1.043	96	297	190	26	62	9	911.58
10P3	1.005	1.04	1.05	328	237	139	21	3	69	1450.3
10K1	1.007	1.048	1.06	333	242	134	4	1	86	1474.3
10F1	1.009	1.02	1.03	28	118	218	14	2	76	851.87
10H1	1.01	1.025	1.036	73	321	207	39	25	41	383.5
10B1	1.012	1.028	1.041	116	335	210	15	71	12	750.75
11M1	1.007	1.044	1.056	295	66	200	16	67	17	3146.8

Specimen	L	F	Pj	D1	D2	D3	I1	I2	I3	Norm
11G1	1.009	1.022	1.032	102	200	12	1	79	11	3087.7
11I1	1.009	1.028	1.039	271	141	7	17	65	18	3244
11E1	1.004	1.029	1.036	286	130	24	34	53	12	1197.2
11Q1	1.005	1.044	1.055	282	109	13	19	71	2	2950.3
11I1	1.008	1.024	1.033	267	132	2	17	67	16	3403.6
11C1	1.006	1.029	1.038	290	169	22	7	76	11	1180.9
11F2	1.008	1.025	1.035	283	185	13	2	76	14	1244.8
11E2	1.007	1.03	1.04	110	216	20	3	78	11	1234.5
11J1	1.006	1.036	1.045	277	121	10	20	69	8	2774.8
11K1	1.009	1.032	1.044	97	240	7	6	83	4	3365.6
11H1	1.005	1.028	1.036	271	100	4	33	56	4	2622
11E3	1.006	1.036	1.046	285	141	17	13	74	9	1229.8
11C2	1.005	1.029	1.036	295	188	25	3	79	11	1191.9
11B1	1.007	1.025	1.034	300	86	209	9	79	6	1146.5
11C3	1.009	1.031	1.043	283	154	15	11	73	13	1148.5
11J2	1.009	1.034	1.045	276	144	9	12	73	12	1128.5
11K2	1.008	1.03	1.04	98	248	8	8	81	5	3159.5
11P1	1.006	1.045	1.056	265	86	355	28	62	0	3830.4
11D2	1.008	1.027	1.036	290	127	20	12	78	4	1228.1
11L1	1.007	1.047	1.059	274	55	184	4	84	4	2269.8
11A1	1.006	1.01	1.016	41	140	231	70	3	20	1044.3
11D1	1.012	1.025	1.038	295	123	25	10	80	1	891.94
11P2	1.006	1.047	1.059	279	92	189	10	80	1	2874.8
11F3	1.005	1.033	1.042	289	198	19	0	79	11	1332.1
11F1	1.01	1.028	1.04	284	154	16	9	76	10	1250
11G2	1.012	1.023	1.036	274	146	7	10	73	13	1354.5
11B2	1.01	1.029	1.041	303	60	211	6	77	11	408.92

Specimen	L	F	Pj	D1	D2	D3	I1	I2	I3	Norm
11G3	1.008	1.027	1.037	102	220	11	5	80	9	1032.3
12I1	1.006	1.031	1.04	328	70	194	27	22	54	2319.6
12K1	1.004	1.03	1.037	299	31	198	4	20	70	2064.3
12K2	1.004	1.031	1.039	307	40	193	9	20	68	2482.5
12C1	1.004	1.031	1.038	285	117	18	30	60	5	1648.8
12F1	1.003	1.037	1.045	329	127	218	78	11	4	1493.3
12D3	1.003	1.027	1.032	261	93	359	51	39	6	1507.5
12D1	1.005	1.027	1.034	278	103	12	66	24	2	801.34
12C2	1.007	1.026	1.035	284	145	16	13	73	10	1492.6
12G1	1.002	1.026	1.032	286	105	196	17	73	0	2036.5
12J1	1.004	1.023	1.029	314	48	205	9	22	66	2400.8
12L1	1.005	1.029	1.037	64	160	302	15	21	64	895.33
12G2	1.003	1.031	1.038	298	83	207	7	81	5	831.97
12H1	1.004	1.024	1.031	292	31	184	13	34	53	1349.7
12F2	1.004	1.03	1.037	316	119	224	19	70	5	1660.1
12E1	1.013	1.018	1.032	313	165	45	13	75	8	1350.3
12I2	1.006	1.028	1.037	313	53	192	19	27	56	1837.5
12M1	1.002	1.045	1.053	347	87	219	22	24	56	2116.9
12D2	1.004	1.025	1.031	262	86	353	36	54	2	1675.2
12K3	1.008	1.027	1.037	323	57	198	13	17	68	1408.5
12A1	1.008	1.029	1.039	69	309	211	58	17	26	549.13
13G1	1.008	1.03	1.04	282	110	13	19	71	2	3674.1
13A2	1.002	1.046	1.055	280	99	190	24	66	1	3196
13A3	1.004	1.042	1.051	283	95	190	35	54	4	3052.4
13E3	1.003	1.047	1.056	275	100	9	65	25	2	3292.3
13F4	1.004	1.047	1.057	276	103	10	47	43	4	3100.5
13F2	1.004	1.047	1.057	89	280	183	40	49	6	3163.5

Specimen	L	F	Pj	D1	D2	D3	I1	I2	I3	Norm
13E1	1.001	1.047	1.055	283	97	188	72	17	2	3335.3
13B1	1.002	1.047	1.056	281	104	13	51	39	2	3319.5
13B2	1.004	1.046	1.056	280	101	11	51	39	1	3070.4
13D3	1.003	1.053	1.063	293	95	196	38	51	9	3435.8
13C1	1.005	1.052	1.063	279	113	11	24	65	5	3051.1
13D5	1.004	1.05	1.061	286	85	192	26	63	9	3517
13G2	1.002	1.047	1.056	282	106	12	19	71	1	3416.7
13C4	1.002	1.048	1.056	280	103	11	38	52	2	2949.3
13C5	1.003	1.044	1.053	277	102	11	69	21	2	3389.4
13A1	1.002	1.049	1.058	274	95	4	21	69	0	3374.6
13D1	1.004	1.052	1.063	290	83	193	28	59	12	3532.9
13G3	1	1.045	1.052	277	118	8	10	79	4	3586.6
13C3	1.005	1.053	1.064	282	110	15	37	53	4	2965.8
13F1	1.002	1.049	1.058	275	100	8	61	29	2	3470
13B4	1.004	1.05	1.061	286	103	195	36	54	1	3355.1
13B3	1.004	1.046	1.056	285	104	194	58	32	1	3468.9
13A4	1.004	1.043	1.053	287	99	192	51	39	4	1890
13D4	1.003	1.052	1.062	280	87	187	28	62	5	3576.8
13F3	1.004	1.048	1.058	97	274	7	10	80	0	3589
13H2	1.005	1.047	1.058	272	107	7	34	55	7	3496
13E2	1.003	1.049	1.059	290	109	200	46	44	1	3415.9
13D2	1.004	1.048	1.059	283	79	189	24	64	9	3459.3
13C2	1.003	1.051	1.062	285	109	16	32	58	2	3317.4
13D6	1.004	1.048	1.058	292	96	196	36	53	8	1167.2
13G4	1.006	1.041	1.052	286	121	16	13	77	3	1457.9
13H1	1.006	1.047	1.058	271	110	7	33	55	9	1779.4
14F3	1.006	1.029	1.037	95	247	354	37	49	14	2618.1

Specimen	L	F	Pj	D1	D2	D3	I1	I2	I3	Norm
14A3	1.005	1.03	1.039	148	278	8	86	2	3	3174.9
14B2	1.007	1.035	1.045	104	270	9	36	53	7	3110
14C1	1.007	1.033	1.043	92	260	355	49	40	6	3241.5
14A1	1.006	1.036	1.046	94	251	344	67	22	8	2860.3
14D1	1.007	1.034	1.045	104	263	358	60	28	9	2816.2
14F1	1.008	1.031	1.042	100	241	360	28	55	19	2965.4
14E1	1.007	1.036	1.046	101	263	2	43	45	9	2900.2
14B1	1.006	1.033	1.042	100	245	6	19	68	12	3133.4
14C2	1.008	1.03	1.041	104	257	0	44	43	14	3024.7
14D2	1.009	1.034	1.046	93	248	348	49	38	13	3083
14F2	1.013	1.034	1.049	119	264	8	48	36	18	2421.5
14A2	1.002	1.033	1.04	110	274	10	51	38	8	2847.3
14C3	1.006	1.033	1.042	88	271	180	42	48	1	1730.7
14E2	1.009	1.035	1.048	107	254	7	32	54	16	1365.8
15A1	1.008	1.003	1.011	94	347	204	20	40	43	4483.8
15C3	1.011	1.001	1.013	92	331	193	21	54	29	4806.5
15B2	1.01	1.001	1.012	90	345	207	22	33	49	4883
15C2	1.009	1.001	1.011	88	333	194	21	47	35	4669.9
15B1	1.009	1.001	1.011	90	342	202	22	38	44	4632.7
15C1	1.002	1.007	1.009	147	52	245	6	39	51	4102.6
16B1	1.005	1.035	1.044	263	23	170	11	69	18	2439.5
16D1	1.004	1.042	1.051	260	69	167	30	59	5	2657.1
16I2	1.004	1.04	1.048	53	308	147	8	63	26	2486.6
16D3	1.009	1.041	1.054	269	66	174	26	62	9	2481.7
16K1	1.007	1.037	1.047	247	64	157	25	65	1	2847.3
16C1	1.007	1.036	1.046	257	50	158	33	54	13	2434.4
16E2	1.006	1.041	1.051	77	312	170	11	71	15	2444.2

Specimen	L	F	Pj	D1	D2	D3	I1	I2	I3	Norm
16H1	1.004	1.041	1.05	261	36	167	14	70	14	2314.2
16H2	1.009	1.035	1.047	261	53	162	32	55	13	2128.6
16E1	1.007	1.04	1.051	276	55	177	24	59	18	2225.4
16I1	1.004	1.035	1.043	247	342	156	2	68	22	2428.9
16A1	1.007	1.024	1.032	71	316	165	10	68	20	2414.5
16J1	1.005	1.046	1.057	244	357	151	8	70	18	2294.3
16D2	1.008	1.037	1.049	261	56	167	22	66	9	2511.9
16F1	1.009	1.039	1.051	276	55	177	26	57	19	1007.1
16E3	1.008	1.038	1.05	277	62	180	24	62	14	1008.9
16K2	1.008	1.034	1.045	250	67	159	38	52	2	1175.4
16I3	1.005	1.036	1.045	52	309	144	6	67	23	1221.6
16G1	1.009	1.036	1.048	264	19	173	5	77	12	1034.1
17A1	1.007	1.027	1.037	25	291	188	29	8	60	1693.5
17M1	1.004	1.04	1.05	352	92	188	54	7	35	3000.8
17L1	1.006	1.042	1.052	12	272	173	46	9	43	2764.4
17C1	1.004	1.024	1.031	13	277	169	28	11	60	2126.1
17G1	1.005	1.027	1.035	165	275	28	39	23	42	2100.7
17D1	1.007	1.027	1.036	19	289	195	26	2	64	2048.1
17B1	1.004	1.03	1.037	19	283	179	33	9	56	1369.4
17K1	1.001	1.042	1.05	18	277	180	49	9	39	1324.1
17E1	1.005	1.029	1.037	68	323	208	35	21	48	1388.7
17G2	1.003	1.023	1.029	191	289	23	57	5	33	1691
17H1	1.008	1.04	1.052	36	296	196	45	10	43	2067.8
18D2	1.005	1.039	1.049	277	62	179	26	59	15	2914.9
18A1	1.007	1.041	1.052	304	51	199	16	45	41	3607.9
18I1	1.002	1.045	1.054	273	42	179	14	69	16	3332.3
18C1	1.009	1.032	1.044	296	51	198	15	59	27	3206.9

Specimen	L	F	Pj	D1	D2	D3	I1	I2	I3	Norm
18D1	1.008	1.041	1.053	283	62	185	24	59	18	3540.3
18B1	1.005	1.038	1.048	283	27	191	6	68	21	3398
18B2	1.004	1.041	1.049	95	358	186	3	64	26	3083.6
18J1	1.002	1.048	1.057	280	56	171	37	44	24	3282.7
18G1	1.005	1.049	1.06	271	52	176	20	65	14	2821.2
18I2	1.004	1.045	1.055	84	325	176	8	74	14	1587.4
18H1	1.007	1.041	1.053	272	21	180	7	70	19	2086.1
18J2	1.002	1.046	1.055	52	280	172	45	34	26	1139.5
19A2	1.007	1.038	1.049	260	31	167	12	72	13	2025.2
19I1	1.002	1.023	1.028	92	294	183	10	79	4	2678.4
19B1	1.005	1.032	1.04	73	278	166	18	70	8	2766.9
19A1	1.004	1.035	1.043	81	292	175	19	68	11	2714.9
19L1	1.007	1.04	1.051	271	21	178	8	68	21	3081.4
19F1	1.008	1.034	1.045	70	288	170	28	56	17	2307
19J1	1.001	1.024	1.028	71	256	165	64	26	2	2296.8
19N1	1.006	1.041	1.051	258	49	159	32	54	14	2785.9
19I2	1.003	1.023	1.028	84	274	175	23	66	4	1596.4
19O1	1.007	1.033	1.044	268	24	174	11	66	21	1821.5
19O2	1.007	1.036	1.046	273	52	177	20	64	16	1760.4
19D1	1.01	1.03	1.042	267	358	177	0	76	14	1943.8
19J2	1.007	1.023	1.032	262	73	172	17	72	3	879.45
20I1	1.001	1.041	1.048	278	42	185	12	69	17	1810.8
20C1	1.013	1.033	1.048	282	36	187	11	65	22	3061.1
20A1	1.008	1.03	1.041	287	55	188	21	59	22	1375.3
20M1	1.013	1.037	1.052	64	309	183	31	36	39	1820.9
20H1	1.003	1.04	1.048	80	310	180	22	58	22	1995.1
20C2	1.017	1.036	1.055	283	37	189	9	68	19	1185.4

Specimen	L	F	Pj	D1	D2	D3	I1	I2	I3	Norm
20D1	1.013	1.037	1.052	254	58	164	10	80	3	1069.2
20L1	1.002	1.039	1.046	266	30	160	26	49	30	1315.3
20K1	1.005	1.04	1.049	65	307	162	15	61	25	1225.6
20N1	1.003	1.041	1.049	74	325	194	27	33	45	988.78
20O1	1.003	1.032	1.039	95	354	191	8	52	36	1579.5
20Q1	1.006	1.039	1.049	94	354	190	7	53	36	1206
21I1	1.002	1.062	1.073	88	324	181	11	70	16	4347.3
21I2	1.002	1.059	1.07	91	338	182	6	74	14	4340.8
21D1	1.005	1.055	1.067	255	57	165	2	87	1	4336.6
21L1	1.005	1.05	1.061	336	95	201	48	24	32	4053.8
21J1	1.004	1.059	1.071	304	84	188	49	33	21	4080
21F1	1.01	1.043	1.057	270	3	179	1	66	24	3962.8
21C1	1.003	1.047	1.056	76	249	344	26	64	3	3934.6
21D2	1.007	1.05	1.062	67	283	157	2	87	2	1303.6
21I3	1.004	1.057	1.069	81	303	179	23	60	18	1932
21E1	1	1.05	1.058	261	77	171	16	74	1	4124.8
21B1	1.004	1.047	1.058	76	281	167	7	82	3	1831.6
21C2	1.006	1.051	1.063	320	81	203	34	38	34	1801.5
21G1	1.006	1.048	1.059	347	116	220	51	27	26	1812.8
22B1	1.005	1.037	1.046	280	58	186	16	68	14	2593.9
22C1	1.004	1.041	1.05	82	302	177	19	66	15	6997.9
22F3	1.005	1.031	1.039	88	261	353	53	37	3	860.26
22F1	1.003	1.031	1.037	90	265	358	31	59	2	2033.6
22F2	1.005	1.032	1.041	93	269	1	49	41	2	1883.3
22E1	1.004	1.032	1.04	182	76	342	62	8	27	2449.1
22G1	1.007	1.026	1.035	117	236	18	17	58	27	1749
22E2	1.008	1.03	1.04	138	244	336	70	6	19	1539.1

Specimen	L	F	Pj	D1	D2	D3	I1	I2	I3	Norm
23B2	1.003	1.023	1.029	293	28	186	10	30	58	916.94
23D1	1.006	1.02	1.027	245	338	138	7	22	67	1070.3
23A1	1.004	1.023	1.029	37	293	189	43	14	43	1312
23G1	1.001	1.025	1.03	309	55	174	32	24	48	962.92
23E1	1.005	1.023	1.03	315	49	167	21	12	66	853.78
23D2	1.004	1.024	1.03	295	30	166	16	18	65	815.22
23E2	1.005	1.023	1.03	278	8	187	0	30	60	571.49
23H1	1.001	1.024	1.029	320	54	153	33	6	56	872.31
23I1	1.008	1.008	1.016	243	333	143	2	10	80	1245.8
23C1	1.003	1.024	1.03	54	320	191	15	13	70	1154.7
23B1	1.006	1.018	1.024	113	21	208	3	35	55	1141
23F1	1.002	1.022	1.026	302	35	188	9	19	68	1064.2
23F2	1.009	1.02	1.03	66	334	188	9	14	73	435.86
23I2	1.004	1.023	1.029	284	16	174	5	14	75	641.17
23G2	1.006	1.026	1.034	64	320	167	14	44	43	473.16
23B3	1.005	1.015	1.021	79	340	184	12	38	50	431.09
23G3	1.005	1.026	1.034	82	351	173	1	42	48	373.76
23I3	1.003	1.017	1.022	271	1	180	0	12	78	463.17
24E1	1.001	1.019	1.022	37	305	150	8	19	69	1213.8
24C1	1.001	1.019	1.022	312	47	149	30	8	59	1319.9
24B1	1.001	1.023	1.027	354	259	166	53	4	36	1334.2
24D1	1.004	1.012	1.017	83	352	180	3	27	63	1283.1
24A1	1.001	1.02	1.024	19	287	140	7	11	76	648.75
27E1	1.003	1.058	1.069	275	98	5	21	69	1	5096.3
27M1	1.002	1.055	1.065	83	286	176	19	69	7	4482.8
27Q1	1.002	1.05	1.06	80	265	170	15	75	1	4075.6
27K1	1.002	1.036	1.043	313	50	161	29	13	58	2853.4

Specimen	L	F	Pj	D1	D2	D3	I1	I2	I3	Norm
27L1	1.003	1.042	1.051	268	75	176	24	65	5	4439.3
27G1	1.003	1.056	1.067	265	60	174	12	77	5	4858.5
27G2	1.004	1.057	1.069	267	79	176	24	66	3	4840.7
27E2	1.004	1.056	1.068	273	85	182	22	68	3	3935.1
27F1	1.003	1.058	1.069	273	74	181	14	75	5	4684.3
27O1	1.002	1.057	1.067	270	54	177	16	71	10	3492.8
27F2	1.004	1.059	1.071	268	96	360	31	59	4	3684.9
27K2	1.002	1.039	1.046	315	56	159	41	13	47	579
27C1	1.011	1.021	1.033	332	63	156	31	2	59	809.42
27L2	1.006	1.047	1.058	264	6	174	1	86	4	1668.2
27M2	1.009	1.054	1.069	261	40	171	5	83	4	1451.2
27B1	1.008	1.032	1.043	285	29	155	27	25	51	570.49
27I1	1.008	1.032	1.043	281	21	170	15	33	53	2753.6
28R1	1.009	1.014	1.022	111	9	217	15	40	46	2432.3
28N1	1.009	1.033	1.044	11	101	260	2	6	83	2244.2
28V1	1.003	1.038	1.046	293	106	201	35	55	3	4365.4
28W1	1.006	1.03	1.039	298	48	198	14	52	34	3219.6
28L1	1.001	1.033	1.038	348	253	159	49	4	41	2855.5
28H1	1.003	1.033	1.04	77	343	167	2	67	23	4348.4
28B1	1.002	1.046	1.055	5	263	171	67	5	22	7052.5
28Y1	1.007	1.031	1.04	111	273	10	51	37	9	1665.7
28V2	1.005	1.027	1.035	114	297	204	9	81	0	3529.7
28U1	1.006	1.051	1.062	275	108	9	36	53	6	5578.6
28O1	1.006	1.032	1.041	359	90	232	7	9	79	2477.1
28A1	1.003	1.044	1.052	321	53	169	16	8	72	7819.2
28F1	1.005	1.039	1.048	70	305	178	28	47	30	3891.2
28R2	1.005	1.03	1.038	120	20	227	13	36	51	1159.3

Specimen	L	F	Pj	D1	D2	D3	I1	I2	I3	Norm
28I1	1.005	1.029	1.038	248	356	155	8	65	23	2320.7
28X1	1.006	1.03	1.039	274	7	184	1	64	26	2204.8
28W2	1.007	1.032	1.042	309	62	205	19	48	35	3435.3
28L2	1.004	1.03	1.038	67	329	162	6	49	40	1491
28D1	1.008	1.042	1.055	267	24	173	11	67	20	2572.6
28S1	1.002	1.05	1.06	275	97	6	52	38	1	2598.8
28J1	1.005	1.03	1.038	261	26	148	33	42	31	848.14
28H2	1.005	1.033	1.041	273	36	172	21	54	28	1390.2
28K1	1.003	1.031	1.038	48	295	159	24	42	39	863.9
28G1	1.006	1.042	1.053	263	15	170	9	67	21	3849.2
29D1	1.001	1.044	1.052	271	134	4	15	69	13	4895.2
29B1	1.003	1.046	1.056	98	272	6	37	53	2	5246.2
29D2	1.008	1.042	1.054	104	242	10	16	68	14	1865.2
29A1	1.003	1.047	1.056	90	268	360	8	82	0	5185.5
29H1	1	1.056	1.065	78	174	347	1	83	7	4146.6
29A2	1.003	1.046	1.056	275	100	5	13	77	1	4867.4
29C1	1.002	1.045	1.054	320	86	177	79	7	9	2802.7
29A3	1.005	1.044	1.055	83	274	173	13	77	2	1173.5
30A1	1.003	1.05	1.06	83	300	184	30	54	17	7948.8
30C1	1.006	1.053	1.065	75	343	168	2	44	46	5836.8
30D2	1.009	1.042	1.055	287	28	177	16	36	50	2614.4
30D1	1.003	1.052	1.062	80	349	173	1	37	53	6613.1
30E1	1.005	1.056	1.068	38	291	187	47	16	39	6336
30B1	1.002	1.054	1.064	93	302	186	19	68	10	6564.4
31B1	1.004	1.013	1.018	302	40	188	15	29	57	912
31E1	1.002	1.018	1.022	85	355	179	1	10	80	1246.2
31D1	1.005	1.011	1.017	306	38	210	4	30	59	740.54

Specimen	L	F	Pj	D1	D2	D3	I1	I2	I3	Norm
31A1	1.009	1.008	1.017	89	359	180	0	21	69	879.88
31C1	1.005	1.014	1.019	300	34	204	5	39	51	858.08
31F1	1.003	1.015	1.019	318	49	177	7	6	81	1142.4
24E1	1.001	1.019	1.022	36	303	153	10	18	69	1213.5
32B1	1.007	1.012	1.02	12	281	122	6	17	72	680.86
32E1	1.002	1.014	1.017	281	72	170	55	31	14	1305.9
32C1	1.004	1.015	1.02	258	65	157	65	24	5	683.53
32A1	1.002	1.016	1.019	325	78	174	61	12	25	688.23

Table 3. IRM Measurement History

Specimen_ID	Instrument Name	Specimen_ID	Instrument Name
IAG11-01B-2	IRM_VSM Low-T	IAG11-01Ed-2	IRM_SRM
IAG11-01B-2	IRM_VSM Low-T	IAG11-01Ed-2	IRM_SRM
IAG11-01B-2	IRM_Sartorius	IAG11-01Ed-2	IRM_SRM
IAG11-01B-2	IRM_Magnon	IAG11-01Ed-2	IRM_SRM
IAG11-01B-2	IRM_VSM Low-T	IAG11-01Ed-2	IRM_SRM
IAG11-01B-2	IRM_VSM Low-T	IAG11-02D-2	IRM_Sartorius
IAG11-01B-2	IRM_VSM Low-T	IAG11-02D-2	IRM_Magnon
IAG11-01E-1	IRM_Sartorius	IAG11-02D-2	IRM_SRM
IAG11-01E-1	IRM_Sartorius	IAG11-02D-2	IRM_SRM
IAG11-01E-1	IRM_MPMS-5S (Old Blue)	IAG11-02D-2	IRM_SRM
IAG11-01E-1	IRM_VSM High-T	IAG11-02D-2	IRM_SRM
IAG11-01E-1	IRM_VSM High-T	IAG11-02D-2	IRM_SRM
IAG11-01E-2	IRM_Sartorius	IAG11-02D-2	IRM_SRM
IAG11-01E-2	IRM_VSM Low-T	IAG11-02D-2	IRM_SRM
IAG11-01E-2	IRM_VSM Low-T	IAG11-02D-2	IRM_VSM Low-T
IAG11-01E-2	IRM_Magnon	IAG11-02D-2	IRM_VSM Low-T
IAG11-01E-3	IRM_Sartorius	IAG11-02D-2	IRM_VSM Low-T
IAG11-01E-3	IRM_VSM High-T	IAG11-02F-2	IRM_VSM Low-T
IAG11-01E-3	IRM_VSM High-T	IAG11-02F-2	IRM_VSM Low-T
IAG11-01E-3	IRM_VSM High-T	IAG11-02F-2	IRM_Sartorius
IAG11-01E-3d	IRM_Sartorius	IAG11-02F-2	IRM_Magnon
IAG11-01E-3d	IRM_VSM High-T	IAG11-02R-2	IRM_VSM Low-T
IAG11-01E-3d	IRM_VSM High-T	IAG11-02R-2	IRM_VSM Low-T
IAG11-01E-3d	IRM_VSM High-T	IAG11-02R-2	IRM_Sartorius
IAG11-01E-3d	IRM_VSM High-T	IAG11-02R-2	IRM_Magnon
IAG11-01E-4	IRM_VSM High-T	IAG11-02R-2	IRM_VSM Low-T
IAG11-01E-4	IRM_VSM High-T	IAG11-02U-1	IRM_Sartorius
IAG11-01E-4	IRM_VSM High-T	IAG11-02U-1	IRM_MPMS-5S (Old Blue)
IAG11-01E-4	IRM_Sartorius	IAG11-02U-2	IRM_Sartorius
IAG11-01E-HT	IRM_Sartorius	IAG11-02U-2	IRM_VSM Low-T
IAG11-01E-HT	IRM_VSM High-T	IAG11-02U-2	IRM_VSM Low-T
IAG11-01E-HT	IRM_VSM High-T	IAG11-02U-2	IRM_Magnon
IAG11-01E-HT	IRM_VSM High-T	IAG11-02Y-2	IRM_Sartorius
IAG11-01Ed-2	IRM_Sartorius	IAG11-02Y-2	IRM_Magnon
IAG11-01Ed-2	IRM_VSM Low-T	IAG11-02Y-2	IRM_SRM
IAG11-01Ed-2	IRM_VSM Low-T	IAG11-02Y-2	IRM_SRM
IAG11-01Ed-2	IRM_Magnon	IAG11-02Y-2	IRM_SRM
IAG11-01Ed-2	IRM_SRM	IAG11-02Y-2	IRM_SRM
IAG11-01Ed-2	IRM_SRM	IAG11-02Y-2	IRM_SRM

Specimen_ID	Instrument Name	Specimen_ID	Instrument Name
IAG11-02Y-2	IRM_SRM	IAG11-03F-2	IRM_SRM
IAG11-02Y-2	IRM_SRM	IAG11-03F-4	IRM_Sartorius
IAG11-02Y-2	IRM_SRM	IAG11-03F-5	IRM_VSM High-T
IAG11-02Y-2	IRM_SRM	IAG11-03F-5	IRM_VSM High-T
IAG11-02Y-2	IRM_VSM Low-T	IAG11-03F-5	IRM_VSM High-T
IAG11-02Y-2	IRM_VSM Low-T	IAG11-03F-5	IRM_Sartorius
IAG11-02Y-2	IRM_SRM	IAG11-03I-2	IRM_VSM Low-T
IAG11-02Z-1	IRM_Sartorius	IAG11-03I-2	IRM_VSM Low-T
IAG11-02Z-1	IRM_MPMS-5S (Old Blue)	IAG11-03I-2	IRM_Sartorius
IAG11-02Z-2	IRM_Sartorius	IAG11-03I-2	IRM_Magnon
IAG11-02Z-2	IRM_VSM Low-T	IAG11-03N-1	IRM_Sartorius
IAG11-02Z-2	IRM_VSM Low-T	IAG11-03N-1	IRM_Sartorius
IAG11-02Z-2	IRM_Magnon	IAG11-03N-1	IRM_MPMS-5S (Old Blue)
IAG11-02Z-4	IRM_VSM High-T	IAG11-03O-1	IRM_Sartorius
IAG11-02Z-4	IRM_VSM High-T	IAG11-03O-1	IRM_MPMS-5S (Old Blue)
IAG11-02Z-4	IRM_Sartorius	IAG11-03O-2	IRM_VSM Low-T
IAG11-02Z-4	IRM_VSM High-T	IAG11-03O-2	IRM_VSM Low-T
IAG11-02Z-HT	IRM_Sartorius	IAG11-03O-2	IRM_Sartorius
IAG11-02Z-HT	IRM_VSM High-T	IAG11-03O-2	IRM_Magnon
IAG11-02Z-HT	IRM_VSM High-T	IAG11-03O-3	IRM_Sartorius
IAG11-02Z-HT	IRM_VSM High-T	IAG11-03O-3	IRM_Sartorius
IAG11-03B-2	IRM_Sartorius	IAG11-03O-3	IRM_Sartorius
IAG11-03B-2	IRM_Magnon	IAG11-03O-4	IRM_VSM High-T
IAG11-03B-2	IRM_VSM Low-T	IAG11-03O-4	IRM_VSM High-T
IAG11-03B-2	IRM_VSM Low-T	IAG11-03O-4	IRM_VSM High-T
IAG11-03E-2	IRM_Sartorius	IAG11-03O-4	IRM_VSM High-T
IAG11-03E-2	IRM_Magnon	IAG11-03O-4	IRM_VSM High-T
IAG11-03E-2	IRM_VSM Low-T	IAG11-03O-4	IRM_Sartorius
IAG11-03E-2	IRM_VSM Low-T	IAG11-03O-HT	IRM_Sartorius
IAG11-03F-1	IRM_Sartorius	IAG11-03O-HT	IRM_VSM High-T
IAG11-03F-1	IRM_MPMS-5S (Old Blue)	IAG11-03O-HT	IRM_VSM High-T
IAG11-03F-2	IRM_VSM Low-T	IAG11-03O-HT	IRM_VSM High-T
IAG11-03F-2	IRM_VSM Low-T	IAG11-03O-HT	IRM_VSM High-T
IAG11-03F-2	IRM_Sartorius	IAG11-03O-HT	IRM_VSM High-T
IAG11-03F-2	IRM_Magnon	IAG11-03O-HT	IRM_VSM High-T
IAG11-03F-2	IRM_SRM	IAG11-03O-HT	IRM_VSM High-T
IAG11-03F-2	IRM_SRM	IAG11-04B-1	IRM_Sartorius
IAG11-03F-2	IRM_SRM	IAG11-04B-1	IRM_MPMS-5S (Old Blue)
IAG11-03F-2	IRM_SRM	IAG11-04B-2	IRM_Sartorius
IAG11-03F-2	IRM_SRM	IAG11-04B-2	IRM_VSM Low-T
IAG11-03F-2	IRM_SRM	IAG11-04B-2	IRM_VSM Low-T

Specimen_ID	Instrument Name	Specimen_ID	Instrument Name
IAG11-04B-2	IRM_Magnon	IAG11-04K-1	IRM_MPMS-5S (Old Blue)
IAG11-04B-4	IRM_VSM High-T	IAG11-04K-2	IRM_Sartorius
IAG11-04B-4	IRM_VSM High-T	IAG11-04K-2	IRM_VSM Low-T
IAG11-04B-4	IRM_VSM High-T	IAG11-04K-2	IRM_VSM Low-T
IAG11-04B-4	IRM_Sartorius	IAG11-04K-2	IRM_Magnon
IAG11-04B-HT	IRM_Sartorius	IAG11-04K-3	IRM_Sartorius
IAG11-04B-HT	IRM_VSM High-T	IAG11-04K-3	IRM_Sartorius
IAG11-04B-HT	IRM_VSM High-T	IAG11-04K-4	IRM_VSM High-T
IAG11-04B-HT	IRM_VSM High-T	IAG11-04K-4	IRM_VSM High-T
IAG11-04H-2	IRM_Sartorius	IAG11-04K-4	IRM_Sartorius
IAG11-04H-2	IRM_VSM Low-T	IAG11-04K-4	IRM_VSM High-T
IAG11-04H-2	IRM_VSM Low-T	IAG11-04K-HT	IRM_Sartorius
IAG11-04H-2	IRM_Magnon	IAG11-04K-HT	IRM_VSM High-T
IAG11-04H-2	IRM_SRM	IAG11-04K-HT	IRM_VSM High-T
IAG11-04H-2	IRM_SRM	IAG11-04K-HT	IRM_VSM High-T
IAG11-04H-2	IRM_SRM	IAG11-05H-2	IRM_Sartorius
IAG11-04H-2	IRM_SRM	IAG11-05H-2	IRM_Magnon
IAG11-04H-2	IRM_SRM	IAG11-05H-2	IRM_VSM Low-T
IAG11-04H-2	IRM_SRM	IAG11-05H-2	IRM_VSM Low-T
IAG11-04H-2	IRM_SRM	IAG11-05H-2	IRM_SRM
IAG11-04H-2	IRM_SRM	IAG11-05H-2	IRM_SRM
IAG11-04H-2	IRM_SRM	IAG11-05H-2	IRM_SRM
IAG11-04H-2	IRM_SRM	IAG11-05H-2	IRM_SRM
IAG11-04H-2	IRM_SRM	IAG11-05H-2	IRM_SRM
IAG11-04I-2	IRM_Sartorius	IAG11-05H-2	IRM_SRM
IAG11-04I-2	IRM_VSM Low-T	IAG11-05H-2	IRM_SRM
IAG11-04I-2	IRM_VSM Low-T	IAG11-05K-1	IRM_Sartorius
IAG11-04I-2	IRM_Magnon	IAG11-05K-1	IRM_MPMS-5S (Old Blue)
IAG11-04J-2	IRM_Sartorius	IAG11-05K-2	IRM_Sartorius
IAG11-04J-2	IRM_Magnon	IAG11-05K-2	IRM_VSM Low-T
IAG11-04J-2	IRM_VSM Low-T	IAG11-05K-2	IRM_VSM Low-T
IAG11-04J-2	IRM_VSM Low-T	IAG11-05K-2	IRM_Magnon
IAG11-04J-2	IRM_SRM	IAG11-05K-3	IRM_Sartorius
IAG11-04J-2	IRM_SRM	IAG11-05K-3	IRM_VSM High-T
IAG11-04J-2	IRM_SRM	IAG11-05K-3	IRM_VSM High-T
IAG11-04J-2	IRM_SRM	IAG11-05K-4	IRM_VSM High-T
IAG11-04J-2	IRM_SRM	IAG11-05K-4	IRM_VSM High-T
IAG11-04J-2	IRM_SRM	IAG11-05K-4	IRM_VSM High-T
IAG11-04J-2	IRM_SRM	IAG11-05K-4	IRM_Sartorius
IAG11-04K-1	IRM_Sartorius	IAG11-05K-HT	IRM_Sartorius
IAG11-04K-1	IRM_Sartorius	IAG11-05K-HT	IRM_VSM High-T

Specimen_ID	Instrument Name
IAG11-05K-HT	IRM_VSM High-T
IAG11-05K-HT	IRM_VSM High-T
IAG11-06F-1	IRM_Sartorius
IAG11-06F-1	IRM_MPMS-5S (Old Blue)
IAG11-06F-2	IRM_Sartorius
IAG11-06F-2	IRM_VSM Low-T
IAG11-06F-2	IRM_VSM Low-T
IAG11-06F-2	IRM_Magnon
IAG11-06F-3	IRM_VSM High-T
IAG11-06F-3	IRM_VSM High-T
IAG11-06F-3	IRM_Sartorius
IAG11-06G-1	IRM_Sartorius
IAG11-06G-1	IRM_MPMS-5S (Old Blue)
IAG11-06G-2	IRM_VSM Low-T
IAG11-06G-2	IRM_VSM Low-T
IAG11-06G-2	IRM_Sartorius
IAG11-06G-2	IRM_Magnon
IAG11-06G-3	IRM_Sartorius
IAG11-06G-3	IRM_VSM High-T
IAG11-06G-3	IRM_VSM High-T
IAG11-06G-3	IRM_MPMS-5S (Old Blue)
IAG11-06G-4	IRM_VSM High-T
IAG11-06G-4	IRM_VSM High-T
IAG11-06G-4	IRM_Sartorius
IAG11-06G-HT	IRM_Sartorius
IAG11-06G-HT	IRM_VSM High-T
IAG11-06G-HT	IRM_VSM High-T
IAG11-06G-HT	IRM_VSM High-T
IAG11-06H-2	IRM_Sartorius
IAG11-06H-2	IRM_VSM Low-T
IAG11-06H-2	IRM_VSM Low-T
IAG11-06H-2	IRM_Magnon
IAG11-06H-2	IRM_SRM
IAG11-06H-2	IRM_SRM
IAG11-06H-2	IRM_SRM
IAG11-06H-2	IRM_SRM
IAG11-06H-2	IRM_SRM
IAG11-06H-2	IRM_SRM
IAG11-06H-2	IRM_SRM
IAG11-07G-2	IRM_Sartorius
IAG11-07G-2	IRM_Magnon

Specimen_ID	Instrument Name
IAG11-07L-2	IRM_Sartorius
IAG11-07L-2	IRM_Magnon
IAG11-07L-4	IRM_VSM High-T
IAG11-07L-4	IRM_VSM High-T
IAG11-07L-4	IRM_VSM High-T
IAG11-07L-4	IRM_Sartorius
IAG11-07O-2	IRM_Sartorius
IAG11-07O-2	IRM_Magnon
IAG11-07Q-2	IRM_Sartorius
IAG11-07Q-2	IRM_Magnon
IAG11-08D-2	IRM_Sartorius
IAG11-08D-2	IRM_Magnon
IAG11-08D-2	IRM_VSM Low-T
IAG11-08D-2	IRM_VSM Low-T
IAG11-08D-2	IRM_VSM Low-T
IAG11-08F-2	IRM_Sartorius
IAG11-08F-2	IRM_Magnon
IAG11-08O-2	IRM_Sartorius
IAG11-08O-2	IRM_Magnon
IAG11-09G-2	IRM_Sartorius
IAG11-09G-2	IRM_Magnon
IAG11-10A-2	IRM_Sartorius
IAG11-10A-2	IRM_Magnon
IAG11-10N-2	IRM_SRM
IAG11-10N-2	IRM_SRM
IAG11-10N-2	IRM_SRM
IAG11-10N-2	IRM_SRM
IAG11-10N-2	IRM_SRM
IAG11-10N-2	IRM_SRM
IAG11-10N-2	IRM_SRM
IAG11-10N-2	IRM_Sartorius
IAG11-10N-2	IRM_Magnon
IAG11-10O-1	IRM_Sartorius
IAG11-10O-1	IRM_MPMS-5S (Old Blue)
IAG11-10O-1	IRM_VSM High-T
IAG11-10O-1	IRM_VSM High-T
IAG11-11F-2	IRM_Sartorius
IAG11-11F-2	IRM_Magnon
IAG11-11G-2	IRM_Sartorius
IAG11-11G-2	IRM_Magnon
IAG11-11M-2	IRM_Sartorius

Specimen_ID	Instrument Name	Specimen_ID	Instrument Name
IAG11-11M-2	IRM_Magnon	IAG11-19O-2	IRM_Magnon
IAG11-12J-2	IRM_Sartorius	IAG11-20H-2	IRM_Sartorius
IAG11-12J-2	IRM_Magnon	IAG11-20H-2	IRM_Magnon
IAG11-12Jd-2	IRM_Sartorius	IAG11-20H-2	IRM_VSM Low-T
IAG11-12Jd-2	IRM_Magnon	IAG11-20H-2	IRM_VSM Low-T
IAG11-12K-2	IRM_Sartorius	IAG11-20H-2	IRM_VSM Low-T
IAG11-12K-2	IRM_Magnon	IAG11-20K-2	IRM_Sartorius
IAG11-13A-2	IRM_Sartorius	IAG11-20K-2	IRM_Magnon
IAG11-13A-2	IRM_Magnon	IAG11-20O-2	IRM_Sartorius
IAG11-13F-2	IRM_Sartorius	IAG11-20O-2	IRM_Magnon
IAG11-13F-2	IRM_Magnon	IAG11-21B-2	IRM_Magnon
IAG11-14E-2	IRM_Sartorius	IAG11-21B-2	IRM_Sartorius
IAG11-14E-2	IRM_Magnon	IAG11-21D-2	IRM_Sartorius
IAG11-15B-2	IRM_Sartorius	IAG11-21D-2	IRM_Magnon
IAG11-15B-2	IRM_Magnon	IAG11-22B-2	IRM_Sartorius
IAG11-15B-2	IRM_VSM Low-T	IAG11-22B-2	IRM_Magnon
IAG11-15B-2	IRM_VSM Low-T	IAG11-22G-2	IRM_Sartorius
IAG11-15B-2	IRM_VSM Low-T	IAG11-22G-2	IRM_Magnon
IAG11-16B-2	IRM_Sartorius	IAG11-23B-2	IRM_Sartorius
IAG11-16B-2	IRM_Magnon	IAG11-23B-2	IRM_Magnon
IAG11-16D-2	IRM_Sartorius	IAG11-23E-2	IRM_Sartorius
IAG11-16D-2	IRM_Magnon	IAG11-23E-2	IRM_Magnon
IAG11-16F-2	IRM_Sartorius	IAG11-23F-2	IRM_Sartorius
IAG11-16F-2	IRM_Magnon	IAG11-23F-2	IRM_Magnon
IAG11-16I-2	IRM_Sartorius	IAG11-23F-4	IRM_Sartorius
IAG11-16I-2	IRM_Magnon	IAG11-23F-4	IRM_VSM High-T
IAG11-17C-2	IRM_Sartorius	IAG11-23F-4	IRM_VSM High-T
IAG11-17C-2	IRM_Magnon	IAG11-23F-4	IRM_VSM High-T
IAG11-17E-2	IRM_Sartorius	IAG11-23I-2	IRM_Sartorius
IAG11-17E-2	IRM_Magnon	IAG11-23I-2	IRM_Sartorius
IAG11-17E-2	IRM_VSM Low-T	IAG11-23I-2	IRM_Magnon
IAG11-17E-2	IRM_VSM Low-T	IAG11-24Ai-2	IRM_Sartorius
IAG11-17K-2	IRM_Sartorius	IAG11-24Ai-2	IRM_Magnon
IAG11-17K-2	IRM_Magnon	IAG11-24Ao-2	IRM_Sartorius
IAG11-18G-2	IRM_Sartorius	IAG11-24Ao-2	IRM_Magnon
IAG11-18G-2	IRM_Magnon	IAG11-24D-2	IRM_Sartorius
IAG11-19B-2	IRM_Sartorius	IAG11-24D-2	IRM_Magnon
IAG11-19B-2	IRM_Magnon	IAG11-27K-2	IRM_Magnon
IAG11-19F-2	IRM_Sartorius	IAG11-27K-2	IRM_Sartorius
IAG11-19F-2	IRM_Magnon	IAG11-27L-2	IRM_Magnon
IAG11-19O-2	IRM_Sartorius	IAG11-27L-2	IRM_Sartorius

Specimen_ID	Instrument Name	Specimen_ID	Instrument Name
IAG11-27Q-2	IRM_Magnon		
IAG11-27Q-2	IRM_Sartorius		
IAG11-28A-2	IRM_Magnon		
IAG11-28A-2	IRM_Sartorius		
IAG11-28A-4	IRM_Sartorius		
IAG11-28A-4	IRM_VSM High-T		
IAG11-28A-4	IRM_VSM High-T		
IAG11-28A-4	IRM_VSM High-T		
IAG11-28D-2	IRM_Magnon		
IAG11-28D-2	IRM_Sartorius		
IAG11-28H-2	IRM_Magnon		
IAG11-28H-2	IRM_Sartorius		
IAG11-28J-2	IRM_Magnon		
IAG11-28J-2	IRM_Sartorius		
IAG11-28L-2	IRM_Magnon		
IAG11-28L-2	IRM_Sartorius		
IAG11-29C-2	IRM_Magnon		
IAG11-29C-2	IRM_Sartorius		
IAG11-29D-2	IRM_Magnon		
IAG11-29D-2	IRM_Sartorius		
IAG11-29D-2	IRM_Sartorius		
IAG11-29I-2	IRM_Magnon		
IAG11-29I-2	IRM_Sartorius		
IAG11-30C-2	IRM_Magnon		
IAG11-30C-2	IRM_Sartorius		
IAG11-30D-2	IRM_Magnon		
IAG11-30D-2	IRM_Sartorius		
IAG11-31A-2	IRM_Sartorius		
IAG11-31A-2	IRM_Magnon		
IAG11-31C-2	IRM_Sartorius		
IAG11-31C-2	IRM_Magnon		
IAG11-31F-2	IRM_Sartorius		
IAG11-31F-2	IRM_Magnon		
IAG11-31F-2	IRM_VSM Low-T		
IAG11-31F-2	IRM_VSM Low-T		
IAG11-31F-2	IRM_VSM Low-T		
IAG11-32C-2	IRM_Sartorius		
IAG11-32C-2	IRM_Magnon		
IAG11-32C-2	IRM_Magnon		
IAG11-32E-2	IRM_Sartorius		
IAG11-32E-2	IRM_Magnon		

Table 4. ChRM Site Means

Site	Latitude	Longitude	Dt	It	Alpha95	Kappa	N	Strike	Dip
1	29.26374516	-113.4114716	235.4	0.6	3.9	67.5	21	209	27
2	29.26447984	-113.4111614	241.4	4	5	18.2	47	207	25
3	29.26450565	-113.4105505	261.3	-7.2	2.1	115.3	40	172	24
4	29.26433542	-113.4103563	257.4	-24.5	4.4	25.8	43	172	24
5	29.2642552	-113.4103873	226.5	-10	4.8	61.1	16	187	25
6	29.2641744	-113.410599	214.2	-13.9	10.6	17.7	11	197	23
7	29.27367722	-113.396284	228.8	6.6	6.3	25.2	22	207	15
8	29.27330154	-113.3961665	224.4	0.1	3.6	72.1	35	197	20
10	29.27371544	-113.3952386	221.6	-14.5	3.2	69.5	30	137	20
11	29.27326097	-113.3945364	233.6	4.5	2.5	89.6	37	217	27
12	29.27399145	-113.3905336	237.3	-8.3	4.3	53	22	151	17
13	29.27435691	-113.3908698	238.4	-12.1	1.2	309.5	48	156	17
14	29.27379071	-113.3908903	231.9	-7.5	2.3	234.3	18	122	14
16	29.27359097	-113.3916657	231.8	-24.3	2.8	102.8	26	137	25
17	29.27310607	-113.3910375	237.4	-15.1	6.1	58.2	10	142	25
18	29.2726361	-113.3908552	238.6	-13.7	3.5	113.4	15	142	25
19	29.27288756	-113.3911896	238	-26.1	8.8	21.4	13	142	25
20	29.27271749	-113.3919684	239.7	-4.2	9.2	32.3	8	107	14
21	29.27246008	-113.3930588	250.1	-5	3	173.8	13	72	19
22	29.27049411	-113.3936322	230.5	-15.4	3.5	145.3	12	117	21
23	29.27086978	-113.3922368	207.3	-8.8	4.7	38.1	26	190	12
24	29.26915878	-113.3944991	215	1	6.7	36.1	13	187	10
27	29.27161099	-113.3927938	215.7	-17	2.4	178.8	21	159	29
28	29.26924604	-113.3950119	227.6	7.7	6.8	15.9	30	189	13
29	29.27070156	-113.3957262	220.1	9.4	8.9	18.3	15	202	14
30	29.26957285	-113.3963192	215.8	-3.4	7.3	58.8	7	147	10
31	29.26791684	-113.3973573	224.8	1.7	7.6	65.7	6	190	18

Table 5. AMS Site Means

Site	K1d	K1i	C1a	C1b	K2d	K2i	C2a	C2b	K3d	K3i	C3a	C3b	N
1	20	23.6	55.7	5.2	279.9	22	55.8	20.2	151.8	56.8	21.8	6.2	12
2	149.5	26.8	68	36.8	247.1	14.8	68.4	28.1	2.9	58.8	40.4	33.6	35
3	167.4	0.9	20.9	8.4	257.8	24.4	21	14	75.3	65.6	14.3	8.4	26
4	354.9	7.8	45.9	15.7	263.7	8.9	45.3	8.8	125.6	78.2	19.8	9.3	24
5	11.2	20.4	22.7	7.9	273.2	20.6	22.4	5.1	142.1	60.3	10.6	2.4	11
6	99.3	2.8	43.2	8.5	189.5	5.8	43.6	9.3	343.7	83.6	12.6	8.5	13
7	29.8	0.6	13.9	7.8	299.7	8.4	13.4	5.1	123.5	81.5	9.1	4.4	17
8	11.1	5.3	23.2	6.5	280.3	8.2	23.5	7	133.7	80.2	8.6	5.9	27
10	8.7	5.3	70	11.8	277.3	14.4	70	3.2	118.2	74.6	12.5	3.6	17
11	25.5	9.8	22.5	10	293.5	11.5	21.3	4	154.9	74.9	13.2	3.7	29
12	69.4	3.2	36.2	10.3	338.6	13.9	36.4	18.1	172.2	75.7	20	7.9	20
13	29.7	4	30	4.2	298.9	11.4	30.1	4.9	138.5	77.9	6.1	2.5	32
14	39.5	11.4	15.2	5.9	307.5	10	14.8	7.7	177.4	74.7	8	6.7	15
16	16.3	8.7	20.3	12.7	284	14.8	20.3	6	135.7	72.8	13.1	5.3	19
17	235.8	0.4	72.3	9.8	325.8	4.8	72.3	8.3	140.9	85.2	13.3	8.8	11
18	7.8	0.2	22.4	6.7	277.8	5.5	21.8	5.3	100	84.5	10.9	2.3	12
19	40.9	6.2	30.2	6	310.7	2.3	30.1	7.2	200.2	83.3	8.2	6.7	13
20	45.6	0.3	27.3	9.7	315.6	10.2	27	4.9	137.5	79.8	11.2	3.7	12
21	244.6	5.8	34.9	10.9	335.7	10.9	35.2	12.6	126.8	77.6	15.9	7.2	13
22	352.7	13.8	30.8	10.4	260.8	7.4	32.3	9.3	143.5	74.2	15.5	10.3	8
23	8.9	5.1	34.6	5.8	278.1	8.6	34.6	3.9	129.5	80	6	3.9	18
24	183.9	4.4	45	9.7	274.8	11.8	44.7	5.3	73.9	77.4	13.7	4.9	5
27	340.3	3.1	23.4	6.7	250	4.9	23.4	4.9	102	84.2	7.5	3.6	17
28	10.4	11.5	20.2	9.9	277.7	12.9	21.4	9.2	140.8	72.6	12.7	9.7	24
29	348.8	7.7	20.6	5.3	257.3	10.9	20.4	10	113.2	76.6	10	6.4	8
30	9.8	5.5	21.8	5.6	278.4	14.2	21.8	3	120.2	74.7	5.7	2.8	6
31	255.3	9.7	21	4.6	346	4.1	21	4.8	98.7	79.5	6.2	4.6	7

Figure 22. ChRM and AMS by Site

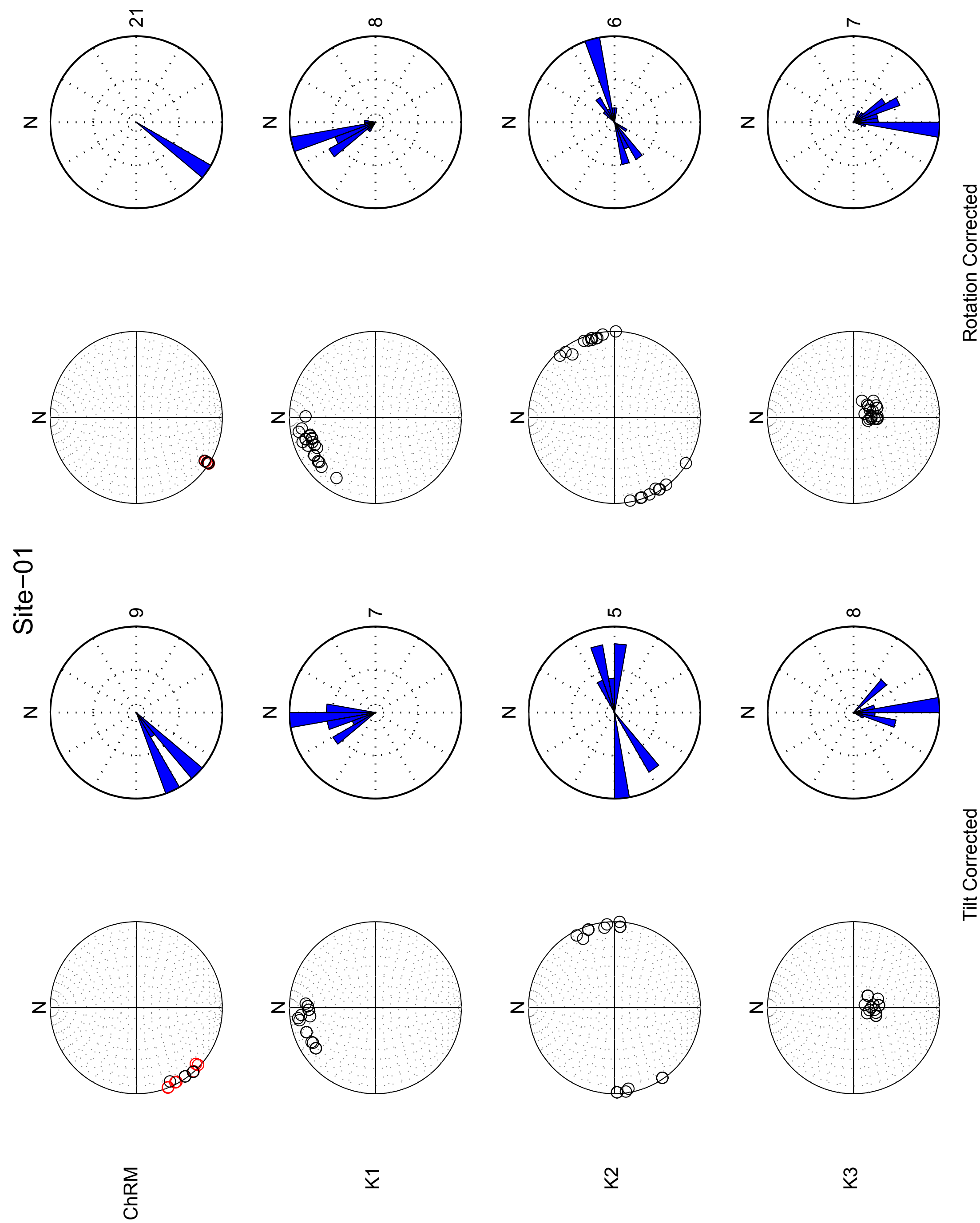

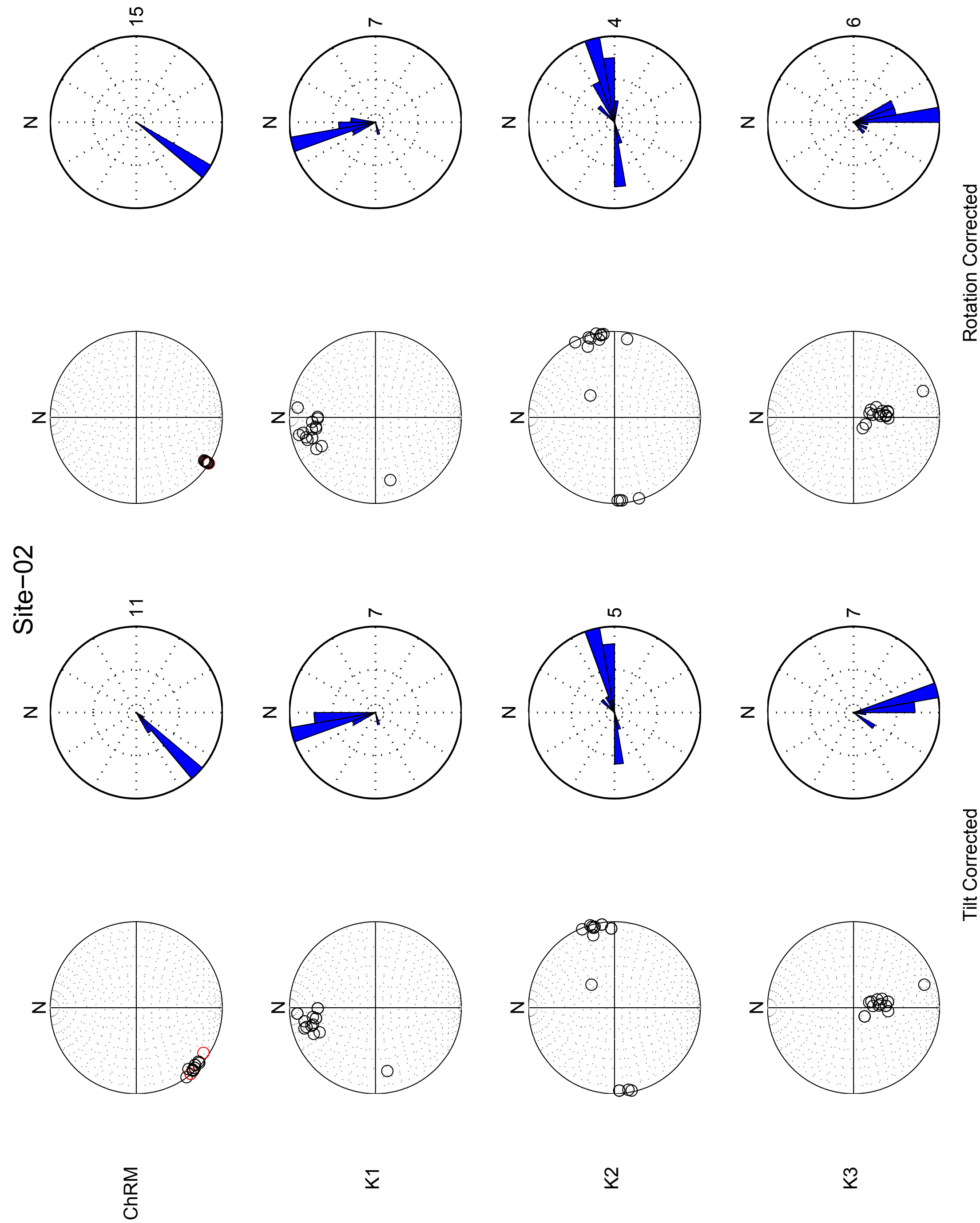
Site−02
ChRM
K1
K2
K3
N
11
7
5
7
15
7
4
6
Tilt Corrected
Rotation Corrected

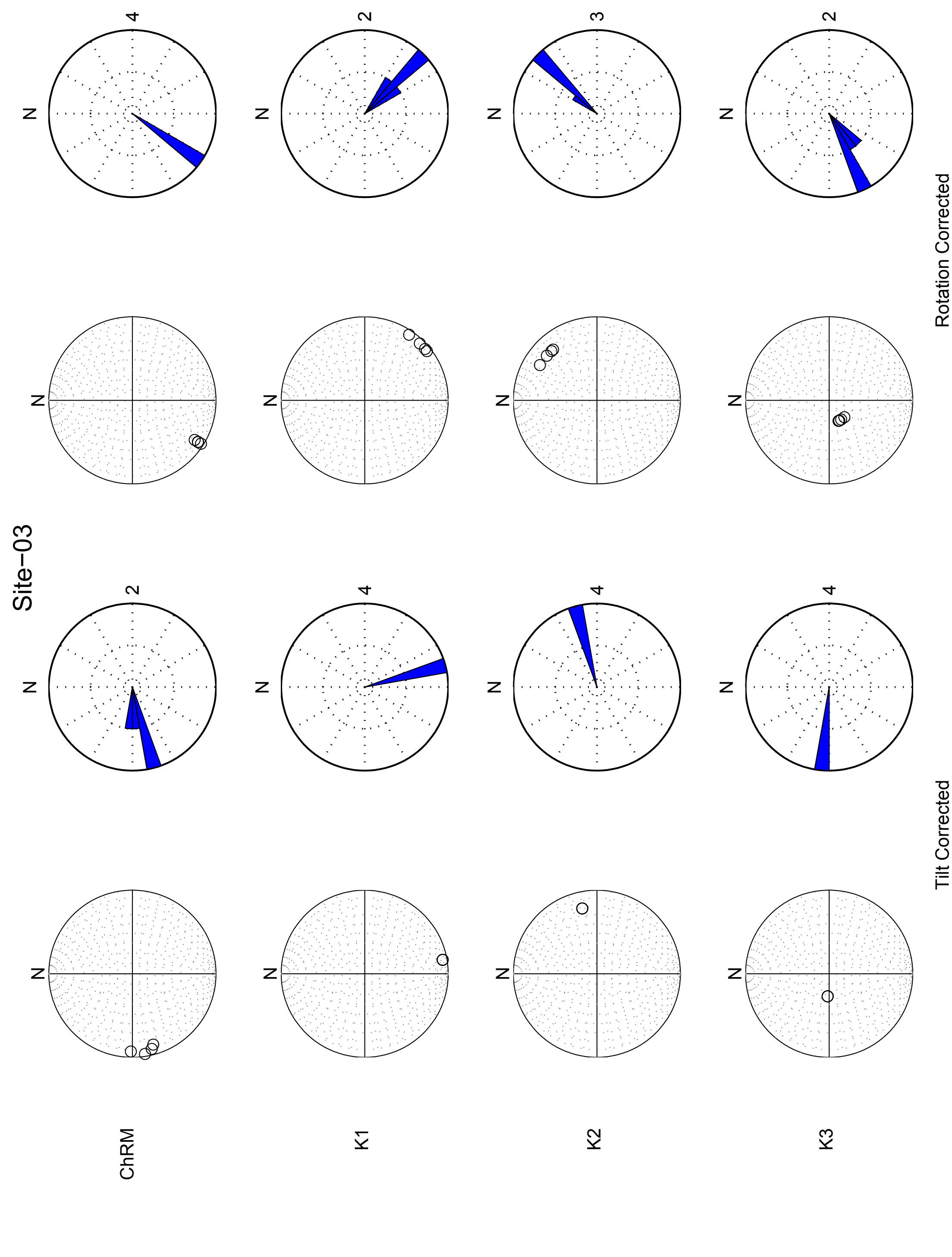
Site−03
ChRM
K1
K2
K3
N
2
4
3
Tilt Corrected
Rotation Corrected

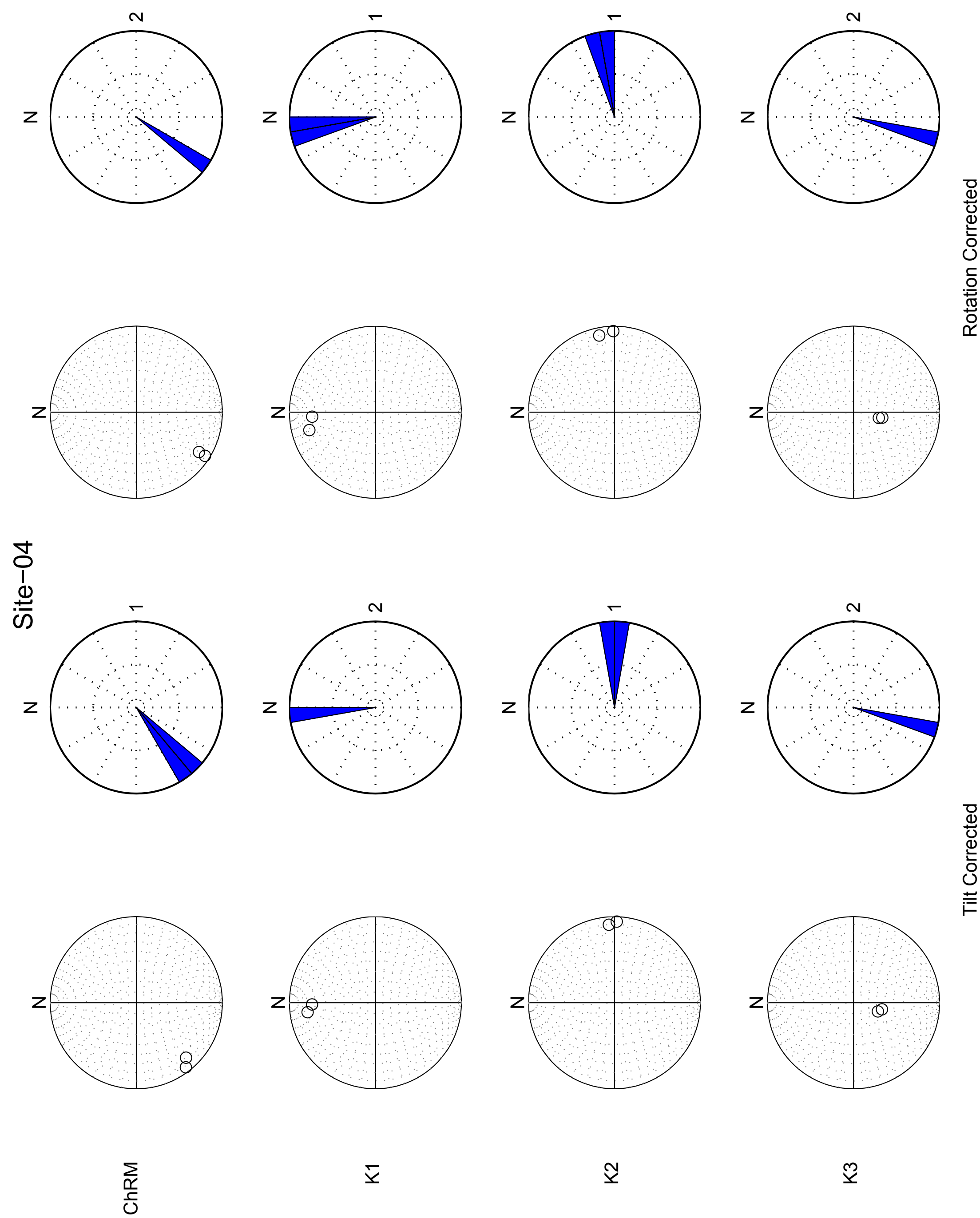
Site−04
ChRM
K1
K2
K3
N
1
2
Tilt Corrected
Rotation Corrected

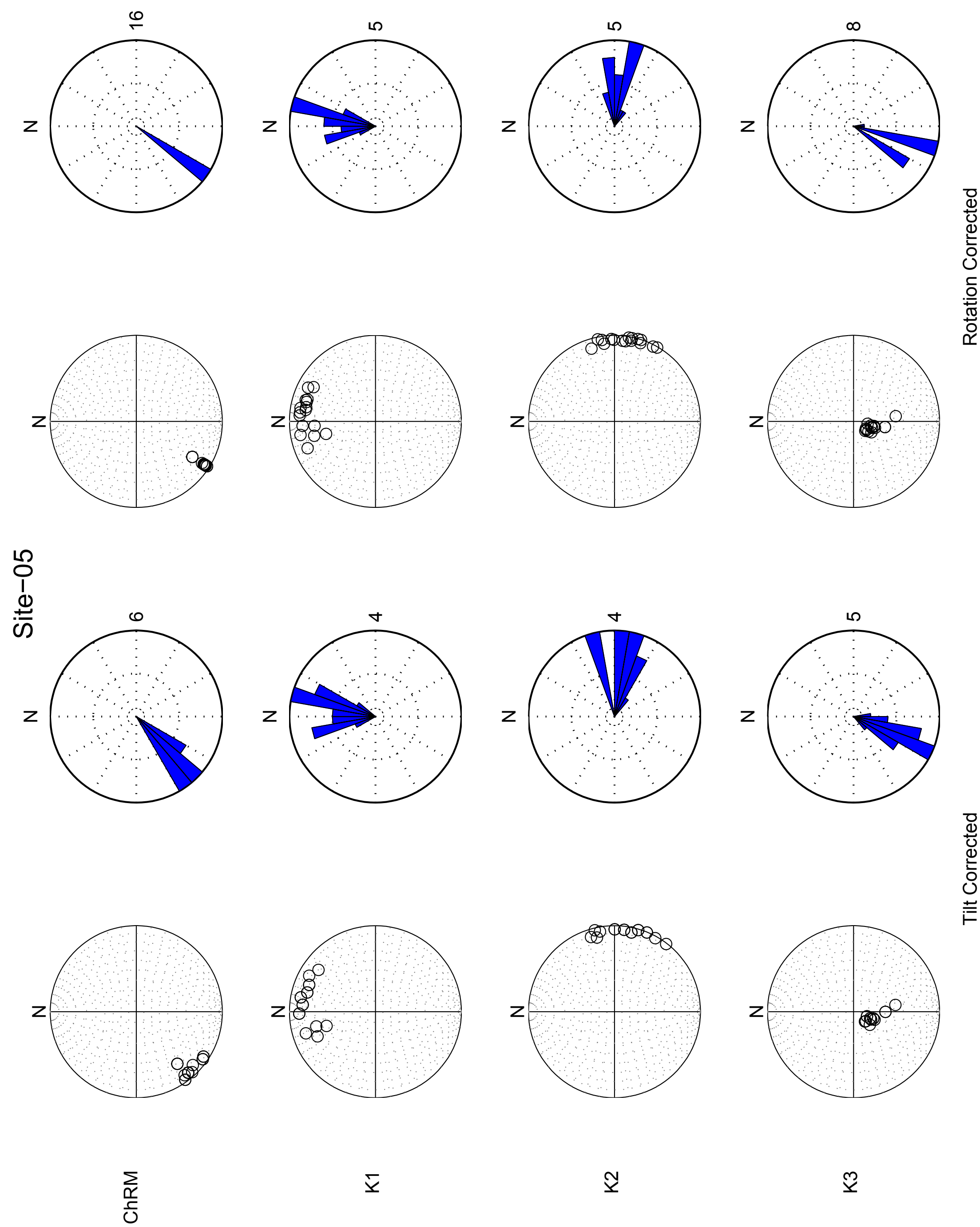
Site−05
ChRM
K1
K2
K3
N
6
4
4
5
16
5
5
8
Tilt Corrected
Rotation Corrected

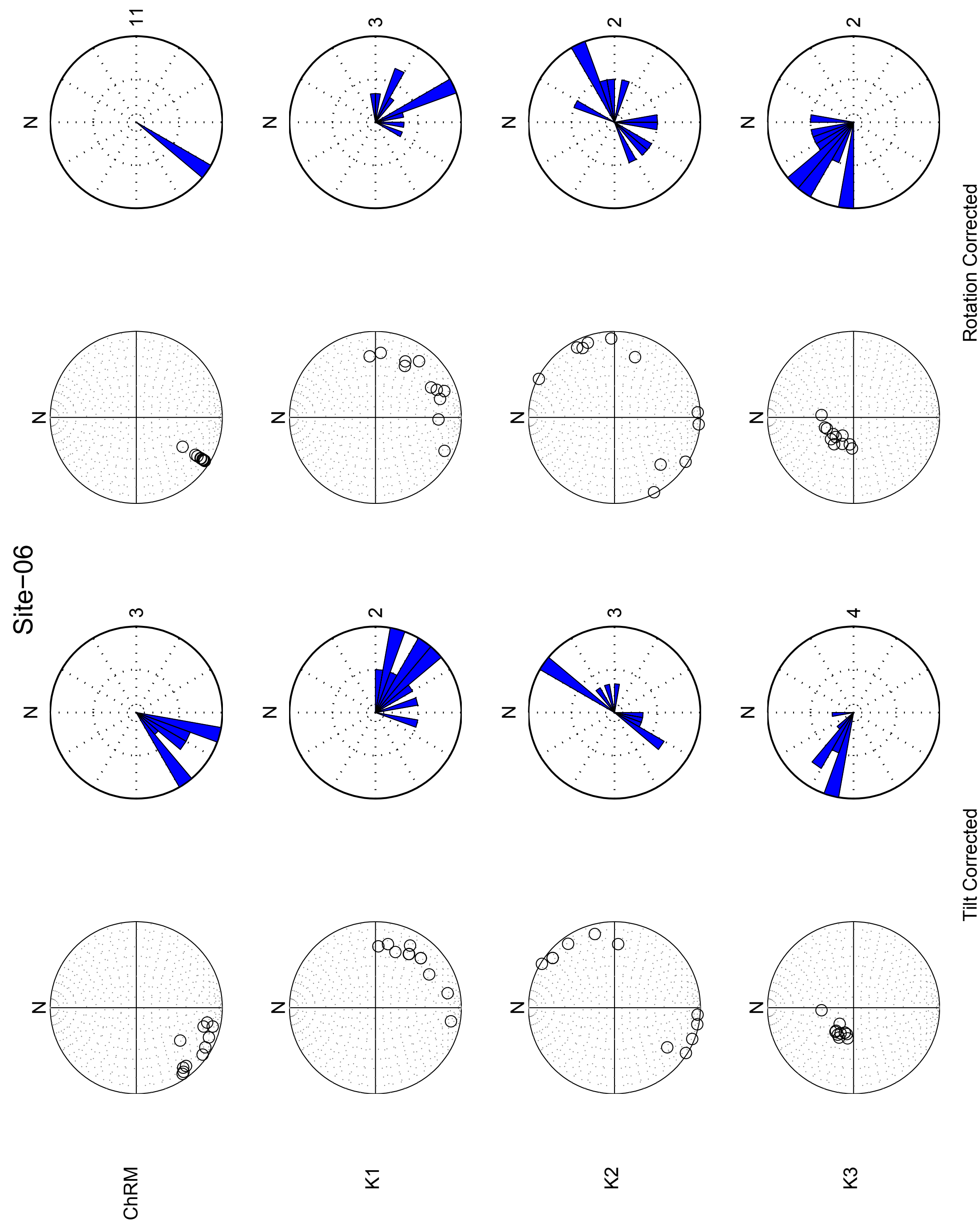
Site−06
ChRM
K1
K2
K3
N
11
3
2
4
Tilt Corrected
Rotation Corrected

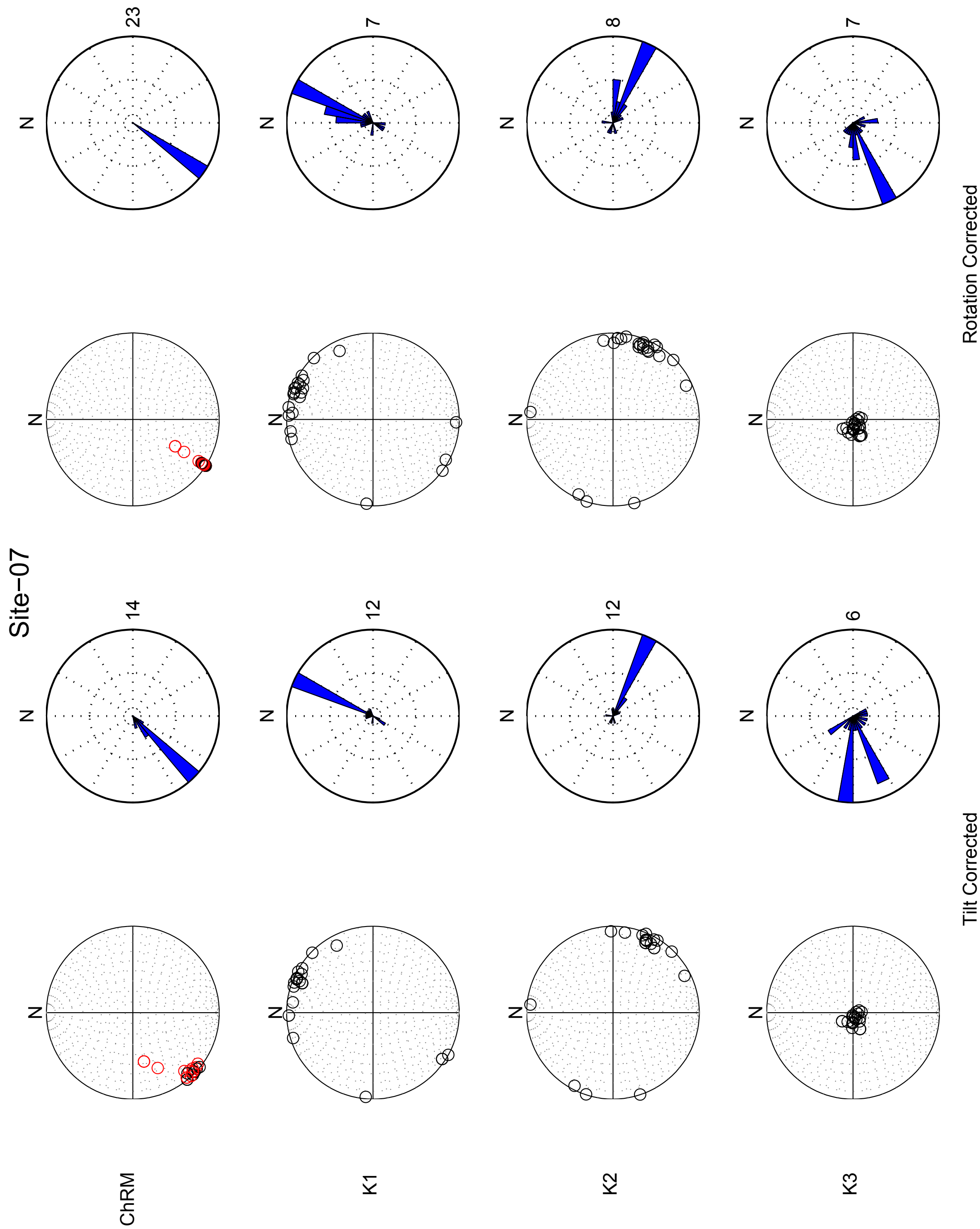
Site−07
ChRM
K1
K2
K3
N
14
12
12
6
23
7
8
7
Tilt Corrected
Rotation Corrected

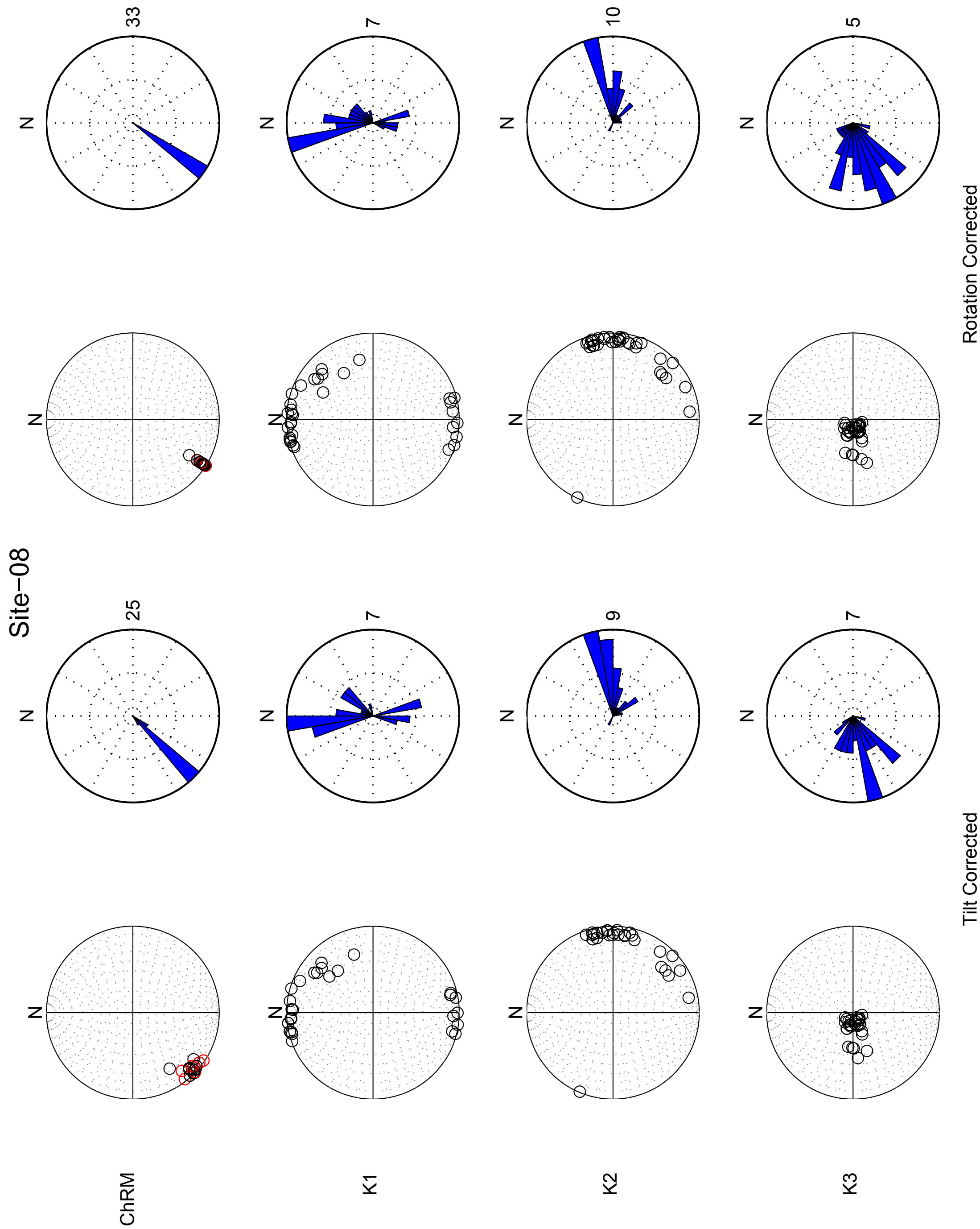
Site−08
ChRM
K1
K2
K3
Tilt Corrected
Rotation Corrected
N
25
7
9
7
33
7
10
5

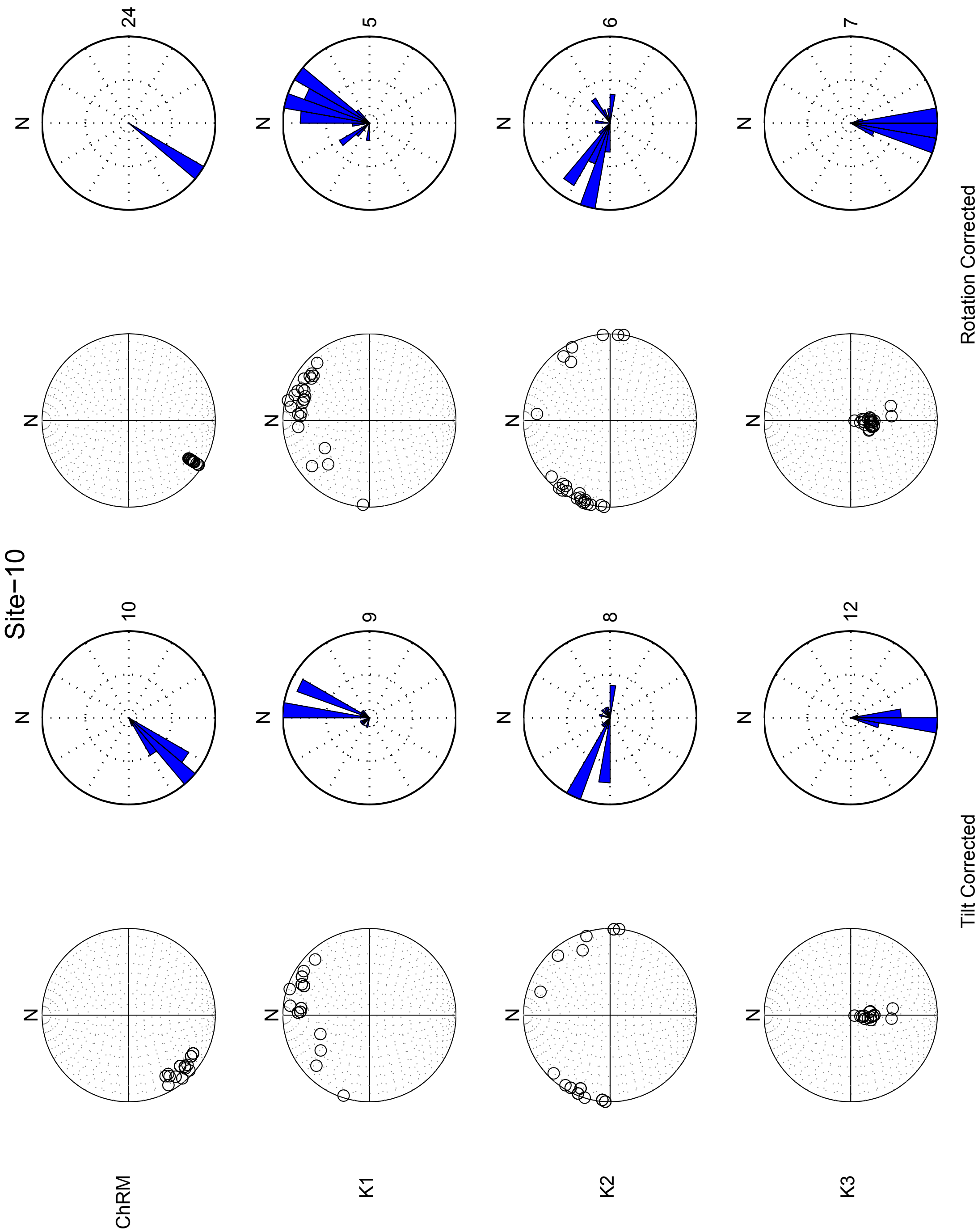

Site−10
ChRM
K1
K2
K3
Tilt Corrected
Rotation Corrected
N
10
9
8
12
24
5
6
7

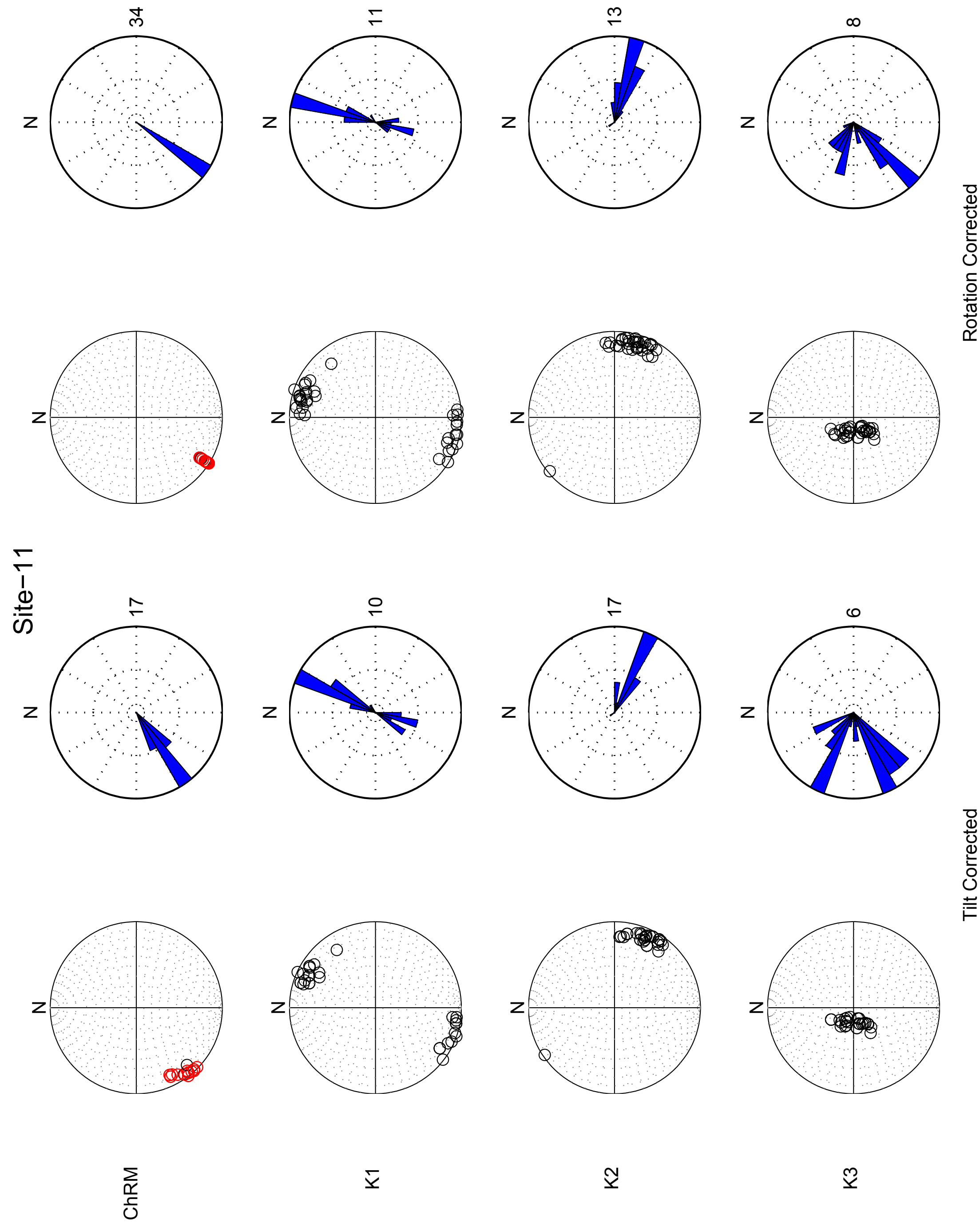
Site−11
ChRM
K1
K2
K3
N
34
11
13
8
17
10
17
6
Tilt Corrected
Rotation Corrected

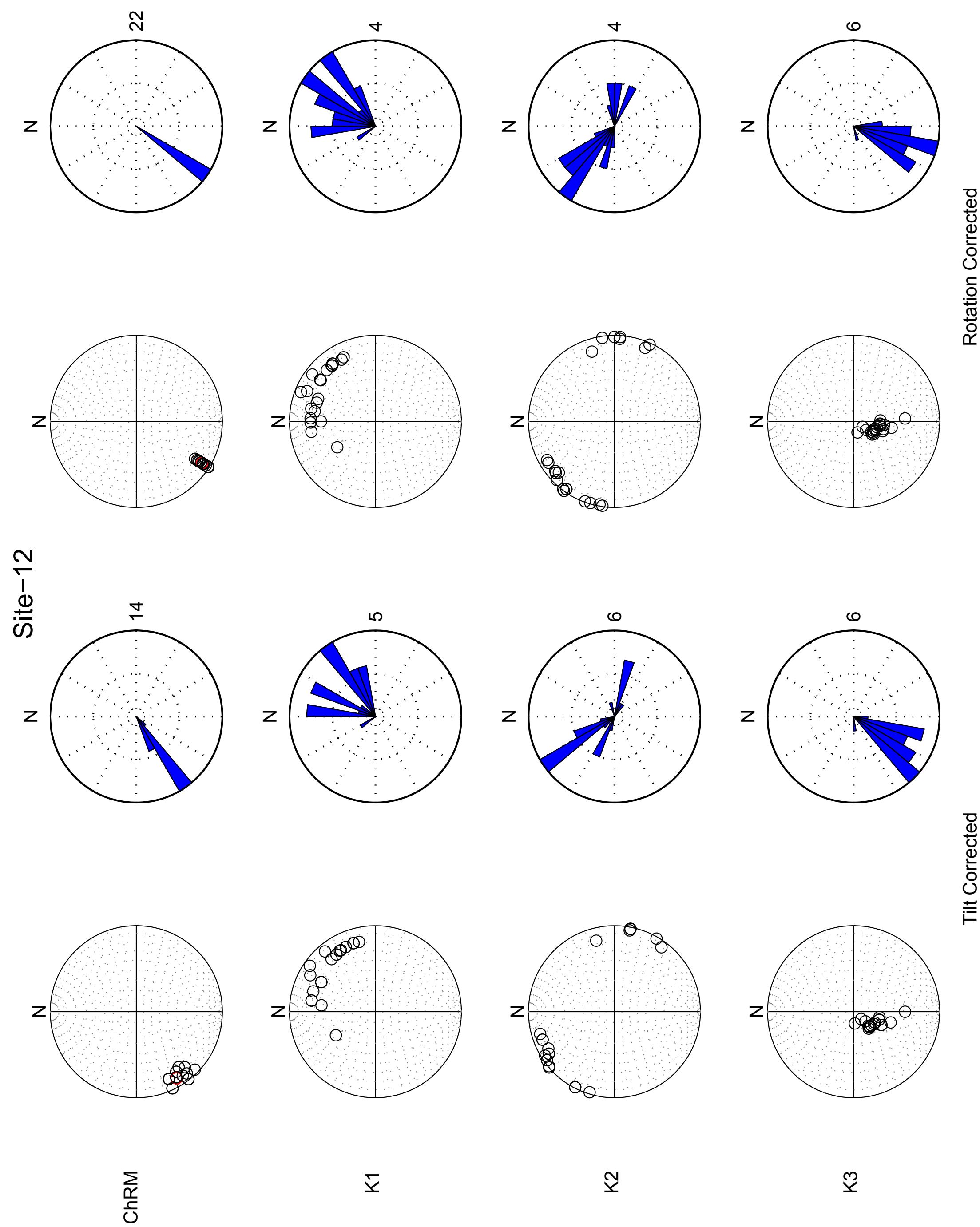
Site−12
ChRM
K1
K2
K3
N
14
5
6
6
22
4
4
6
Tilt Corrected
Rotation Corrected

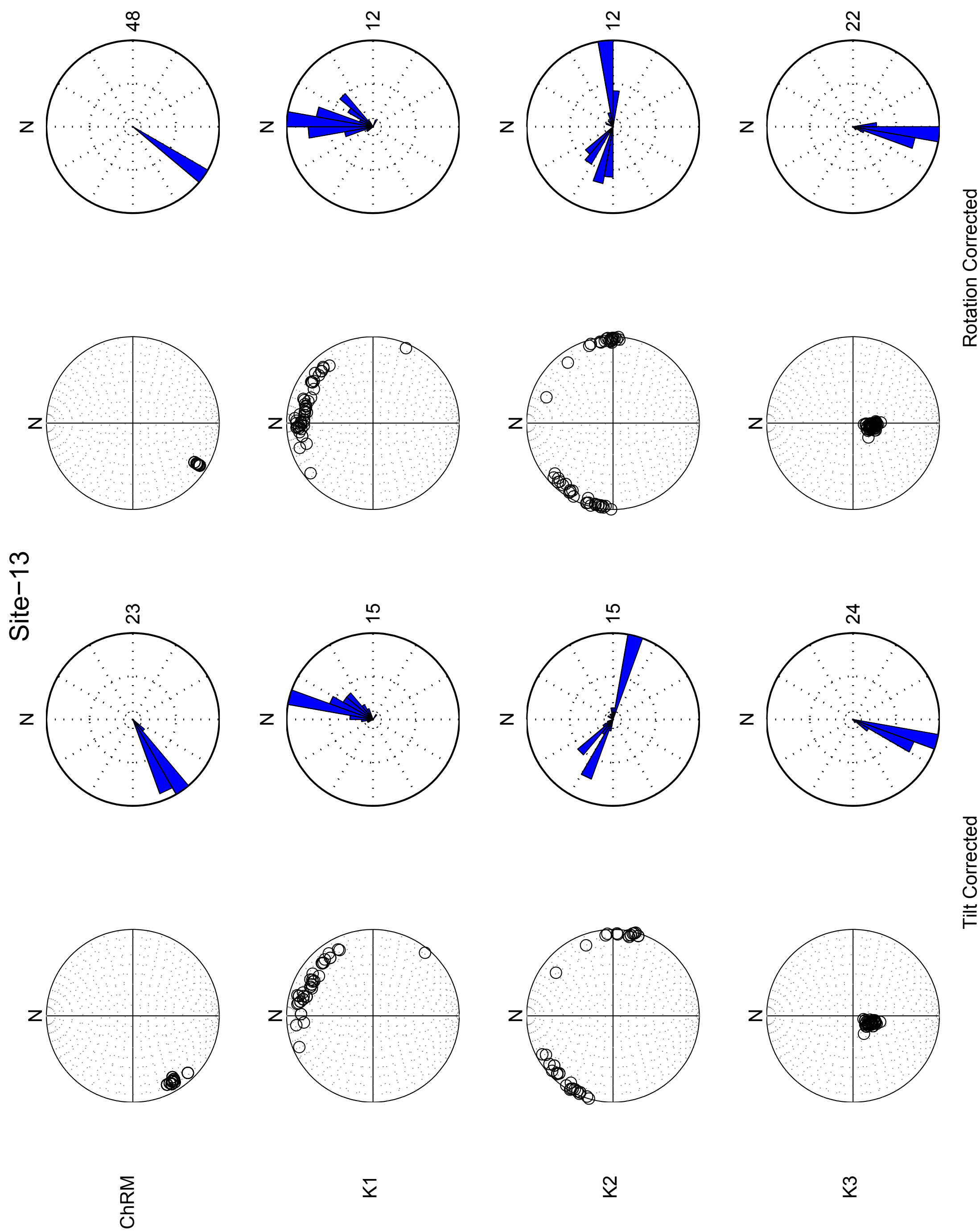
Site−13
ChRM
K1
K2
K3
N
23
15
15
24
48
12
12
22
Tilt Corrected
Rotation Corrected

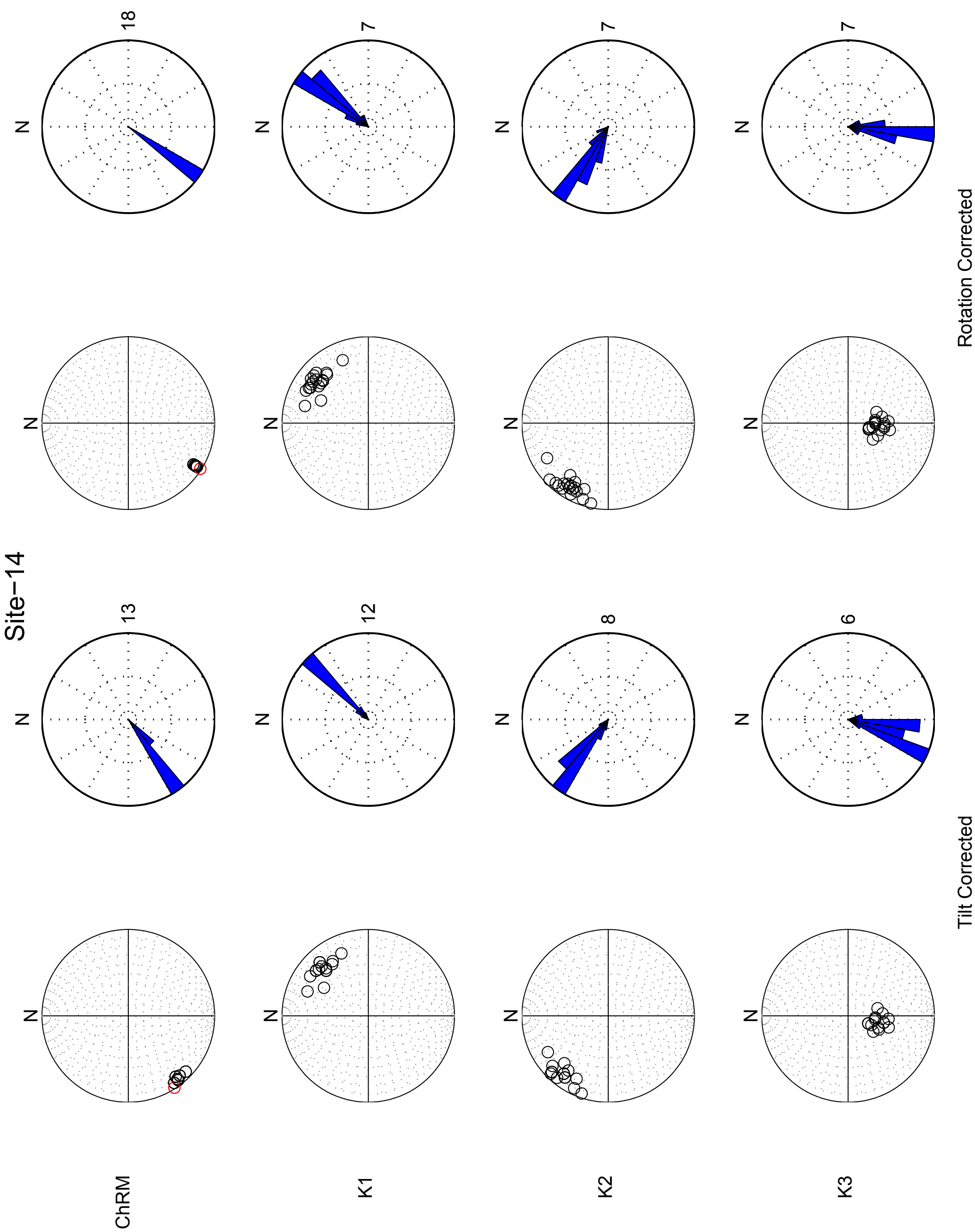
Site−14
ChRM
K1
K2
K3
N
13
12
8
6
18
7
7
7
Tilt Corrected
Rotation Corrected

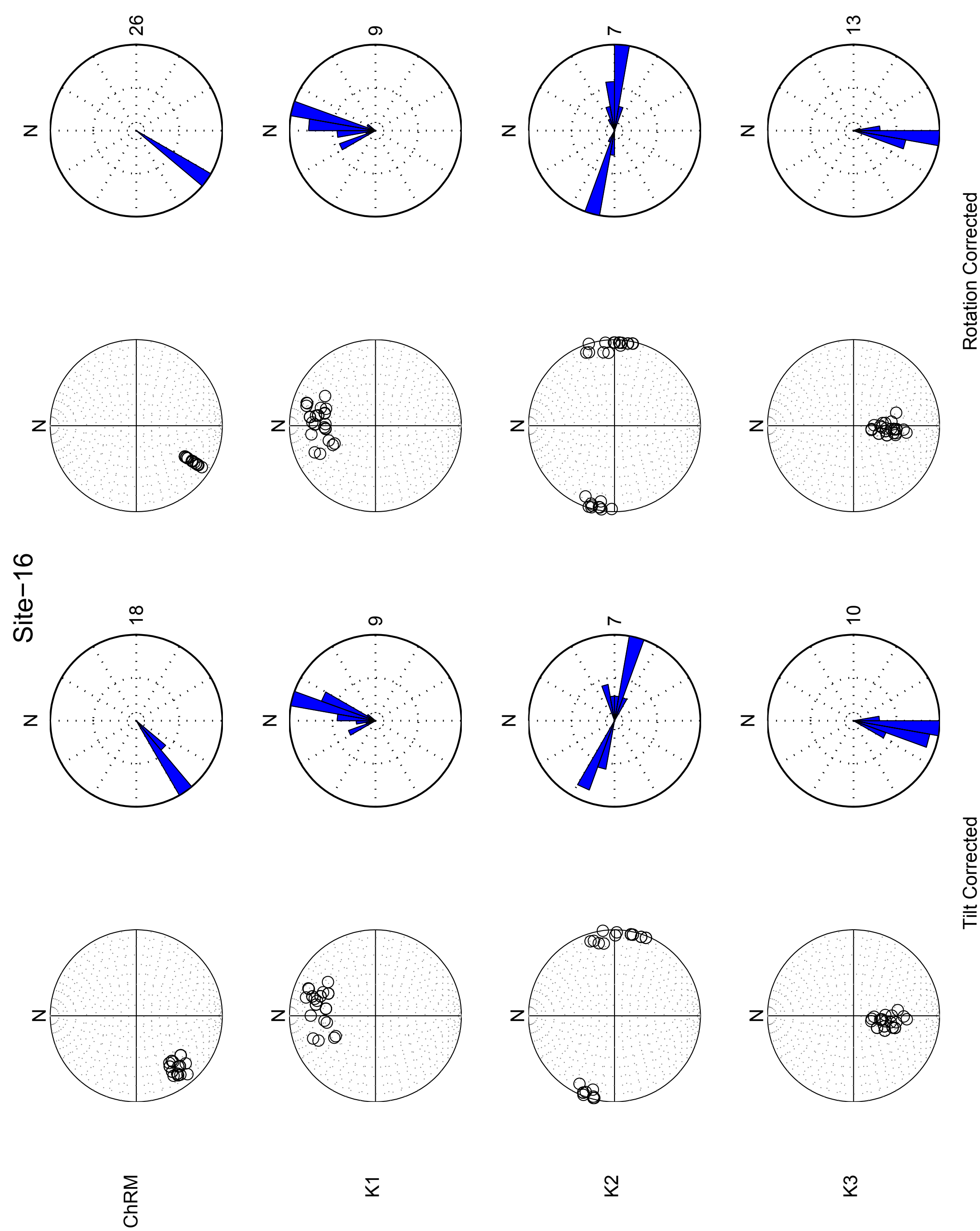
Site−16
ChRM
K1
K2
K3
N
26
9
7
13
18
9
7
10
Tilt Corrected
Rotation Corrected

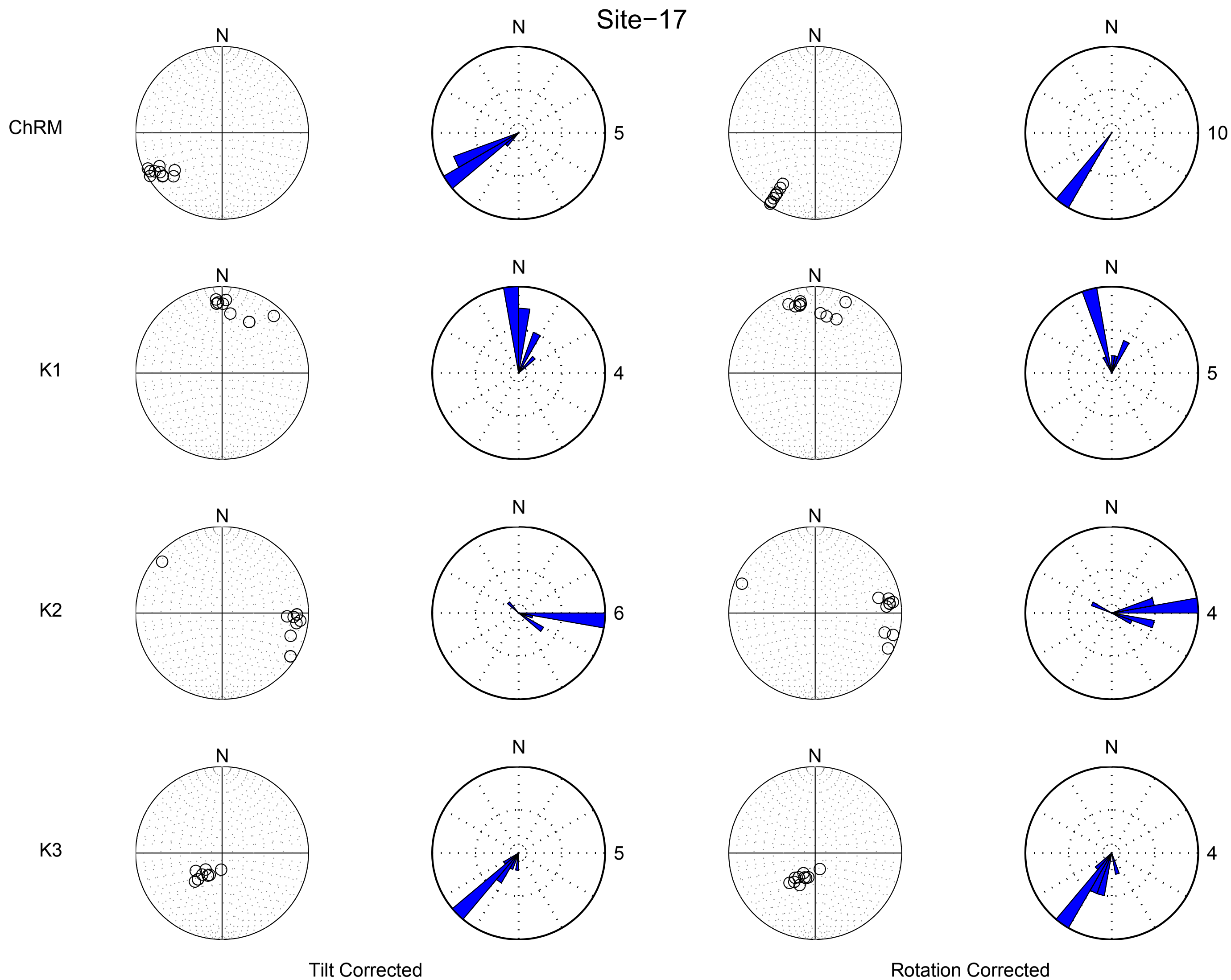
Site−17
ChRM
K1
K2
K3
N
5
10
4
6
Tilt Corrected
Rotation Corrected

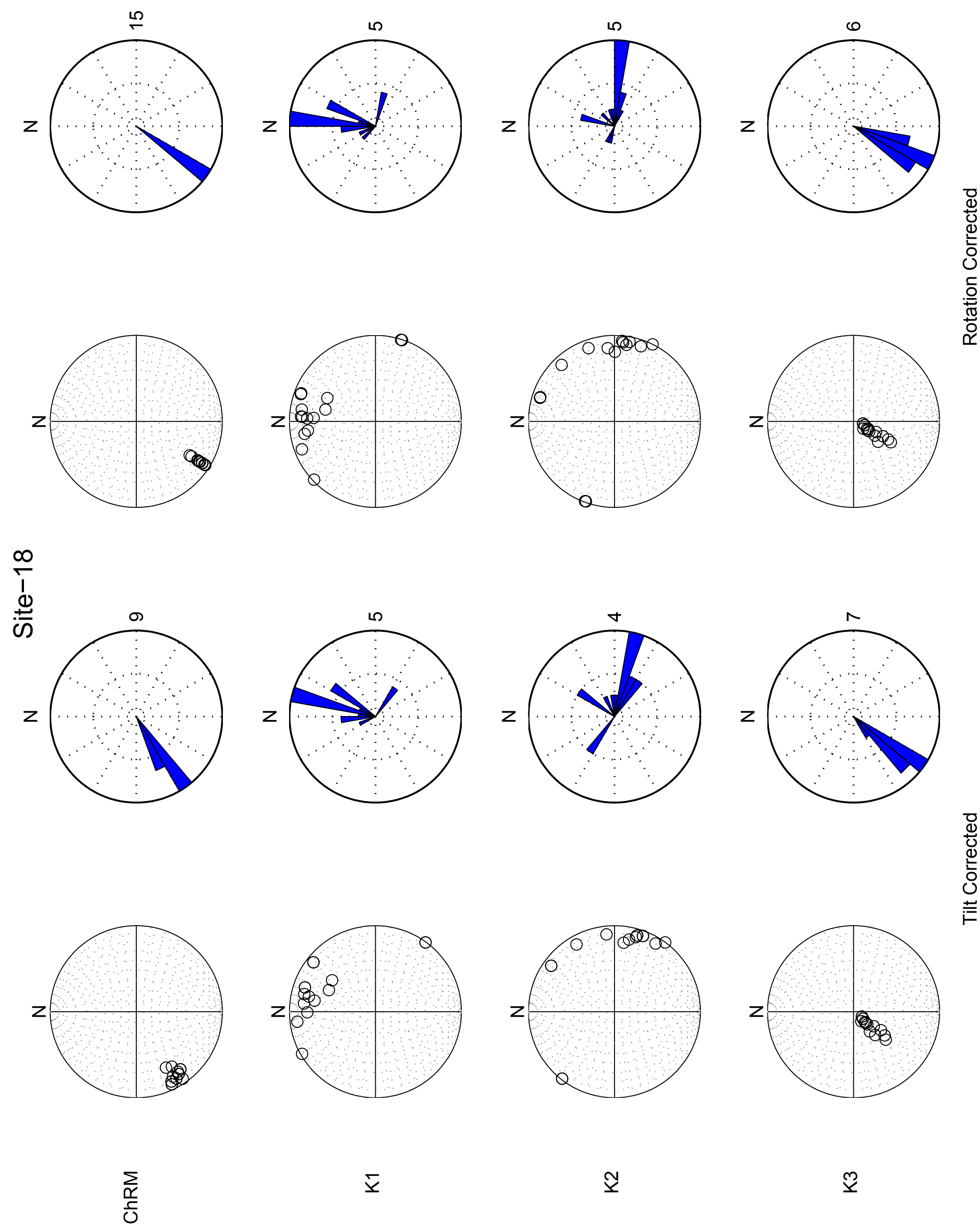

Site−18
ChRM
K1
K2
K3
N
9
5
4
7
15
5
5
6
Tilt Corrected
Rotation Corrected

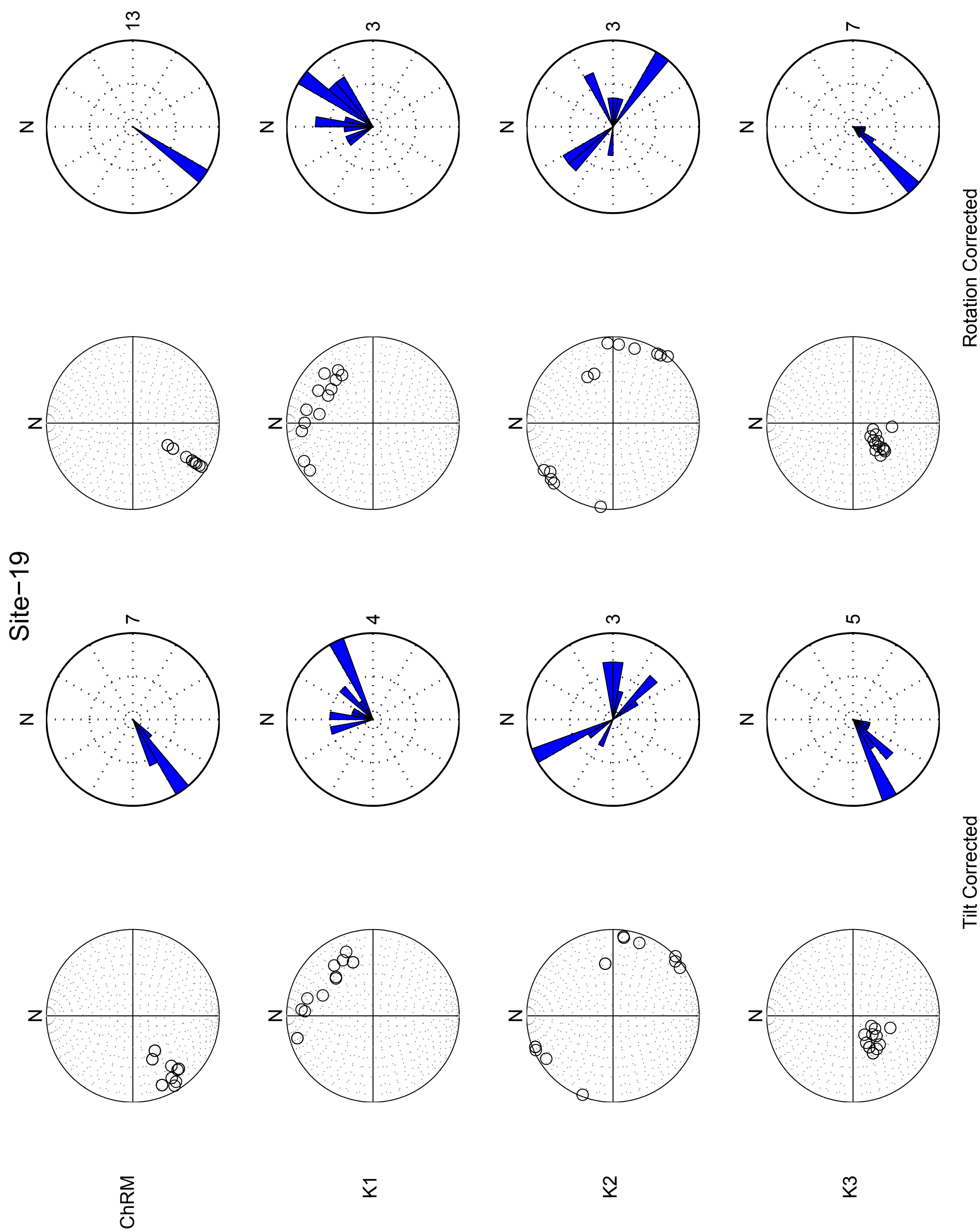

Site−19
ChRM
K1
K2
K3
Tilt Corrected
Rotation Corrected
N
7
4
3
5
13
3
3
7

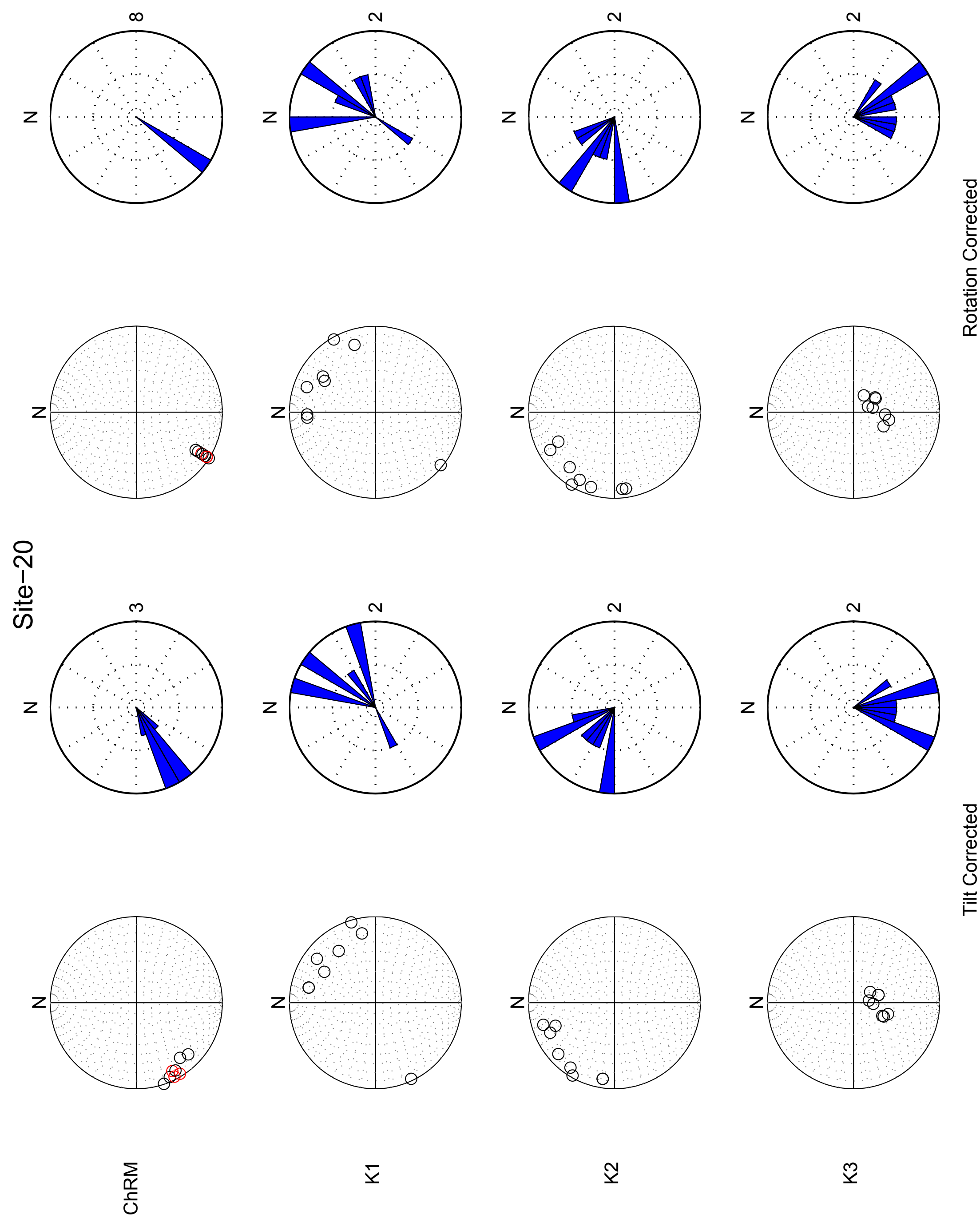
Site−20
ChRM
K1
K2
K3
N
3
8
2
Tilt Corrected
Rotation Corrected

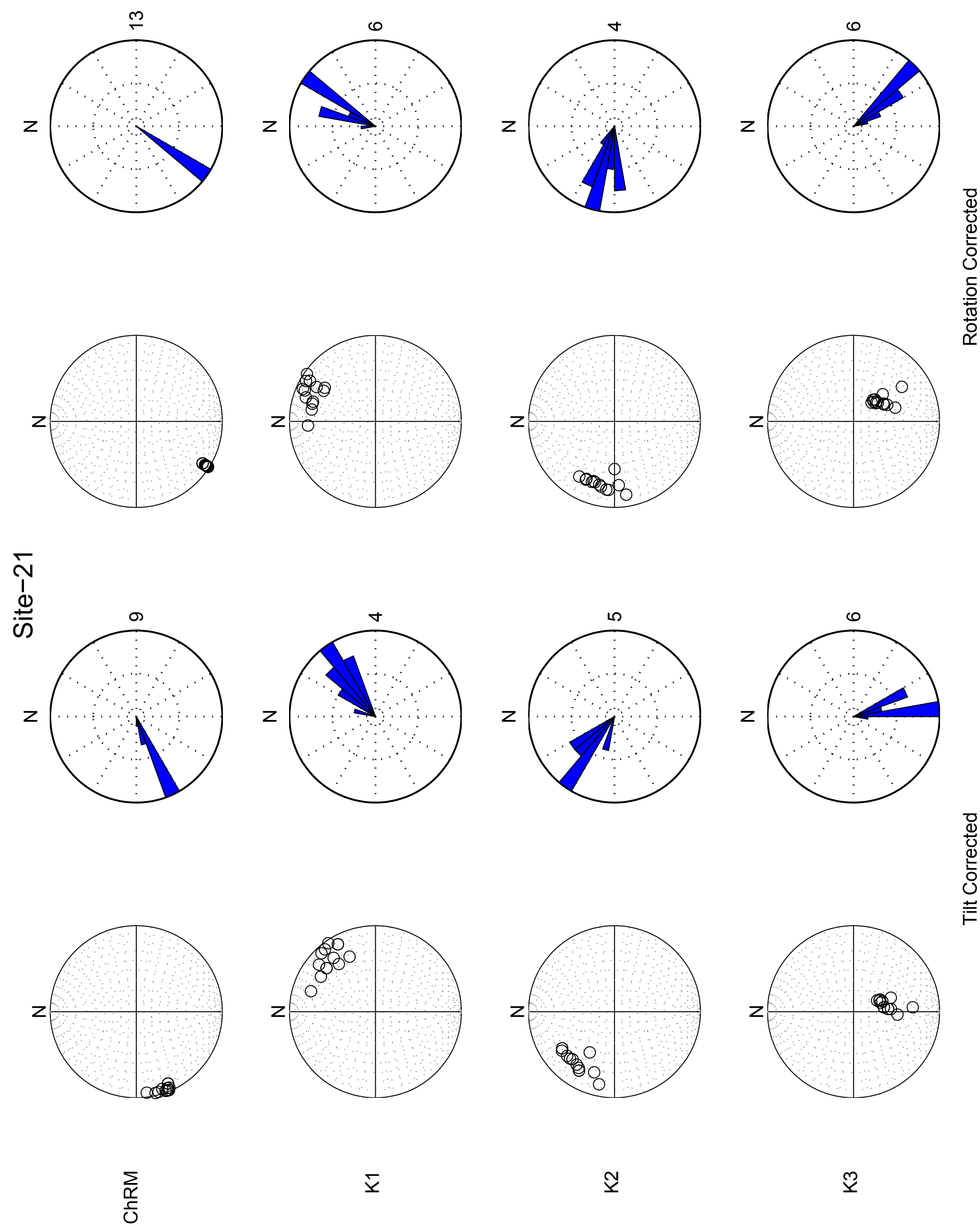
Site−21
ChRM
K1
K2
K3
N
9
4
5
6
13
6
4
6
Tilt Corrected
Rotation Corrected

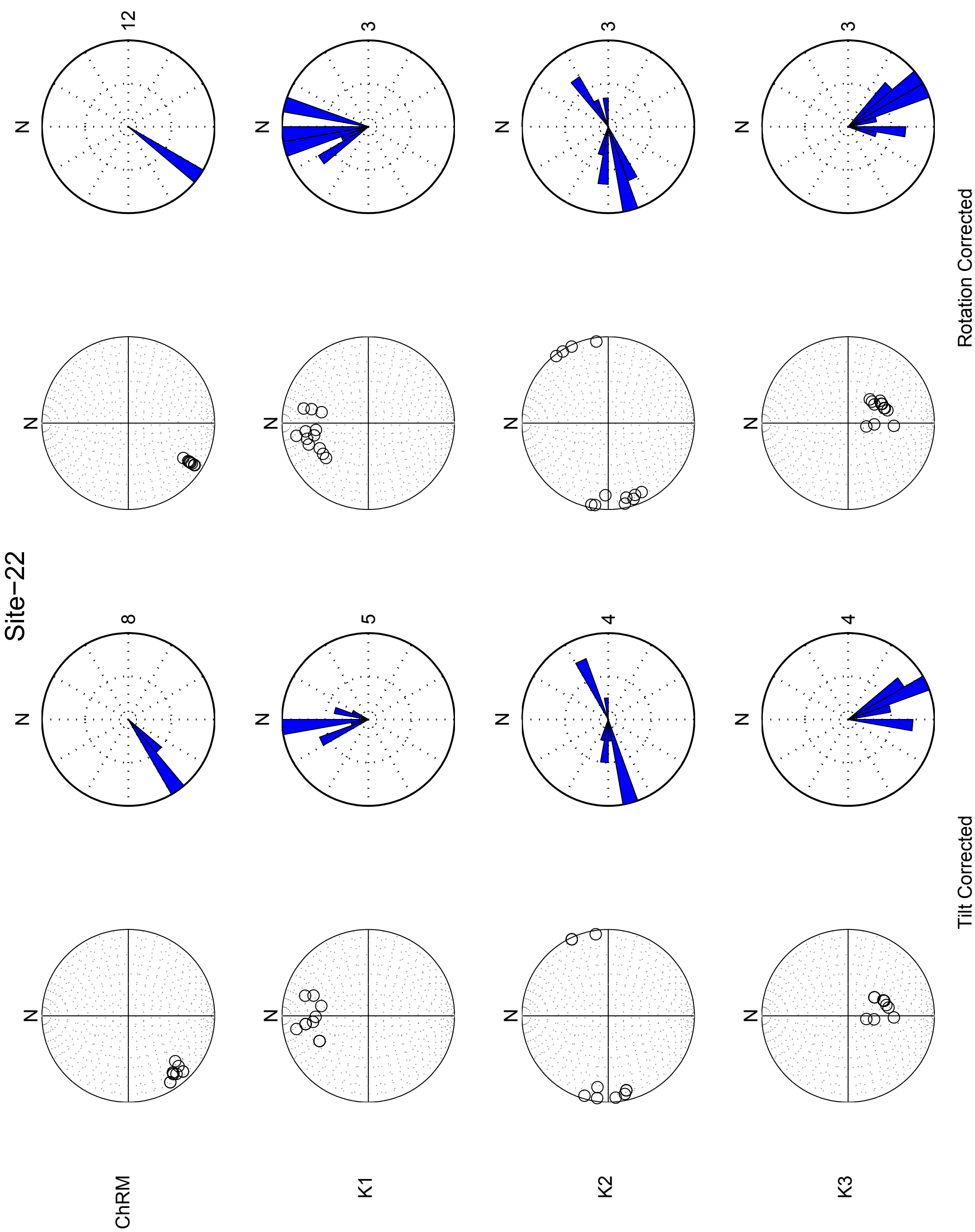

Site−22
ChRM
K1
K2
K3
N
12
8
5
4
3
Tilt Corrected
Rotation Corrected

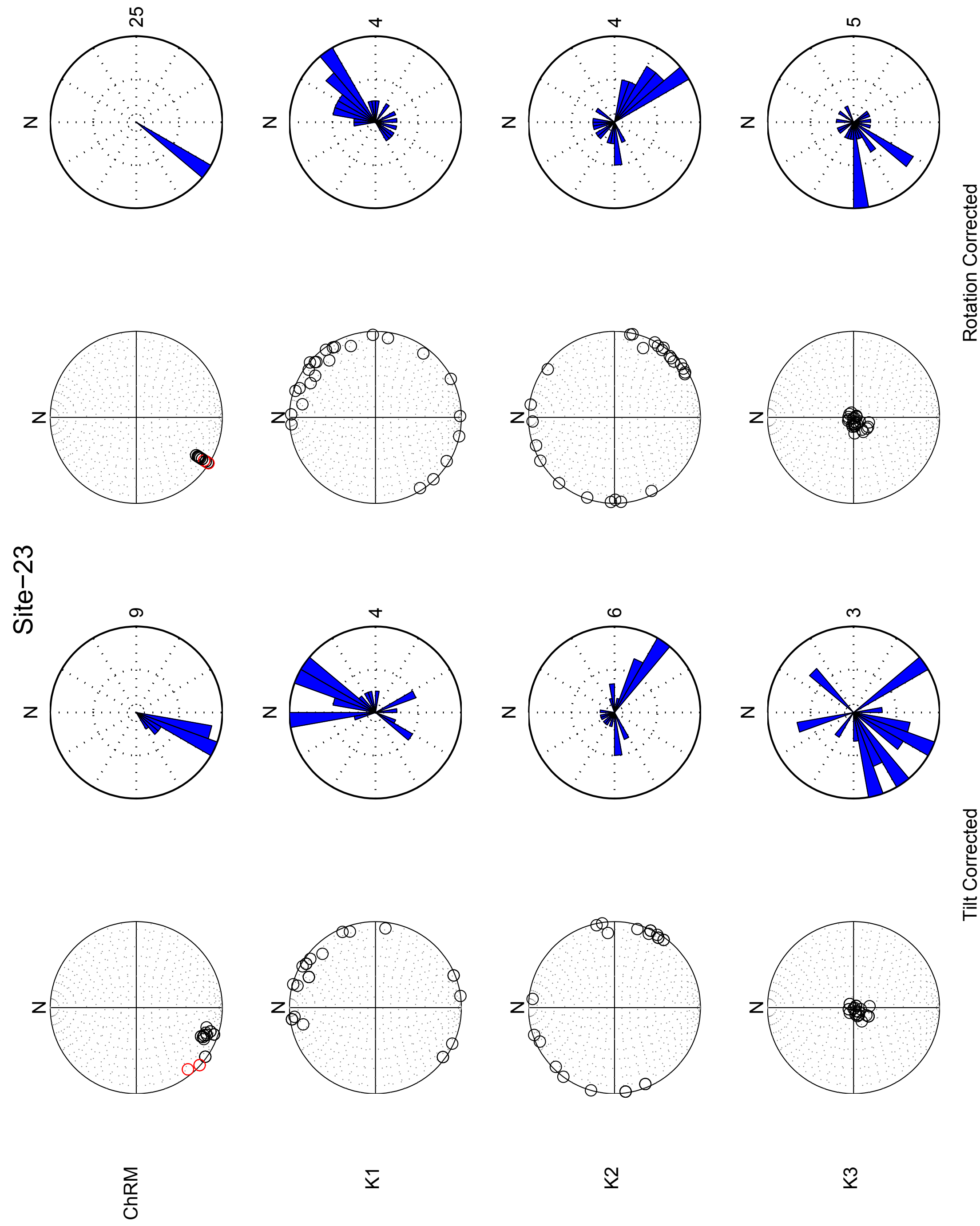
Site−23
ChRM
K1
K2
K3
N
25
4
4
5
9
4
6
3
Tilt Corrected
Rotation Corrected

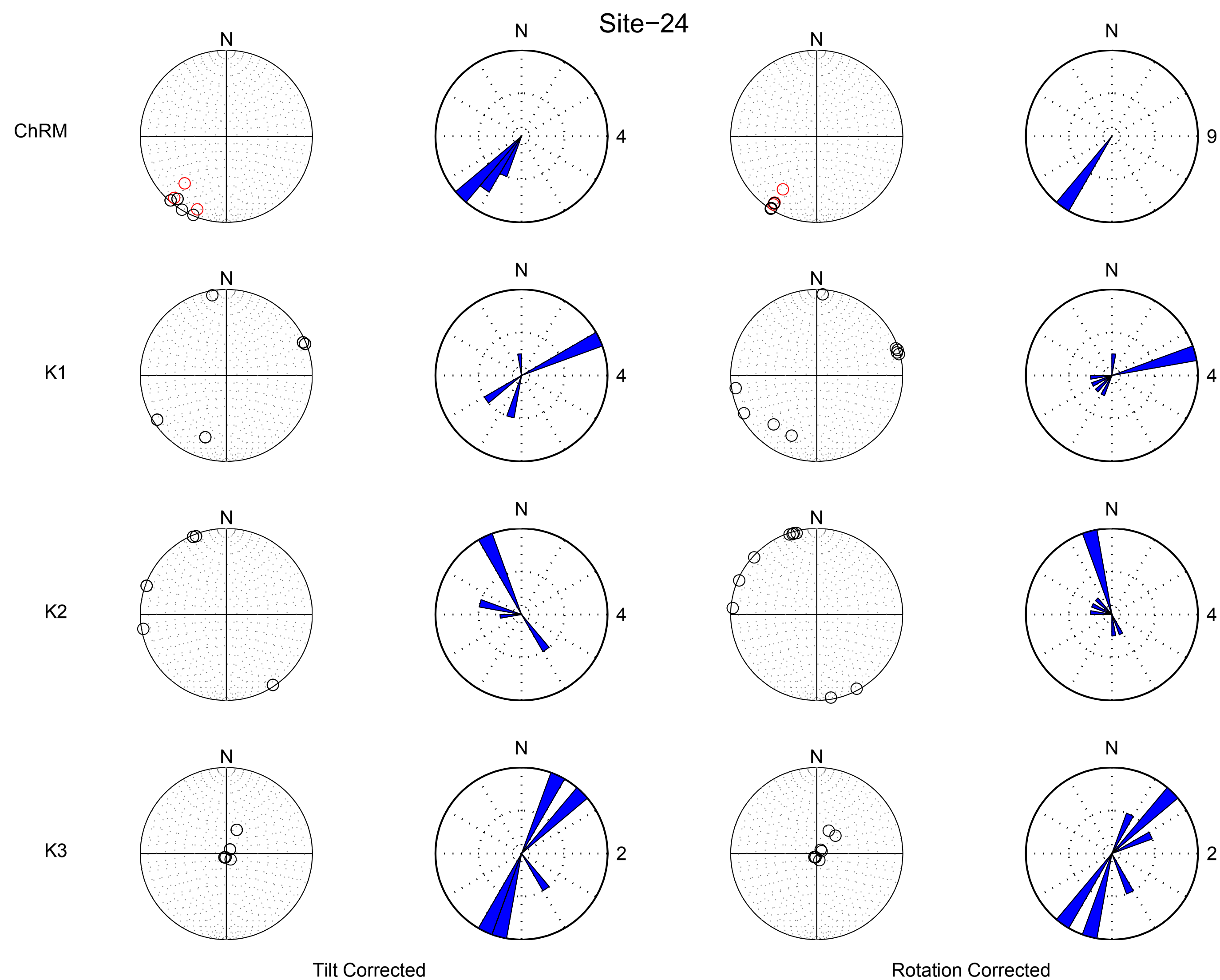
Site−24
ChRM
K1
K2
K3
N
4
9
2
Tilt Corrected
Rotation Corrected

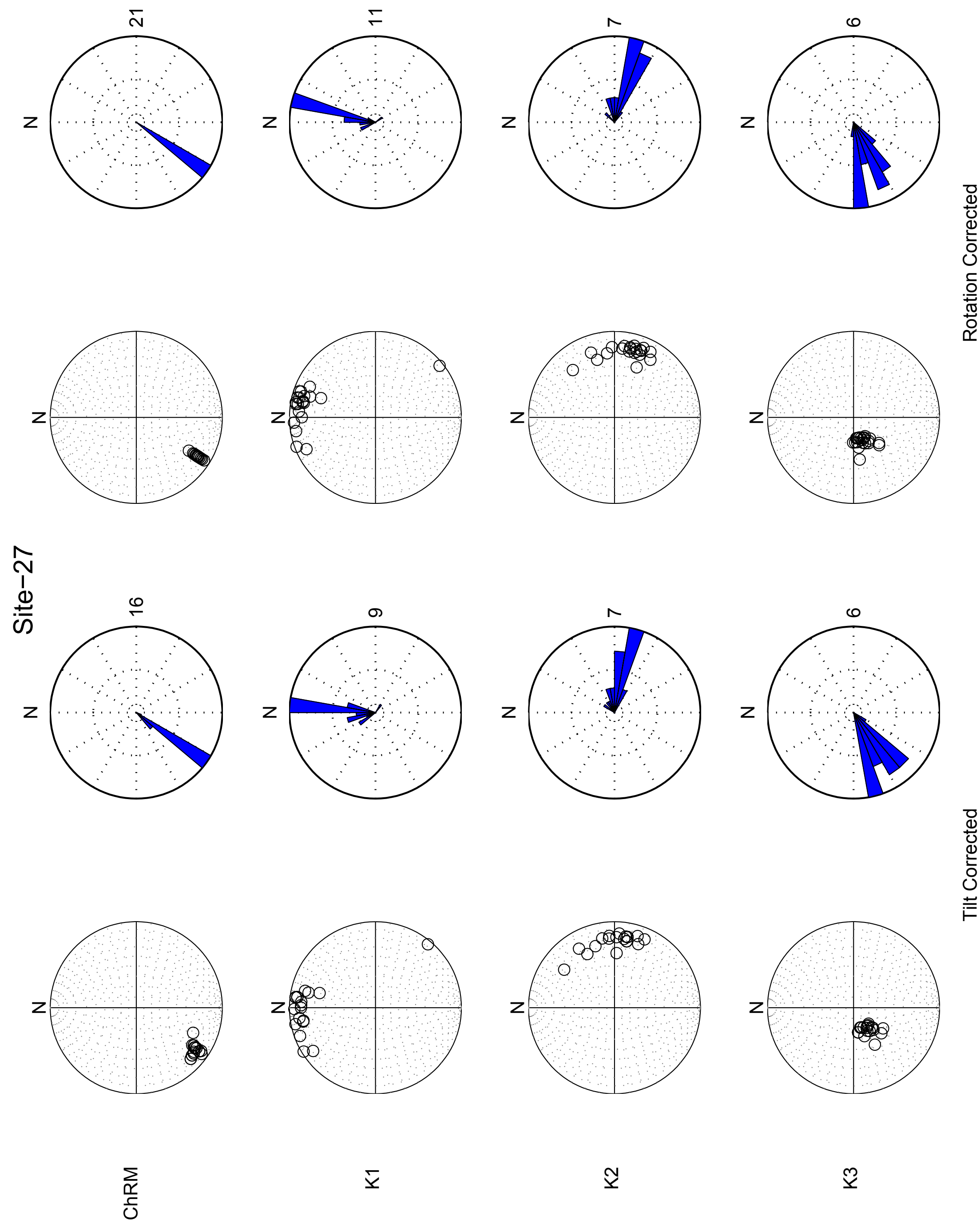

Site−27
ChRM
K1
K2
K3
N
16
9
7
6
21
11
7
6
Tilt Corrected
Rotation Corrected

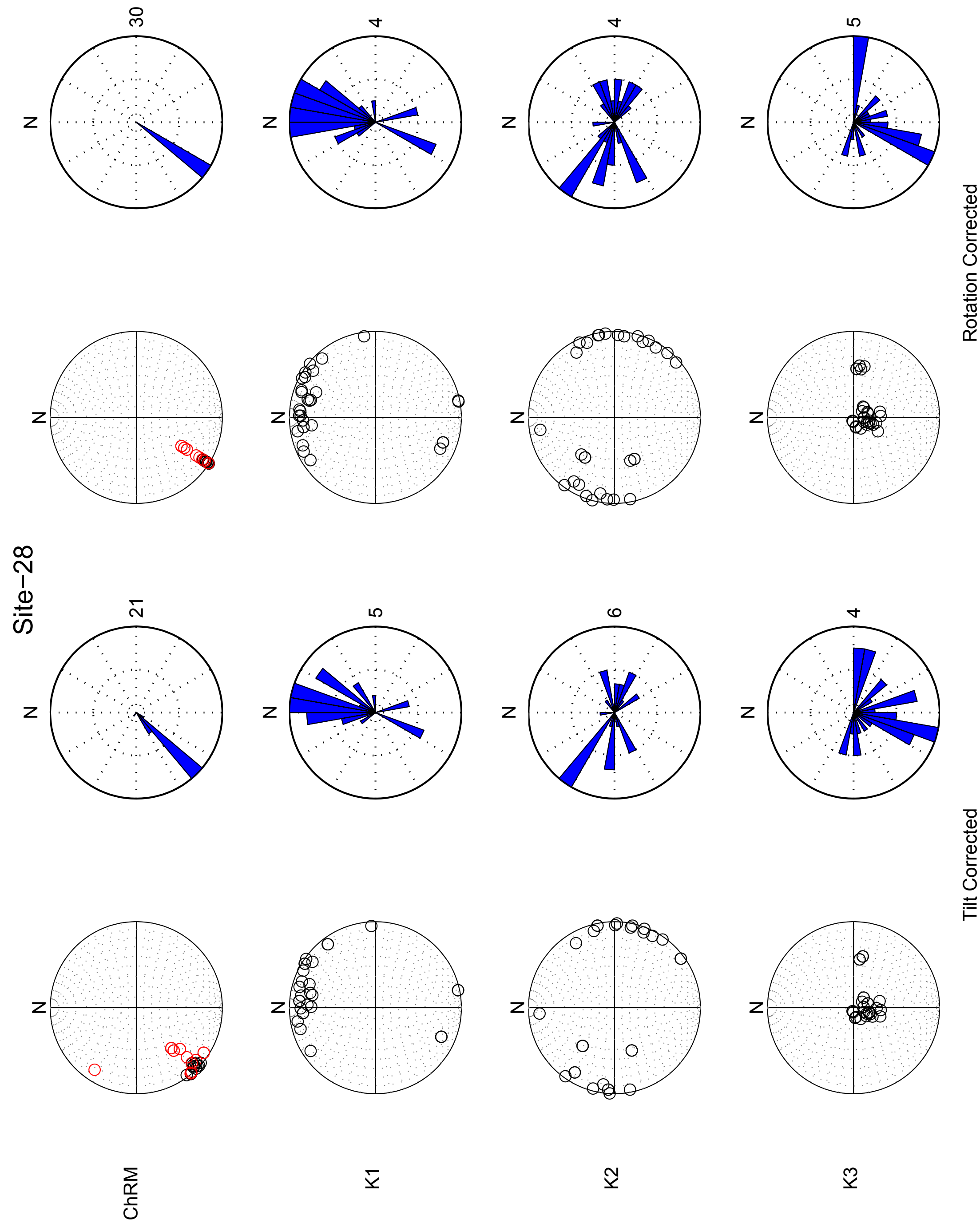
Site−28
ChRM
K1
K2
K3
Tilt Corrected
Rotation Corrected
N
21
5
6
4
30
4
4
5

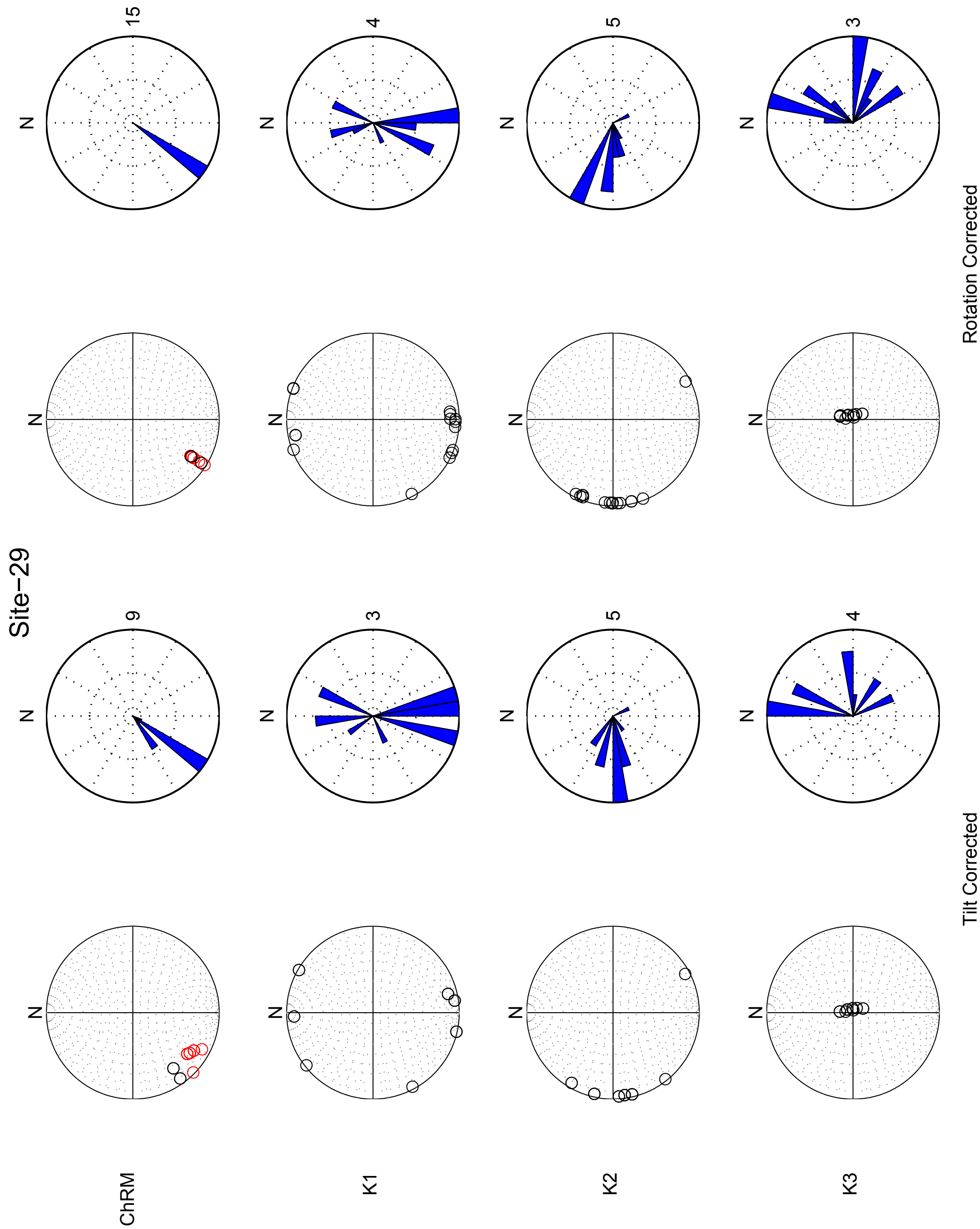
Site−29
ChRM
K1
K2
K3
N
9
3
5
4
15
4
5
3
Tilt Corrected
Rotation Corrected

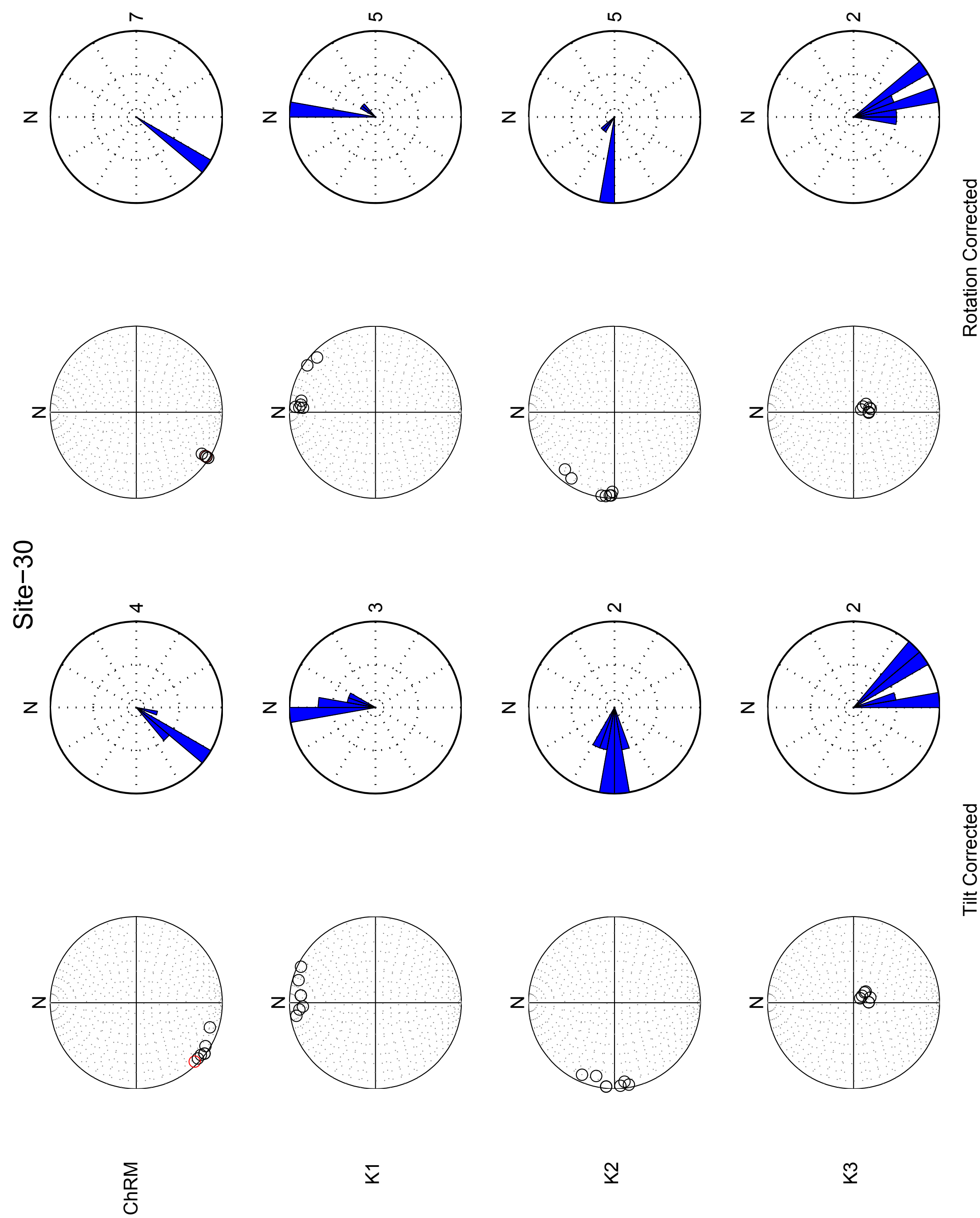
Site−30
ChRM
K1
K2
K3
N
7
5
5
2
4
3
2
2
Tilt Corrected
Rotation Corrected

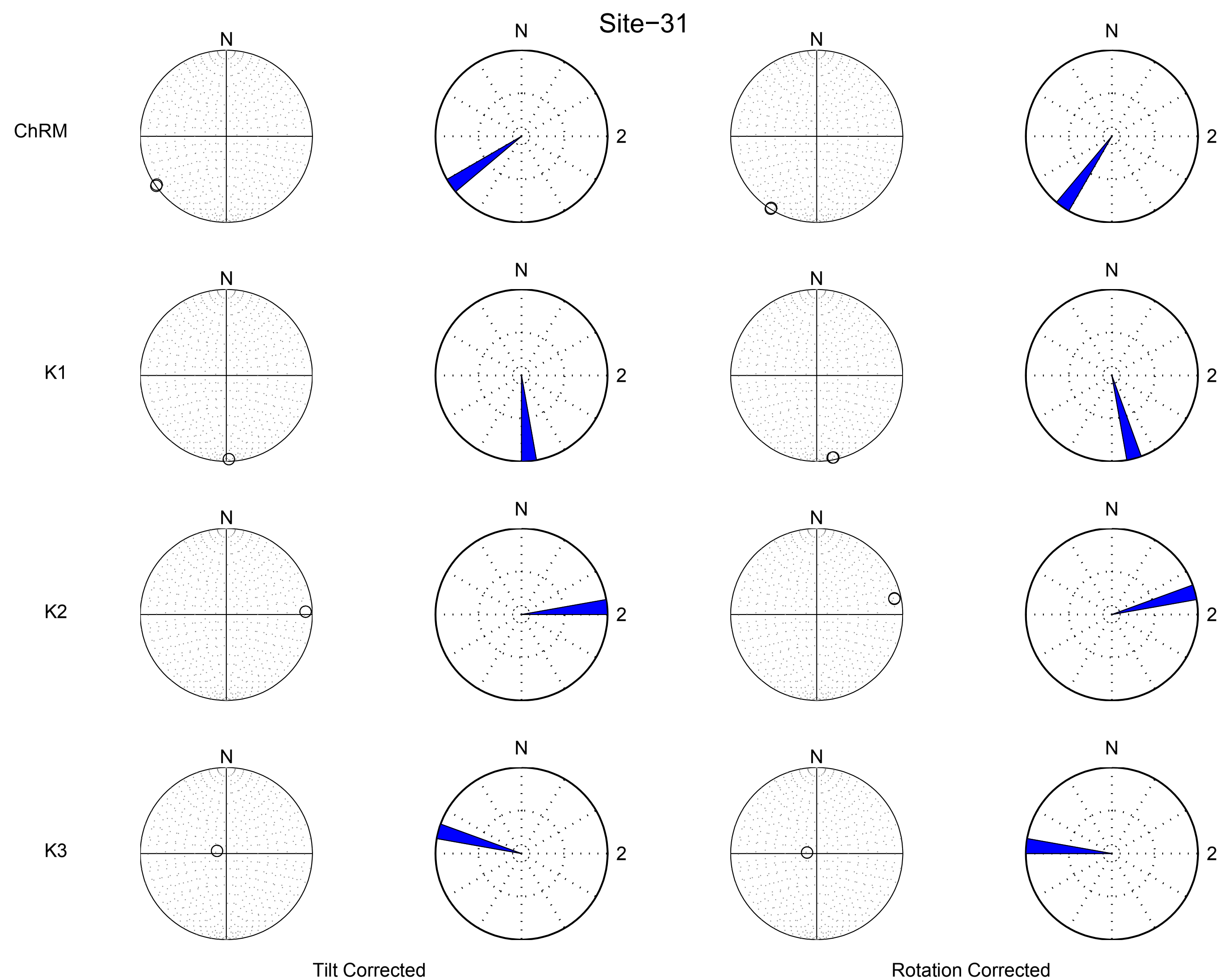
Site−31
ChRM
K1
K2
K3
N
2
Tilt Corrected
Rotation Corrected

Figure 23. Mean ChRM